The role of membrane-actin adhesion in regulating stem cell viscoelastic properties and blebability during chondrogenic differentiation.

Sliogeryte, Kristina

The role of membrane-actin adhesion in regulating stem cell viscoelastic properties and blebability during chondrogenic differentiation

Kristina Sliogeryte

This thesis is presented as part of the requirement for the degree of

Doctor of Philosophy

School of Engineering and Materials Science

Queen Mary University of London

Mile End Road

London E1 4NS

2015

STATEMENT OF ORIGIN

I, Kristina Sliogeryte, confirm that the research included within this thesis is my own work or that where it has been carried out in collaboration with, or supported by others, that this is duly acknowledged below and my contribution indicated. Previously published material is also acknowledged below.
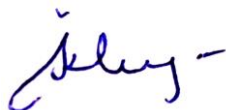
I attest that I have exercised reasonable care to ensure that the work is original, and does not to the best of my knowledge break any UK law, infringe any third party's copyright or other Intellectual Property Right, or contain any confidential material.

I accept that the College has the right to use plagiarism detection software to check the electronic version of the thesis.

I confirm that this thesis has not been previously submitted for the award of a degree by this or any other university.

Signature:

Date: 02.02.2015

ABSTRACT

This thesis examines how chondrogenic differentiation of human mesenchymal stem cells (hMSCs) regulates the interaction between the cell membrane and the actin cortex, thereby controlling cell biomechanics. The thesis also investigates the viscoelastic properties of primary articular chondrocytes and the effect of dedifferentiation. Micropipette aspiration was used to measure the pressure required for membrane-cortex detachment as well as the apparent equilibrium and instantaneous moduli based on fitting the standard linear solid model to the temporal changes in aspiration length induced by a step negative pressure. Simultaneous live cell confocal imaging of actin dynamics was achieved by transfecting cells with LifeAct-GFP.

The studies herein demonstrate that the strength of the membrane-cortex adhesion increased from 0.15 kPa in stem cells to 0.71 kPa following chondrogenic differentiation of hMSCs. This effect was associated with a reduced susceptibility to mechanical and osmotic bleb formation and an increase in the apparent modulus of the differentiated stem cells as well as reduced cell migration. Differentiated stem cells expressed greater levels of the membrane-cortex ERM (ezrin, radixin and moesin) linker proteins at both gene and protein level. Transfection of undifferentiated stem cells with dominant active ezrin-T567D-GFP increased the strength of the membrane-cortex bond. This suggests that increased expression of ERM in differentiated cells is responsible for the reduced blebability and increased modulus observed. Differentiated cells also exhibited greater F-actin density and slower actin remodelling, based on FRAP analysis of cells transfected with LifeAct-GFP, which may also influence cellular viscoelastic properties. Finally the thesis demonstrates that dedifferentiation of primary chondrocytes also increased F-actin density and expression of ERM linker proteins with associated alterations in membrane-actin adhesion and cellular viscoelastic properties. In summary this study provides new insights into the role of membrane-actin cortex adhesion and the expression of ERM linker proteins in regulating the mechanical properties of chondrocytes and mesenchymal stem cells.

ACKNOWLEDGEMENTS

TABLE OF CONTENTS

LIST OF FIGURES

LIST OF TABLES

CHAPTER 1
Stem cell mechanics and structure

1.7.5   Mechanically induced blebbing

1.8   A<small>IMS AND</small> O<small>BJECTIVES</small>

1 STEM CELL MECHANICS AND STRUCTURE

1.1 Stem cells

1.1.1 Introduction to stem cells

Stem cells are undifferentiated cells that have the ability to self renew and to differentiate under specific conditions into other types of cells with specialised cell functions and properties (Li and Xie, 2005). Stem cells can divide symmetrically into two daughter cells or asymmetrically into a daughter cell and a differentiated cell. Their ability to differentiate down to specific lineages has led to increasing use of stem cell implantation within tissue engineering and regenerative medicine strategies (Mironov*, et al.*, 2004). Usually stem cells are classified into totipotent, pluripotent and multipotent classes. Totipotent cells can differentiate into any type of cell and therefore have the ability to form an entire organism. Pluripotent cells can give rise to any cell type of all germ layers, such as ectoderm, mesoderm and endoderm, but are unable to form a whole organism. Multipotent stem cells have an ability to differentiate into cells within a particular lineage (Bhattacharyya, 2012). According to their origin they can be classified into embryonic or adult multipotent stem cells

Embryonic stem cells usually are derived from the developing blastocysts, but they can be proliferated in vitro. The first embryonic stem cells were derived from mice (Evans and Kaufman, 1981) but subsequent work by J Thomson led to the first human embryonic stem cell line in 1998 (Thomson*, et al.*, 1998). Human embryonic stem cells cultured in vitro can divide up to 300 times and possess the characteristics of stem cells (Amit*, et al.*, 2000). However, the scientific applications of human embryonic stem cells in research are limited, due to ethics and regulations.

Adult stem cells are undifferentiated cells that are found in many organs and tissues such as blood vessels, skeletal muscle, skin, bone marrow and others. The major roles of adult stem cells are to maintain and repair the tissue in which cells exist. Like other stem cells, these cells exhibit characteristics such as self-renewal and differentiation, However the proliferation of these cells in vitro is limited (Digirolamo*, et al.*, 1999). In the tissue adult stem cells are found in very small numbers.

The advantage of using adult stem cells as part of a tissue engineering therapy is that they are absent of immunogenicity and can be cultured in vitro, differentiated into the required lineage and later reintroduced into the patient. However, adult stem cells can be sparse in vivo and difficult to isolate from tissue or difficult to culture and expand in in vitro conditions. Some examples of adult stem cells are hematopoietic stem cells, epithelial stem cell, neural stem cell or mesenchymal stem cell. The following section will be focused on mesenchymal stem cells.

1.1.2 Human mesenchymal stem cells – isolation and morphology

Human mesenchymal stem cells (hMSC) are the precursors for cells that originated from mesoderm cells such as osteocytes, adipocytes and chondrocytes. The richest source of hMSCs are in the bone marrow, however they can also be found in a variety of tissues including peripheral blood, placenta, umbilical cord, skeletal muscle and adipose tissue (Pittenger, *et al.*, 1999).

The first isolation of bone marrow cells was made by Friedenstein and co-workers (Friedenstein, *et al.*, 1976). Mononucleated cells including stem cells can be isolated from bone marrow by a density gradient centrifugation. Red blood cells sediment at the bottom, whilst the platelets rinse to the top and leaving the mononucleated cells in the middle layer. These isolated mononucleated cells are then plated in a culture dish and the hMSCs are separated based on their ability to adhere to the substrate. The resulting hMSCs can be expanded for more than 50 population doublings without senescing or differentiating, however their proliferation rate does reduce beyond 30 population doublings (Reyes, *et al.*, 2001). Experimental studies have shown that hMSCs can undergo up to 15 population doublings while maintaining an ability to differentiate toward the osteogenic lineage, however they failed to differentiated into adipocytes (Bruder, *et al.*, 1997, Digirolamo, *et al.*, 1999).

HMSCs are characterised by having a relatively long and narrow cell body, a large nucleus with dispersed chromatin network. However, it is unclear whether the isolated hMSC population is homogeneous or whether other cell types from the bone marrow aspirate persist in culture. For example fibroblasts have a similar morphology and attachment making it difficult to distinguish a pure population of hMSCs. For better separation, molecular surface markers such as CD44 and STRO-1 can be used to identify the hMSCs (Ishii, *et al.*, 2005).

1.1.3 Stem cell differentiation and mechanobiology

The multipotency of MSCs is characterised by their capability to differentiate into different mesodermal and non-mesodermal tissues (Fig. 1.1) (Pittenger, *et al.*, 1999). Chemical stimuli in the form of specific growth factors and media components can be used to stimulate differentiation down different lineages. For example adipogenic differentiation can be induced in expanded hMSCs with culturing media containing 1-methyl-3-isobutylxanthine, dexamethasone, indomethacin and insulin. Differentiated cells show developed lipid vacuoles and express lipoprotein lipase (LPL) and specific fatty acid binding protein aP2 (Pittenger, *et al.*, 1999).

Additional supplements such as β-glycerolphosphate, ascorbic acid, dexamethasone and foetal bovine serum in culture medium can lead cells toward osteogenic differentiation (Pittenger, *et al.*, 1999). Cells cultured in such conditions demonstrate osteoblastic morphology, increased expression of alkaline phosphatase and calcium rich mineralised extracellular matrix (Birmingham, *et al.*, 2012).

To promote chondrogenic differentiation of hMSCs requires growth factors such as TGF-β ideally coupled with a three dimensional environment and serum free culture medium. The growth factors regulate expression of cartilage specific genes/proteins such as collagen type II and aggrecan (Johnstone, *et al.*, 1998).

Besides chemical induction of stem cell differentiation, mechanical stimuli can also be used. The mechanical strain applied to hMSCs was shown decrease of differentiation toward adipogenic lineage (Sen, *et al.*, 2011). However, uniaxial cyclic strain can be used to stimulate differentiation toward the osteogenic lineage (Sumanasinghe, *et al.*, 2006). Some studies have reported that hydrostatic pressure and compression play a key role in increasing differentiation toward the chondrogenic lineage (Wagner, *et al.*, 2008). The precise cellular mechanisms through which these mechanical stimuli regulate stem cell differentiation are yet unclear.

In addition, it has been reported that matrix stiffness can be used to induce stem cell differentiation. Stem cell differentiation to specific phenotypes is sensitive to tissue stiffness. The matrix which mimic soft brain tissue can induce to neurogenic differentiation, stiff matrix which mimic collagenous bone tissue can induce to osteogenic lineage, and matrix comparatively softer can present muscle tissue and

induce cells to myogenic differentiation (Engler*, et al.*, 2006, Reilly and Engler, 2010). Cells cultured on different stiffness of matrices exhibited changes in cytoskeleton structure, forming actin cortex on soft substrates and more defined stress fibre structure on stiff substrates (Ayala*, et al.*, 2011, Yeung*, et al.*, 2005) and changes in gene expression to specific cell phenotypes (Witkowska-Zimny*, et al.*, 2012).

Not only matrix stiffness but also matrix nanotopography (roughness) provides a guidance to stem cell differentiation (McNamara*, et al.*, 2010). The study has demonstrated that stem cells cultured on substrates with lamellar wrinkles, spread adopting pattern shape and are more likely to differentiate to osteogenic lineage. However, cells on substrate with hexagonal patterns remain rounded and differentiate into adipogenic lineage (Guvendiren and Burdick, 2010).
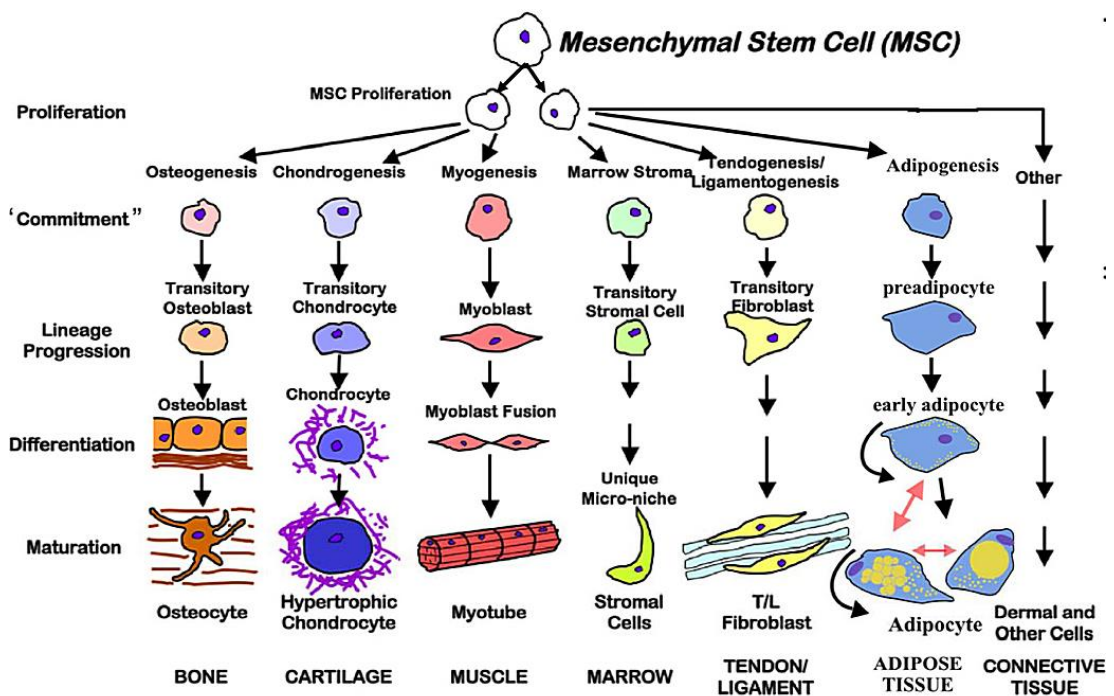
Figure 1.1: Mesenchymal stem cell differentiation. The stepwise cellular transitions from the mesenchymal stem cell to highly differentiated phenotypes are depicted schematically. The individual lineage pathways are arranged from left (best understood) to right (least understood) (Caplan and Bruder, 2001).

1.1.4 Stem cell mechanical properties and their response to differentiation

Differentiation of stem cells has previously been shown to result in changes in cellular and sub cellular mechanical properties. This in turn may influence cell functions such as mechanotransduction, cell migration and gene expression. During hMSC differentiation, the cell's mechanical properties change according to the specific lineage. Cell elastic modulus can be used as an indicator to explain mechanical properties of cells. Cells with a higher elastic modulus are stiffer and deform less compared with softer cells. For example, MSCs induced toward the osteogenic lineage become stiffer while MSCs directed toward adipogenic differentiation are softer compared to naïve hMSCs. To estimate exact elastic properties of a cell is a crucial challenge as it depends on the technique used and the environmental conditions.

1.2 Experimental analysis of cell mechanics

1.2.1 Introduction to different techniques

The most commonly assessed mechanical property of cells is the stiffness/elastic modulus. To determine the mechanical properties of a single cell requires the deformation (d) resulting from a force (F). This provides the structural stiffness (F/d) that may then be used for estimation of the elastic modulus based on analytical models with associated assumptions. The other properties like viscoelastic behaviour and relaxation are time dependant parameters. These parameters can be determined using a number of experimental systems, each of them have advantages and disadvantages.

Which experimental technique will be used depends on the cell type, size and mechanical properties. For investigations of elastic properties of large samples of material, such as tissue, it is comparatively easy to obtain mechanical parameters testing the tension or compression using various methods including stress relaxation and micro/nano indentation. Determination of mechanical properties of individual cells or cell aggregates presents a number of difficulties and the traditional methods used for other materials are unsuitable. Sometimes the stress and strain cannot be measured due to the small size of samples.

Much of the work on cell mechanical properties has involved the following principal techniques: optical tweezers and stretchers, micropipette aspiration, microplates, microneedles (cell poker), cell compression systems, 3D compression, atomic force microscopy (AFM) and scanning acoustic microscopy (SAM). The techniques discussed in the following sections have been used to measure the mechanical properties of a range of cell types. Some techniques, which have been used to investigate molecular mechanical properties rather than cellular properties, are not considered here. The micropipette aspiration system is discussed in more details and the methods used to extract biomechanical parameters of single cells are explained.

1.2.2 Atomic force microscopy

The atomic force microscope (AFM) was invented by Binning, Quate and Gerber in 1986 (Binnig*, et al.*, 1986). A scanning probe microscope can be used for imaging, measurement and manipulation of single cell matter. AFM stiffness measurement is performed by sensing the forces between the cantilever tip and the sample (Fig. 1.2 A). The flexible cantilever acts as a spring and thus accurately measuring cantilever deflection using a position sensor and laser beam deflection yields force data. The larger the cantilever deflection, the higher the force. By controlled vertical movement of the cantilever it is possible to generate a force displacement curve for a given point (Fig. 1.2 B) (Dufrene, 2002).

 AFM can be used in a liquid environment and at 37°C making it suitable for measuring the properties of live cells with minimal preparation artefacts. Compared with other techniques, AFM can be operated in a number of different ways to obtain the information on both a cellular and molecular level. Using force-distance curves, the elastic and adhesion parameters can be estimated. Also the spatial distribution of stiffness can be obtained using a technique known as force mapping, where the array of force-distance curves can be taken over the surface of the cell and mapped in a colour scale relief map (Fig. 1.2 C) (Gaboriaud*, et al.*, 2008). The AFM technique provides the ability to accurately control strain rates and to apply forces in the pico-Newton range. Depending on the investigation, the cantilever tip can be modified in a number of different ways. For example attaching spheres can increase surface contact area (Hsiao*, et al.*, 2008). Also the cantilever tip or spheres can be chemically modified to enable biochemical interactions between the tip and the cell. As with any indentation method which produces force-displacement data, it is necessary to couple

the experimental data with an analytical model to derive mechanical properties such as cell elastic modulus. The light microscope is used for AFM to position the cantilever tip and sample.
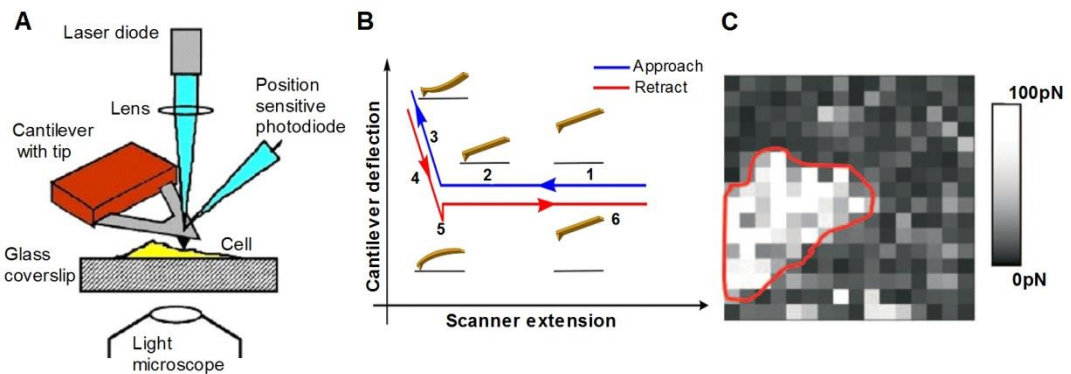
Figure 1.2: AFM technique. (A) A schematic representation of the AFM technique used in measurement of cell properties. (B) A typical force-distance curve with positions of cantilever indicated at (1) equilibrium state, (2) the tip approaches the surface, (3) the deflection of cantilever on the surface, (4) retraction of cantilever, (5) cantilever detaches from the surface and (6) the tip returns to equilibrium position (Maver*, et al.*, 2013). (C) Spatially resolved map of adhesion forces between tip coated with heparin and surface of *M. bovis* BCG cell (Gaboriaud*, et al.*, 2008).

1.2.3 Optical tweezers and traps

Optical tweezers, also known as optical traps or laser traps, were developed by Arthur Ashkin, who first showed particle manipulation using a light beam (Ashkin, 1970, Ashkin*, et al.*, 1986).

The basic principle of optical tweezers is that the laser is focused on a dielectric particle, such as a silica bead, whose refractive index is higher than the suspension medium. That produces a gradient force in the pico-Newton range which moves the particle towards the focal point of the beam. Effective trapping is only realised when particles are optically resolvable. Trapping efficiency increases with laser intensity, but high power can be destructive to biological samples. The beads are coated chemically which allows attachment to the cell surface or to specific molecules.

This technique can be used to measure mechanical properties of single cells (Fig. 1.3 A). A study has reported that red blood cells were directly trapped and cell shape

recovery after deformation was measured (Bronkhorst, *et al.*, 1995). Another study has indicated that the shear modulus of red blood cells can be estimated from cell deformation. Silica beads were attached to the cell membrane and manipulated by the deforming cell (Fig. 1.3 B) (Henon, *et al.*, 1999). The cell deformation under applied forces is imaged by using a light or fluorescence microscopy. Due to the limited force application range, optical tweezers are unable to extent large deformations. In contrast a new related technique called optical stretcher has been developed based on a double beam trap in which two opposite laser beams trap the object in the middle (Fig. 1.3 C). This requires the refractive index of the object to be larger than the surrounding environment and the beam size to be larger than the trapped object (Guck, *et al.*, 2000). Recent studies have shown that optical stretcher can be used successfully for measuring cell deformation which allows estimating the mechanical properties of cells (Fig. 1.3 D). An optical stretcher was successfully used for red blood cells and fibroblasts to determine mechanical properties (Guck, *et al.*, 2001).
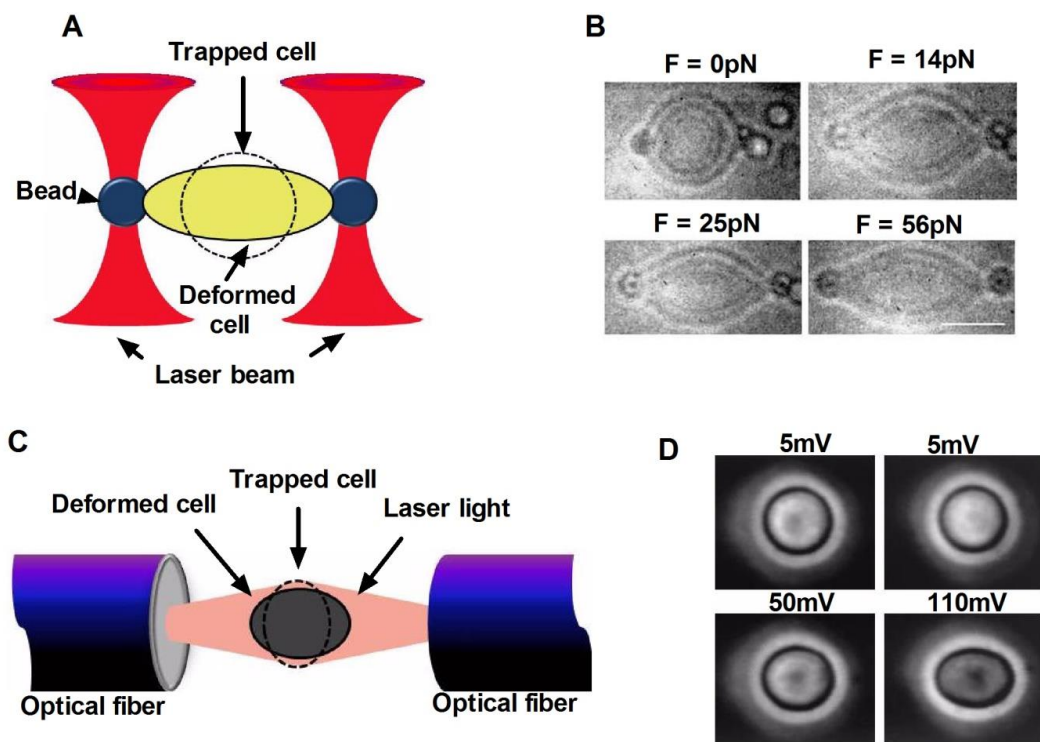
Figure 1.3: (A) Schematic illustration of optical tweezers focused on beads attached to a cell. (B) Brightfield images of red blood cell deformation in response to range of applied forces. Scale bar, 5 μm. Modified from (Henon, *et al.*, 1999). (C) Representation of optical stretcher. (D) Phase contrast images of red blood cell deformation during the process of stretching by changing laser power. Modified from (Guck, *et al.*, 2001).

1.2.4 Cyto compression system

In cyto compression a single isolated cell is compressed between the two parallel surfaces measuring the applied force and the deformation of the cell (Fig 1.4). The applied forces are monitored using a force transducer while the deformation of the cell with time is recorded using a light microscope. This compression testing system is capable of determining the mechanical properties of cells such as yeast cells and plant cells (Blewett, *et al.*, 2000, Smith, *et al.*, 2000) and can be used for other materials such as alginate microspheres (Wang, *et al.*, 2005). This technique has been used to study the mechanical properties of plant cells, such as bursting forces. The experiment has shown that the bursting force of two week old tomato cells was 3.6 mN (Blewett, *et al.*, 2000). Another study has shown the bursting force was 8.7 µN for attached mouse myoblast cells (Peeters, *et al.*, 2005). This compression technique has also been implemented for microbial cells to understand the mechanical properties of the cell wall (Smith, *et al.*, 2000). Other researchers have investigated mechanical properties of animal cells (Zhang, *et al.*, 1992), bacteria (Shiu, *et al.*, 1999) and microspheres (Wang, *et al.*, 2005).
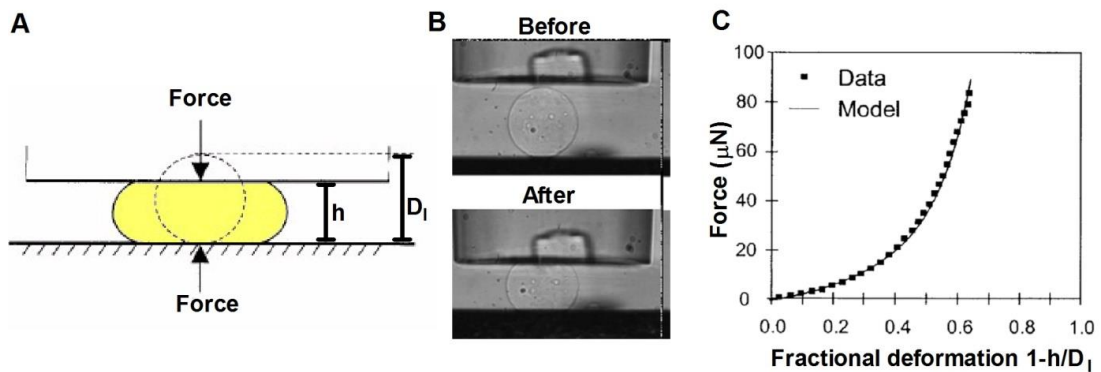
Figure 1.4: (A) A schematic representation of a cyto compression system. The top plate is moved at constant velocity to compress the cell. D_i is the initial height of the cell before deformation and h is the height of cell after deformation. The plate is connected to force transducer which measures force as a function of time (Smith, *et al.*, 2000). (B) Representative brightfield images of an alginate microsphere before and after compression. (C) Plot of applied forces versus deformation for an alginate microsphere (Wang, *et al.*, 2005).

1.2.5 3D scaffold compression

Another type of compression system has been used by applying the compression forces on cells seeded in 3D agarose or alginate scaffolds and measuring the deformation of the cell (Knight, *et al.*, 2006) (Fig. 1.5). The deformation of the cell and organelles is monitored using a fluorescence microscope. The elastic properties of the cell can be estimated from cell deformation knowing the mechanical properties of the scaffolds. Cells under static compression have shown viscoelastic stress relaxation, which generate cell deformation and changes from ellipsoid to more spherical morphology. Previous studies have shown that for cells seeded in 1.2% and 2% alginate, compression resulted a similar cell deformation and the estimated elastic modulus was 3kPa (Knight, *et al.*, 2002). As cells behave in a viscoelastic manner, finite element models incorporating viscoelastic properties provide more accurate results of cell properties. This technique has the advantage of estimating the cell deformation in 3D environment applying global strain, which is closer to physiological conditions rather than localised cell membrane compression as it often appears in other techniques. The same experimental technique was used to quantify the intracellular displacement in response to mechanical loading of cell (Knight, *et al.*, 2006) and to investigate the role of cell deformation changes in extracellular matrix (Chowdhury and Knight, 2006). This technique is mainly used for cells which need extracellular matrix, such as chondrocytes, or cells induced to undergo chondrogenic differentiation.
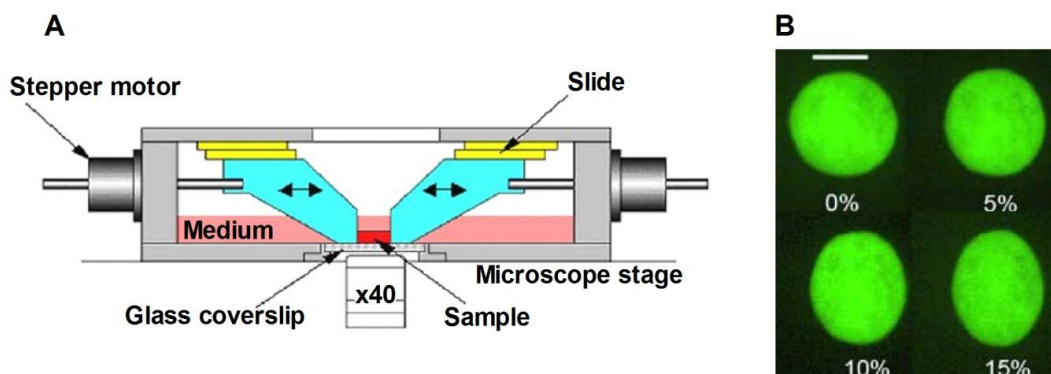
Figure 1.5: (A) A schematic cross sectional representation of 3D compression system. The sample of cells in agarose is plated on glass coverslip in medium. The compression is applied via sliding platens controlled by PC. (B) Fluorescence images of isolated chondrocyte in agarose construct at 0, 5, 10 and 15% of compression stain (Bader and Knight, 2008).

1.2.6 Scanning acoustic microscopy (SAM)

Mechanical properties of cells, such as material density, thickness, elasticity, acoustic wave velocity and attenuation coefficient of living and dead cells are important to understand the behaviour of cells. These properties can be determined by acoustic microscopy. The major advantages of acoustic microscopy are that the biomechanical properties of cells can be measured relatively quickly, with excellent spatial resolution in a non-destructive manner (Strohm and Kolios, 2009). The intensity can be kept sufficiently low that it doesn't interact with the cell, while temperature changes are negligible, which doesn't damage the biological sample (Kujawska, *et al.*, 2004). The operational principle of an acoustic and optical microscope is related; however acoustic microscopes use waves of high frequency sound or ultrasound to create images and apply force to the object. Acoustic microscopy is based on reflection of sound waves; the sound wave is pointed on the sample and while part of waves will be transmitted across the interface another part will be reflected back (Fig. 1.6). The reflected waves are used to determine mechanical properties of material. The source of sound is a piezoelectric transducer which acts as a sender and receiver.

Acoustic impedance is the product of the density and velocity of sound in the material. When the acoustic impedance is determined, the relation of material mechanical properties can be estimated. The mechanical properties, such as bulk modulus, Young's modulus and shear modulus can be estimated as a function of material density and velocity.
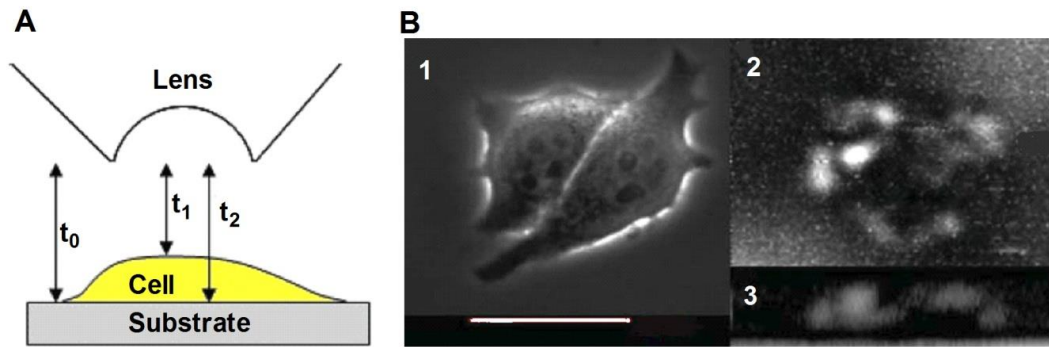
Figure 1.6: (A) The illustration of acoustic microscopy setup. Ultrasound echoes are used to calculate the thickness and the sound speed in the sample. (t_1) is the time of ultrasound echoes from the sample, (t_2) the substrate and sample interaction and (t_0) is substrate reference. (B) Optical image with phase contrast (1) and ultrasound horizontal (2) and vertical (3) scans of cell attached on the surface. Scale bar 50 μm. (Strohm and Kolios, 2009).

1.2.7 Microplates

Microplates are a relatively new technique and have not been used as widely as optical tweezers. The basic principle of microplates is two different rigidity plates pulled from rectangular glass bars, which can move parallel each other (Fig. 1.7 A). Microplates can be used to measure compression or traction parameters of cells (Bufi*, et al.*, 2015, Thoumine and Ott, 1997). In some cases the microplates can be chemically treated to support cell adhesion or spreading. The first rigid microplate is used to hold cells and second flexible plate works as a stress sensor. The force can be measured in the range of 1 nN to 1μN. This method has been used to measure mechanical properties of fibroblast cells (Fig. 1.7 B) and isolated cell nuclei (Thoumine*, et al.*, 1999).
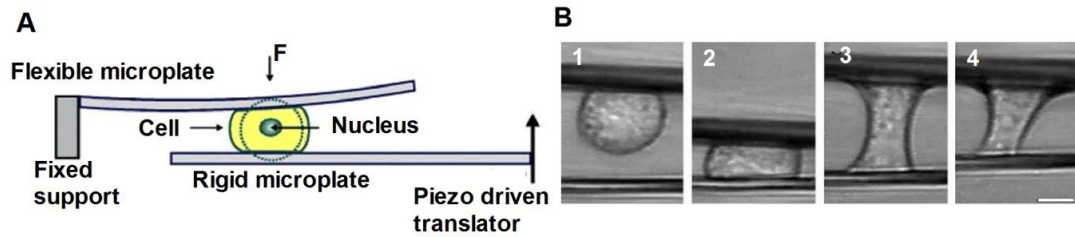
Figure 1.7: (A) A schematic illustration of the microplate technique. Cells are deformed between flexible and rigid plates. The calibrated flexible plate is used as a sensor based on plate deflection to estimate the actual forces applied (Guck*, et al.*, 2010). (B) Brightfield images of fibroblast cell adherent to the rigid plate (1), the rigid plate moved forward allowing cell attach to other plate (2), the plate is pulled away (3) and moved further until rupture of adhesion (4) (Thoumine and Ott, 1997).

1.2.8 Microneedles (cell poker)

Measuring cellular viscoelasticity is important for a deeper understanding of cytoskeleton structure and functions in many physiological and pathological processes. Other method has been evaluated to measure deformability for a range of different cells including erythrocytes (Daily*, et al.*, 1984) and leukocytes (Zahalak*, et al.*, 1990). The cell poking experiment with mouse embryonic carcinoma cells showed that carcinoma cells were about 20% more resistant to indentation then compared with vinculin deficient cells (Goldmann, 2000).

The principle of the cell poker technique is to measure cell deformation after intending with glass stylus. From the data of cell membrane deformation during time and the theory of elastic response, a relaxation constant can be estimated (Fig. 1.8). This technique also can be used to estimate cell relaxation time after deformation (Duszyk*, et al.*, 1989).
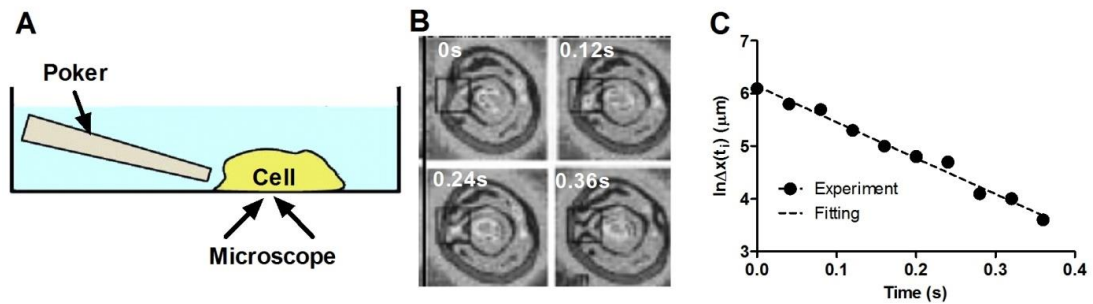
Figure 1.8: (A) A schematic illustration of cell poking device. Cell is attached on the coverslip in a buffered environment. The cell poker is coated with BSA to prevent cell adhesion. (B) Cell shape recovery during the time after indentation. (C)The rate of relaxation is determined from the analysis of images and elastic response theory. Modified from (Goldmann, 2000).

1.2.9 Micropipette aspiration for measurement of cell mechanics

The micropipette aspiration system is a well established technique, which is used for determining the elastic, viscoelastic properties and surface tension of single living cells. The technique is typically performed on rounded cells or isolated cells in suspension (Tan*, et al.*, 2008a, Trickey*, et al.*, 2000) but may also be used with adherent cells (Ra*, et al.*, 1999, Zhao*, et al.*, 2002). A single cell is partially or fully aspirated into a micropipette with an inner diameter smaller than the diameter of the cell (Fig. 1.9 A). The resulting deformation of the cell is measured using optical microscopy in terms of the aspirated length (L) inside the micropipette. The initial diameter of micropipettes can be in range from less than 1µm to 10 µm (Lim*, et al.*, 2006). The negative pressure which is required for aspiration is usually generated by reducing the height of water within a water reservoir connected to the micropipette (Rand and Burton, 1964, Trickey*, et al.*, 2000).

The micropipette is held in a micromanipulator mounted on an inverted microscope capable of imaging cell deformation during aspiration (Fig 1.9 B) The cell elongation inside the micropipette termed the aspirated length (L) is used in combination with theoretical models to evaluate the mechanical properties of the cell.

The micropipette aspiration technique was chosen due to its availability in the host laboratory and its suitability for estimation of the mechanical properties of individual cells including stem cells with simultaneous confocal visualisation of actin cytoskeleton structure and dynamics.
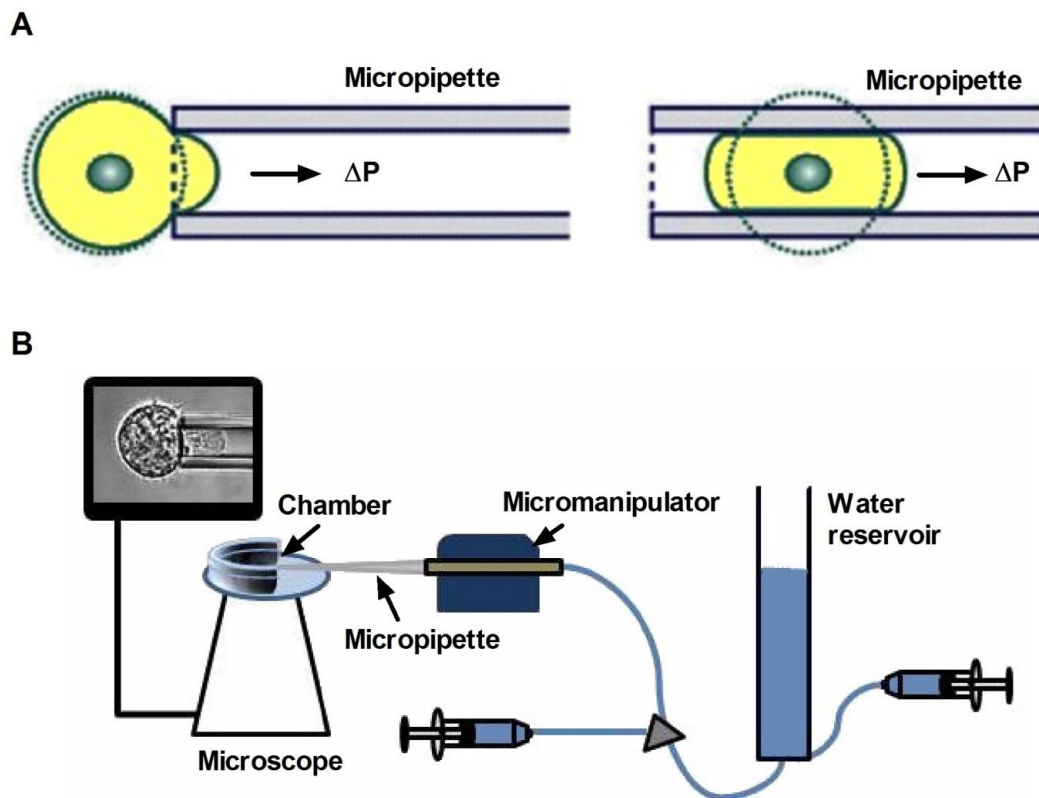
Figure 1.9: A schematic representation of micropipette aspiration system. (A) The cell is partially and fully aspirated inside the micropipette (Guck*, et al.*, 2010). (B) A schematic depicting micropipette aspiration setup. The pressure inside the micropipette is controlled by reducing the height of water in a reservoir connected to the micropipette. The micropipette position is controlled by micromanipulator and images of cell aspiration are captured using a brightfield microscope.

1.3 Theoretical models for analysis of micropipette aspiration

1.3.1 Liquid drop model

Previous studies have shown that in some cell types, such as leukocytes, the deformation of the cell into the micropipette may be modelled as a liquid drop. For a cell to behave as a liquid drop, increasing aspiration pressure causes the cell to move into the micropipette up to the point where a hemispherical projection is formed such that the aspirated length equals the micropipette inner radius. Any further increase in pressure will result in complete aspiration of the cell through the micropipette. Micropipette aspiration is a unique technique to test whether the cell behaves as liquid-like. The equation is based on the law of Laplace described by Rand et al. and

presents cortical tension of the cell surface outside the micropipette and aspirated into the micropipette is given in equation (1.1) (Rand and Burton, 1964).

$$P_3 - P_2 = \frac{2T}{R_c} \quad \text{and} \quad P_3 - P_1 = \frac{2T}{R_p} \tag{1.1}$$

where P_1, P_2 and P_3 are pressures inside the micropipette, environmental and inside the cell respectively. T is the cortical tension, R_c and R_p are radii of the cell and the micropipette respectively shown schematically in figure 1.10. The cortical tension of whole cell maybe calculated as follows:

$$\Delta P = P_2 - P_1 = 2T\left(\frac{1}{R_p} - \frac{1}{R_c}\right), \quad \left(\Delta P = \Delta P_c, \ when \ \frac{L}{R_p} = 1\right) \tag{1.2}$$

This necessitates measuring the aspiration pressure (ΔP) which is equal to critical pressure (ΔP$_c$) then the aspirated length (L) equals the inner radius of the micropipette (R_p) assuming the cell behaves as a liquid drop. For each cell the value of (R_c) depends on the cell volume and shape.
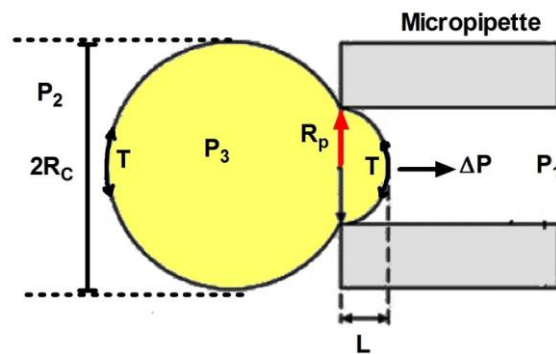
Figure 1.10: Schematic drawing of the cell with radius R_c partially aspirated inside the micropipette of radius R_p (red arrow). The pressure into the micropipette (P_1), environmental pressure (P_2) and the pressure inside the cell (P_3).

1.3.2 Standard Linear Solid – Elastic Model

When cells behave as a solid rather than a liquid drop increasing the suction pressure beyond the point where the aspirated length equals the micropipette inner radius does not cause the cell to flow completely into the micropipette. To derive the mechanical properties, the cell is assumed to behave as a homogenous and incompressible material. The elastic model is derived by simplifying the viscoelastic model, where

the time factor is neglected. The Young's modulus (E) is related to the shear modulus (G) as:

$$E = 2(1 + v)G \qquad , \qquad (1.3)$$

where v is the Poisson's ratio, which for biological materials is normally given as 0.5 (Trickey, *et al.*, 2006). In micropipette aspiration where the pipette radius is small compared to the radius of the cell, the elastic modulus can be approximated using the incompressible elastic half space model (Theret, *et al.*, 1988). The aspirated length is assumed to be proportional to the applied pressure ($\triangle$P) and inversely proportional to shear modulus (Lim et al., 2006)

$$\frac{L}{R_p} = \frac{\Phi \, \Delta p}{2\pi G} \qquad (1.4)$$

where L is aspirated length, R_p the pipette radius, G- shear modulus, Φ is the wall function, which is dependent on ɳ, the wall parameter. The wall parameter can be calculated as a ratio of inner (a) and outer (b) radii of the micropipette, ɳ = (b − a)/a. the wall function was implemented as a solution of a boundary problem (Theret, *et al.*, 1988), using the micropipettes, which have a wall parameter close to 0.5, the wall function is assumed to be a constant number $\Phi = 2$ (Sato, *et al.*, 1990). The equation can be modified to calculate the Young's modulus directly as follows:

$$E = \frac{3R_p \Delta p}{2\pi L} \, \Phi \qquad (1.5)$$

To estimate the Young's modulus of the cell, the following protocol, where the pressure of 1 cm H_2O (0.098 kPa) is applied in a series of 7-10 steps is used (Fig. 1.11 A). The aspirated length at equilibrium state is plotted against applied pressure (Fig. 1.11 B). The slope of the line is proportional to the elastic modulus, which represents cell elastic properties. However, this model is not often used as it has some disadvantages. Firstly, it is difficult to explain the mechanical properties of cell. Secondly, it has dependence on time intervals between pressure steps. Equilibration time has an effect on slope shape, which is a resulting different mechanical property of cell. Lastly mechanical properties depend on the loading pressure and the geometry of the micropipette.
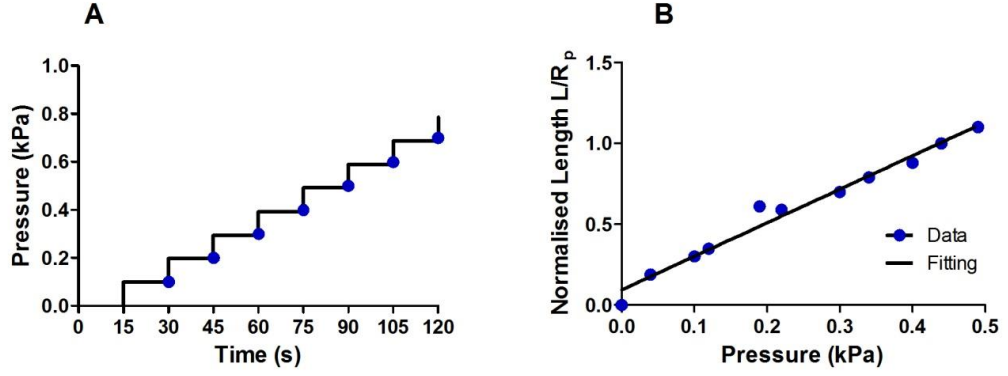
Figure 1.11: A schematic representation of the micropipette aspiration protocol for the elastic solid model. (A) Seven steps of pressures are applied with time. Measurements of aspirated length were taken at the end of relaxation indicated by (blue) dots (B) Normalised aspirated length versus applied pressure fit with linear regression. The Young's modulus is determined from the slope of the fit curve. Data is adapted from Jones et al. (Jones, *et al.*, 1999).

1.3.3 Standard Linear Solid - Viscoelastic Model

The elastic solid model was modified by involving viscoelastic behaviour of the cell (Sato, *et al.*, 1990). The viscoelastic model consists of a linear spring with elastic constant k_1 connected in parallel with another linear spring with elastic constant k_2 and in series with a dashpot with viscosity μ. Applying a negative step pressure into the pipette with radius R_p, the aspirated length $L(t)$ can be estimated as a function of time t:

$$L(t) = \frac{3R_p\Delta p}{\pi E} \times \left[1 + \left(\frac{k_1}{k_1+k_2} - 1\right)exp\left(-\frac{t}{\tau}\right)\right] h(t) \tag{1.6}$$

Where h(t) is the unit step function defined as follows:

$$h(t) = \begin{cases} 1 & t > 0 \\ \frac{1}{2} & t = 0 \\ 0 & t < 0 \end{cases} \tag{1.7}$$

For simplicity, two limits can be defined for equation (1.6) as

$$L_S = lim_{t\to\infty} L(t) = \frac{2R_p\Delta p}{\pi k_1}, \tag{1.8}$$

$$L_{0+} = lim_{t \to 0+} L(t) = \frac{k_1}{k_1+k_2} L_s, \tag{1.9}$$

Equation (1.6) can be modified as:

$$L(t) = \frac{2R_p \Delta p}{\pi k_1} \left[1 - \frac{k_2}{k_1+k_2} \, exp\left(-\frac{t}{\tau}\right) \right] h(t) \tag{1.10}$$

Thus L_s can be obtained using aspirated length $L(t)$ at the time point t_∞. Elastic constant k_1 can be estimated from L_s using equation (1.8). The constants k_2/k_1+k_2 or k_2 and τ are obtained by a least-squares method to fit the experimental data to equation (1.10). For the viscoelastic model, the time constant τ is:

$$\tau = \frac{\mu}{k_1} \left(1 + \frac{k_1}{k_2} \right), \tag{1.11}$$

The viscosity constant μ can be calculated from equation (1.11).

$$E_0 = \frac{3}{2}(k_1 + k_2), \tag{1.12}$$

$$E_\infty = \frac{3}{2} k_1 \tag{1.13}$$

And the instantaneous modulus (E_0) and the equilibrium modulus (E_∞) can be calculated using equations (1.12-1.13) respectively (Sato, *et al.*, 1990). The equilibrium modulus is equivalent to the Young's modulus calculated using the elastic model see section (1.3.2).

The SLS model was used in many micropipette aspiration studies, and typically works under assumption of instantaneously applied pressure. However, the loading time during micropipette aspiration is not accounted for. The Bolzmann superposition standard linear solid (BSLS) model was implemented to account for this (Merryman, *et al.*, 2009). The analysis has indicated that viscous dependant deformation occurs with loading time longer than 2.5 seconds. There are no differences in viscoelastic parameters between models applying pressure instantaneously.

To estimate viscoelastic properties of the cell, the cell is aspirated into micropipette applying a step of negative pressure (Fig. 1.12 A). The pressure height varies from 4 cm H_2O (0.39 kPa) to 18 cm H_2O (1.77 kPa) according to the cell type (Ribeiro, *et al.*, 2012). When the cell is partially aspirated and deformation occurs, the tongue of

the aspirated cell is suddenly increased in length followed by aspirated length equilibration (Fig. 1.12 B).
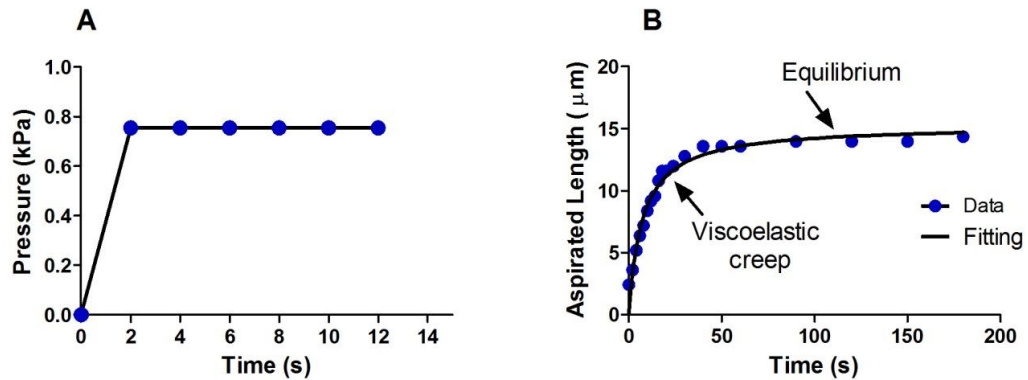
Figure 1.12: A schematic of the micropipette aspiration protocol for the viscoelastic model. (A) A step pressure application. (B) Data of aspirated length verse time fit with non-linear regression. Sudden application step of pressure results in an initial jump in aspirated length followed by slower elongation until the equilibrium state is reached.

1.4 Stem cell mechanical properties

Micropipette aspiration and AFM are the most commonly used techniques to determine the elastic properties of single cells in suspension and attached on a substrate. The mechanical properties of different types of cells are presented in (Table 1.1). The elastic properties of undifferentiated hMSCs have been reported with an equilibrium modulus of 0.1-0.37 kPa and instantaneous modulus of 0.46-0.88 kPa (Tan*, et al.*, 2008a, Yu*, et al.*, 2010). The environmental temperature can affect cell mechanics as cells appear to be stiffer and have lower viscosity at 20°C compared with cells at 37°C. Another factor affecting cell mechanics is cytoskeleton organisation. Pharmacological disruption of the cytoskeleton has led to changes in cell elastic and viscoelastic properties (Tan*, et al.*, 2008a), indicating that cytoskeletal structure plays an important role in determining the mechanical properties of the cell.

After hMSC differentiation mechanical properties appear to be altered. These changes can be due to actin cytoskeleton reorganisation. Studies have indicated that

hMSCs induced toward the osteogenic lineage for 10 days decrease in elastic modulus from 3.2 kPa to 2 kPa (Titushkin and Cho, 2011). However, a similar study has indicated that viscoelastic properties such as the equilibrium and instantaneous modulus significantly increased in hMSCs cultured in osteogenic media for 21 days (Yu*, et al.*, 2010), which might be due to measurement techniques and conditions. Typically, micropipette aspiration is used to deform the cell and elastic properties are estimated as a global cell response to deformation, while AFM is based on local deformation on adherent cells. Another study has shown that cell elastic properties are dependent on cell morphology. For this study, osteoblasts were used in two different morphologies, rounded and spread cells. Spread cells appeared to be stiffer with an elastic modulus of 5.8 kPa compare to a rounded cell with elastic modulus of 2 kPa (Darling*, et al.*, 2008). Changes of cell morphology and shape are related to actin cortex rearrangement that influences cell mechanical properties.

When hMSCs are differentiated down the adipogenic lineage, cell mechanical properties have shown changes. Adipocytes appeared to be softer than undifferentiated hMSCs and osteoblasts with equilibrium and instantaneous moduli of 0.09 kPa and 0.42 kPa respectively (Yu*, et al.*, 2010). Mechanical properties of adipocytes in both rounded cells and spread cells appeared to be the same (Darling*, et al.*, 2008). This indicated that the actin cortex is not very dense and does not drastically rearrange with changes in cell shape.

Mechanical properties such as elasticity or viscosity can be used as biomarkers to predict differentiation probability. Gonzalez-Cruz et al. have reported that adipose derived stem cells differentiated toward osteogenic, adipogenic and chondrogenic lineages have shown correlation in mechanical properties. To compare spherical cells to spread cells on the surface, they were softer and less viscous. Significant correlations of mechanical properties exist for spherical cells. While cells induced toward the osteogenic lineage have shown high elastic modulus, and cells differentiated down chondrogenic lineages exhibited high viscosity, cells induced to undergo adipogenic differentiation appeared larger in size and more compliant compared with other groups (Gonzalez-Cruz*, et al.*, 2012).

In summary can be noted that mechanical properties of cells are influenced by stem cell differentiation, that adipogenesis decreases in cell stiffness and osteogenesis

increases in cell stiffness compared to undifferentiated stem cells. However there is limited information about chondrogenic differentiation of hMSCs. The mechanism regulating these changes during stem cell differentiation is still unclear. For further understanding, the cytoskeleton structure and membrane-actin cortex interaction should be studied during stem cell differentiation to chondrogenic lineage.

Table 1.1: Mechanical properties of hMSCs in undifferentiated and lineage specific conditions.

Cell type	Technique	Mechanical properties (kPa)	References
hMSC	Micropipette aspiration	$E_\infty = 0.37 \pm 0.13$ $E_0 = 0.89 \pm 0.29$	(Tan, *et al.*, 2008a)
hMSC	Micropipette aspiration	$E_\infty = 0.09 \pm 0.04$ $E_0 = 0.46 \pm 0.09$	(Yu, *et al.*, 2010)
Osteogenic differentiation	Micropipette aspiration	$E_\infty = 0.22 \pm 0.04$ $E_0 = 0.89 \pm 0.22$	(Yu, *et al.*, 2010)
Osteogenic differentiation	AFM	$E = 2.1 \pm 0.4$	(Titushkin and Cho, 2011)
Osteoblasts	AFM	$E = 2.6 \pm 2.0$ $E_\infty = 0.60 \pm 0.78$	(Darling, *et al.*, 2008)
Adipogenic differentiation	Micropipette aspiration	$E_\infty = 0.09 \pm 0.02$ $E_0 = 0.42 \pm 0.05$	(Yu, *et al.*, 2010)
Adipocites	AFM	$E = 0.9 \pm 0.8$ $E_\infty = 0.71 \pm 0.74$	(Darling, *et al.*, 2008)
Adipodenic differentiation	AFM	$E = 0.09 \pm 0.02$	(Titushkin, *et al.*, 2013)
Chondrocytes	AFM	$E = 1.4 \pm 1.1$ $E_\infty = 0.45 \pm 0.42$	(Darling, *et al.*, 2008)

1.5 Actin microfilaments

1.5.1 Actin molecular structure and turnover

Actin filaments are formed from actin monomers called G-actin which consist of 375 amino acid polypeptides and are regulated by hundreds of different actin binding proteins (Fig. 1.13). The formation of an actin trimer from G-actin monomers requires the energy storing ATP molecule. Under physiological conditions actin monomers are assembled in double polar helices, where all monomers are polarised and facing the same direction. In the filaments any single actin monomer is in contact with four other actin monomer neighbours, however the strongest bond is along the longitudinal axis (Bray, 2001). Actin filaments are polar structures and they have two ends called a pointed end (minus end) and barber end (plus end). This was found according to the visualisation, which has shown that when a filament is covered with myosin heads, the heads are pointed toward the minus end and the tails are toward to plus end (Letourneau, 2009). When the system reaches the equilibrium state the addition and the dissociation of monomers are equal. The filament elongation of subunits occurs at the barbed point, while irreversible hydrolysis and filament destabilisation results in monomer dissociation at the pointed end. The polymerization at the barbed end and depolymerisation at the pointed end are ATP-ADP dependant processes and known as filament treadmilling.

Actin is an intracellular protein mostly found in eukaryotic cells, accounting for 1-5% of total cellular protein. Actin filaments are 5-10 nm in diameter and highly concentrated in the actin cortex near the cell membrane (Gittes, *et al.*, 1993, Lodish, *et al.*, 2000). Polymerized actin forms different structures in eukaryotic cells. The first is structure of polymerized actin occurs as filament bundles, named stress fibres. These stress fibres are made from 10 to 30 single actin fibres bound together with specific proteins. They are mainly found at the ends of the complexes connected to cell-cell or cell-substrate boundaries (Pellegrin and Mellor, 2007). The second structure consists of actin cross linked filaments mainly located under the plasma membrane and is called the actin cortex (Mofrad and Kamm, 2006).
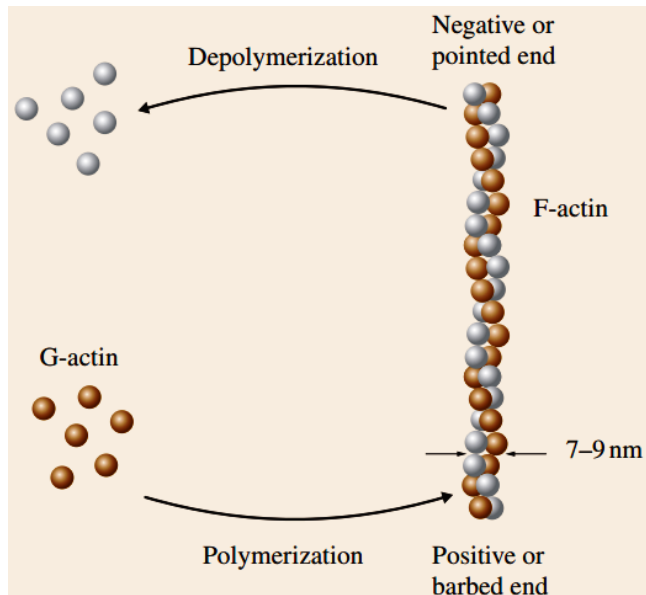
Figure 1.13: A schematic representation of F actin polymerization from G-actin monomers. F-actin has barbed and pointed ends. Actin elongation starts at the barbed end where G-actin is polymerized. At the pointed end G-actin is released during depolymerisation (Kamm*, et al.*, 2010).

1.5.2 Actin structures

The actin cortex is located under the plasma membrane and consists of a thin layer of cross linked actin filaments, actin binding proteins and myosin motors proteins (Fig. 1.14 A). The actin cortex plays a crucial role in many developmental and physiological events such as cell migration forming plasma membrane protrusions, cell shape changes due to actin filament reorganisation, morphogenesis or cell division (Lieleg*, et al.*, 2010, Risler, 2009, Tojkander*, et al.*, 2012).

Actin cortex together with the plasma membrane is responsible for changes in cell shape and resists external or internal forces. The membrane alone is unable to resist the forces and shear stresses which are generated by the cell's actomyosin interactions and also driven by extracellular matrix through adhesion proteins (Stamenovic and Ingber, 2002). The changes in cell shape are the main actomyosin driven process in many biological functions, such as cell growth, division or mitosis. The actin cortex plays an important role in many mitosis stages including nuclear envelope breakage, positioning of the mitotic spindle through interactions with microtubules, cell rounding and cytokinesis. Actin cortex reorganisation is essential during formation of the contractile ring in the cleavage furrow. There was observed

that three actin reorganization stages occur during cytokinesis. The first is reorganisation of the actin cortex and F-actin patch formation; the second, some F-actin patches are fused with each other and organised into short F-actin bundles; in the final stage short F-actin bundles reorganise into long bundles in the centre of the furrow (Noguchi and Mabuchi, 2001). However, in mammalian cells the ring formation is regulated by reassembly of actin filaments including formins, myosin II and anillin (Green, *et al.*, 2012).

The actin structure is important in cell migration. During cell migration, the lamellipodium is formed at the front edge which is a thin and dense network constructed of short and branched actin filaments that push the plasma membrane forward, causing cell movement (Fig. 1.14 B). Actin filaments are oriented and elongation occurs on the barbed end facing toward the leading edge, the direction of cell movement. Interaction between actin and the cell membrane produces the forces, which drive the formation of a membrane protrusion at the leading edge (Xue, *et al.*, 2010). The stable system behind the lamellipodia, which consists of F-actin filaments and other motor proteins responsible for filament contraction is called lamellum (Ridley, 2011, Verkhovsky, *et al.*, 1995).

It is believed that focal adhesions are also involved in lamellipodia formation. The transition region between lamellipodia and lamellum was found, where acto-myosin retraction interacted with substrate adhesions (Ponti, *et al.*, 2004). In lamellipodia a thin (about 0.1-0.3 μm) hair like membrane protrusion can be found, named filopodia. It is a very dynamic protrusion that contains parallel actin bundles (Xue, *et al.*, 2010). In migrating cells the filopodia are formed by direct polymerisation of parallel actin filaments involving formin family proteins (Pollard, *et al.*, 2000). Formins are found to exist in the tip of filopodia and nucleate the actin (Schirenbeck, *et al.*, 2005). Both formin mDia1 and the Arp2/3 complex are involved in actin nucleation (Bovellan, *et al.*, 2014)

The dynamics of extension and retraction of filopodia are controlled by balancing the retrograde flow and the rate of actin assembly at the tip (Mallavarapu and Mitchison, 1999). The binding of actin filaments to each other is necessary for filopodia formation. Individual actin filaments lack of stiffness required to push the membrane and form protrusions, therefore a critical step in filopodia formation is actin filament

cross linking (Xue*, et al.*, 2010). Filopodia are present in many cellular functions including cell migration, adhesion to the substrate or axonal growth cones (Faix and Rottner, 2006).

By contrast some cells are using bleb-based migration. Blebs are membrane protrutions formed at the leading edge of the migrating cell, resulted by actin network contraction. The contraction is highly dependant on myosin II, which generates tension in actin network by sliding actin filaments. The myosin II activity causes increase in local hydrostatic pressure, that can rupture actin network or leads to membrane-actin cortex detachment (Charras and Paluch, 2008).

 Accordingly to the cell type and the mechanism they are using to move, the cell migration is classified into amoeboid and mesenchymal modes. The amoeboid migrating cells represent heterogenous group, while varying in cell size and compartment. However, they share the similar morphological aspect during migration, protruding and retracting the cellular extensions. Different amoeboid cells use different movement strategies, such as contraction-based blebbing or actin polymerisation driven gliding (Lämmermann and Sixt, 2009). The first group is rounded, blebby cells that are lack of adhesion to the substrate and use a protrutive migration. Second group of cells are elongated that are able to generate filopodia with weak interactions to substrate (Friedl*, et al.*, 2001, Friedl and Wolf, 2010). Indivudual cells that have a high level of adhesive interactions to the substrate and actin contractility are defined as mesenchymal migrating cells and migration is based on actin polymerisation and lamellipodium formation. Examples of cells using an amoeboid or mesenchymal cell migration modes are leukocytes and fibroblasts (Vallenius, 2013).

Another structure which involves actin organisation is microvilli. This structure exists in the epithelial cells and is involved in the secretion and absorption of various molecules. Absorption requires a good sealing of cells and an asymmetric cellular organisation between apical and basal domains of the cell. The mechanism involves the shrinkage and functional separation between the apical and basal domains (Brown and McKnight, 2010). Intestinal microvilli consist of arrays of actin filaments that create actin bundles. Actin filaments are polymerized at the tip of the bundle (Revenu*, et al.*, 2012). Actin linker proteins, such as ezrin, radixin, moesin

(ERM) play a role in shaping microvilli, while other proteins involved in capping and cross-linking found at the plus end of actin filaments are responsible for morphogenesis of microvilli. Actin bundling proteins, such as vilin and fimbrin are responsible for organising filaments in regular and parallel arrays, resulting in the formation of actin filament bundles (Fath and Burgess, 1995).
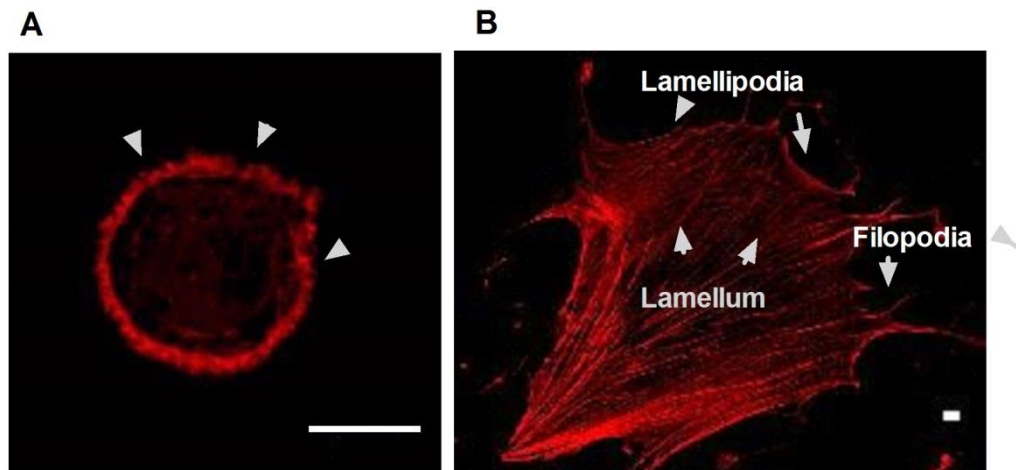
Figure 1.14: Actin cellular structures in non-muscle cells. (A) A fixed hMSC cell in suspension with actin stain in red. A dense cortex consists of F-actin layers under the plasma membrane (arrow heads). Scale bar 10 μm. (B) A fixed hMSC cell attached to a substrate with actin stain in red. Filopodia can be seen arising from lamellipodia. The body behind the lamellipodia is the contractive lamellum. Scale bars 10 μm.

1.5.3 Mechanical properties of actin gels

F-actin networks can be formed in vitro, where actin monomers are polymerised involving cross-linking proteins. These structures of F-actin are quite different from the structures found in live cells. However, they are used as a model system to measure and better understand mechanical properties of actin organisation.

Actin systems formed in vitro adapt mechanical properties, which are in between fluid and elastic solid. Generally, such a behaviour is described as viscoelastic and depends on the time scale as a result of internal stress relaxation (Stricker, *et al.*, 2010). Viscosity of actin structures can be eliminated by changing the ability of cross-linker proteins to unbind from actin filaments. Actin networks formed with

enough static cross-linker proteins like biotin-avidin, normally approximate elastic solid properties (MacKintosh*, et al.*, 1995). In physiological conditions, cross-linker proteins are dynamic with high binding affinity to F-actin. Modulation of dissociation rates of cross-linker proteins to bind and unbind actin filaments leads to changes in viscoelastic properties of the actin network. This suggests that cross-linkers play a key role in the viscous response of F-actin structures during actin rearrangement and the regulation of cell shape (Lieleg*, et al.*, 2010). A nonlinear mechanical response has been shown for the F-actin network under large deformation forces. For a low density actin network with a low concentration of cross-linkers, softening occurs at large strains, however, a high density actin network with high concentration of cross-linkers has been shown to stiffen at intermediate strains and soften at large strains (Gardel*, et al.*, 2006, Gardel*, et al.*, 2004). A similar behaviour has been found for an actin network formed with different cross-linkers, such as α-actinin and filamin (Esue*, et al.*, 2009). The stiffness of the F-actin network can dramatically increase in the presence of cross-linkers. This suggests that cross-linkers are dominating the elastic properties of the entire actin network. Modifications of actin structure and cross-linker proteins have shown changes in elastic and viscoelastic properties that could be a key factor for cells in different physiological processes (Gardel*, et al.*, 2006).

1.5.4 Role of actin in cell mechanics

Cell migration is based on membrane protrusion at the leading edge generated by F-actin structures which push the cell forward. It is suggested that polymerisation of F-actin generates forces, which act as stimuli to change cell shape at the leading edge. Experiments have shown that F-actin created traction stresses on extracellular matrix are on the order of 20 Pa (Gardel*, et al.*, 2006). Cell motility from the filopodia also is driven by F-actin polymerization. The stress generated in filopodia are significantly lower, however these variations might arise from the different time scales and geometry of the measurements (Cojoc*, et al.*, 2007).

In lamella F-actin structure is dependent on myosin II motor proteins. Transportation of F-actin network from the leading edge toward cell body in a myosin II dependant process is named retrograde flow. Some data have shown that when retrograde flow decreases, the rate of membrane protrusion increases (Jurado*, et al.*, 2005). It was suggested that adhesion ''motor-clutch'' play an important role in controlling

interactions between F-actin and the extracellular matrix. At the leading edge with low adhesion, the F-actin speed is fast and inversely related to traction stress, however with high adhesions the F-actin speed is slow and directly related to traction stress (Gardel, *et al.*, 2008). A recent study has shown that same "motor-clutch" system can act as a mechanical sensor (Chan and Odde, 2008).

Actin mechanics in stress fibres

Stress fibres are structures consisting of F-actin, myosin II motor proteins and α-actinin. Typically, a stress fibre has one end connected at the point of adhesion and the other is terminated close to the nucleus. It is believed that stress fibres work as sensors to determine transmitted forces and stresses at the adhesion points (Stricker, *et al.*, 2010).

The dynamic properties of stress fibres depend on the distribution of myosin II motors. The spacing of myosin II motors can decrease or increase according to the activity of myosin. Some experiments have shown that elastic properties of stress fibres are dependent on myosin activity (Lu, *et al.*, 2008). This suggests that myosin II motors play a key role in dictating the mechanical properties of stress fibres.

Moreover, the nonlinearity of elastic properties in stress fibres has been investigated. The tensile test confirmed that the elastic modulus increases depending on the magnitude of strain. This nonlinearity of stress-strain in fibres can be important to determine forces transmitted from the environment (Stricker, *et al.*, 2010). The rupture forces of stress fibres have been estimated much larger than the forces generated at the adhesion points. This suggests that stress fibres in cells exist in the pre-strained state and this plays a role in determining the forces between intracellular and extracellular environments (Deguchi, *et al.*, 2006).

Actin mechanics in cortex

Actin cortex is a thin F-actin network, which together with the membrane regulates cell shape and drives cell motility. F-actin cortex can generate tension of cell which is employed from the contractility of Myosin II motors. Tension generated through myosin contractility within the actin cortex can inhibit membrane protrusions (Fischer, *et al.*, 2009).

When the bond between the actin cortex and membrane is disrupted a membrane protrusion occurs known as a bleb. Bleb formation can be seen in many biological

processes, such as apoptosis, cell division, or cell migration. Bleb initiation in migrating cells starts with expansion and the bleb can reach the size of 1-2 μm. A new actin cortex formed under the membrane with myosin II contractility drives the bleb retraction. During the retraction process the bleb stiffness increases according to the newly formed actin cortex (Charras, *et al.*, 2008, Charras, *et al.*, 2006). The primary component responsible for mechanical properties of the cell is the actin cortex, however other soluble and insoluble cytoskeletal components cannot be excluded. Experimental measurements have shown that the actin cortex behaves as a viscoelastic solid with mechanical relaxation resembling a glassy material (Bursac, *et al.*, 2005). The stiffness of cortical actin can vary from a few Pascal's (Pa) for neutrophil and other soft cells to hundreds of Pascal's for chondrocytes and other stiff cells (Hochmuth, 2000). Cortical stiffness of adherent cells can vary in response to the stiffness of extracellular matrix. Moreover, the elastic properties of the actin cortex have a linear relationship with the applied forces on the cortex (Solon, *et al.*, 2007).

1.6 Membrane – actin interaction

The cell's ability to maintain organisation of the plasma membrane, such as membrane rafts and integrated proteins is an important perform. During physiological processes like endo- or exocytosis and cell division, the cell needs to remodel its interactions between the actin cortex and membrane. Membrane-actin cortex linkage plays an important role in stability. There are many linker proteins such as spectrin, utrophin, dystrophin, filamin, myosin1 and ezrin, radixin and moesin (ERM) that are involved in membrane-actin cortex adhesions. Previous studies have indicated that ERM proteins are involved in cell mechanics and effect membrane elastic properties (Titushkin and Cho, 2006). Moreover, they were found to regulated stem cell differentiation (Titushkin and Cho, 2011, Titushkin, *et al.*, 2013). In this section particular attention is paid to the ERM family of linker proteins.

ERM is a family of membrane-actin cortex linker proteins closely related to adhesion dynamics between the plasma membrane and actin cortex (Sato, *et al.*, 1992). They are essential for the formation of cellular structures such as microvilli, cell-cell

contacts and membrane organisation (Fehon*, et al.*, 2010). This requires close communication between actin filaments, cell membrane and membrane-actin cortex associated linker proteins. ERM proteins exist in two forms: a dormant and an active conformation. The active form is involved in interactions with cell membrane and actin cortex, while the dormant form is present in the cytoplasm. Changes in protein conformation are the principal differences between these forms. Two domains play a role in intramolecular and intermolecular interactions, the 296 amino terminal residues known as N-ERMAD (N-ERM associated domain) and 107 carboxy terminal residues known as C-ERMAD (C-ERM associated domain) (Fig. 1.15 A) (Louvet-Vallee, 2000). The dormant form of ERM proteins have close conformation structure, which involves the C-terminus head connected to the N-terminus tail (Gary and Bretscher, 1995). Conformation changes to active form can be released by phosphorylation of Rho associated protein kinase (ROCK) or PIP_2 (phosphatidylinositol 4,5-biphosphate binding (Fig 1.15 B) (Hirao*, et al.*, 1996). During ERM protein activation, the N-terminus binds to the plasma membrane and the C-terminus to the actin cortex. Behind the direct membrane binding, ERM proteins can bind membrane proteins like receptor CD44 (Tsukita*, et al.*, 1994) or intracellular adhesion molecule-2 (ICAM-2) (Heiska*, et al.*, 1998). Besides the role of membrane-actin cortex interaction, ERM proteins are involved in cancer growth, controlling the signals between metastasis associated cell surface molecules and transduction components (Hunter, 2004).
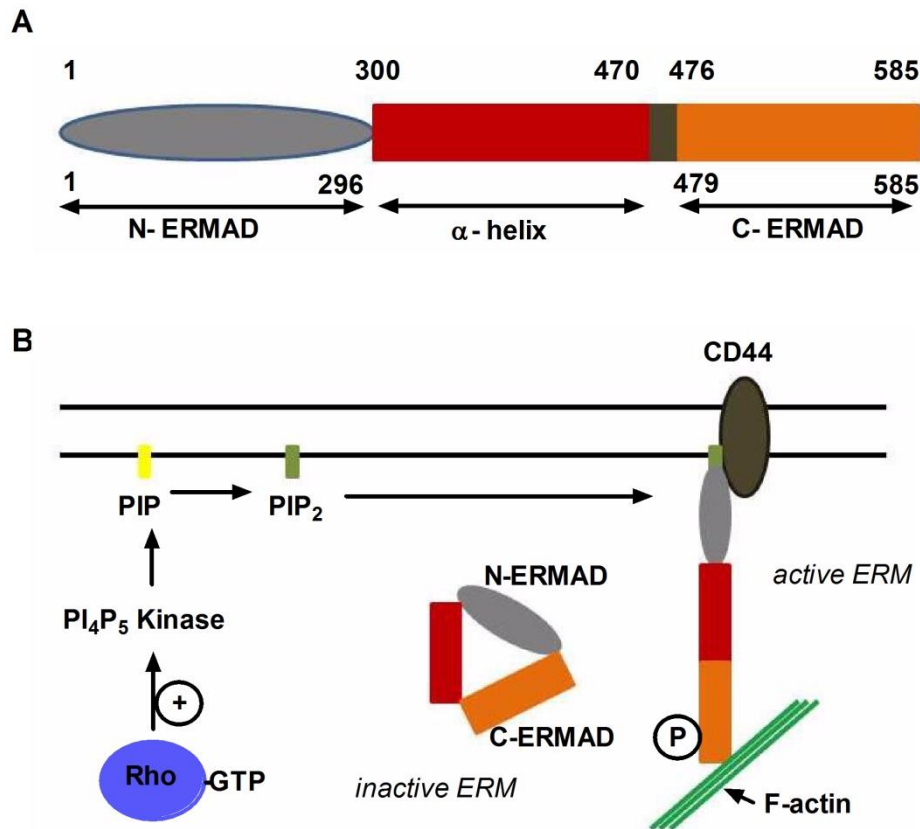
Figure 1.15: Domain organization of ERM proteins and activation structure. (A) All ERM proteins have a similar domain structure. The amino terminal N-ERMAD (N-ERM associated domain; grey) is connected to α-helical content (red) followed by a linker with carboxy terminal C-ERMAD (C-ERM associated domain; orange) which contains the F-actin binding site. (B) ERM proteins are activated through PIP_2 binding and phosphorylation, which reduces the affinity of the N-terminal for the C-terminal. These unmask binding sites for F-actin and specific proteins, such as CD44. The N-terminal of activated ERM protein binds to the membrane, while the C-terminal binds to F-actin. Figure is modified from (Louvet-Vallee, 2000).

The level of ERM protein expression differs in different cell types. Epithelial cells express more ezrin, however endothelial cells express mainly moesin (Berryman, *et al.*, 1993). Some studies have shown that ERM proteins are closely related to actin cortex remodelling and resulting changes in cell biomechanical properties (Titushkin and Cho, 2011). Other study has demonstrated that ERM linker proteins are involved in new cortex formation during bleb retraction. Linker proteins flow into bleb followed by actin filaments and myosin, which form linkers between membrane and

new cortex (Charras, *et al.*, 2006). Resent study has shown that membrane-actin cortex interaction decreased by interfering molecular modification of linker molecules resulted increased blebbing and reduced directional migration of mesendoderm progenitor cells in zebrafish (Diz-Munoz, *et al.*, 2010).

Additional studies are required to better understand why cells express ERM linker proteins and how they are associated with cell physiological processes, such as cell signalling as ERM can interact with transmembrane receptors, involved in cell development and differentiation, in cell polarity ERM organises the actin cortex and regulates stability of adherent junctions, regulating cell shape during mitosis (Fehon, *et al.*, 2010). Recent studies have shown the connection mechanism of ERM proteins to the membrane and actin cortex, the head-to-tail unfolding, is regulated by phosphorylation. However little is known about how phosphorylation is controlled and what is the major factor involved.

Membrane-actin cortex interaction and specifically number of linkers can be estimated by measuring membrane tether. The membrane tether forces are measured by pulling membrane tube. The most commonly used technique is optical tweezers (Dai and Sheetz, 1999, Titushkin and Cho, 2006). Knowing the membrane tether forces, the friction coefficient of membrane-cortex can be estimated that gives ability to calculate the surface density of the protein molecules that connect cell membrane and actin cortex. The equation is given as follows:

$$n = \frac{\eta}{B\tau} \qquad (1.14)$$

n is the surface density of the proteins, η is the friction coefficient, B is membrane bending modulus and τ is a typical protein connection time (Datar, *et al.*, 2015). However, to measure the number of linkers independently and to estimate the absolute values are difficult.

1.7 Cell blebbing

1.7.1 Cell membrane structure and mechanics

In the 19th century it was believed that cells have a surrounding barrier layer, which protects the internal cell structure from the outer environment. In 1925, Gorter and

Grendel demonstrated that an extracted erythrocyte cell membrane on water forms a thin layer, with a surface area computed as twice the cell area. This led to the conclusion that the membrane is a bilayer and consists of two equal and oppositely orientated lipid layers (Gennis, 1989). In the past scientists believed that the primary functions of the lipid membrane is to provide a barrier to maintain the ion gradient, to facilitate transport of specific molecules across the cell membrane and to protect the internal organelles from the external environment. However, the latest research has shown that membranes are involved in many other processes and cell functions, such as membrane protein folding, interaction of proteins, cell fusion, vesicle trafficking and signalling (Kung, 2005, Vogel and Sheetz, 2006).

The plasma membrane basically consists of lipids and proteins, which can be composed in different proportions, changing the fluidity and the specific properties of the membrane (Fig. 1.16). The most commonly found family of lipids include phospholipids, glycolipids and cholesterol. There is a distribution of asymmetry of lipids in the membrane, the majority of anionic lipids facing the cytoplasm and large glycosylated groups are facing the extracellular environment (Janmey and Kinnunen, 2006). Membrane asymmetry occurs in animal cells, the inner leaflet of the plasma membrane bi-layer is more concentrated with phospholipids, which are involved in activating signal pathways responsible for cell cycle, migration and survival (Cantley, 2002). Two groups of proteins embedded into membrane play a crucial role in cell communication with the environment and transporting materials into and out of the cell. Integral proteins are mainly responsible for transport through the membrane, while peripheral proteins are involved in the function of cell communication (Aplin*, et al.*, 1998). The plasma membrane, together with embedded membrane proteins presents a complex system, involved in a diverse range of biological processes like the transport of molecules across the membrane through channels and pumps, signalling involved by interaction of binding proteins and membrane receptors. All these processes require a dynamic membrane, which allows fast reorganisation of structure.
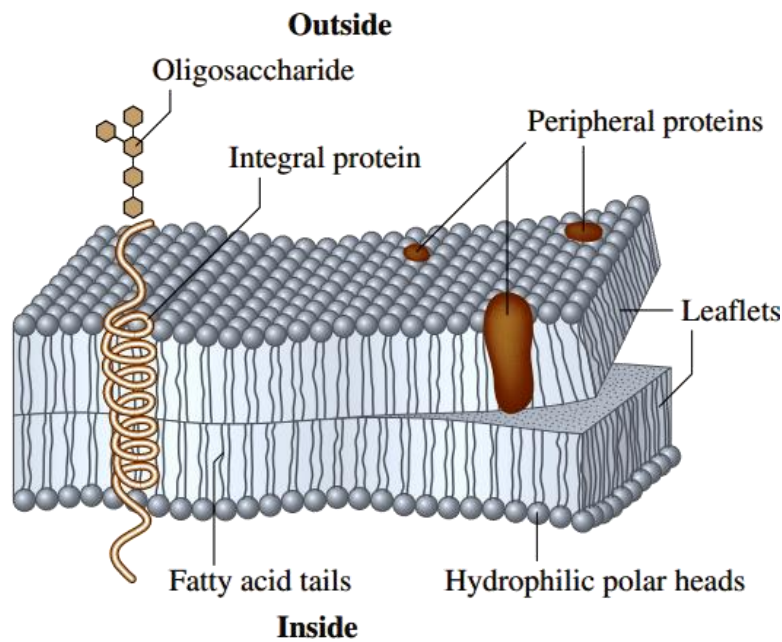
Figure 1.16: A model of membrane structure. Membrane consists of two internal and external lipid leaflets. Lipid hydrophilic heads are orientated on the exterior surfaces and hydrophobic tails are pointed inside. The membrane is embedded with integral and peripheral proteins (Kamm, *et al.*, 2010).

Mechanical properties of the plasma membrane rely on the chemical composition of the membrane and the forces invoked between the membrane components. The elastic properties of the membrane are characterised by several elastic constants that correlate the membrane resistance to different geometries of deformation: stretching, bending and shear. The cell membrane maintains a lipid bilayer density and surface pressure of the order of 30 mN/m. During physiological conditions like osmotic swelling the spacing between lipids increases and can lead to membrane rupture. The rupture occurs when the applied strain is slightly above the optimal lipid packing (Janmey and Kinnunen, 2006).

The shear deformation of the membrane bilayer in eukaryotic cells has no resistance. The lipids and embedded transmembrane proteins can freely move past each other. The protein mesh under membrane, such as actin or actin-spectrin networks, provides resistance to shear stress. The lipid bilayer and protein composition involved in viscoelastic properties of cells (Discher, 2000). Absence of membrane resistance to shear provides a limitation to how forces can be applied. Some studies suggested that motor proteins, such as myosin I play a role in binding the phosphoinositides or acidic lipids into the inner membrane layer by anchoring to the surface (Takeda and

Chang, 2005). However, it is unclear whether membrane mechanical stability can be formed within a lipid bilayer and motor proteins or actin proteins are necessary for stabilization of the membrane.

There is a different situation with membrane bending. Lipid bilayers themselves are able to resist bending forces. In nature lipids in the inner leaflet prefer to pack in curved bilayers, which is due to chemical interactions. The majority of bilayers involved in the plasma membrane can form a wide variation of different structures and those lipid compositions are unstable in planar membranes formation. Lipids, such as phosphatidylcholine (PC) and phosphatidylserine (PS), are found in both inner and outer membrane bilayers, however lipids like cholesterol and other important lipids are unable to form the bilayers on their own, except in mixture with other lipids. Destabilisation of membranes is essential for the biological function of plasma membranes; their ability to change shape and form vesicles. When the membrane is forced to bend, the lipid density of the outer leaflet increases while the lipid density of the inner leaflet decreases. The energy imbalance of lipids results in the bilayer flipping, lipids from the dense inner leaflet area move to the outer leaflet, leading to lipid scrabbling (Janmey and Kinnunen, 2006).

Membranes are able to resist stretching forces, which cause an increase in the distance between lipid heads. Eukaryotic cells like leukocytes have greater surface area than needed to cover cell volume, so that lipid bilayers are not stretched during membrane deformation (Janmey and Kinnunen, 2006). Many cellular events, such as tubular invagination involve changes in lipid composition and interaction with specific membrane proteins. The proteins which are used for tube formation are responsible for changes in the mechanical properties of the membrane (Itoh, *et al.*, 2005).

To study mechanical properties of the cell membrane, an experimental technique is required. The most common techniques used are micropipette aspiration and optical tweezers to estimate bending rigidity, shear stress or membrane tension. Membrane tension can be determined by applying a known negative pressure on the cell membrane (Evans and Yeung, 1989). Changes of membrane area under applied pressure provide the information about membrane bending properties (Evans, 1983).

Optical tweezers can be used to measure the membrane tethered force (Cuvelier, *et al.*, 2005) from which membrane tension can be estimated (Datar, *et al.*, 2015).

1.7.2 Stages of bleb formation

Bleb formation can be divided into three stages: nucleation, expansion and retraction. This mechanistic life cycle of bleb formation comes from non-migrating cells, however, a number of studies suggest the similar bleb formation mechanism for motile cells. How bleb retraction occurs is not clear in migrating cells; the cell body moves forward as a contraction appears at the rear edge (Charras and Paluch, 2008). In this section I have concentrated on bleb formation stages and explained more in details.

Bleb nucleation

Bleb nucleation is a result of contraction of the actomyosin cortex in the cell. Two different mechanisms of bleb nucleation were observed experimentally (Fig. 1.17 A). The first mechanism involves membrane actin cortex detachment due to local intracellular pressure changes. The myosin motor proteins contract resulting in compression forces on the cytoplasm. While the cytosol is trapped under compression and flows very slowly, the localised pressure initiates membrane-actin cortex detachment and bleb nucleation (Charras, *et al.*, 2005). The second nucleation mechanism is related to rupture of the actin cortex, however the biochemical mechanism is still unclear. The precise location where the bleb is nucleated, can be determined by decreased adhesion between membrane and actin cortex. Some studies have shown that phosphatidyl-inositol 4,5-bisphosphate (PIP_2) plays an important role in membrane actin cortex adhesions, by regulating the ERM actin membrane linker proteins or its involvement in chelation with myristoylated alanine-rich C-kinase substrate (MARCKS) (Sheetz, *et al.*, 2006). Experiments have shown that bleb expansion as a result of membrane actin cortex detachment does not contain actin cortex (Charras, *et al.*, 2005). Blebbistatin inhibition of myosin contractility blocks bleb formation (Cheung, *et al.*, 2002). The other nucleation mechanism suggested, that myosin contractions lead to breakage of actin cortex and the cytosol flows inside, forming a bleb (Paluch, *et al.*, 2005).

Bleb expansion

After bleb nucleation, the pressure generated by actomyosin contraction causes the cytosol to flow through the bleb neck generating bleb expansion (Fig. 1.17 B). The cytosol flow increases in volume resulting in membrane surface area expansion (Bovellan*, et al.*, 2010). The process of bleb expansion usually lasts from 5 to 30 s. It was suggested that there are a few mechanisms regulating change in surface area during cytosol flow. First, the cytosol flow can initiate changes in membrane tension that breaks the bond between the membrane and the actin cortex increasing surface area for membrane expansion. A second suggestion is that extra membrane folds can be stored and the surface area increases due to unfolding of the membrane folds. However, the experiments have shown that this process alone cannot result in surface growth during bleb expansion (Charras and Paluch, 2008). The third suggestion is that slow cytosol flow and slow bleb expansion allows membrane lipids flow inside the bleb to form an extended surface area. The lipid flow was observed in membrane tethers (Hochmuth and Marcus, 2002), however, this needs further experimentation to investigate the formation of membrane tethers during blebbing. Bleb expansion can stop for a few reasons. The local intracellular pressure decreases below the expansion threshold or the actin cortex starts to reassemble initiating bleb equilibration (Fig. 1.17 C) (Tinevez*, et al.*, 2009). The reassembly of the actin cortex under the plasma membrane starts when the turnover signal is triggered. The half life of turnover is about 45 s which is comparable with the time for bleb expansion of about 30 s. How cells know that reassembly of the actin cortex necessary is unclear. The actin cortex could be formed from short F-actin filaments, which might be polymerised involving nucleators, such as the Arp2/3 complex. However the membrane actin cortex linker proteins, such as ERM play an important role in reassembly of the actin cortex in the bleb. Ezrin seeds flow to the bleb independently of actin, which collects single F-actin filaments followed by recruitment of tropomyosin and the α-actinin cross-linking protein. Finally, the myosin motor proteins concentrate along the cortex initiating retraction (Charras*, et al.*, 2006).

Bleb retraction

The last stage of bleb retraction involves the reformation of a new actomyosin cortex (Fig. 1.17 D). Re-polymerisation of a new actin cortex starts in the bleb expansion stage, when the localised intracellular pressure slows down. When the bleb is

stabilised the myosin II motor drives the contraction followed by bleb retraction, this process is slower than bleb expansion (Charras and Paluch, 2008). During this process the bleb membrane with the actin cortex crumpling and once the process is complete the bleb cortex can be integrated into the cell cortex or can be depolymerised and replaced by new cortex (Bovellan*, et al.*, 2010, Charras*, et al.*, 2006).
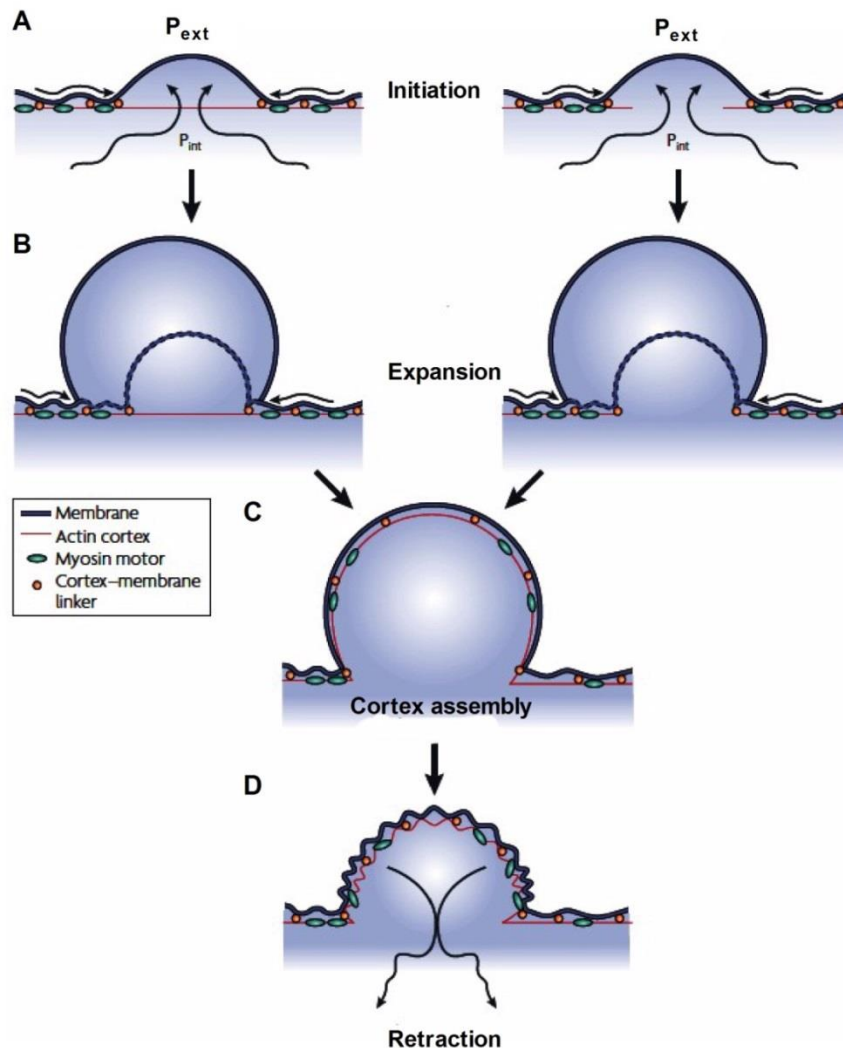
Figure 1.17: The bleb formation stages. The bleb formation can be divided into three phases: bleb initiation, expansion and retraction. (A) Bleb initiation can be due to bond rupture between the actin cortex and membrane (left model) or rupture of actin cortex (right model). (B) The intracellular pressure drives the bleb expansion through the expanded actin cortex (left model) or the fluid flows through the actin cortex hole and stretches the membrane (right model). (C) As intracellular pressure decreases and equilibrates, a new actin cortex starts to form under the plasma membrane. (D) Additional myosin motor proteins together with new actin cortex result in bleb retraction (Charras and Paluch, 2008).

1.7.3 Apoptotic blebbing

Apoptotic blebbing is a common feature associated with programmed cell death. The mechanism that is responsible for apoptotic blebbing is believed to be direct and involved in the activation of myosin II (Charras and Paluch, 2008, Croft, *et al.*, 2005). Experiments have shown that blebbing is not essential for apoptosis as inhibition of cell blebbing does not stop apoptosis (Nicotera, *et al.*, 1999). It was suggested that apoptotic blebbing can be involved in signalling mediated by membrane proteins on the bleb surface which separate from the cell body and act as chemo attractants for macrophages (Segundo, *et al.*, 1999). Blebs can also be formed in necrosis, which is the last stage of cell death. During this process cells lose membrane stability, lyse and release cell content, which contain damage associated molecular patterns (DAMPs). In late stage apoptosis, blebs can break away from the cell and form apoptotic bodies. Apoptotic bodies are involved in apoptotic cell clearance. The smaller bodies are more ready phagocytosis than the entire cell (Wickman, *et al.*, 2013).

1.7.4 Blebbing during cell attachment and migration

The blebbing process has been observed during the first minutes of cell spreading on the substrate. The rounded cell shape changes to flatten during cell spreading on the substrate. Extension of lamellipodia on the adherent substrate results the rapid spreading (Charras and Paluch, 2008). Membrane blebs disappear after cells are fully flattened on the surface. Why this process appears during cell spreading is not well understood (Erickson and Trinkaus, 1976).

The mechanism which causes cell blebbing is not well known and specific triggers are believed to exist for different types of cells. Depending on the mechanism of bleb initiation, different models can be suggested. A first possible model suggests that bleb nucleation can occur through local membrane actin cortex detachment, which can be initiated from a weakening of the bond between membrane and cortex. This could be achieved by changing stability of ERM linker proteins. Also, formation of polarised blebbing could be a result of tearing of the actin cortex at the leading edge. A second possible model suggests that local rupture of the actin cortex appears. Experimentaly it is difficult to distinguish which mechanism happens first. Both models suggest that the cell's leading edge is subjected to more blebbing than the rear. The leading edge is younger and the actin cortex is weaker. Myosin contractility

plays an important role in cell migration. Bleb initiation can be triggered by myosin motors localised at the leading edge of the cell. The pressure which is generated by actomyosin contractility is necessary for bleb growth (Charras and Paluch, 2008, Paluch and Raz, 2013).

During cell movement forces must be generated on the substrate to translocate the cell body. In motile cells the cell body is translocated by contraction of the rear edge, involving adhesion of the lamellum and substrate. It is unclear how blebbing cells move when there is a lack of focal adhesions. It is believed that some weak adhesions are necessary and play a role in cell motility (Tozluoglu, *et al.*, 2013). Also it was demonstrated that rearward cortical flow drives bleb based migration on adhesive and non-adhesive substrates (Ruprecht, *et al.*, 2015). Another possibility that bleb based migration can be achieved under conditions by creating a low 2D adhesions or high 3D confinement (Welch, 2015).

Some cells, such as fish keratocytes use membrane protrusions (lamellipodia) for motility (Svitkina, *et al.*, 1997), other cells such as zebrafish primordial germ cells (Danio rerio) use bleb base motility (Blaser, *et al.*, 2006). It has been shown that some type of cells switch between motility modes during migration (Bergert, *et al.*, 2012). Which protrusion mode will be dominant is not clear. Actomyosin contractility and adhesions between cell and substrate may play a key role. Cell blebbing is dependent on myosin motors, and a lower concentration of myosin contractility can result the lamellipodia formation. A weak adhesion between membrane and actin cortex might cause bleb motility, also a strong substrate adhesion initiates lamellipodia motility (Friedl and Wolf, 2003, Goudarzi, *et al.*, 2012, Liu, *et al.*, 2015).

1.7.5 Mechanically induced blebbing

Besides physiological blebbing that is induced by many different biological processes, blebbing can be achieved by mechanical stimulation. Mechanically induced blebbing can be divided into few groups. First, the cell is mechanically compressed between two rigid surfaces causing the intracellular pressure to distribute according to the loading force. Such as blebbing initiation can be made using atomic force microscopy. Cells on the substrate are compressed by a spherical cantilever tip (Hemsley, *et al.*, 2011). The weaker interactions between membrane and actin cortex

are unable to sustain the localised pressure which results in bleb formation. Blebbing can be caused by actin cortex rupture followed by membrane delamination and expansion (Charras and Paluch, 2008). Laser ablation has been used to break the actin cortex and initiate bleb formation (Goudarzi, *et al.*, 2012, Tinevez, *et al.*, 2009). Third, the micropipette aspiration technique can be used to form cell blebs. The cell membrane is delaminated by applying a negative pressure on the cell surface. Pipette aspiration experiments have shown that multi bleb formation is associated with actin cortex remodelling (Rentsch and Keller, 2000) and bleb retraction is closely related to myosin motors and talin proteins (Merkel, *et al.*, 2000).

1.8 Aims and Objectives

Previous studies have described changes in stem cell mechanics during differentiation and in particular, focused on changes in nucleus mechanics and chromatin condensation and that regulate cell function.

The overall aim of this thesis is to examine the role of membrane-actin cortex interaction in modulating hMSC mechanics during chondrogenic differentiation. The work has been divided into four objectives:

1) Develop micropipette aspiration protocols for measuring the viscoelastic properties of stem cells during differentiation

2) Determine the viscoelastic properties of hMSCs and the influence of chondrogenic differentiation

3) Determine the role of membrane-actin cortex interactions in regulating stem cell mechanics, blebbing and migration during differentiation.

4) Determine the viscoelastic properties of isolated chondrocytes and
    - The role of membrane-actin cortex interaction
    - The effect of dedifferentiation with passage in monolayer

CHAPTER 2
Methods

2.7.1   Introduction

2.7.2   Methods

2.7.3   Statistics

2.7.4   Results

2.7.5   Discussion

2 METHODS

2.1 Culture media

2.1.1 Media reagents

Dulbecco's Modified Eagle Media (DMEM). low glucose DMEM, high glucose DMEM, low glucose DMEM (Pyruvate, no L-Glutamine, no Phenol Red), Insulin-Transferrin-Selenium-G supplement 100X, (Gibco, Paisley, UK); foetal bovine serum (FBS), penicillin/streptomycin, sodium pyruvate solution 100 mM, bovine serum albumin (BSA), L-Glutamine solution 200 mM, HEPES solution 1 M, L-proline 40 mg/ml, Linoleic acid-water soluble, L-ascorbic acid, Dexamethasone-water soluble, Trypsin/EDTA, phosphate buffered saline (PBS) (Sigma-Aldrich, Poole, UK); recombinant human transforming growth factor beta-3 (TGF-β3) (PromoKine, Heidelberg, Germany).

2.1.2 Stem cell expansion media

The following media was used for culturing human bone marrow derived mesenchymal stem cells (hMSCs) based on previous studies (Thorpe, *et al.*, 2010). Expansion media (X-PAN) consisted of low glucose DMEM 10% FBS and 1% penicillin/streptomycin. The media was prepared by mixing 56.2 ml FBS and 5 ml penicillin/streptomycin which was then filtered through sterile 0.22 μm filter and added into 500 ml DMEM. The X-PAN media was stored in the fridge at 4°C for 1-2 months.

2.1.3 Chondrogenic differentiation media

Chondrogenic differentiation medium (CDM) consisted of high glucose DMEM supplemented with 100 U/ml penicillin and 100 μg/ml streptomycin, 1 mM Sodium pyruvate, 1.5 mg/ml BSA, 40 μg/ml L-proline, (1x) Insulin-Transferrin-Selenium-G supplement, 4.7 μg/ml Linoleic acid, 50 μg/ml L-ascorbic acid, 100 nM Dexamethasone, 10 ng/ml TGF-β3. This media has been used in numerous previous studies to induce chondrogenic differentiation of hMSCs (Pattappa, *et al.*, 2013). The CDM base media was prepared by dissolving 750 mg of BSA into 20 ml DMEM and adding 5 ml penicillin/streptomycin, 5 ml sodium pyruvate and 500 μl L-proline. The solution was mixed well and then filtered through a sterile 0.22 μm filter and added into remaining 480 ml of DMEM. The CDM base media was stored in the fridge at 4°C for up to 1-2 months. The final media for cell culture was prepared daily as growth factors need to be stored at low temperatures to maintain their activity.

Required supplements and volumes for final chondrogenic media are given in the table 2.1.

Table 2.1: The supplements and quantities required for preparation of chondrogenic differentiation media.

Item with stock concentration	Final concentration	Quantity (µl)
CDM base		1000
Insulin-Transferrin-Selenium-G-Supplement (100X)	1X	10
Linoleic acid 4.7 mg/ml	4.7 µg/ml	1
Dexamethasone 100 µM	100 nM	1
TGF-β_3 10 µg/ml	10 ng/ml	1

2.1.4 Chondrocyte media

Dulbecco's Minimal Essential Medium (DMEM) supplemented with 16% FBS and 1% penicillin/streptomycin was used for isolated chondrocytes and cultures. The media was prepared by mixing 100 ml FBS, 5 ml L-glutamine (200 mM), 10 ml HEPES buffer, 5 ml penicillin/streptomycin and 0.075 g L-ascorbic acid. The mixture was filtered through the 0.22 µm sterile filter into 500 ml DMEM bottle of media. Sterile media was then aliquoted into sterile 80 ml containers with 50 ml per container. The aliquots of media were stored in the freezer at -20°C. Prior to cell culture, the frozen medium is thawed in a 37°C water bath and osmolality measured and set to be about 310-330 mOsmol/kg.

2.1.5 Imaging media

For micropipette aspiration experiments, cells were suspended in imaging media (IM) consisting of low glucose DMEM 10% FBS and 1% penicillin/streptomycin, 4 mM L-Glutamine solution, 25 mM HEPES. The media was prepared by mixing 59.2 ml FBS, 5 ml penicillin/streptomycin, 11.8 ml L-glutamine solution and 14.8 ml HEPES. The solution was mixed and filtered through a sterile filter into 500 ml DMEM. The IM was aliquoted into 80 ml sterile containers with 50 ml volume and stored in the freezer at -20°C.

2.2 Cell source and culture

2.2.1 HMSCs

Human bone marrow derived mesenchymal stem cells (hMSCs) from bone marrow aspirates were purchased from commercial source (Lonza, Wokingham, UK) as previously described (Pattappa*, et al.*, 2013). All studies described herein used cells from a male donor, age 40 (hMSC-003). Aliquots of purchased cells were stored in liquid nitrogen.

Prior to an experiment, culture media and a frozen aliquot of hMSCs were thawed in a 37°C water bath. As soon as the sample appeared thawed, the cell suspension was transferred into a 50 ml falcon tube and X-PAN medium was added drop by drop, while gently swirling the tube. The final volume of 15 ml X-PAN medium added and invert mixed. The cell suspension was centrifuged at 1300 rpm for 15 minutes. The supernatant was carefully aspirated, ensuring that cell pellet was undisturbed. The pellet was suspended in 1 ml of X-PAN medium, then gently mixed and prepared for cell counting and viability assessment using the trypan blue exclusion assay. Trypan blue stains the nuclei cells of that have sustained damage to their cell membrane, leaving healthy or live cells unstained. A 10 μl cell suspension was mixed with 10 μl trypan blue (0.4%) and pipetted into a haemocytometer chamber. The cells were counted using a brightfield microscope. The total cell number was calculated as follows based on the mean number of cells in three squares in the haemocytometer.

$$\text{Total number of cells} = \text{Mean number of counted cells} \times \text{Dilution factor} \times 10^4 \times \text{Volume of suspended cells} \qquad (2.1)$$

The viability of cells was calculated as follows and found to be 90-95% for all experiments.

$$Cell\ viability\ \% = \frac{number\ of\ unstained\ cells}{total\ number\ of\ cells} x100 \qquad (2.2)$$

HMSCs were cultured in 24-well plates at a density of 5 x 10^3 cells/cm^2 in X-PAN medium which was replaced every 2-3 days. At confluence of 80-90%, after

approximately 7-9 days in culture, the media was removed and cells were washed with 10 ml PBS. The PBS solution was then replaced with 3 ml Trypsin-EDTA (0.25%) and the flask placed into a $37^{o}C$, 5% CO_2 incubator for 3-5 minutes. Detachment of cells was checked by light microscopy prior to addition of 10 ml X-PAN medium to completely wash cells from the surface. The cell suspension was transferred into a 50 ml falcon tube and centrifuged 1300 rpm for 3 minutes. The cell pellet was resuspended in 1 ml X-PAN medium. Cells were passaged in 24-well plates up to passages 8.

2.2.2 Chondrogenic differentiation

Cells at passages 3-8 were cultured for two days in X-PAN medium allowed cells to attach the culture plate. Afterwards, the X-PAN medium was replaced with CDM and cultured for seven days. During the differentiation period, the medium was replaced with fresh medium every 2-3 days.

2.2.3 Primary chondrocytes

The method employed to isolate chondrocytes from bovine articular cartilage was adapted from previous studies (Lee, *et al.*, 1998). The front feet of 12-24 months old bovine steers were acquired within 2 hours slaughter. The bovine feet were scrubbed in warm water, followed by soaking in 2% virkon solution for 20 min and immersed in 70% methyl alcohol for 15 min. The clean bovine feet were opened and the cartilage removed within the sterile laminar flow hood. The full depth cartilage attached to the metacarpal surface of the joint was removed using a scalpel and immersed in culturing medium (DMEM + 16% FBS) ensuring that the cartilage pieces were fully covered with medium to prevent dehydration. The cartilage slices from 2-3 different joints were pooled for each experiment. Prior to cartilage isolation the pronase and collagenase solutions were prepared in the required volume of DMEM media with 10% of FBS. Solutions were filtered with sterile 0.22 μm filter. The culturing media was aspirated from the cartilage slices and cartilage diced for better digestion. The pieces of cartilage were placed in a 50 ml falcon conical tube with 10 ml of pronase solution. A pronase solution with an activity of approximately 34 units/ml was prepared by mixing pronase substrate (Sigma-Aldrich, Poole, UK) with (DMEM +16% FBS). The tube was placed in the $37^{o}C$ on a rotamixer for 1 hour. The pronase was then replaced with 30 ml of collagenase solution and the tube then moved back in the $37^{o}C$ oven on the rotamixer for 14-16 hours. The collagenase

solution was prepared with an activity of 100 units/ml mixing collagenase substrate (Sigma-Aldrich, Poole, UK) with DMEM +16% FBS. The solution with digested cartilage tissue was filtered through a 70 μm filter to remove cartilage particles or aggregates of cells and centrifuged at 2000 rpm for 5 minutes. The cell pellet was collected, resuspended in 20 ml of culture medium and then re-centrifuged at 2000 rpm for 5 minutes. The supernatant was aspirated and cells suspended in 10 ml culture medium. Trypan blue expansion assay was used to check the viability of cells and the cell number was counted using a haemocytometer. The cell viability was calculated to be 95-98% for all experiments.

2.2.4 Chondrocyte dedifferentiation

Freshly isolated chondrocytes were seeded at density of 7.0 x 10^4 cell/cm^2 either in 24- or 6-well plates. For all experiments, cells were cultured for nine days in culture medium at 37^oC with 5% CO_2. In the following chapters, freshly isolated chondrocytes are named as passage 0 (P0), whilst those cultured for 9 days in culture medium are named as passage 1 (P1). Prior to experiments for cells cultured in 24-well plates, the medium was aspirated and replaced with 500 μl of PBS. After 5-20 seconds the PBS was removed and 200 μl of trypsin-EDTA solution was added. The plate was placed into an incubator for 3-5 minutes for cell detachment. The cell detachment was checked under light microscope and additional culture medium of 1 ml was added to wash detached cells from the surface. The suspended cells were collected into a 15 ml falcon conical tube and centrifuged at 1300 rpm for 3 minutes. The pellet was collected, suspended in fresh IM and placed in water bath for 10 minutes, allowing cells to recover after detachment. Cells cultured in 6-well plates were used for protein isolation,

2.3 Micropipette aspiration system

2.3.1 Manufacturing micropipettes

Pulling micropipettes

The micropipettes were prepared by pulling borosilicate glass capillaries (outer diameter of 1 mm, inner diameter of 0.58 mm; Narishige, Japan) with a programmable pipette puller Flaming/Brown Model P-97 (Sutter Instrument, USA).

The glass capillary was mounted on the holder, heated and pulled using the parameters given in table 2.2.

Table 2.2: Parameters used to pull the micropipettes from borosilicate glass capillaries.

No.	Heat	Pull	Velocity	Time mode	Delay mode	Pressure
1	Ram + 20	0	120	200	-	200

Polishing

Micropipettes with a diameter of 6-8 μm for hMSCs and 5-6 μm for chondrocytes were used based on the cell size. This is due to the requirements for the cell/micropipette diameter ratio of less than 2.5 in order to use the Standard linear solid model (Zhao*, et al.*, 2009). To prevent damage of cell membrane, a microforge (MF-900; Narishighe, Japan) was used to produce micropipettes with a smooth (polished) flat tip

The microforge consists of a side view microscope with an in-built ocular micrometer and platinum wire filament mounted with a glass bead. The procedure involved using the heated glass bead to cut the tip of the micropipette at a specific (inner) diameter, measured using the micrometer. Once cut, the tip of the pipette was polished using the glass-bead mounted on microforge.

Coating

Polished micropipettes were coated with Sigmacote (Sigma, UK) to prevent adhesion between the cell and the micropipette. Sigmacote is an organopolysiloxane in heptane, which reacts with silanol groups on glass to produce a neutral or hydrophobic thin film. The film reduces adhesion and prevents adsorption of many basic proteins. The polished micropipettes were treated with Sigmacote by dipping into the solution for 5-10 seconds. Coated pipettes were dried on the microforge above the glass bead. After the tips of micropipettes were bended at 10 degree, which allows to focus along the micropipette without changing focus plane.

2.3.2 Pump system

Micropipette aspiration uses negative (suction) pressure generated by reducing the height of water in a reservoir that is connected to the micropipette. Previously, this type of apparatus was used to generate pressures by vertically moving the water in a columnar reservoir where the height was monitored by a manometer (Rand and

Burton, 1964). With such a method it is difficult to control the magnitude and temporal characteristics of the applied pressure.

Therefore the precise temporal control of pressure during aspiration was achieved by using a PC-controlled peristaltic pump (MCP, Standard, Ismatec) to regulate changes in aspiration pressure by modulating the height of water in the reservoir with heigh of 400 mm and inner diameter approximately 50 mm. The schematic diagram of aspiration system incorporated with peristaltic pump is shown in figure. 2.1.

The pump system is controlled by custom written LabView software (LabView Manufacturer), enabling precise control of water height to $\pm$ 0.1 cm (0.01 kPa). This system enables aspiration pressure to be applied in two different regimes. For determination of the viscoelastic properties, a step pressure is applied and held for the required time. While pressures are applied via the apparatus, the temporal changes in aspirated cell length are measured from the images captured by confocal microscopy as described in section 2.5.2. In contrast, to determine the pressure required to detach the membrane from the actin cortex, aspiration pressure is applied in a series of increments with fixed time between each increment. In both manipulation regimes the rate of pressure applied can be controlled.
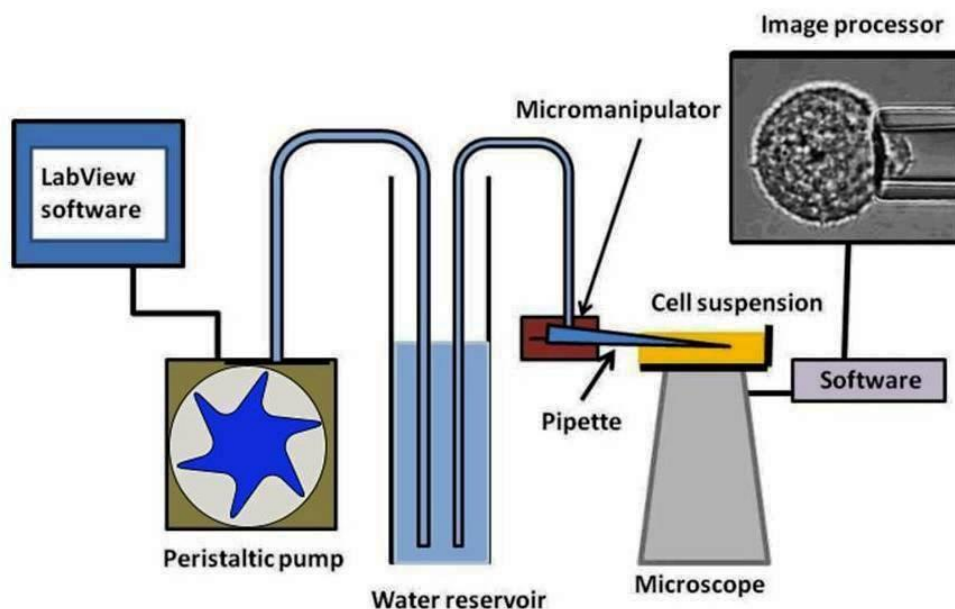
Figure 2.1: A schematic representation of micropipette aspiration system. The height of water in the reservoir is adjusted by the peristaltic pump, which is controlled with LabView software. The reservoir is connected to the pump and the micropipette by water filled silicon tubing.

2.4 Protocols for micropipette aspiration

2.4.1 Cell manipulation

The protocol for micropipette aspiration and measurements of cellular viscoelastic properties was similar to that previously described but with the addition of the pump system as described above (Jones, *et al.*, 1999, Sato, *et al.*, 1990).

A chamber for micropipette aspiration was custom made from a glass frame which was adhered to a coverslip using silicone grease (Fig. 2.2). The chamber was placed on the microscope stage in such a way as to allow access to the micropipette from the side whilst maintaining the cells hydrated in a drop of imaging media (IM).
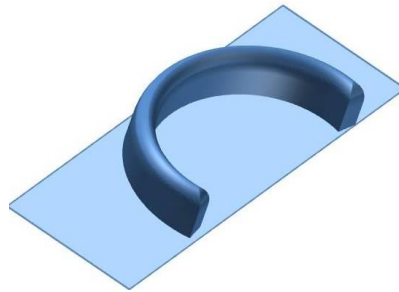
Figure 2.2: A schematic illustration of the chamber used for micropipette aspiration.

A cell suspension of about 0.5 ml at density of 15 x 10^3 cells/ml was placed in the chamber mounted on microscope stage. The cells were let to equilibrate and settle down for 1-2 minutes. The aspiration experiments were performed at room temperature as in many previous studies (Jones, *et al.*, 1999, Yu, *et al.*, 2010). Micropipettes were pre-filled with IM and mounted on an automated micromanipulator (Eppendorf, Germany). The aspiration pressure inside micropipettes was tested by placing the micropipette in contact with a cell and the pressure adjusted to be zero such that the cell was neither aspirated nor pushed away. A negative tare pressure of 0.5 cmH$_2$O (0.049 kPa) was applied to ensure that cell was held onto the micropipette. The micropipette with the attached cell was then lifted to ensure that cell was not attached to the chamber surface. The negative pressure was applied according to the required protocol and cell deformation was imaged using brightfield and/or confocal microscopy. All micropipette aspiration experiments were performed within 1 hour after cell detachment from monolayer culture. Sufficiently short time and room temperature did not effect measurements.

This was confirmed by no any trends in experiments observed in terms of cell mechanical properties during micropipette aspiration.

2.4.2 Measurements of viscoelastic properties

The viscoelastic behaviour of the cell can be modelled by using a standard linear solid (SLS) model (Sato, *et al.*, 1990). In this model, the cells are assumed to be a homogenous and incompressible viscoelastic material. The model consists of combination of parallel spring and a dashpot for more details see section 1.3.3. The SLS model can characterise both cell relaxation and creep behaviour. In previous studies, this model was used to estimate viscoelastic cell behaviour from the micropipette aspiration experiments (Tan, *et al.*, 2008a, Trickey, *et al.*, 2000). In this model the viscoelastic characteristics of the cell can be determined from the equations as follows:

$$L(t) = \frac{\Phi a \Delta p}{\pi E} \times \left[1 + \left(\frac{k_1}{k_1 + k_2} - 1\right) exp\left(-\frac{t}{\tau}\right)\right], \qquad (2.3)$$

Where the L(t) is the temporal change in aspirated cell length over time t. The elastic constants k_1, k_2 and time τ can be estimated from a non-linear regression method by curve fitting the experimental data to (equation 2.3). The apparent viscosity μ, the equilibrium E_∞ and the instantaneous E_0 moduli can de estimated from (equations 2.4-2.6).

$$\tau = \frac{\mu}{k_1}\left(1 + \frac{k_1}{k_2}\right), \qquad (2.4)$$

$$E_0 = \frac{3}{2}(k_1 + k_2) \qquad (2.5)$$

$$E_\infty = \frac{3}{2}k_1, \qquad (2.6)$$

The experimental protocol for SLS model was initiated by applying a pressure of 7.7 cmH$_2$O (0.76 kPa) over a period of 2 seconds see the protocol 1 in table 2.3. Cell movement inside the micropipette was imaged by brightfield microscopy for a period of 180 seconds.

2.4.3 Membrane – actin cortex detachment pressure and cortical tension

The cell's cortical tension and the strength of the bond between the membrane and the actin cortex can be estimated using the following protocol 2. The aspiration pressure was applied in seven increments of 1.5 cmH$_2$O (0.147 kPa) with 15 seconds between each increment. For each increment, pressure was increased linearly over 15 seconds. The details of the other parameters used in this protocol can be found in table 2.3. The aspiration experiments were recorded for 210 seconds and aspirated length measured during the time. The detachment pressure of the membrane and actin cortex was estimated as the pressure at which the membrane was detached from the cortex, initiating bleb formation.

The cortical tension of the cell can be calculated according to the Laplace law, as described in section 1.3.1. When the aspirated pressure is sufficient to cause aspirated length to be equal to the micropipette radius, the cortical tension can be estimated from following equation:

$$T = \frac{\Delta P}{2\left(\frac{1}{R_p} - \frac{1}{R_c}\right)} \tag{2.7}$$

where T is cortical tension, ΔP is applied negative aspirated pressure, R_p and R_c are the internal radius of micropipette and the radius of the cell outside the micropipette, respectively. The internal radius of micropipette was measured from images assuming that there is no an optical abberation. More details on error calculation see section 2.5.5.

Table 2.3: Aspiration parameters used to determine viscoelastic properties and membrane-actin cortex adhesion of the cell.

Parameters	Protocol 1 Values	Protocol 2
Tare pressure: P_T (cmH$_2$O)	0.5	0.5
Initial time: T_0 (secs)	2	2
Step pressure: ΔP (cmH$_2$O)	7.7	1.5
No of steps:	1	7
Time interval: T_1 (secs)	0	15
Step time: T_2 (secs)	2	15
Hold time: T_{hold} (secs)	180	6
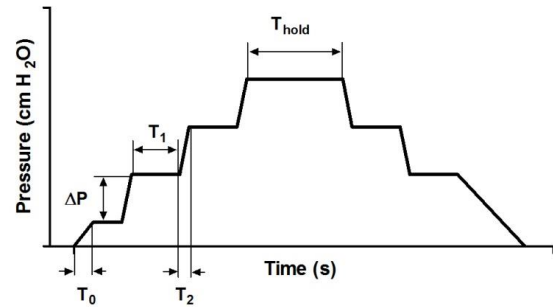
2.5 Imaging

2.5.1 Confocal theory

Confocal fluorescence microscopy has become a widely used and important tool in biology and biomedical sciences. A diagram illustrating the principles of confocal microscopy is presented in figure 2.3. The light is emitted by the laser excitation source is focused through the light source excitation pinhole, is reflected by a dichromatic mirror and is focused onto the emission detector pinhole scanned across the specimen. The fluorescence emitted light from the specimen has a large wavelength due to stokes shift and therefore passes back through the dichromatic mirror and is focussed on the emission detector pinhole. The excitation pinhole ensures only the focal plane is illuminated thereby minimising photobleaching and phototoxicity and maximising confocality. Thus the detector pinhole ensues that only light from the focal plane is passed through to the photomultiplier. Brightfield imaging can also be performed using a confocal microscope. The light which passed through the specimen is collected into transmitted light detector. The contrast of brightfield images depend on objective and condenser numerical aperture.

For optical images the lateral resolution is defined as the distance by which two objects are separated from each other. The distance is equal to the radius of the smallest point source in the image knows as first minimum of the airy disk. The lateral resolution is given as follows:

$$r_{lateral} = 0.4\lambda/NA \tag{2.8}$$

Where λ is the wavelength of emission light and NA is the numerical aperture of the objective. Resolution in the z-axis is worse than the lateral resolution and is proportional to the wavelength and refraction index of the medium and inverse proportional to the square of the numerical aperture of the objective. The numerical aperture has a greater effect on axial resolution compared to wavelength. The axial resolution is given as follows:

$$r_{axial} = 1.4\lambda\eta/NA^2 \qquad\qquad (2.9)$$

where the η is presented as an index of refraction.

The primary advantage of confocal microscopy is therefore the ability to produce thin optical sections though the specimen by moving the vertical position of the objective to move the focal plane. The contrast of scanned specimens is also improved due to the elimination of fluorescence in background.

The disadvantages of confocal are primarily the limited number of excitation wavelengths available with common lasers, which have very narrow bandwidths or are expensive. Another negative aspect that is particularly relevant when imaging living biological specimens is that irradiation with high intensity laser can be harmful. Lastly, the high cost of confocal microscopy and operation systems.
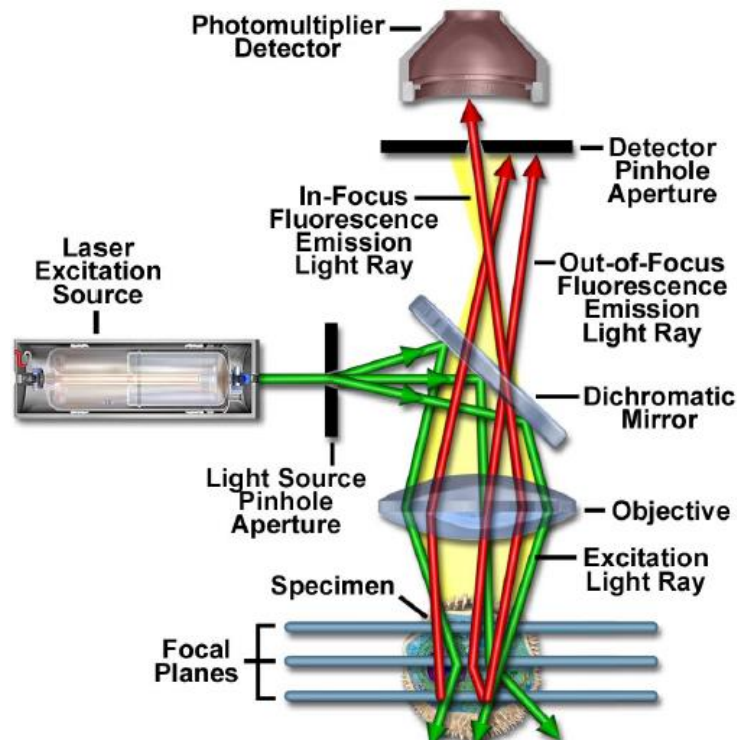
Figure 2.3: A schematic representation of laser scanning confocal microscope (Claxton, et al., 2006). The Excitation light (green arrows) passes the pinhole, is reflected from the dichromatic mirror, extended by objective and focused on specimen. Emitted light (red arrows) from the specimen is extended by objective, passes the dichromatic mirror and is collected in the detector. Emitted light which is not focused is eliminated by detector pinhole.

2.5.2 Imaging protocol for micropipette aspiration

Both brightfield and fluorescence imaging were performed using a laser scanning confocal fluorescence microscope (SP2, Leica). Brightfield imaging was used during micropipette aspiration. The fluorescence application was used to image the actin cortex labelled with LifeAct-GFP and actin-GFP for live cells and Alexa555-phalloidin for fixed cells (for more details see section 2.7). Fluorescence imaging will be explained more in details in later chapters. For brightfield imaging a 488 nm laser was employed with a x63/1.4 NA objective. Image brightness and contrast properties are controlled by the power of laser accompanied with offset and gain. The settings used for brightfield imaging are given in table 2.4, producing images with a normal pixel size of 0.19 μm. These values were used to achieve brightfield imaging during the micropipette experiments.

Table 2.4: Confocal microscope setting parameters for brightfield imaging.

Parameters	Brightfield
Line average	1
Frame average	1
Objective	x63
Zoom	2.5
Scanning speed	400 Hz
Image format	512 x 512
488 nm laser	25%

2.5.3 Quantification of aspirated length

The aspirated length (L) of the cell into the micropipette was measured using a semi-automated Matlab code. The code is designed to select the image and to measure the aspirated length as indicated in figure 2.4. The initial point of aspiration (L=0) is defined as the edge of the micropipette tip. The end point of aspirated length is determined as the longest aspirated length in the middle section of micropipette. The length is measured parallel to the axis of the micropipette. The series of measurements are automatically saved to an excel file and the SLS model fitted to the data using Matlab (Appendix A2). The fit approximation (equations 2.3 - 2.6) enables the determination of the viscoelastic parameters; equilibrium modulus (E_∞), instantaneous modulus (E_o) and viscosity (μ).
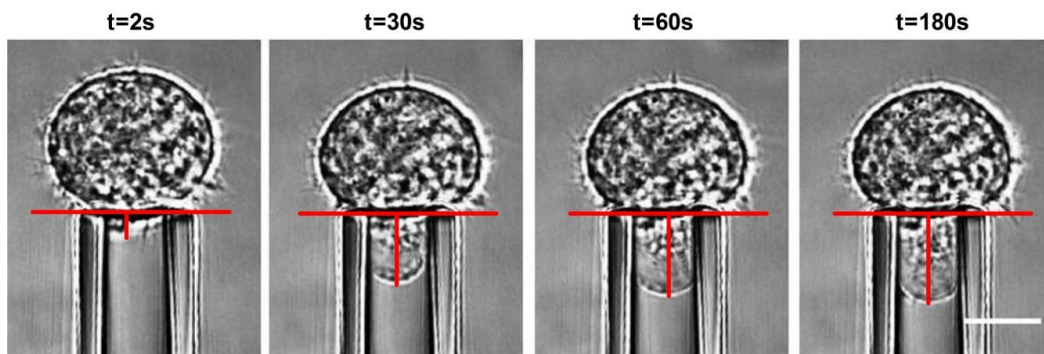
Figure 2.4: Measurement of aspirated length. The aspirated length (shown in red) is measured from brightfield images taken at different time points up to 180 seconds following the application of a step change in pressure. Scale bar 10 μm.

2.5.4 Exclusion criteria

Some cells were excluded from calculation of viscoelastic properties based on the following exclusion criteria:

1) Cell did not show any aspiration during the 180 seconds period (Fig. 2.5 A). Although this may be the result of an exceptionally stiff cell is it more likely to be due to a poor seal between the cell and the micropipette

2) Cell membrane ruptures during aspiration (Fig. 2.5 B). Typically this occurred when a portion of membrane detaches from the entire cell and was aspirated rapidly further into the micropipette.

3) The theoretical SLS model did not fit the data such as $R^2 > 0.95$ (Fig. 2.5 C).
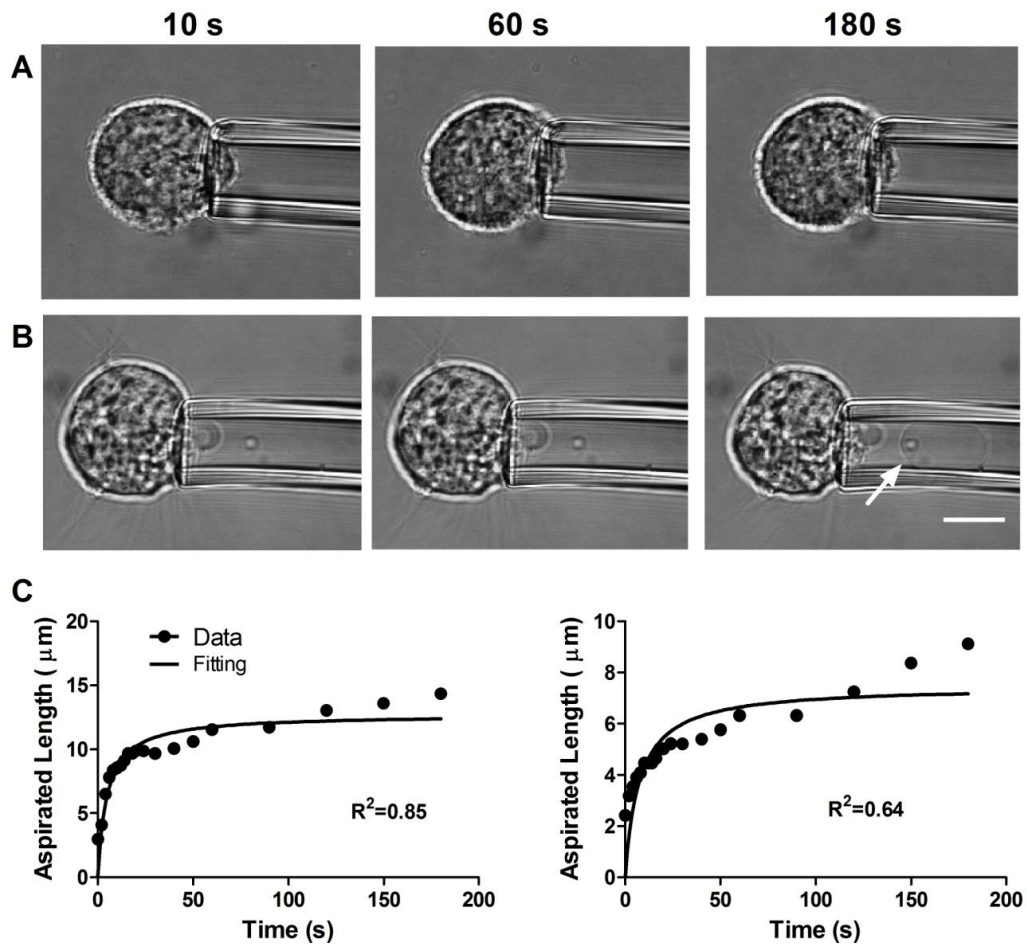
Figure 2.5: Cells excluded from analysis. (A) Cell shows no aspiration during 180 seconds. (B) The membrane ruptures (arrow) during the micropipette aspiration. The ruptured membrane is indicated with the arrow. Scale bar 10 μm. (C) The theoretical model does not fit the experimental data ($R^2 < 0.95$).

2.5.5 Errors associated with aspiration measurements

In this study all measurements of aspiration length were estimated assuming that there is no an optical aberration. However, previous studies have demonstrated that an error occurs due to optical abberation. This can be corrected by implementing correction coefficient which depent on retractive indices of buffer (1.33) and glass (1.49), and focusing error (3.2%) (Engström and Meiselman, 1994, Jones, *et al.*, 1999). This gives the correction coefficient 0.92 which indicates that our measurements being overestimated by 8%.

The error of aspiration length during micropipette aspiration measured from images was estimated to be ±1 pixel, which is equivalant to 0.19 μm. According to the error of aspirated length measurements introduced above, the viscoelastic properties such as the equilibrium and instantaneous moduli and viscosity have errors of ±4.8 Pa, ±7.0 Pa and ±160,9 Pa.s respectively.

2.5.6 Statistical analysis of micropipette aspiration data

For this study, the parameters such as aspirated length, equilibrium modulus, instantaneous modulus and viscosity are assumed to be non-normally distributed and for this reason we used non parametric statistics. The data in the graphs are presented as a population with bar indicating the median values. The significant differences between the samples are determined using the Mann Whitney U test. Significant difference was reported at * $p<0.05$, ** $p<0.01$ and *** $p<0.001$.

2.6 Pilot study – Morphology and mechanical behaviour of hMSCs

2.6.1 Methods

This study tests the hypothesis that passage number of hMSCs has no effect on cell viscoelastic behaviour estimated using micropipette aspiration coupled with the SLS theoretical model.

HMSCs were seeded in 24-well plates and cultured as described in section 2.2.1. At passages P1, 3, 4 and 5, cells were trypsinized and resuspended in pre-warmed PBS. The chamber with cell suspension was mounted on the stage of scanning laser confocal microscope. Brightfield images of fields of cells were captured using a

x40/1.4 NA oil immersion objective with a pixel size of 0.73 μm. Cell diameter was estimated by averaging the horizontal and vertical diameters measured for individual cells using the semi-automated Matlab Code (Appendix A1).

The micropipettes were pulled and polished as described in section 2.3.1. It was important to keep the ratio of cell diameter to micropipette inner-diameter ratio of 2.5-3 for estimation of the viscoelastic properties of the cell, as cell diameter is not involved in SLS theoretical model.

The viscoelastic properties of the cell were estimated using the micropipette aspiration system as described in section 2.3.2. The single cell was held on the tip of the micropipette by applying a negative tare pressure of 0.5 cmH$_2$O (0.05 kPa). Then a step pressure of 5.5 cmH$_2$O (0.54 kPa) was applied in 2 seconds and held for 90 seconds. Brightfield images were recorded every 2 seconds using a x63/1.4 NA oil immersion objective. The aspirated length was measured as described in section 2.5.3. Determination of cell viscoelastic properties, the equilibrium modulus, the instantaneous modulus and the viscosity, was performed by fitting the temporal change in aspiration length with the theoretical SLS model as described in section 2.4.2.

2.6.2 Results
Effect of passage on cell size
The cell diameter distributions during hMSCs passages are shown in figure 2.6. The median values of the cell diameter of the hMSCs in passages P1, P3, P4 and P5 were calculated to be 15.8 μm, 15.6 μm, 18.8 μm and 20.3 μm respectively. With increasing passage number hMSCs show a wider spread of cell size distribution. Cell size does not change from P1 to P3 but increases from P3 to P4 and again from P4 to P5, the differences being statistically significant (Fig. 2.7).
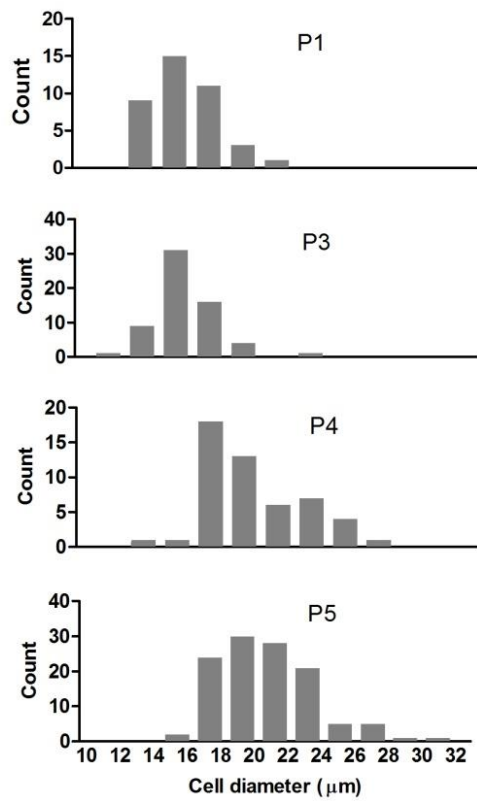
Figure 2.6: Histograms representing cell size distribution of hMSCs from passages P1 to P5. Cell number in each group is as follows: P1 (39), P3 (62), P4 (51) and P5 (117) cells.
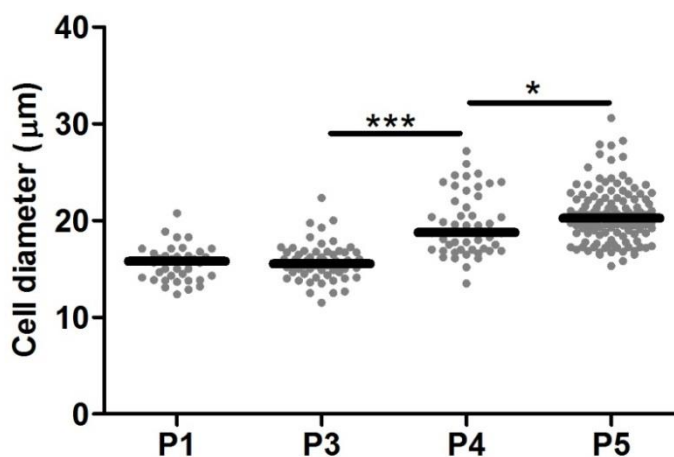
Figure 2.7: Cell size during hMSCs aging. The plot presents the cell size distribution of whole population with median values of different passages. Mann-Whitney U test, * p<0.05, *** p<0.001.

Effect of passage on viscoelastic behaviour of hMSCs

The effect of passage on hMSCs mechanics was estimated using the micropipette aspiration system. The exclusion criteria were adopted as described in section 2.5.4. The total number of tested cells is given in table 2.5 along with the number that were successfully analysed using the SLS model, which ranged from 44% to 80% of the total. There was no correlation between the percentage of cells successfully aspirated and used for analysis and the passage number.

Representative images of cells aspirated inside the micropipette during the aspiration are presented in figure 2.8. Cells exhibited viscoelastic behaviour during the aspiration (Fig. 2.9 A). Aspirated length suddenly increased by applying a negative pressure and equilibrated. The aspirated length at 90 seconds, the equilibrium and the instantaneous moduli showed no correlation in response to passage number up to P5 (Fig. 2.9 B-D).

Table 2.5: Numbers of cells used for the micropipette aspiration experiments. Values in parentheses indicate the percentage of the total number of tested cells that passed the exclusion criteria.

Cell type	Total No of cells	No of successful aspirations	No used for model $R^2>0.95$
P1	13 (100%)	7 (54%)	6 (46%)
P2	5 (100%)	5 (100%)	4 (80%)
P3	15 (100%)	12 (80%)	10 (67%)
P4	13 (100%)	11 (85%)	8 (62%)
P5	18 (100%)	8 (44%)	8 (44%)
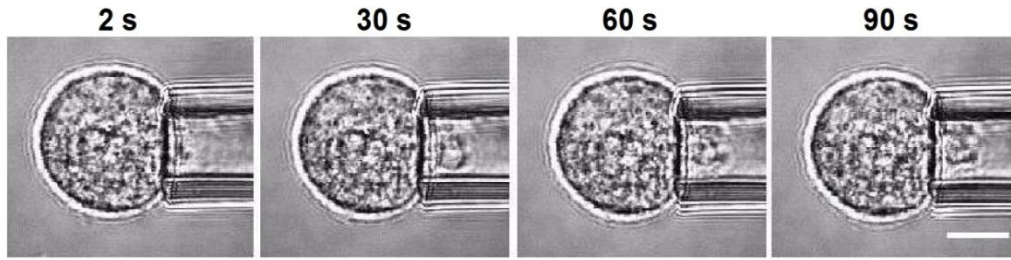
Figure 2.8: Representative brightfield images of cell aspirated inside the micropipette. Images are showing cell at 2, 30, 60 and 90 seconds after the applied a negative pressure of 5.5 cmH$_2$O (0.54 kPa). Scale bar represents 10 µm.
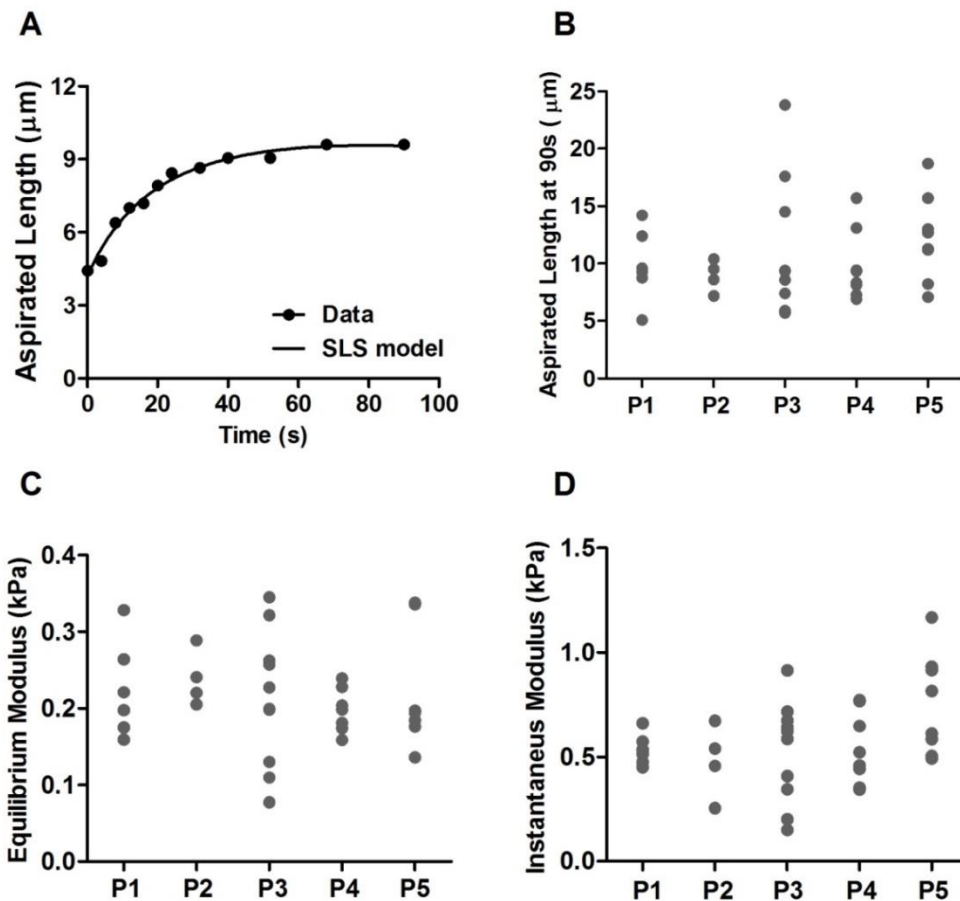
Figure 2.9: The effect of passage number on the viscoelastic properties of hMSCs. (A) Typical cell behaviour of cell aspirated length versus time with a nonlinear regression curve fitting applying SLS theoretical model. (B) Aspirated length at 90 seconds, (C) the equilibrium modulus and (D) the instantaneous modulus. The data is presented as a population. There were no correlations between passage number and viscoelastic properties. Nonparametric correlation Spearman test. See table 2.5 for number of cells used for experiments.

2.6.3 Discussion

This pilot study has demonstrated that the micropipette aspiration system can successfully be used for estimating the viscoelastic properties of hMSCs. The effect of passage number on cell mechanics was examined by applying a step of negative pressure of 5.5 cmH$_2$O (0.54 kPa). The results show that hMSCs behave as a viscoelastic solid in agreement with previous micropipette aspiration studies of hMSCs and other cells (Jones*, et al.*, 1999, Tan*, et al.*, 2008a).

Passage number induced a change in the morphology of hMSCs. Cells in later passages P4 and P5 are significantly larger compared to P1 with a median diameter of 18.8 µm and 20.3 µm respectively (Fig. 2.7). This pilot study has demonstrated so hMSCs the passage number did not correlate with the aspirated length at 90 seconds and the two viscoelastic parameters, equilibrium and instantaneous moduli. This suggests that different passage number of cells can be used for further experiments.

2.6.4 Modification to the micropipette aspiration protocol

Based on previous experiments, the micropipette aspiration protocol was modified as follows:

- The micropipette aspiration and all live cell imaging were performed in imaging media (IM) rather than PBS as mentioned in previous studies (Yu*, et al.*, 2010). This provides similar environment as cells were cultured. The composition of this imaging media is given in section (2.1.5).
- Cell shape is important for micropipette aspiration. To ensure that cells round up after trypsinization, cells were left to equilibrate for 10-15 minutes in order to recover a spherical morphology (Fig. 2.10)
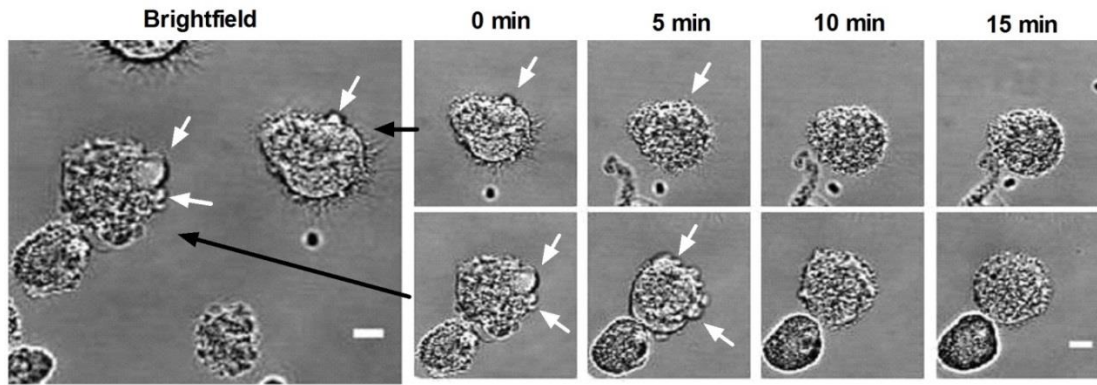
Figure 2.10: HMSCs showing extensive blebbing. Brightfield images of two individual live hMSCs showing extensive blebbing following detachment with trypsin. White arrows indicate membrane blebs. Blebs were fully retracted after 10-15 minutes. Scale bar presenting 10 μm.

- Coating of micropipettes is essential to prevent cell-glass adhesion. Coated micropipettes were dried above the microforge to remove any sigmacote residue, which could affect a smooth cell aspiration into the micropipette and the precision of measurements of aspirated length. Representative images of the micropipette dried overnight and on the microforge are presented in figure (2.11).
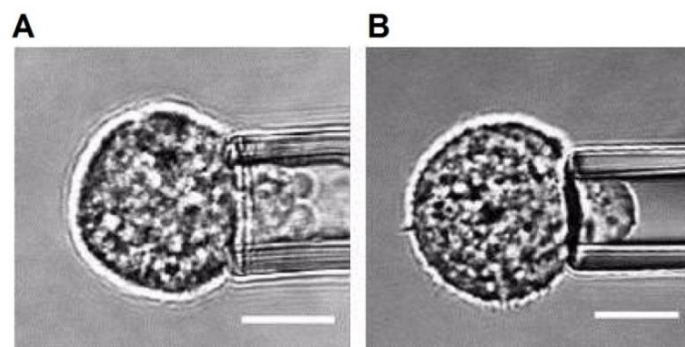
Figure 2.11: Representative brightfield images of cell aspirated inside the micropipette. The micropipette coated with sigmacote and (A) dried overnight at room temperature, (B) dried on a microforge regulating temperature.

2.7 Pilot study – Effect of LifeAct-GFP on cell mechanics

2.7.1 Introduction

Actin is a major component of the cytoskeleton in eukaryotic cells and plays a crucial role in many fundamental cellular processes, such as cell division (Heng and Koh, 2010), polarisation, cell shape (Fletcher and Mullins, 2010), migration (Pollard and Cooper, 2009) and differentiation (Titushkin and Cho, 2011). Furthermore, the cortical F-actin is involved in regulating cellular mechanical properties (Yourek, *et al.*, 2007) and also bleb formation (Charras, *et al.*, 2006). Mechanical rupture disassembly of the underlying actin cytoskeleton results in membrane detachment from the cortex and formation of a membrane bleb. With the increasing awareness of the importance of actin organisation and dynamics, the visualisation of actin in living cells has become an essential tool. Many studies have relied on injecting small amounts of fluorescently tagged phalloidin or genetically coupled fluorophores to actin. However, these applications are limited for living cells.

The other commonly used method for imaging actin remodelling and dynamics in live cells is by transfecting cells so that they express actin coupled to a fluorescent protein such as GFP (Endlich, *et al.*, 2007). This technique labels both the F-and the G-actin which can be useful for assessing the relative dynamics (Engelke, *et al.*, 2010) but also reduces the signal to noise when visualising F-actin structures (Lee, *et al.*, 2013). More importantly, studies have reported that this method directly disrupts actin dynamics during cell cytokinesis and migration (Aizawa, *et al.*, 1997), influences cell adhesion contacts with extracellular matrix (Feng, *et al.*, 2005) and alters the viscoelastic behaviour of cells and the apparent moduli (Pravincumar, *et al.*, 2012).

A study of Riedl et al. first described the use of LifeAct tagged to a fluorescent protein for labelling the F-actin with reduced artefacts (Riedl, *et al.*, 2008). LifeAct is a 17-amino-acid peptide that binds to actin and because of its small size and absence from mammalian cells, is perfect for binding F-actin with minimal disruption. Furthermore, LifeAct has higher affinity to F-actin than to G-actin and has been shown not to affect cell migration or polarization (Riedl, *et al.*, 2008). However, little is known about how LifeAct affects actin dynamics during cell deformation and the associated viscoelastic mechanical properties of whole cells.

This initial pilot study was therefore conducted to examine the effect of LifeAct-GFP on actin dynamics and remodelling in response to mechanical distortion during micropipette aspiration. The study also compared the results with those obtained using actin-GFP. The effect of LifeAct-GFP and actin-GFP on cell mechanical properties was investigated using confocal fluorescence microscopy in combination with micropipette aspiration system and the theoretical SLS model.

2.7.2 Methods

hMSCs were seeded and cultured as described in section 2.2.1. Cells were induced to chondrogenic differentiation for 7 days as explained in section 2.2.2.

Actin-GFP transfection

Undifferentiated hMSCs were transfected with actin-GFP using a plasmid. The plasmid actin-GFP was a kind gift from N. Gavara (Queen Mary University of London). Prior to the experiment, agar plates were inoculated with bacterial cells (E. coli) transformed with the plasmid and incubated at 37°C overnight. Single bacterial colonies were expanded in culture for 16-20 hours on shaker at 37°C in the incubator (more details in Appendix B). Plasmid DNA from E. Coli was purified using a High Pure plasmid isolation kit (Roche Diagnostics, Burgess Hill, UK) to prepare up to 150 μg of plasmid DNA from 2 ml bacterial culture. The resulted plasmid DNA was used for further studies.

Cells were tranfected by lipofection using Lipofectamine LTX Plus (Invitrogen, UK). Briefly, prior to transfection, cells were cultured in antibiotic free media, consisting of low glucose DMEM and 10% FBS for 30 min to 1 hour. Cells were transfected with 0.5 μg of DNA. Cells were cultured for 6 hours in transfection media as described in table 2.6, followed by replacement with new culturing media. The micropipette aspiration experiments were performed the following day.

Table 2.6: Procedure of preparation of transfection media.

Procedure	Volume	Steps
Opti-MEM medium	25 µl	Dilute Lipofectamine reagent
Lipofectamine Reagent	4 µl	in Opti-MEM medium
Opti-MEM medium	25 µl	Dilute DNA in Opti-MEM
DNA	0.5 µg	medium and add PLUS
PLUS reagent	0.5 µl	reagent
Diluted DNA with PLUS reagent		Add diluted DNA to diluted
Diluted Lipofectamine reagent		Lipofectamine reagent
Incubate for 5 min at room temperature		Incubate

LifeAct-GFP transfection

Undifferentiated hMSCs and those differentiated to chondrogenic lineage were transfected with adeno virus with LifeAct – TagGFP2 (Ibidi, Germany). The reagent was directly added to the cells cultured in monolayer. Prior to experiments the required amount of virus was calculated as follows:

$$Virus\ needed\ (\mu l) = \frac{Cell\ number\ seeded}{Viral\ titer} \times MOI \qquad (2.10)$$

The MOI is multiplicity of infection and viral titer is 1×10^7 IU/µl. IU is infection units. The coefficient MOI is described as a number of virus particles required to infect one cell. The MOI value can differ between cell types, for this reason an experimental optimisation procedure is required. Undifferentiated hMSCs were seeded at density of 5×10^3 cells/cm^2. Prior optimisation experiments cells were cultured for two days in X-PAN media. Different MOI values were chosen according to the provider's protocol as given in table 2.7. The reagent of LifeAct was directly added to culture dishes and incubated for one or two days at 37°C, 5% CO$_2$. Cells were imaged and transfection efficiency estimated using the equation as follows:

$$Transfection\ (\%) = \frac{Number\ of\ transfected\ cells}{Total\ number\ of\ cells} \times 100 \qquad (2.11)$$

Table 2.7: Conditions used for optimisation of virus concentration.

MOI	Culture plates	Cell number	Amount of virus (µl)
100	24 well	5000	0.1
200	24 well	5000	0.2
300	24 well	5000	0.3
500	24 well	5000	0.5
1000	24 well	5000	1

Two days prior to the micropipette aspiration experiments, cells were transfected by adding the required amount of adenovirus LifeAct-TagGFP2 F-actin marker directly to the culture plates. Cells were then incubated for two days at 37°C, 5% CO_2. After incubation, the media containing virus was removed (and appropriately disposed according to the safety protocol) from the plates and cells were prepared in suspension by treating with trypsin.

Visualization of actin structure in fixed cells

F-actin was visualised in hMSCs cultured in monolayer and in suspended cells. In both cases cells were transfected on coverslips in 24 well plates with either LifeAct-GFP or actin-GFP as described above. Cells were fixed in 4% paraformaldehyde (PFA) for 10 minutes, permeabilized for 5 minutes in 0.5% Triton X-100/PBS and stained with phalloidin Alexa Fluor555 (25 µl/ml in PBS + 0.1% BSA for 20 minutes). Coverslips with cells in monolayer were then washed in PBS and mounted with ProLong Gold. Cells in suspension were then washed in PBS and suspended in distilled water. The drops of stained cells in suspension were placed on coverslips and allowed to dry. Coverslips with cells were mounted with ProLong Gold and both cases of prepared cells were imaged using laser scanning confocal fluorescence microscope (TCS SP2) with a x40/ 1.25 NA immersion objective lens.

Micropipette aspiration

Cells were aspirated at 7.7 cmH$_2$O (0.76 kPa) as described in section 2.4.2 and imaged over 180 seconds. The change in aspirated length during time was measured from brightfield images as explained in section 2.5.3. For each cell, these data were fitted using the SLS model to calculate the viscoelastic parameters as described previously in section 2.4.2. In addition the viscoelastic properties like the equilibrium

modulus, the instantaneous modulus and the viscosity were estimated by curve fitting the theoretical model to experimental data.

2.7.3 Statistics

The data of transfection efficiency within a field of view was assumed to be normally distribution and values presented as mean with standard deviation. The Student's t-test was used to determine the significant differences.

The aspirated length of hMSCs and the viscoelastic parameters of cells were assumed to be non-parametric. The plots were presented as a population with a bar indicating the median values. According to the data distribution the Mann-Whitney U test was used to identify statistical significance differences presented as follows: * $p < 0.05$, ** $p < 0.01$ and *** $p < 0.001$.

2.7.4 Results

Optimisation of LifeAct-GFP transfection

In order to study the F-actin structure, cells were transfected with LifeAct-tagGFP2. To optimise the transfection conditions, images were analysed from trials using a range of MOIs: 100, 500 and 1000. Cells imaged on the following day showed no obvious difference between the different concentrations of virus. (Fig. 2.12). After an additional day, the number of transfected cells increased and differences between the different MOIs can be seen. We found that the MOI of 1000 is too high as many cells show an over expression; fluorescence intensity was saturated. For further studies the efficiency of transfected cells were calculated at different MOI of 100, 200, 300 and 500. Results have indicated that there were no correlation between transfection efficiency and virus concentration (Fig. 2.13). This could be due to incorrect volume of virus used for required number of cells. For lower MOIs, such as 100 and 200, it is difficult to measure the required volume of virus. For further experiments a MOI of 300 was chosen and the transfection efficiencies of hMSCs and differentiated cells were 54% and 49%, respectively (Fig. 2.14).
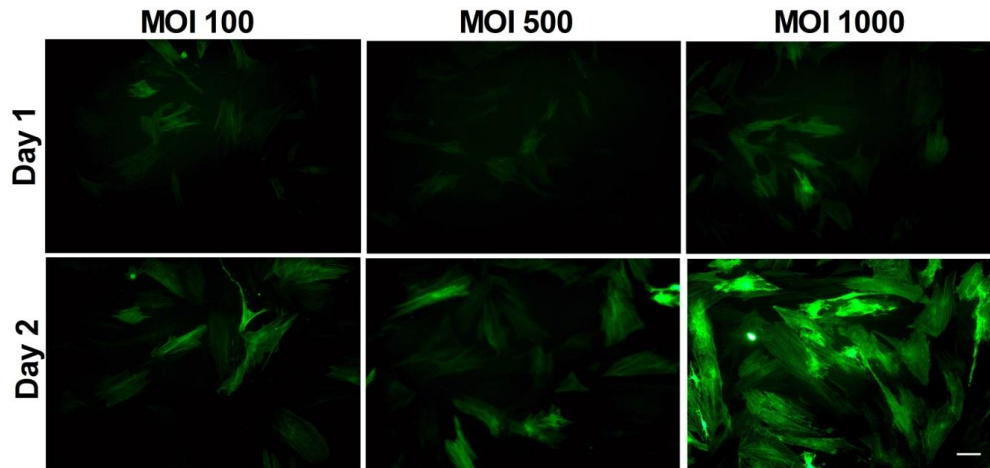
Figure 2.12: Representative fluorescence images of cells transfection with different concentration of LifeAct adenovirus. HMSCs were transfected with LifeAct-GFP reagent using different multiplicity of infection (MOI) concentration of virus for one and for two days. The MOI of 100, 500 and 1000 are shown in images.
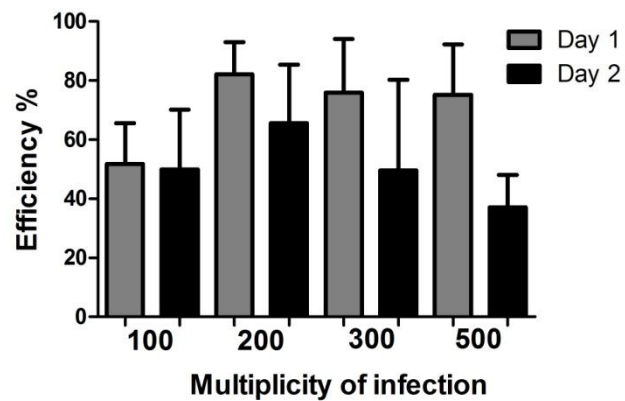
Figure 2.13: Percentage of transfected cells after using different concentration of virus. Cells were transfected for one and for two days with different multiplicity of infection (MOI) values. The plots of mean values are based on 10 fields of view. Error bars indicate standard deviation.
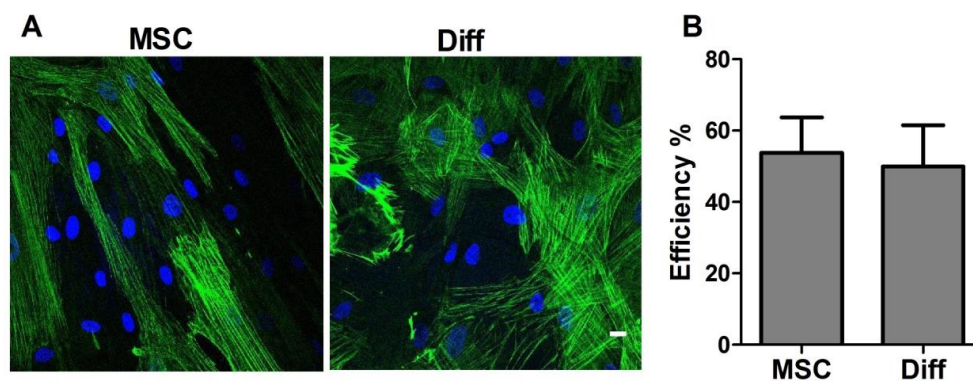
Figure 2.14: Comparison of LifeAct-GFP transfection in hMSCs and following chondrogenic differentiation (Diff) cells transfected with LifeAct-GFP with MOI of 300. (A) Representative confocal 2D reconstruction images two days after start of transfection. F-actin labelled with LifeAct-GFP (green) and cell nuclear stained with Hoechst 33342 (blue). Scale bar 20 μm. (B) The plot of transfection efficiency based on 10 and 9 fields of view for hMSC and Diff cells respectively. Error bars indicate standard deviation.

Colocalization of actin in culture monolayer and cell suspension

Undifferentiated hMSCs were transfected with either LifeAct-tagGFP2 virus or actin-GFP plasmid and then fixed and co-stained with Alexa phalloidin prior to visualisation with laser scanning fluorescence confocal microscopy. Cells in monolayer exhibited characteristic stress fibre bundles with perfect colocalization of LifeAct-GFP with Alexa phalloidin (Fig. 2.15 A and B). Cells fixed in suspension had a rounded morphology with dense cortical actin underlying the ruffled cell membrane but without stress fibres. The LifeAct-GFP signal colocalised with the Alexa phalloidin signal (Fig. 2.15 C and D). Moreover, results have indicated that LifeAct-GFP exhibited a lower background cytoplasmic signal compared to Alexa phalloidin.

A similar study of F-actin organisation labelled with actin-GFP in rounded cells and cells in monolayer was performed. In this case cells there had also near perfect colocalization of actin-GFP with Alexa phalloidin (Fig. 2.16 A and B). However, in rounded cells colocalization indicated that actin-GFP had a high background cytoplasmic signal compared to Alexa phalloidin (Fig. 2.16 C and D).
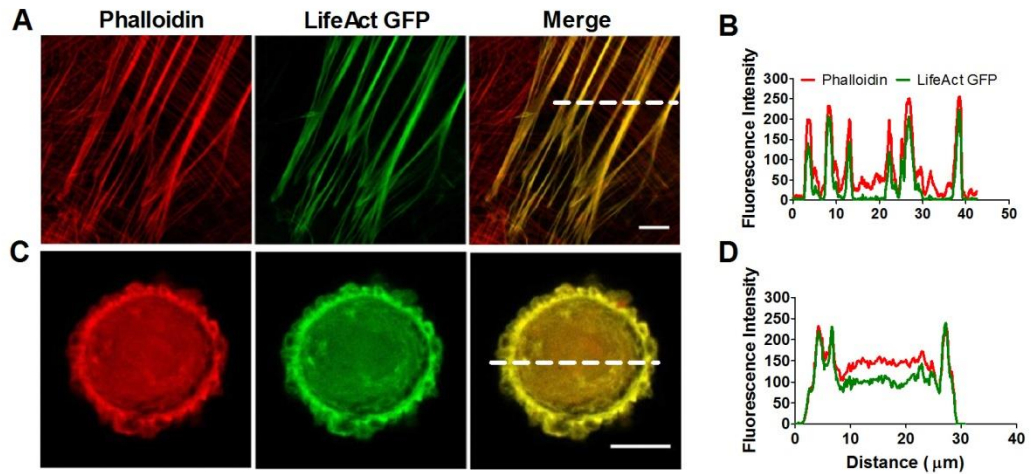
Figure 2.15: Colocalization of F-actin with LifeAct-GFP and phalloidin. HMSC cells were transfected with LifeAct-tagGFP2 virus, and maintained in monolayer (A) or suspension (C) prior to fixation and counter staining with Alexa-phalloidin. Representative confocal section images with correspondence plots showing fluorescence intensity profiles across the actin stress fibres in monolayer (B) and cortical actin for cells in suspension (D). Scale bars represent 10 μm. White dotted lines indicate position of intensity profile.
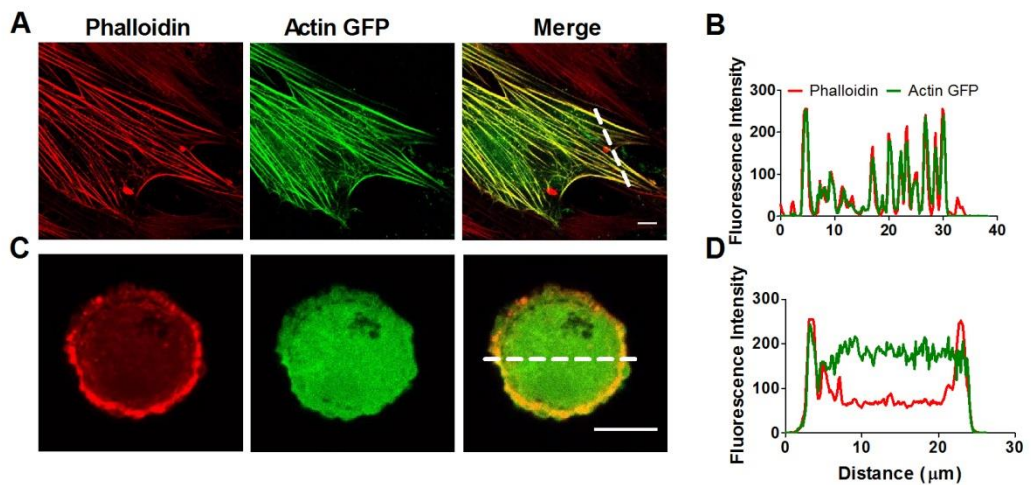
Figure 2.16: Colocalization of F-actin with actin-GFP and Alexa phalloidin. HMSC cells were transfected with actin-GFP plasmid, and maintained in monolayer (A) or suspension (C) prior to fixation and counter staining with Alexa-phalloidin. Representative confocal section images with correspondence plots showing fluorescence intensity profiles across the actin stress fibres in monolayer (B) and cortical actin for cells in suspension (D). Scale bars represent 10 μm. White dotted lines indicate position of intensity profile.

F-actin dynamics during the micropipette aspiration

Representative time lapse images showing F-actin dynamics during micropipette aspiration of cells transfected with LifeAct-GFP and actin-GFP can be seen in figure 2.17 A and C, respectively. Figures 2.17 B and D show the corresponding analysis of temporal changes in fluorescence intensity on the leading and the rear edges of the cell. The leading edge is defined as the hemispherical end of the aspirated portion of the cell. The rear edge is a portion of the cortical actin on the opposite side to the micropipette.

The data shows the sudden detachment of the membrane from the actin cortex and extension of a membrane bleb characterised by a drop in fluorescence intensity at the leading edge. This is followed by remodelling of an actin cortex beneath the membrane at the leading edge of the bleb. These events are much clearer in the cell expressing LifeAct-GFP compared to those expressed actin-GFP. However, the former exhibited multi blebs such that the actin cortex at the leading edge did not reform before further blebs occurred. Analysis has shown that actin remodelling is slow and the intensity at the rear edge does not change during the aspiration time.
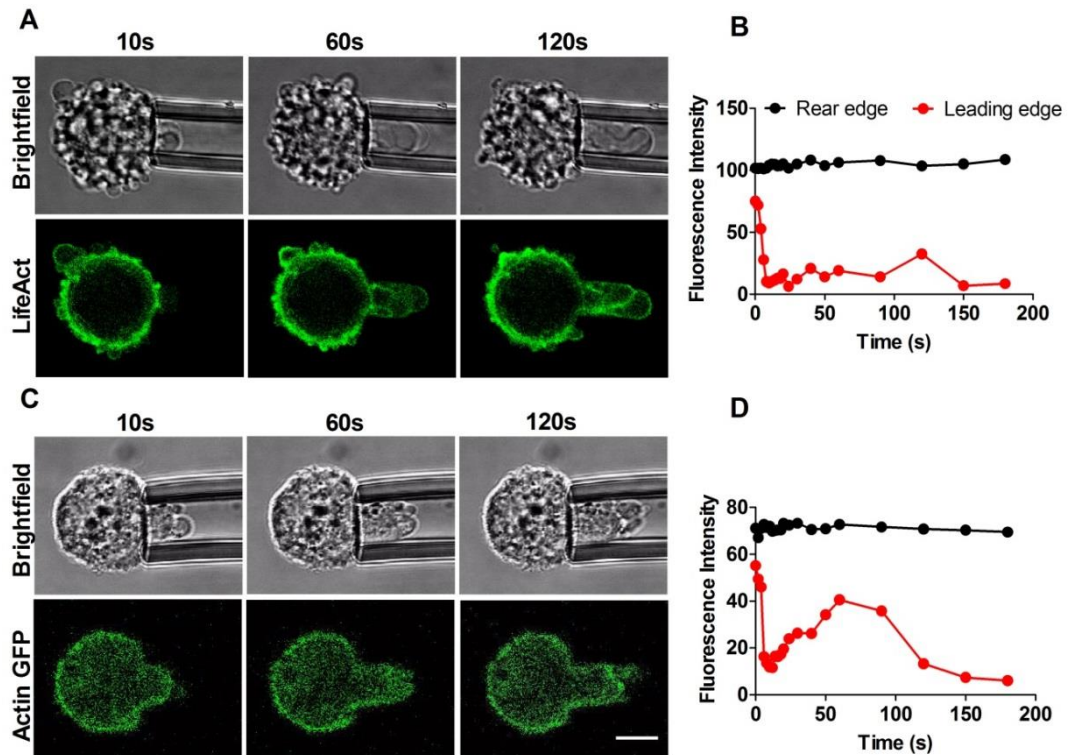
Figure 2.17: F-actin dynamics during the micropipette aspiration. Representative brightfield and confocal fluorescence images of F-actin dynamics during micropipette aspiration at 10, 60 and 120 seconds after the application of a 0.76 kPa aspiration pressure. HMSC cells were transfected with (A) LifeAct-GFP and (C) actin-GFP. Scale bar represents 10 μm. Representative plots of F-actin fluorescence intensity on the leading and the rear edges of cells transfected with (B) LifeAct-GFP and (D) actin-GFP. Number of cell LifeAct (n=38), Actin-GFP (n=39).

Effect of LifeAct and Actin-GFP on cell mechanics

In order to test whether the LifeAct-GFP and the actin-GFP have effect on cell mechanics and associated actin distortion and remodelling, additional micropipette aspiration experiments were performed. Undifferentiated hMSCs were transfected with LifeAct-GFP virus or actin-GFP and subjected to a step change in aspiration pressure. The resulting temporal change in aspirated length was fitted with the SLS model to estimate the viscoelastic parameters as described in section 2.4.2. In addition, differentiated hMSCs were transfected with LifeAct-GFP and subjected to identical micropipette aspiration. It was not possible to transfect these differentiated cells using the actin-GFP plasmid, differentiated cells have low proliferation rate, which involve in transfection. Corresponding control groups consisted of cells not exposed to transfection conditions. The numbers of cells in all groups used for

aspiration experiments are presented in table 2.8. The exclusion criteria for aspirated cells were used as described in section 2.5.5.

Cells in all groups exhibited viscoelastic behaviour; the cell aspirated length suddenly increased and equilibrated (Fig. 2.18 A). The aspirated length at 180 seconds was not affected by transfection with LifeAct-GFP compared to the control group (Fig. 2.18 B). However, by contrast cells transfected with actin-GFP showed a significantly reduced aspiration compared to control cells. The data for aspirated length at 180 seconds correlated with that for equilibrium modulus such that there was no significantly difference between cells transfected with LifeAct-GFP and control (Fig. 2.18 C), but cells transfected with actin-GFP had significantly greater equilibrium modulus compared to control cells. However, the data of the instantaneous modulus showed no significant differences associated either with LifeAct-GFP or actin-GFP compared to control (Fig. 2.18 D).

For further study, we wanted to test whether the LifeAct-GFP transfection has an effect on mechanical properties of differentiated cells. HMSCs were differentiated and transfected with LifeAct-GFP. The same micropipette aspiration experiments were performed as described above. Results indicated that there were no significant differences in the aspirated length, the equilibrium modus and the instantaneous modulus of differentiated cells transfected with LifeAct-GFP compared to control cell (Fig. 2.19 A, B and C).

Table 2.8: Number of cells used for the micropipette aspiration to test the effect of LifeAct-GFP and actin-GFP on cell viscoelastic properties.

Cell type	Total No of cells	No of successful aspirations	No used for model R^2>0.95
hMSCs control	68 (100%)	67 (99%)	52 (76%)
hMSCs LifeAct-GFP	40 (100%)	38 (95%)	28 (70%)
hMSCs actin GFP	40 (100%)	39 (98%)	22 (55%)
Diff control	23 (100%)	23 (100%)	16 (70%)
Diff LifeAct-GFP	41 (100%)	38 (93%)	18 (44%)
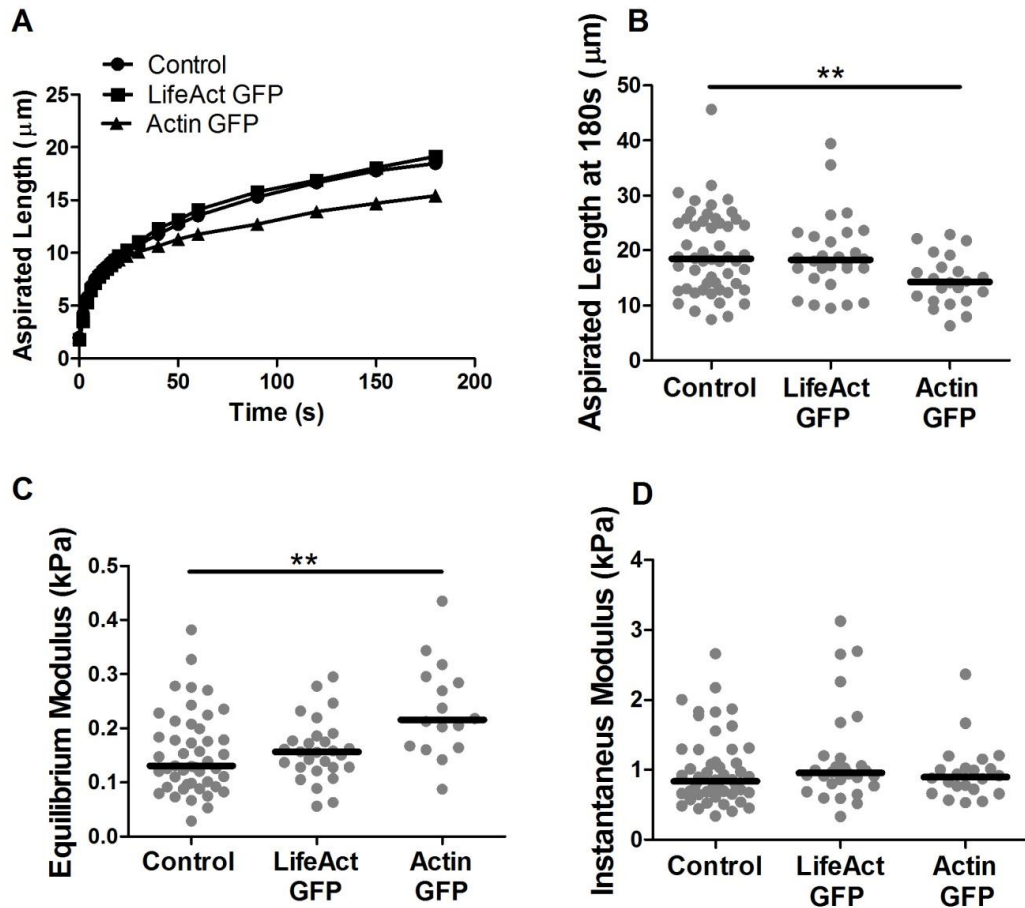
Figure 2.18: Effect of LifeAct-GFP and actin-GFP on viscoelastic properties of hMSCs. (A) Plots of median values of aspirated length verse time. Corresponding scatter plots showing (B) aspirated length at t=180 seconds and the viscoelastic properties; (C) equilibrium modulus and (D) instantaneous modulus of cells transfected with LifeAct-GFP and actin-GFP. Data pooled from two independent experiments. Mann-Whitney U test (**$p<0.01$). See table 2.7 for n values.
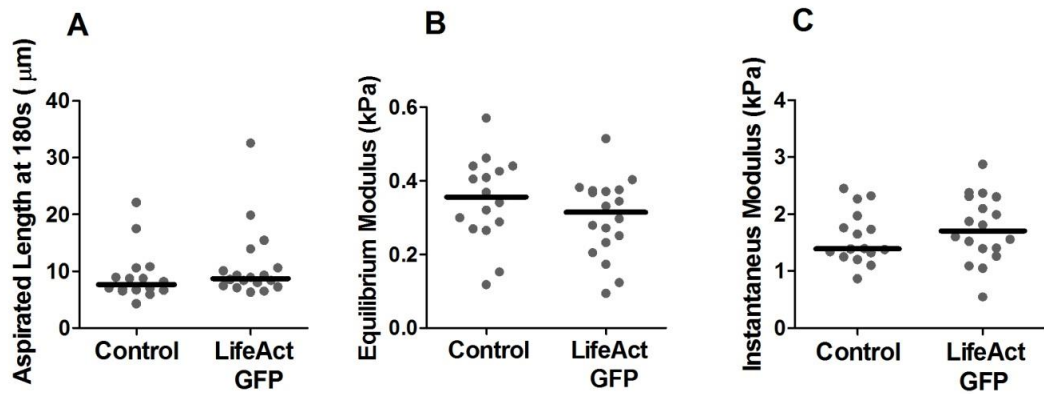
Figure 2.19: The viscoelastic properties of cells induced to chondrogenic lineage in response to LifeAct-GFP transfection. Corresponding scatter plots showing (A) aspirated length, (B) equilibrium modulus and (C) instantaneous modus. Mann-Whitney U test. See table 2.7 for n values.

2.7.5 Discussion

Both undifferentiated hMSCs and chondrogenically differentiated hMSCs were successfully transfected with LifeAct-GFP using an optimised concentration of virus (MOI=300). This produced transfection efficiency of about 50% in both undifferentiated hMSCs and differentiated cells. However, the transfection with actin-GFP has shown a much lower transfection efficiency that could be due to different methods. The transfection efficiency with actin-GFP reached about 2% to 5% for hMSCs and much less than 1% for differentiated hMSCs.

LifeAct-GFP perfectly colocalized with F-actin labelled with Alexa phalloidin without disrupting actin structure. Furthermore, micropipette aspiration shows that LifeAct-GFP can be effectively used as a marker of F-actin in living cells without disrupting the biophysical properties of the cell and associated deformation and remodelling of the actin cortex. Our findings agree with previously reported study that LifeAct does not interfere with actin dynamics (Riedl, *et al.*, 2008) but are the first to report that LifeAct-GFP does not interfere with mechanically induced actin deformation and remodelling. Thus, F-actin remodelling and the growth of a new actin cortex following mechanical stimuli can be effectively observed with minimal artefact. In contract, cells transfected with actin-GFP become stiffer as quantified by shorter aspirated lengths and a higher equilibrium modulus compared to non-transfected controls. These findings agree with the previous study where

chondrocytes were transfected with actin-GFP (Pravincumar*, et al.*, 2012). However, in this previous study the aspiration pressure was applied a slower rate of 0.35 cmH_2O/s (0.034 kPa/s) and so exhibited changes in cell viscoelastic properties. Furthermore, LifeAct-GFP has no effect on cell viscoelastic properties of chondrogenically differentiated hMSCs. In conclusion, LifeAct provides a versatile and valuable marker for visualization of F-actin in living cells without disrupting actin remodelling and biomechanics and associated cellular viscoelastic behaviour.

CHAPTER 3
Differentiation regulates stem cell mechanics

3   DIFFERENTIATION REGULATES STEM CELL MECHANICS

3.1 Introduction

During stem cell differentiation certain genes are activated and turned off, resulting in changes in cell structure and function. Mechanical forces are known to influence stem cell differentiation (Engler *, et al.*, 2006, Sen *, et al.*, 2011, Sumanasinghe *, et al.*, 2006). Previous studies have also suggested that cellular mechanical properties change during stem cell differentiation, which is depending on the lineage that cells differentiated to osteogenic lineage increases in stiffness and differentiated to adipogenic lineage decreases in cell stiffness (Yu *, et al.*, 2010). Also, single cell mechanical properties can be used as predictable biomarkers to identify cell populations and to signify differentiation (Gonzalez-Cruz *, et al.*, 2012). The majority of studies focus on hMSC differentiation down osteogenic and adipogenic lineages. However, very limited work has been done to determine changes in cell's viscoelastic properties during stem cell differentiation down a chondrogenic lineage.

Controlling hMSC differentiation towards a chondrogenic lineage has potential applications in regenerative medicine and tissue engineering for the repair of articular cartilage. The aim of the studies outlined in chapter is therefore to characterise the mechanical behaviour of hMSCs and to estimate the viscoelastic properties of undifferentiated hMSCs and hMSCs differentiated down a chondrogenic lineage. Biomechanical analysis is conducted using a micropipette aspiration system.

3.2 Methods

3.2.1 Cell preparation

HMSCs were cultured in X-PAN media on 24 well plates for either 2 or 9 days (D2 and D9) as described in section (2.2.1). Separate cells were cultured for 2 days in X-PAN media and then a further 7 days in chondrogenic differentiation media as described in section (2.2.2). HMSCs were analysed at day 2 (MSC D2) and day 9 (MSC D9) after seeding while chondrogenic differentiation was initiated at day 2 and assessed at day 9 (Diff).

3.2.2 Collagen type II expression

Collagen type II extracellular matrix expression was identified as a marker of chondrogenic differentiation using immunohistochemistry. Collagen type II staining was performed on undifferentiated hMSCs (MSC D9) and cells differentiated down the chondrogenic lineage (Diff). In both cases cells were cultured on coverslips and then fixed with 4% PFA as described in section (2.7.2). After fixation coverslips were rinsed in PBS and blocked with goat serum for 30 min. Cells were incubated for 1 hour at room temperature with the primary antibody, rabbit polyclonal anti-collagen type II antibody (Abcam, Cambridge, UK) at a concentration of 1:200. The primary antibodies were diluted in immuno wash buffer, which consisted of PBS + 0.1% bovine serum albumin (BSA). Then coverslips were washed with PBS and incubated at room temperature in the secondary antibody, Alexa Fluor 488 conjugated goat anti-rabbit IgG antibody (Molecular Probes, Paisley, UK) at a concentration of 1:1000 and nuclei stained with Hoechst H33342 (Sigma-Aldrich, Poole, UK) at a concentration 1:200 for 1 hour. Coverslips were finally rinsed in PBS and mounted with ProLong Gold for confocal microscopy.

Coverslips with cells stained for collagen type II were imaged using a confocal microscope with a 488 nm laser and with a x40/1.25 NA oil immersion objective. Images of cell monolayers of undifferentiated hMSCs and cells differentiated toward the chondrogenic lineage were taken. The laser intensity and parameters of offset and gain were kept constant for all images. The quantification analysis of fluorescence intensity of collagen type II was estimated using ImageJ software. The background black pixels were eliminated from analysis and only fluorescence with certain threshold was calculated.

3.2.3 Cell size measurements

Cell size distribution was estimated from measurements of rounded cells in suspension. Cells were trypsinized and allowed to recover their spherical morphology for 10-15 minutes. A drop of cell suspension was placed on a coverslip and brightfield images were taken using a confocal microscope with a x40/1.2 NA oil immersion objective. The cell diameter was estimated as the average of the horizontal and vertical diameters measured using a semi-automated Matlab routine.

3.2.4 Micropipette aspiration

The differentiated cells (Diff) and hMSCs were detached from the surfaces using trypsin and suspended in 1 ml imaging media containing 5 μl calcein AM (Invitrogen, Paisley, UK) prior to micropipette aspiration. Calcein AM staining was performed to test cell viability and to check whether cell aspiration in fluorescence and brightfield images have the same trend.

The micropipette aspiration system as described previously in section (2.3.2) was used in this study to estimate the viscoelastic properties of single undifferentiated hMSCs and hMSCs differentiated down the chondrogenic lineage. Detached cells in suspension were placed in a special chamber on the stage of confocal microscope. Individual cells were held on the micropipette by applying a negative tare pressure of 0.5 cmH$_2$O (0.049 kPa). The experiment was initiated by applying a step of 7.7 cmH$_2$O (0.76 kPa) negative pressure. The resulting cell deformation inside the micropipette was captured using fluorescence and brightfield imaging with a x63/1.4 NA oil immersion objective over 180 seconds. The aspirated length of the cell inside the micropipette was estimated from the images and plotted versus aspiration time. During aspiration, the cell volume was calculated as described in section (3.2.5) and the change in volume calculated at 180 seconds normalised to pre-aspiration values. The viscoelastic parameters; equilibrium modulus, instantaneous modulus and viscosity were, determined using a theoretical SLS model as described in detail in section (2.4.2).

3.2.5 Quantification of volume during aspiration

Cell morphological properties volume and surface area, were also calculated during micropipette aspiration. The following assumptions are made:

- Cell assumed to have a smooth surface

- Rotation symmetry of cell about long axis of micropipette
- Cell adopts oblate ellipsoid morphology for cell body outside the micropipette
- Aspirated length inside the micropipette has hemispherical end with radius equal to radius of micropipette

For volume estimation the cell is divided into two regions, the cell outside the micropipette and the cell aspirated part inside the micropipette as indicated in figure 3.1.
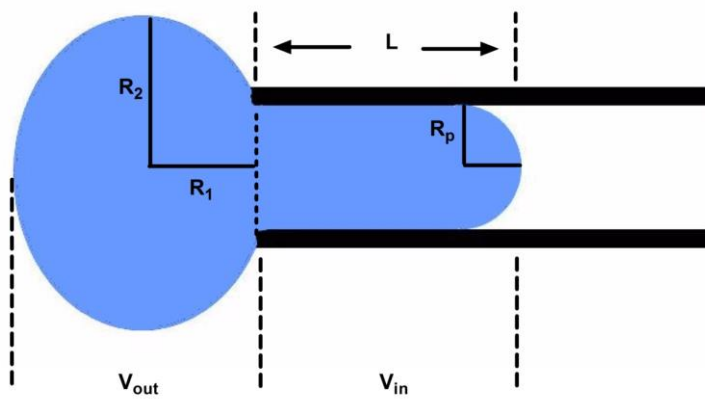
Figure 3.1: A schematic representation of cell aspiration inside the micropipette. Cell volume of aspirated cell was calculated as a sum of volume of cell outside the micropipette and the volume of cell in the micropipette.

The initial volume of the cell is estimated from the first image when the cell is held onto the micropipette by the tare pressure, but is not aspirated inside the micropipette, the equation is given as follows:

$$V_0 = \frac{4}{3}\pi R_1 R_2^2 \qquad (3.1)$$

where V_0 is an initial volume, R_1 and R_2 are radii of cell outside the micropipette. We assumed that radius R_2 is equal to the third radius.

Volume during the micropipette aspiration can be estimated as follows:

$$V = V_{out} + V_{in} \qquad (3.2)$$

$$V_{out} = \frac{4}{3}\pi R_1 R_2^2 \qquad\qquad (3.3)$$

$$V_{in} = \pi R_p^2 \left(L - R_p + \frac{2R_p}{3}\right) \qquad\qquad (3.4)$$

where V is the volume during aspiration, V_{out} and V_{in} are volumes of cell part outside and inside the micropipette respectively. L is aspirated length and R_p radius of micropipette.

However, this estimation of cell volume during micropipette aspiration gives an error related to optical abberation, resulting overestimated aspirated length. More details see section 2.5.5. This overestimation of aspirated length provides 22% larger values of cell volume during aspiration.

The measurement error is estimated to be 1 pixel which gives value equal to 0.19 μm. According to this value, the error of volume measurements before and after aspiration is ±136 μm^3 and ±187 μm^3 respectively.

In addition, assumptions that aspirated portion of the cell have hemispherical end also gives an error as many cells showed multi blebbing during aspiration that was not a hemispherical end and also did not occupate entire volume into the micropipette. However, to estimate an error related to those assumptions is difficult, but would be possible with more precise measurements by taking z-section images of cells stained with calcein AM and constructing 3D images.

3.2.6 Statistics

The fluorescence intensity of collagen type II staining was assumed to have a normal Gaussian distribution. The plots were therefore presented with mean values and standard deviation. For statistical analysis the unpaired Student t test was used to estimate the significant differences between the groups.

The data of cell diameter, the cell volume change during aspiration and the viscoelastic parameters were all assumed to be non-parametric. The data was plotted as a population scatter with bars indicating median values. The Mann-Whitney U test was used to determine significant differences between cell groups. The significant

differences for both parametric and non-parametric data were presented as (* p<0.05, ** p<0.01 and *** p<0.001), unless otherwise stated.

3.3 Results

3.3.1 Differentiation media induces chondrogenic differentiation of hMSCs

The representative collagen type II immunofluorescence images of hMSCs cultured in X-PAN media (MSC D9) and chondrogenic differentiation media (CDM) are given in figure 3.2A. Cells cultured in CDM showed greater collagen type II staining compared to the minimal level seen in undifferentiated hMSCs. Quantitative image analysis showed that the fluorescence intensity of collagen type II staining was greater in differentiated cells, the difference being statistically significant (p<0.001) (Fig. 3.2 B).
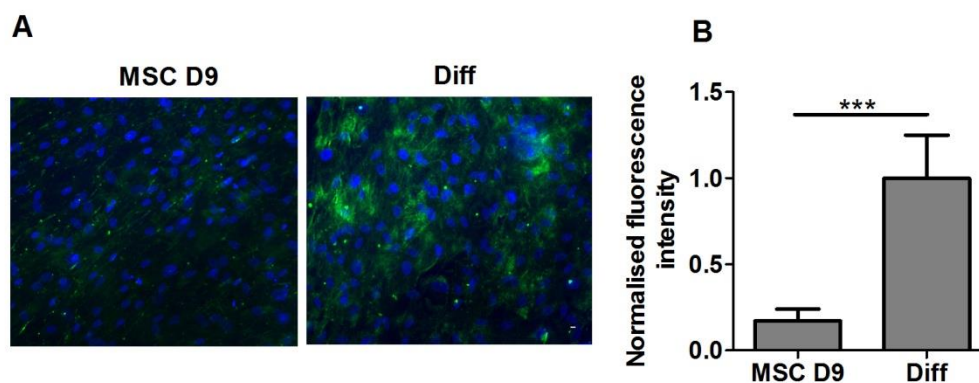
Figure 3.2: Culture of hMSCs in CDM increased collagen type II expression indicative of chondrogenic differentiation. (A) Confocal fluorescent images showing brighter collagen II staining in differentiated cells (Diff) compared to hMSCs (MSC D9). Measurements were obtained of hMSCs and those differentiated to chondrogenic lineage at same culture time point. Collagen type II (green), cell nuclei (blue). Scale bar 10 μm. (B) Histogram showing the corresponding fluorescence intensity as measured from confocal images. The data is presented as a mean with error bars indicating standard deviation for n=9 fields of view (*** p<0.001, two tailed t-test).

3.3.2 Cell size distribution

The frequency distributions for cell size are shown in figure 3.3 alongside representative brightfield images. Data shown for hMSCs prior to differentiation (MSC D2) and for cells cultured from day 2 to 9 in either basal X-PAN media (MSC D9) or chondrogenic media (Diff). The cell numbers for diameter measurements in each group ranged from 147 to 293 cells. Culture of hMSCs in X-PAN media resulted in a significant increase in cell size from a median diameter of 19.9 μm at day 2 to 21.4 μm at day 9 ($p<0.001$). Cells cultured in chondrogenic differentiation media showed a greater increase in cell size to a median diameter of 24.4 μm, the difference from non-differentiated cells at day 9 being statistically significant ($p<0.001$).
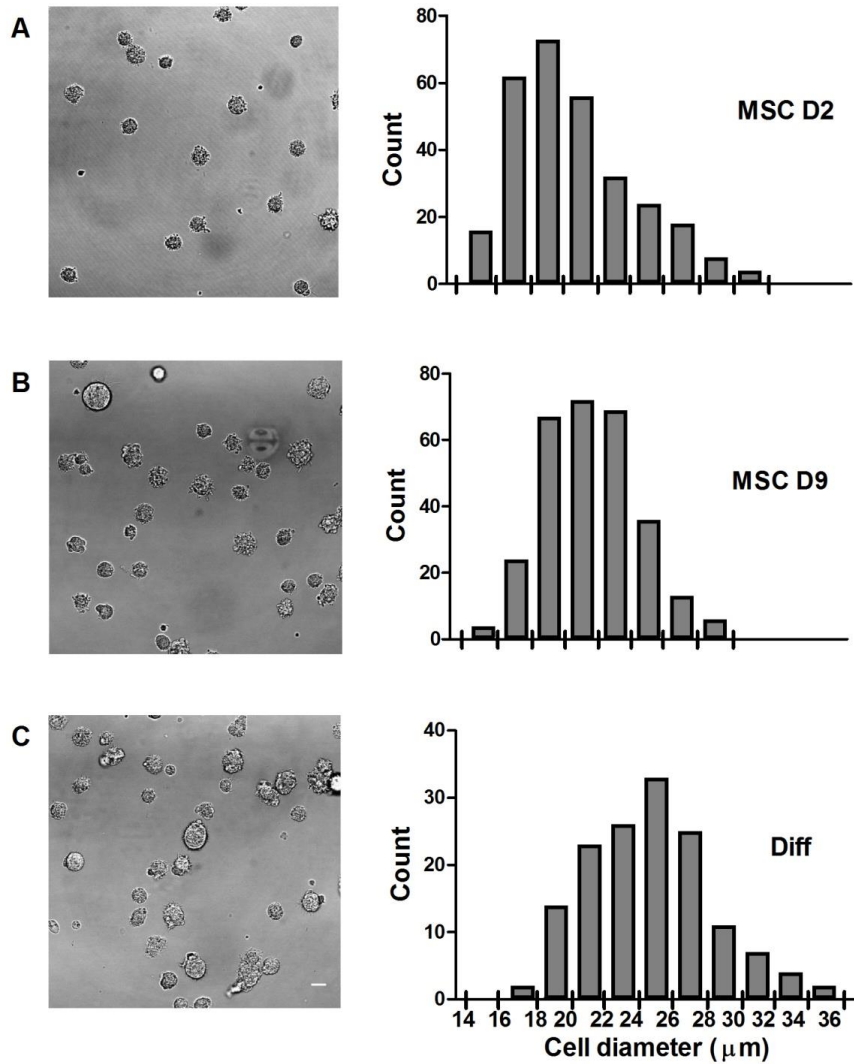
Figure 3.3: The cell size distributions for undifferentiated hMSCs and cells differentiated down a chondrogenic lineage. Representative brightfield images (left) and corresponding frequency distributions (right) for hMSCs cultured in X-PAN media for (A) two, (B) nine days and (C) for cells cultured in chondrogenic differentiation media from day 2 to day 9. Scale bar 20 μm.

3.3.3 Cell aspiration

Cells subjected to a negative pressure of 7.7 cmH$_2$O (0.76 kPa) in 2 seconds were aspirated inside the micropipette and held for 180 seconds. The numbers of cells used for the micropipette aspiration experiments in each group are indicated in table 3.1. Typically 50-55% of cells were successfully aspirated and fitted by the SLS model. The resulting sample size (n=45-59) was similar to, or larger than that used in previously published micropipette aspiration studies providing greater precision

(Pravincumar*, et al.*, 2012, Yu*, et al.*, 2010). As indicated the majority of cells exhibited a successful aspiration and were used for further studies. Brightfield and fluorescent images of a single cell visualised at the 180 seconds period of aspiration are given in figure 3.4 A. In addition, no changes in fluorescence intensity of calcein AM show that the cell membrane remains intact throughout aspiration (Fig.3.4 B). During the aspiration process, an uneven cell deformation inside the micropipette can be seen. This process appears to involve membrane detachment from the actin cortex and subsequent bleb formation as described in more detail in the following chapter.
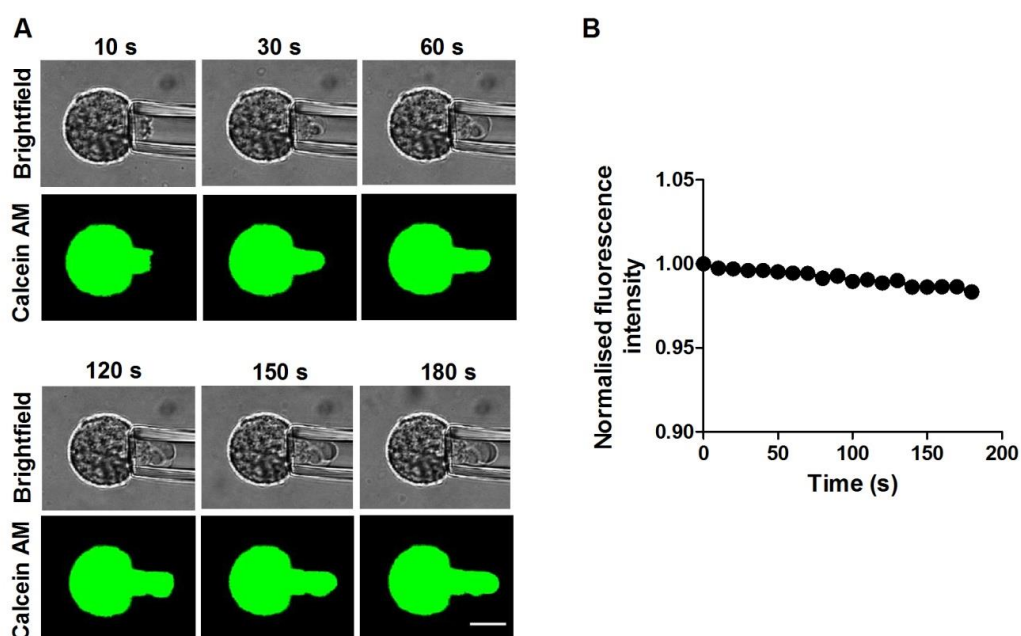
Figure 3.4: Representative single hMSCs during aspiration into the micropipette. (A) Brightfield and fluorescent images of cells aspirated at different time points. Cells were stained with calcein AM (green). Scale bar 10 μm. (B) The plot represents fluorescence intensity of the cell outside the micropipette.

The fluorescent images suggest that this phenomenon is not associated with a membrane rupture. For all three cell groups the temporal change in aspirated length exhibited behaviour characteristic of a viscoelastic material with a rapid elongation in the first 60 seconds followed by a more gradual elongation usually reaching approximate equilibrium within 180 seconds (Fig. 3.5).
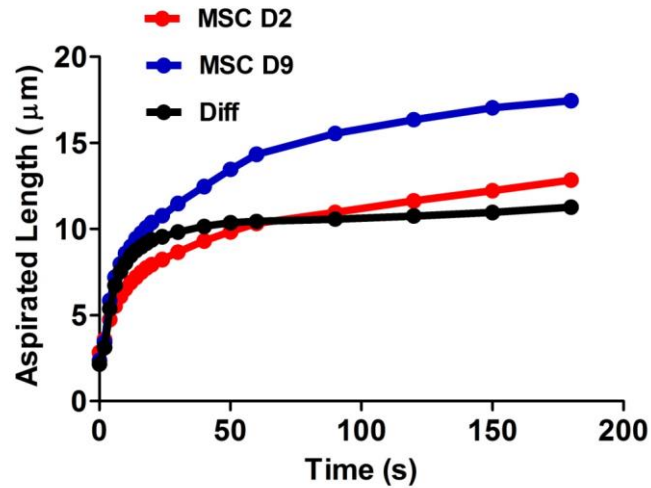
Figure 3.5: Plots of median aspirated length temporal changes of undifferentiated hMSCs at day 2 and day 9 (MSC D2 and MSC D9) and cells differentiated toward the chondrogenic lineage (Diff). Cells were aspirated by applying a negative pressure of 7.7 cmH$_2$O (0.76 kPa).

3.3.4 Volume changes during the micropipette aspiration

The change in cell volume during micropipette aspiration was estimated for undifferentiated hMSCs and cells differentiated toward the chondrogenic lineage. The process of aspiration was associated with a volume decrease in all cell groups. Representative median plots of volume changes during aspiration can be seen in figure 3.6. All groups of cells exhibited similar volumetric behaviour reflecting the viscoelastic cell deformation.
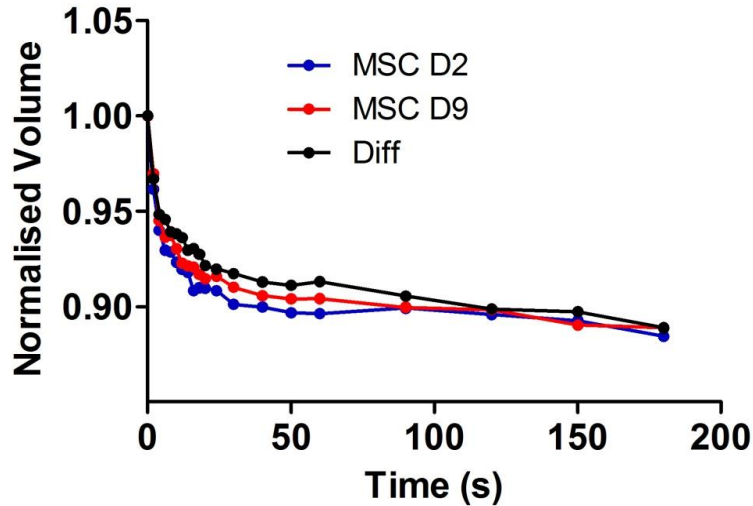
Figure 3.6: Plots of median volume changes during the micropipette aspiration of undifferentiated hMSCs at day 2 and day 9 and cells differentiated toward the chondrogenic lineage.

Data analyses of volumes before aspiration, at time zero, and after aspiration, at 180 seconds, show statistically significant differences (Fig. 3.7). The cell deformation during the aspiration process was associated with highly significant differences in volume before and after aspiration of MSC D2 and MSCs differentiated chondrogenically ($p < 0.001$). Furthermore, the MSC D9 have exhibited significant volume changes as well ($p < 0.01$). The differences in cell size between the three groups prior to the aspiration reflect the difference in diameter measured for cells in suspension (Fig. 3.3).
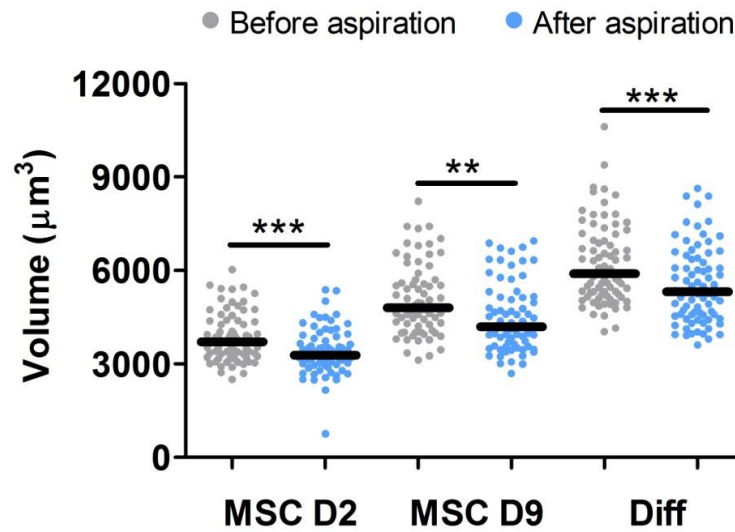
Figure 3.7: The volume changes of control and chondrogenic hMSCs before and after aspiration. The data is presented as a population with median value indicated by bar. Mann-Whitney U test, ** $p<0.01$, *** $p<0.001$.

3.3.5 Modes of aspirated length response

Individual undifferentiated hMSCs and those differentiated toward the chondrogenic lineage were subjected to a step of negative pressure which resulted in partial cell aspiration inside the micropipette. The aspiration process was visualised over 180 seconds and the aspirated length plotted versus time for each cell. Cells exhibited different modes of response depending on whether or not the aspiration length reached equilibrium within 180 seconds. The change in aspirated length from time 120-180 seconds was calculated to characterise the mode of response.

The aspirated modes were characterised by criteria of percentage changes in aspirated length between 120 and 180 seconds. Cells which exhibited an aspirated length increase more than 5% were named as increased mode. In contrast, cells which exhibited aspirated length decrease more than 5% were named as decrease mode, and cells with changes of aspirated length between these two modes were named as equilibrate.

Cells exhibited increase mode when the aspirated length continued to increase without reaching equilibration (Fig. 3.8 A). During equilibrium mode, the aspirated length rapidly increased initially followed by equilibration (Fig. 3.8 B). Cells

exhibited decrease mode when the aspirated length suddenly increased, and appeared to reach equilibrium before retracting (Fig. 3.8 C). Modes of increase and equilibrate were dominant for all cell groups (Fig. 3.8 D). A small number of undifferentiated hMSCs (MSC D2 and MSC D9) and cells differentiated (Diff) showed retraction. There was no statistically significant difference of cell groups showing each response (Table 3.1).
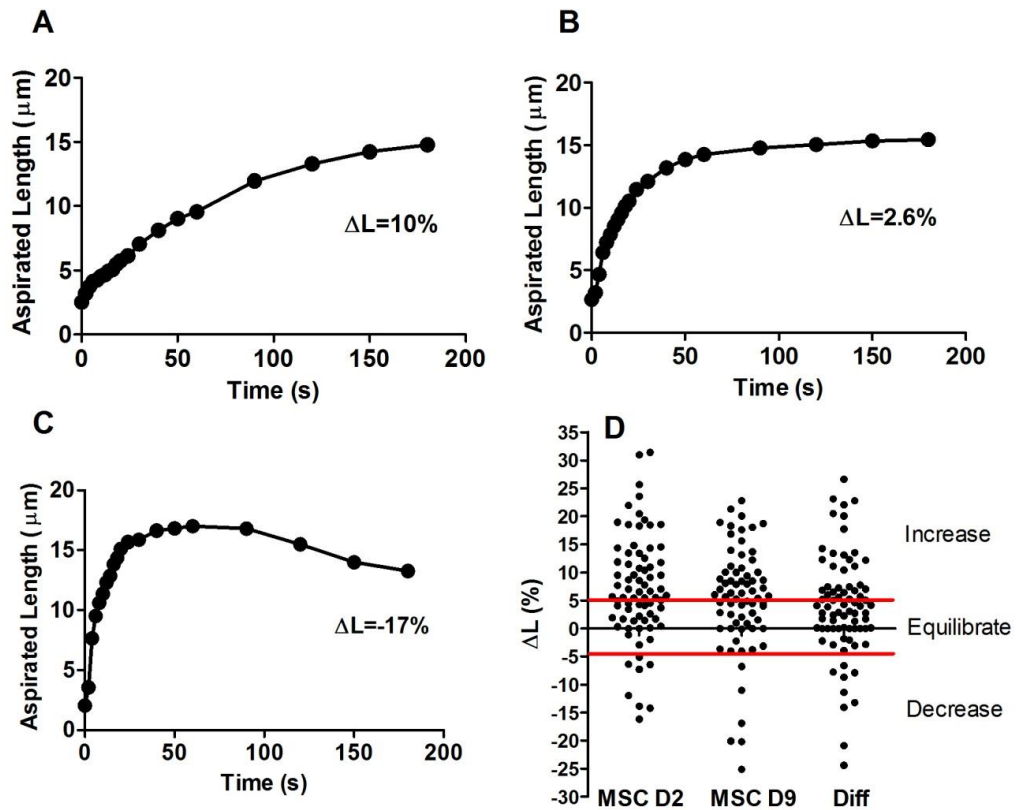
Figure 3.8: Representative plots are showing the temporal changes in aspiration length during aspiration process. The three characteristic modes of response depending on the change in aspirated length measured at 180 seconds. Representative plots of separate cells showing each mode: (A) increase, (B) equilibrate and (C) decrease. (D) Scatter plot showing percentage change in aspirated length between 120-180 seconds. Red lines present characterization criteria for different modes. There were no significant differences between the three groups of cells. (Mann-Whitney U test).

Table 3.1: Representative number of cells showing each mode during the micropipette aspiration. Numbers indicate the percentage of the total number cells showing each response.

Cell type	Cells showing increase mode (%)	Cells showing equilibrate mode (%)	Cells showing decrease mode (%)
MCS D2	41	54	5
MCS D9	55	36	9
Diff	42	46	12

3.3.6 Viscoelastic properties

The total number of cells and successfully aspirated cells are indicated in table 3.2. Cells were excluded from the viscoelastic parameters analysis with conditions:

- Cells did not show visible aspiration during 180 seconds.
- The theoretical SLS model did not accurately fit the aspiration length versus time data ($R^2 < 0.95$)

Table 3.2: Representative number of cells used for the micropipette aspiration. Numbers indicate the percentage of the total number cells tested.

Cell type	Total No of cells	No of successful aspirations	No used for model $R^2 > 0.95$
MCS D2	116 (100%)	78 (67%)	59 (51%)
MCS D9	85 (100%)	69 (81%)	45 (53%)
Diff	82 (100%)	78 (95%)	45 (55%)

The SLS model was used to estimate the three viscoelastic parameters; equilibrium modulus, instantaneous modulus and viscosity with results presented in figure 3.9. The final aspirated length at 180 seconds was shorter for differentiated cells compared to undifferentiated cells at day 2 and day 9, the differences being statistically significant (Fig. 3.9 A). There was also a significant increase in final aspirated length from day 2 to day 9 for hMSCs (p<0.001). This correlated with differences in equilibrium modulus such that hMSCs at day 9 were softer than those

at day 2 (Fig. 3.9 B). Differentiated hMSCs exhibited higher equilibrium (Fig. 3.9 B) and instantaneous moduli (Fig. 3.9 C) compared to undifferentiated cells (p<0.001). Differentiated cells had lower viscosity than undifferentiated hMSCs (p<0.001) (Fig. 3.9 D).
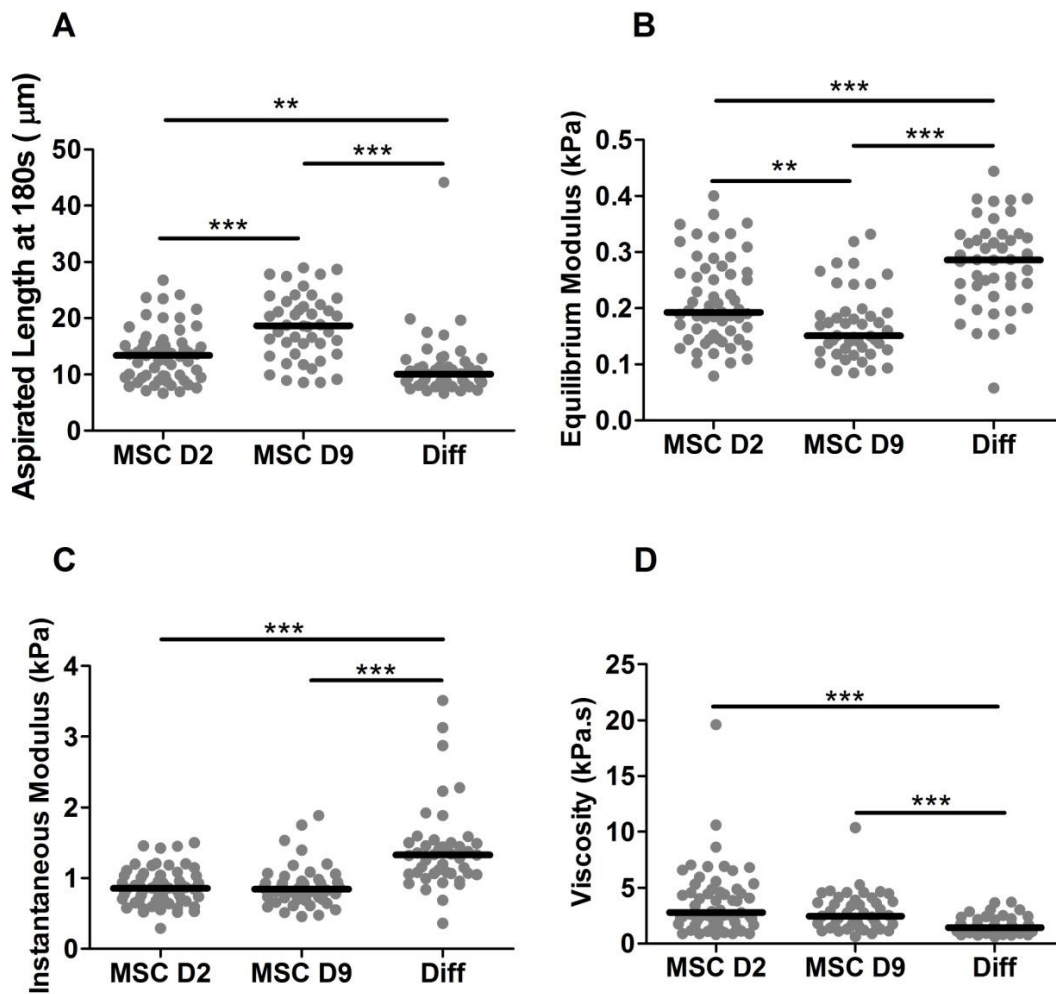
Figure 3.9: The aspirated length and viscoelastic properties of undifferentiated hMSCs (MSC D2 and MSC D9) and hMSCs differentiated to the chondrogenic lineage (Diff). (A) The aspirated length at 180 seconds, (B) the equilibrium modulus, (C) the instantaneous modulus and (D) the viscosity of cells assessed with micropipette aspiration. The data is presented as a population with median value indicated by bar. Mann-Whitney U test, ** p<0.01, *** p<0.001.

3.4 Discussion

3.4.1 Cell size changes during culture

In this study we demonstrated that cell size changes are associated with culture time. Undifferentiated hMSCs significantly increased in cell size over a seven day culture period. Moreover, chondrogenic differentiation resulted in a greater increase in cell size compared to undifferentiated hMSCs. The increase in cell size is likely to be due to increased metabolic activity possible due to enhanced nutrient availability in culture. For example, glucose is transported into the cell and converted to energy, which regulates metabolic activity, protein synthesis and cell size. A previous study has demonstrated that TGF-β present in the media regulates glucose synthesis and cell size (Wu and Derynck, 2009).

In addition, differentiated cells exhibited wider variability in cell size compared to undifferentiated hMSCs. This may be an effect of heterogeneity in the population such that not all cells will differentiate down a chondrogenic lineage. In such a case, a flow cytometer could be used for cell sorting and size measurements.

3.4.2 Volume changes associated with micropipette aspiration

All cell groups show volume decrease during micropipette aspiration (Fig. 3.6), such that, the post aspiration volume at 180 seconds was significantly decreased compared to pre-aspiration volume (Fig. 3.7). This agrees with a similar previous study of chondrocytes fully aspirated inside a micropipette (Jones, *et al.*, 1999). By contrast, a separate study showed chondrocyte volume increases during partial aspiration inside the micropipette (Pravincumar, *et al.*, 2012). However, this is due to different assumptions in the equations used to calculate cell volume such that cell portion outside the micropipette was assumed to be spherical. In the present study the cell outside the micropipette is in fact shown to be an oblate ellipsoid.

However, the mechanism responsible for volume decrease is not well known, but is likely to be due to changes in intracellular pressure and associated transport of intracellular water within the cell (Trickey, *et al.*, 2006). During mechanical loading of cartilage tissue, chondrocyte nucleus exhibit a similar decrease in volume (Guilak, 1995). However, this could also be due to osmotic effects, since compression results in exudation of water from matrix which increases extracellular osmotic pressure causing the cell volume reduction due to the negatively charged proteoglycans in the

extracellular matrix (Lai, *et al.*, 1991). This osmotic charge was in agreement with this hypothesis, for cells embedded into non-charged agarose gel compression results in cell deformation without volume reduction (Freeman, *et al.*, 1994). In our study cells are not surrounded by a charged extracellular matrix and yet still reduce in volume during deformation. It is therefore possible that the reduction in volume observed with micropipette aspiration is due to either a greater level of cell deformation or a difference in the nature of the deformation, compared to that which occurs with compression in a 3D hydrogel. For example the development of loading induced blebs is seen in micropipette aspiration but not with compression in agarose.

3.4.3 Cell behaviour during aspiration

Cells aspirated inside the micropipette exhibited three different modes of behaviour associated with changes in aspirated length measured at 120-180 seconds. These were classified as increase, equilibrate and decrease. These findings conform to a previous study by Tan et al. showing different modes of behaviour during the micropipette aspiration of hMSCs. It was suggested that differences in cell behaviour could be associated with differences in actin organisation (Tan, *et al.*, 2008a). They showed that cells treated with the F-actin disrupting agent, cytochalasin D, showed increased aspirated length without reaching equilibrium state. In the present study, the majority of undifferentiated hMSCs cultured for 9 days (55%) also failed to reach equilibrium (table 3.1). Increased actin density and gene expression of filamin and tubulin proteins was found in hMSCs differentiated down an osteogenic lineage (Titushkin and Cho, 2011, Yu, *et al.*, 2010). However, this could be a case of stronger and thicker cortical actin in cells differentiated down a chondrogenic lineage resulting in more cells exhibiting equilibrium mode. Moreover, there were no statistically significant differences between cell groups and modes of behaviour (Fig. 3.8). The present study demonstrated that a minority of cells (5-12%) exhibited deceased mode due to retraction of aspirated length. Previous studies suggest that retraction in the micropipette is associated with reformation and remodelling of the contractile actin cortex (Brugues, *et al.*, 2010).

3.4.4 Stem cell differentiation regulates cell mechanical properties

The micropipette aspiration data of aspirated length versus time exhibited characteristic solid like viscoelastic creep behaviour in both control and chondrogenic cell types. This agrees with previous studies of hMSCs (Tan, *et al.*,

2008a) and other cell types (Sato, *et al.*, 1990, Trickey, *et al.*, 2000), but differs from the behaviour reported for neutrophils or red blood cells (Hochmuth, 2000). Only about 50% of cells fitted the theoretical SLS model with an R^2 value greater than 0.95. In particular the SLS model fitted least well to those cells that exhibited either a decrease mode or an increase mode (Fig. 3.10). However, there were no significant differences in the viscoelastic properties when using all cells including those with R^2 less than 0.95.
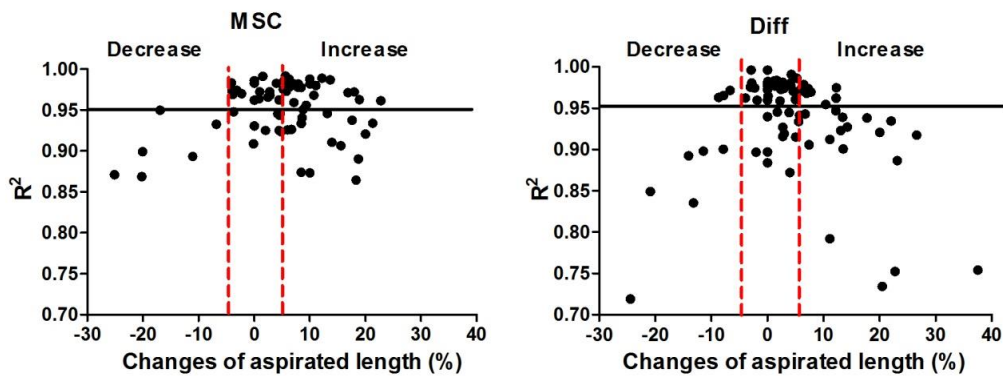
Figure 3.10: Relationship between R^2 of theoretical SLS model and the percentage change in aspirated length over 120-180 seconds. Horizontal black line presents threshold of R^2 value which was a criteria for estimation of cell viscoelastic properties. Data shown for hMSCs (left) and differentiated cells (right).

The equilibrium modulus and the instantaneous modulus of undifferentiated hMSCs were in a range of 0.15-0.19 kPa and 0.84-0.86 kPa respectively, similar to the previously reported values obtained using micropipette aspiration (Tan, *et al.*, 2008a, Yu, *et al.*, 2010). Interestingly, undifferentiated hMSCs cultured for two days have significantly higher equilibrium moduli than cells cultured for nine days. However, the mechanism responsible for the reduction in cell modulus during culture time is unclear. It is possible that changes in confluence and associated actin organisation are involved. However, previous studies have demonstrated that confluence significantly increased the modulus of osteoblasts and fibroblasts (Jaasma, *et al.*, 2006).

Compared to undifferentiated hMSCs, cells differentiated to a chondrogenic lineage exhibited significantly higher equilibrium and instantaneous moduli with values of 0.29 kPa and 1.33 kPa respectively (Fig. 3.9). The same trend of changes in

viscoelastic properties associated with chondrogenic differentiation was reported on undifferentiated human embryonic stem cells (hESCs) and those induced to chondrogenic differentiation using transforming growth factor-β1 (TGF-β1) (Koay, *et al.*, 2009), However, the absolute values of both equilibrium and instantaneous moduli of undifferentiated and differentiated hESCs were different to those of the present study. These differences are more likely due to cell type rather than AFM technique. They also demonstrated that equilibrium and instantaneous moduli of undifferentiated hMSCs with values of 0.73 kPa and 1.16 kPa respectively, which differ from present study. This difference on cell mechanical properties could be due to technique. Micropipette aspiration measures global cell deformation of single rounded cells, however the reported experiments were performed on cells attached on a substrate using AFM.

The mechanism responsible for changes of cell biomechanical properties during stem cell differentiation remains unclear. Studies have reported that the mechanical properties of stem cells, like other cells, are dependent on actin cytoskeleton organisation and dynamics. Disruption of the actin cytoskeleton with drugs such as cytochalasinD, causes the modulus to significantly decrease and the viscosity to increase in many cell types including hMSCs (Tan, *et al.*, 2008a). However, disruption of microtubules with nocodazole has not been shown to significantly decrease the modulus of hMSCs (Titushkin, Igor A and Cho, Michael R, 2009). Osteogenic differentiation of hMSCs is associated with alterations in actin microfilament organisation from widespread thin bundles of actin filaments in undifferentiated cells to a few thick filaments or stress fibres in differentiated cells (Pablo Rodríguez, *et al.*, 2004). However, changes in actin organisation are not the only potential modulator of differences in cell mechanics during differentiation. Previous studies report alterations in nucleus stiffness which may influence apparent whole cell modulus (Pajerowski, *et al.*, 2007).

In addition the bond between the cell membrane and the actin cortex may also change during differentiation thereby potentially regulating cell mechanics measured by micropipette aspiration.

CHAPTER 4
Differentiation influences bleb formation

4   DIFFERENTIATION INFLUENCES BLEB FORMATION

4.1 Introduction

In the previous chapter we showed that hMSCs appear softer than chondrogenically differentiated hMSCs during aspiration. This chapter examines whether this is due to increased susceptibility to blebbing such that aspiration causes membrane detachment and bleb formation. Blebs occur as spherical membrane protrusions which follow membrane-actin cortex detachment and are then retracted following formation of a new actomyosin cortex (Charras and Paluch, 2008). Bleb regulation is different from other physiological membrane protrusions. Usually, bleb growth is regulated by changes in intracellular pressure. By contract, lamellipodia and filopodia growth is initiated by actin polymerization pushing the membrane forward. Cell blebbing is often thought to be a sign of apoptosis. However, recent studies have shown that cell blebbing is also observed in healthy cells. The role of bleb formation, both in physiological and pathological cases, is still not well understood. Studies have shown that blebs are required for motility, especially in three dimensional (3D) environments where lamellipodia initiation is limited (Charras and Paluch, 2008, Friedl and Wolf, 2010).

In the current studies cell blebbing is used as a biomechanical marker to study the interaction between cell membrane and actin cortex. Previous studies have shown bleb formation when cells are subjected to a negative pressure during the micropipette aspiration. The results have indicated that bleb formation is associated with uncoupling of the membrane from the actin cortex followed by new actin cortex growth (Rentsch and Keller, 2000). Another study has indicated that mechanically induced cell blebbing is associated with stem cell differentiation and changes in membrane-actin cortex linker proteins (Hemsley, *et al.*, 2011).

In this study we tested the hypothesis that the susceptibility to bleb formation is altered during hMSC differentiation.

4.2 Methods

4.2.1 Effect of differentiation on bleb formation during micropipette aspiration

Undifferentiated hMSCs and hMSCs differentiated down a to chondrogenic lineage were cultured for seven days as described in sections (2.2.1 and 2.2.2). The cells were then transfected with LifeAct-GFP for F-actin visualization. Two days prior to micropipette aspiration, the adenovirus with LifeAct-GFP was directly added to the cell culture plates and cultured for a further two days. More details of LifeAct-GFP concentrations and the protocol used for transfection are described in pilot study 2.7. Prior to micropipette aspiration cells were trypsinized and suspended in IM. The cell suspension was placed in a water bath at 37°C allowing cell shape recovery for 10-15 minutes. Cells were then mounted in a chamber on the stage of an inverted confocal microscope and subjected to micropipette aspiration by applying a step negative pressure of 7.7 cmH$_2$O (0.76 kPa) in 2 seconds (see section 2.4.2 for experimental protocol). An argon 488 nm laser was used to produce fluorescent and brightfield images. Offset and gain were used to obtain the best quality images during aspiration. Both fluorescent and brightfield images were collected every 2 seconds over a 180 seconds period. Bleb initiation and formation was monitored from brightfield images and quantified in terms of the percentage of cells exhibiting no blebs, one bleb or multiple blebs (multi blebbing).

Actin cortex remodelling was quantified by measuring the fluorescence intensity in two regions of interest (ROI) positioned over the actin cortex. (ROI1) presents the fluorescence intensity on the leading edge, which is defined as the hemispherical end of the aspirated portion of the cell. (ROI2) presents fluorescence intensity on the rear edge, which is a portion of the cortical actin on the opposite side to the micropipette (Fig. 4.1). The mean fluorescence intensity in each ROI was measured at every time increment using the LAS AF Lite (Leica, Germany) software.
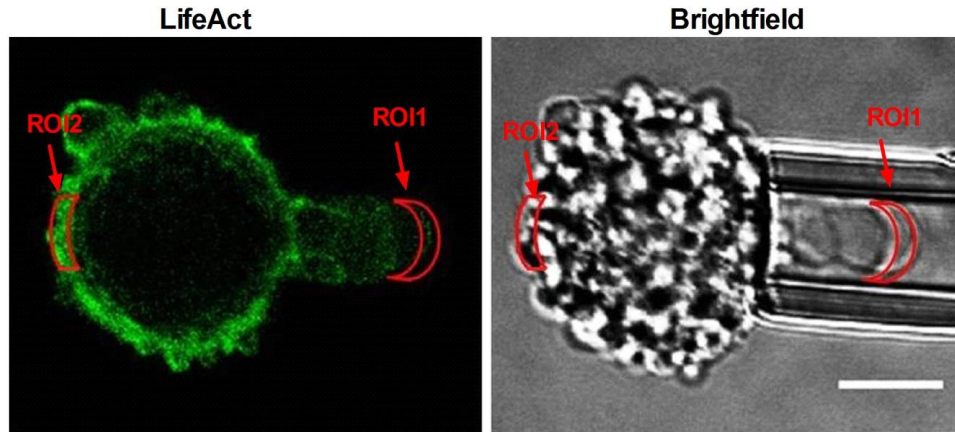
Figure 4.1: Fluorescent (left) and brightfield (right) images of a single cell showing the positions of the ROI used to measure cortical actin intensity during micropipette aspiration. Scale bar represents 10 μm.

4.2.2 Effect of differentiation on bleb formation during hypo-osmotic challenge

Bleb formation in undifferentiated hMSCs and chondrogenically differentiated hMSCs was also examined in response to sudden hypo-osmotic challenge (100 mOsm/kg). Prior to experiments the osmolality of the IM was measured at approximately 330 mOsm/kg using a freezing point depression osmometer (3250, Advanced Instruments, Norwood, USA). Cells were trypsinized and suspended in IM and placed in a water bath for shape recovery for 10-15 min. For control groups the cells were placed on a glass coverslip and imaged using brightfield microscopy. For hypo-osmotic challenge, the osmolality was first adjusted to 100 mOsm/kg by adding distilled water to the cell suspension which was then gently mixed and placed on a glass coverslip for imaging. In both cases brightfield images of cells were taken for 7 minutes. The percentage of cells with blebs was counted from the images. The projected area of each cell was measured using ImageJ and converted into cell volume based on the assumption that the cells are spherical.

The measurement error in this study was estimated to be 1 pixel which gives value equal to 0.73 μm. According to this value, the error of volume measurements before and after hypoosmotic challenge is ± 13 μm^3.

4.2.3 Statistical analysis

The volume of cells in iso-osmotic and hypo-osmotic conditions was assumed to be non-parametrically distributed and median values were presented. The Mann Whitney U test was used to determine the significant differences between groups.

For data on cell blebbing the Chi-squared test was used to determine the significant differences between groups and blebbing modes. For both type of statistical tests the statistical significances are presented as (*** $p < 0.001$), unless mentioned.

4.3 Results

4.3.1 Mechanically induced membrane bleb formation

In order to better understand the mechanism through which differentiated cells appear stiffer than hMSCs (chapter 3), the formation of membrane blebs was examined during micropipette aspiration. Cells exhibited three characteristic modes of behaviour depending on whether they formed one bleb, multiple blebs or no blebs. For cells exhibiting no blebs, the aspirated portion of the cell smoothly elongated into the micropipette and showed no membrane-actin cortex separation (Fig. 4.2 top). By contrast, in a subpopulation of cells micropipette aspiration resulted in the formation of a clear membrane bleb whereby the cell membrane separated from the cortex and elongated into the micropipette (Fig. 4.2 middle). This type of behaviour was named one bleb, as clear transparent bleb expansion was visible into the micropipette. In a further subpopulation of cells multi blebbing behaviour was observed (Fig. 4.2 bottom). At early time points, bleb formation was followed by additional successive blebs that resulted in elongation of aspirated length. This behaviour was particularly apparent in time lapse movies (Sliogeryte, *et al.*, 2014).
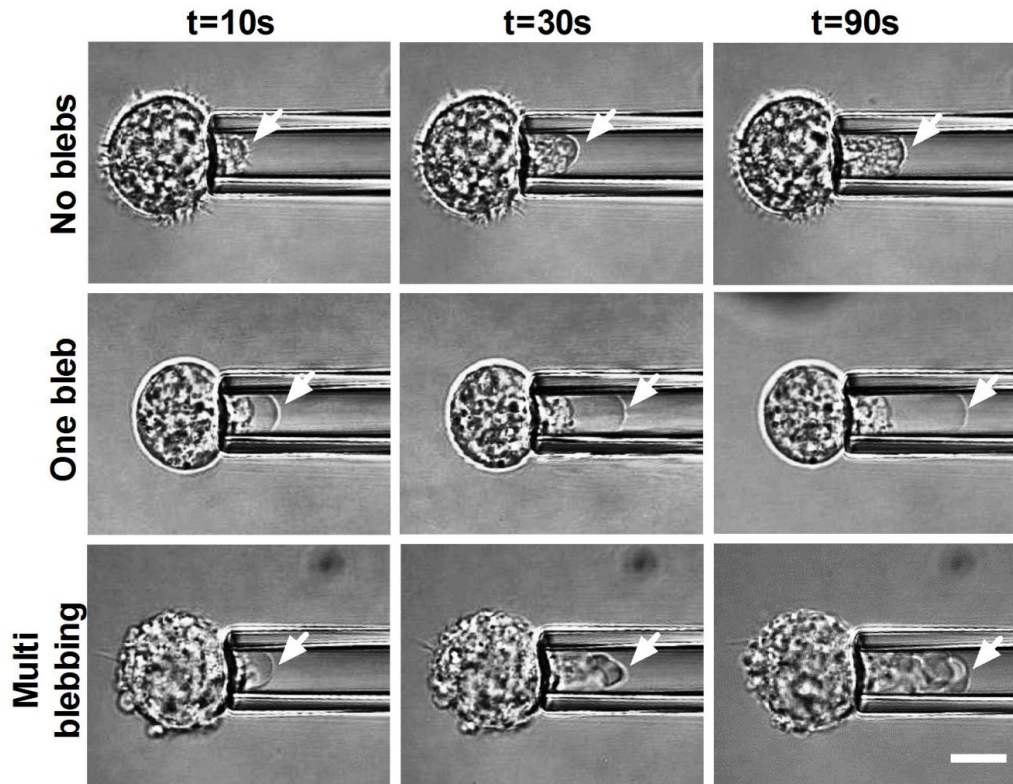
Figure 4.2: Brightfield microscopy time lapse images of three representative cells showing different modes of blebbing during micropipette aspiration. Scale bar represents 10 μm.

More than 80% of undifferentiated hMSCs exhibited multi blebbing behaviour with approximately 15% showing one bleb behaviour and only 1% not exhibiting bleb formation at all (Fig. 4.3). By contrast more than 50% of chondrogenically differentiated cells showed no blebs during the aspiration. Thus, hMSCs had a greater propensity to form membrane blebs during micropipette aspiration compared to differentiated cells (p<0.001).
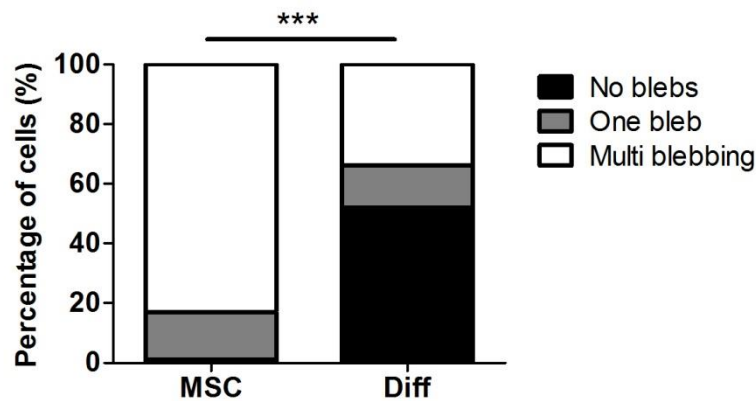
Figure 4.3: Chondrogenic differentiation of hMSCs reduces susceptibility to mechanically induced membrane blebbing. The percentages of cells exhibiting blebbing behaviour were significantly different between the two cell groups. (Chi-squared test, *** $p < 0.001$).

4.3.2 Actin remodelling during micropipette aspiration and bleb formation

Additional studies investigated the distortion and remodelling of the cortical actin cytoskeleton during micropipette aspiration and associated blebbing. F-actin was visualised using LifeAct-GFP. Preliminary studies described in chapter 2 found that LifeAct-GFP does not influence cell deformation and biomechanical properties estimated by micropipette aspiration section (2.7).

In both undifferentiated and differentiated hMSCs, blebbing was associated with a sudden drop in LifeAct-GFP intensity measured at the leading edge of the cell, or in this case the bleb, within the micropipette (Fig. 4.4). However the subsequent behaviour was very different between the two cell types. In undifferentiated hMSCs the actin cortex quickly reformed over 180 seconds as shown by an increase in LifeAct-GFP intensity at the leading edge which returned to the previous level. By contrast in differentiated cells the actin remodelling is minimal at the leading edge during micropipette aspiration.
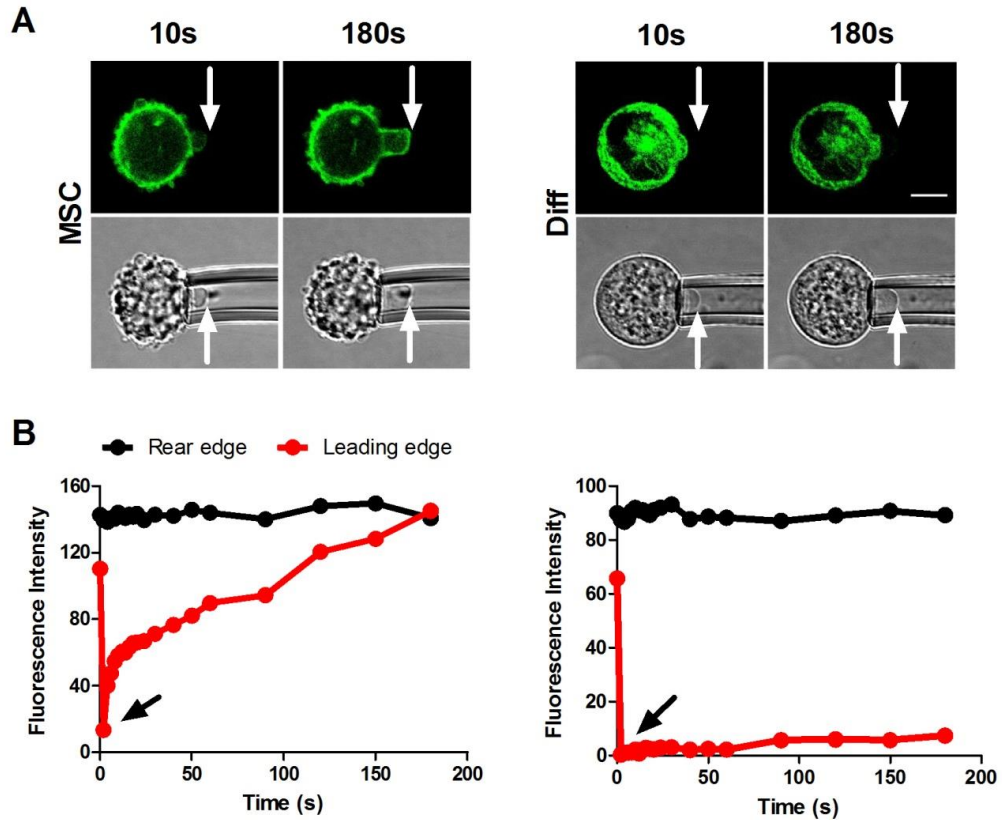
Figure 4.4: Actin remodelling in response to one bleb behaviour of undifferentiated hMSC and chondrogenically differentiated cells. (A) Representative fluorescent and brightfield images of hMSCs and differentiated cells aspirated into the micropipette. White arrows indicate the leading edge of the cells. Actin is labelled with LifeAct-GFP (green) to show the cortex displacement into the micropipette. Scale bar 10 μm. (B) The plots of fluorescence intensity of actin cortex at the leading and rear edges during the aspiration. Black arrows indicated the cortex breakage and decreased fluorescence intensity.

Actin cortex remodelling and new cortex growth forming visible rings was observed in undifferentiated hMSCs associated with multi blebbing behaviour during micropipette aspiration (Fig. 4.5 A). The analysis has demonstrated that LifeAct-GFP fluorescence intensity decreased in both undifferentiated and differentiated hMSCs (Fig. 4.5 B). However, new bleb formation and actin cortex remodelling was more visible in undifferentiated hMSCs with changes of fluorescence intensity resulting in peaks which can be observed on the plot. This again suggests that the rate of actin remodelling is faster in undifferentiated hMSCs compared to hMSCs differentiated to the chondrogenic lineage as seen in single blebs.
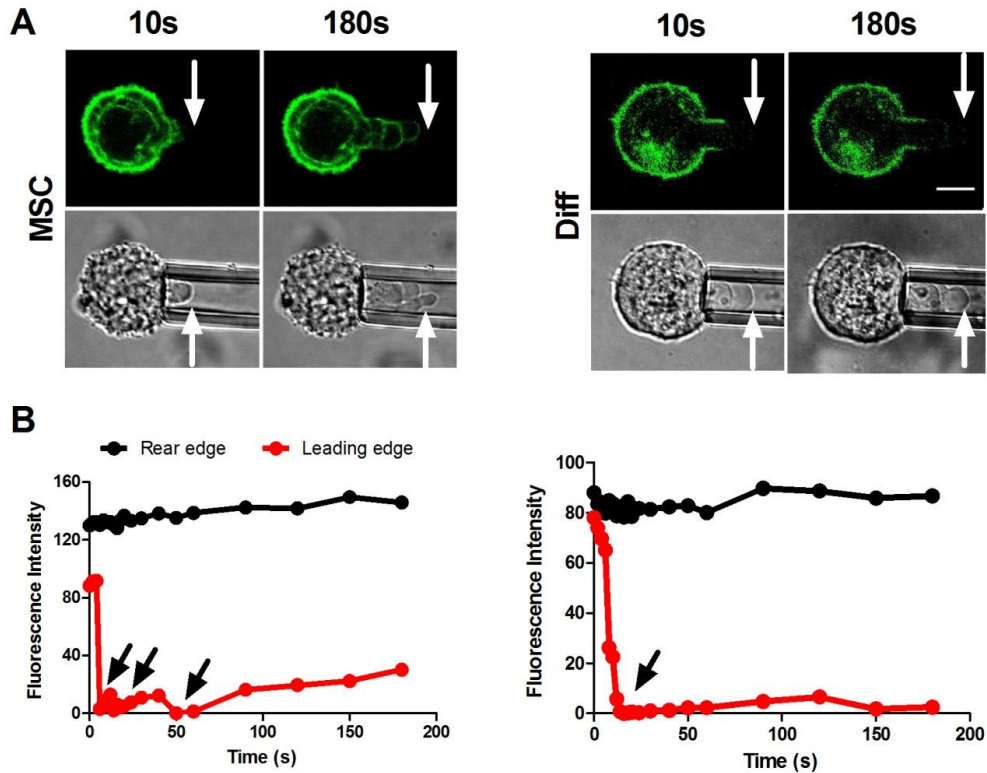
Figure 4.5: Actin remodelling in response to multi blebbing behaviour of undifferentiated hMSC and chondrogenic differentiated cells. (A) Representative fluorescent and brightfield images of cells aspirated into the micropipette. White arrows indicated the leading edge of the cells. Actin is labelled with LifeAct-GFP (green) to show the cortex displacement into the micropipette. Scale bar 10 μm. (B) Plots of actin cortex fluorescence intensity at the leading and the rear edges. Black arrows indicated the cortex breakage and decreased fluorescence intensity due to a new bleb formation.

A subpopulation of cells has demonstrated weak changes of actin cortex intensity with no obvious breakage (Fig. 4.6A left). Such actin remodelling was observed in hMSCs differentiated to the chondrogenic lineage which showed no bleb formation. Some cells have exhibited a clear breakage of actin cortex as a sudden decrease in fluorescence intensity followed by remodelling of a new actin cortex during the aspiration (Fig. 4.6 A and B right). The fluorescence intensity of the actin cortex at the rear edge has shown no changes in both cases for cells during aspiration.
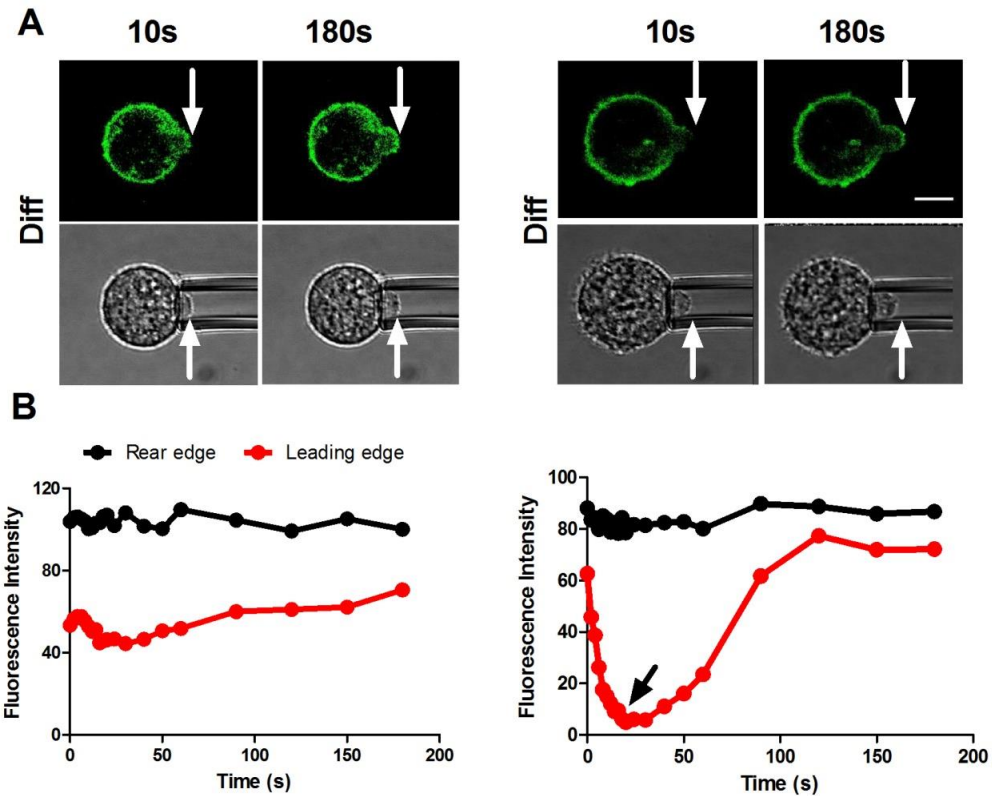
Figure 4.6: Actin cortex remodelling during cell deformation without bleb formation in chondrogenically differentiated cells. (A) Representative fluorescent and brightfield images of two chondrogenically differentiated cells partially aspirated into the micropipette and visualised at 10 and 180 seconds. White arrows indicate the leading edge of the cell. No bleb behaviour is associated with no breakage of actin cortex (left) and cortex breakage (right). Actin is labelled with LifeAct-GFP (green) to show the cortex displacement into the micropipette. Scale bar 10 μm. (B) Representative plots of fluorescence intensity of actin cortex with no breakage (left) and cortex breakage (right) at leading and rear edges during the aspiration. Black arrow indicates the fluorescence drop at the leading edge during cortex breakage.

4.3.3 Hypo-osmotic blebbing

Further studies were conducted to investigate whether hMSCs with increased susceptibility to membrane bleb formation during aspiration also exhibited increased blebbing in response to intracellular swelling during hypo-osmotic challenge. Undifferentiated hMSCs and hMSCs differentiated to the chondrogenic lineage were placed in suspension and subjected to a sudden reduction in extracellular osmolality from 330 mOsmol/kg to 100 mOsmol/kg. For both cell groups hypo-osmotic challenge resulted in cell swelling (Fig. 4.7).
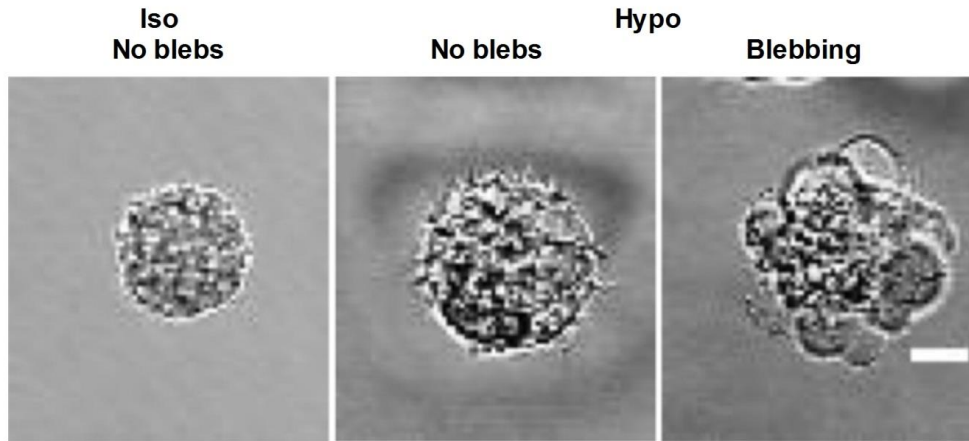
Figure 4.7: Representative brightfield images showing the characteristic appearance of hMSCs in iso-osmotic conditions and following hypo-osmotic challenge. Brightfield images showing cells in suspension in iso-osmotic (300 mOsm/kg) and hypo-osmotic (100 mOsm/kg) environment. A subpopulation of cells in the hypo-osmotic condition exhibited multiple membrane blebs. Scale bar, 10 μm.

In a subpopulation of cells the intracellular swelling was associated with formation of multiple membrane blebs. Undifferentiated hMSCs were more susceptible to hypo-osmotic induced membrane blebbing with 82% of cells exhibiting blebs compared to 62% of differentiated hMSCs ($p<0.001$) (Fig. 4.8 A).

There was no significant difference in cell volume between hMSCs and differentiated cells (Fig. 4.8 B). Furthermore, hypo-osmotic challenge was associated with a similar degree of cell swelling in both cell types such that cell volume measured after 2-8 minutes was significantly increased compared with corresponding cells in iso-osmotic conditions. This indicates that the increased blebbing with hypo-osmotic challenge in hMSCs is not due to a difference in swelling. For differentiated cells, those cells showing blebbing exhibited significantly greater swelling compared to non-blebbing cells. However, this difference in swelling between blebbing and non-blebbing cells was not observed in hMSCs. The cause of the different behaviour in hMSCs and differentiated cells is unclear. In addition, the assumption that cells adopted a spherical morphology after hypo-osmotic challenge gives an error for volume calculation as cells are not exacly spherical but have an irregular shape due to membrane blebbing. However, to estimate an error due to assumptions is not possible because that cell area was measured in 2D cross section which does not give

information about other dimention. To estimate an error, the surface area should be measured that provides an idea of over estimation, since a sphere maximises the enclosed volume of a surface for a given surface area.
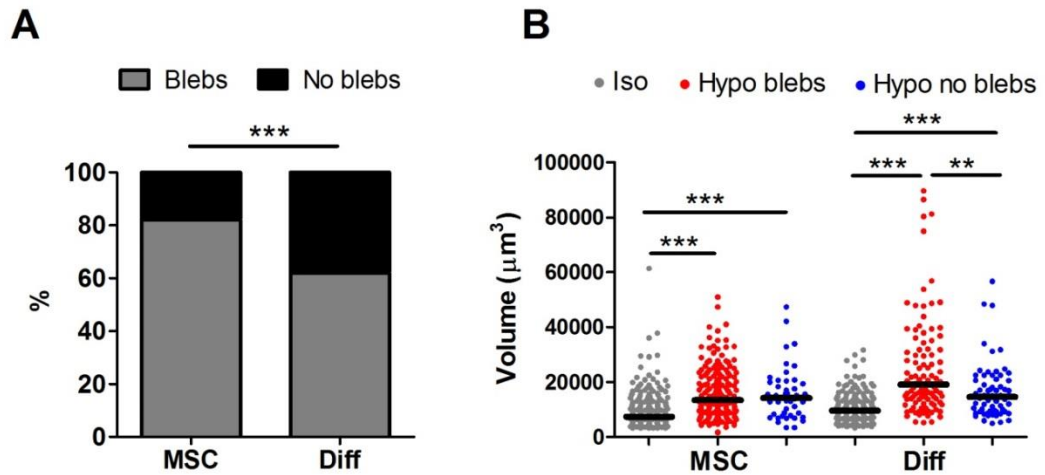
Figure 4.8: Hypo-osmotic challenge induces more blebbing in hMSCs compared to differentiated cells despite similar cell swelling. (A) Percentage of cells showing bleb formation in response to hypo-osmotic challenge. Chondrogenic differentiation reduces bleb formation (Chi-squared test *** p<0.001). (B) The volume of undifferentiated hMSCs and hMSCs differentiated to the chondrogenic lineage in response to hypo-osmotic challenge. Both type of cells show a similar significant increase in cell volume (Mann-Whitney U test, ** p<0.01, *** p<0.001). Plots presented as population with bars showing median values.

For better understanding of cell behaviour and cell blebbing under hypo-osmotic challenge, cell shape recovery and bleb retraction was monitored over 30 minutes. Brightfield images of two representative cells at different time points after the onset of hypo-osmotic challenge are presented in figure 4.9 A. For cells exhibiting membrane blebbing, this typically occurred in the first 10 minutes and was followed by bleb retraction and recovery of spherical cell morphology. Those cells without blebs maintain a spherical morphology whilst reducing in volume. The rate of volume recovery is similar for both blebbing and non-blebbing cells (Fig.4.9 B).
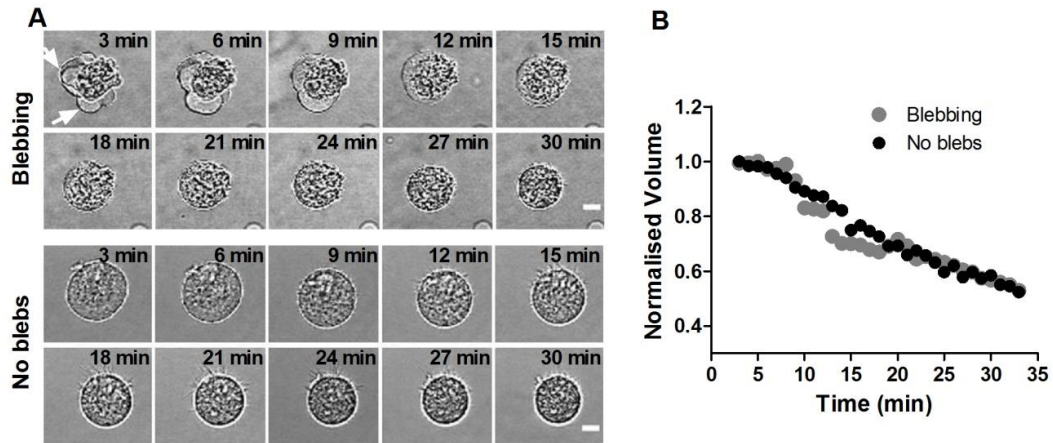
Figure 4.9: Cell shape and volume changes during hypo-osmotic challenge. (A) Representative timelapse brightfield images of two hMSCs exposed to hypo-osmotic pressure for a period of 30 minutes, blebbing (top) and no blebbing (bottom). White arrows indicate onset of blebs. Scale bars, 10 μm. (B) Corresponding temporal changes in cell volume.

4.4 Discussion

4.4.1 Mechanically induced cell blebbing

The process of mechanically induced blebbing and associated membrane-actin cortex detachment results from either mechanical force pulling the membrane from the cortex or raised intracellular pressure (Henon, *et al.*, 1999, Rentsch and Keller, 2000). Alternatively mechanical loading may induce localised breakdown of the cortical actin, leading to bleb formation. This study has demonstrated that micropipette aspiration can be used to induce bleb formation in agreement with previous studies. Undifferentiated hMSCs and hMSCs differentiated to a chondrogenic lineage were subjected to a step negative pressure which induced blebbing into the micropipette for a subpopulation of cells. Cells exhibited different behaviour, with either single or multi blebbing. Previous studies reported that Walker carcinoma cells aspirated into the micropipette also showed multi blebbing behaviour (Rentsch and Keller, 2000). In this case membrane blebbing was temperature dependent such that more frequent bleb formation occurred at 37°C compared to that at room temperature. A separate study demonstrated that membrane blebbing is associated with cortical actin remodelling with the formation of a new actin cortex underneath the membrane within the bleb (Schutz and Keller, 1998). The authors

suggested that bleb formation is due to pressure differences during the aspiration and cortical tension associated with contraction. This agrees with other studies in which bleb formation and bleb size were dependant on cortical tension such that cells with higher cortical tension were more likely to form membrane blebs (Brugues, *et al.*, 2010, Tinevez, *et al.*, 2009).

4.4.2 Actin cortex remodelling during the micropipette aspiration

In this study we demonstrated that the micropipette aspiration technique can be successfully used not only for estimation of cell mechanical properties but also for observations of actin dynamics and remodelling. Using LifeAct-GFP, cell deformation into the micropipette was observed to be associated with cortical actin remodelling and the reformation of a new actin cortex following blebbing. Undifferentiated hMSCs demonstrated much faster actin remodelling following bleb formation compared to hMSCs differentiated to the chondrogenic lineage (Fig. 4.4). Within 2 minutes the actin cortex was fully remodelled. It was not possible to quantify the rate of actin cortex remodelling for cells showing multi blebbing behaviour. However, undifferentiated cells demonstrated clear actin cortex reformation in each successive bleb which was not visible in differentiated cells (Fig. 4.5). This agrees with previously reported studies showed actin remodelling during micropipette aspiration (Rentsch and Keller, 2000). It is well known that actin remodelling is essential in bleb formation of living cells (Charras and Paluch, 2008, Charras, *et al.*, 2006). This suggests that stem cell differentiation influences the dynamics of actin remodelling. The slower rate of actin remodelling in differentiated cells could be due to reduced availability of actin monomer possibly associated with increased polymerised F-actin in the rest of the cell.

Furthermore, in some differentiated cells actin remodelling during micropipette aspiration was associated with actin cortex breakage (Fig. 4.6). However, this was not always followed by bleb formation. This suggests that the remaining membrane-actin cortex interaction is strong enough in differentiated cells to maintain the internal pressure. Stem cell differentiation is known to increase the density of F-actin microfilaments, providing more binding sites between actin and cell membrane (Titushkin, Igor A and Cho, Michael R, 2009). One possible explanation is that bleb formation is cell type dependant due to differences in bond strength between the membrane and the actin cortex.

4.4.3 Hypo-osmotic swelling regulates bleb formation

Undifferentiated hMSCs and cells differentiated toward the chondrogenic lineage exhibited bleb formation under hypo-osmotic challenge (Fig. 4.7). However, differentiated cells were less susceptible to blebbing (Fig. 4.8 A). Similar bleb formation during hypo-osmotic challenge was reported in a mouse myeloma NS1 cell line (Ušaj, *et al.*, 2009). However, other cell lines, such as murine melanoma (B16-F1), Chinese hamster lung fibroblast (V79) and Chinese hamster ovary cells (CHO), show hypo-osmotic induced cell swelling without membrane blebbing.

In addition this study demonstrated that both groups of cells, undifferentiated hMSCs and hMSCs differentiated to the chondrogenic lineage, increased in volume during the hypo-osmotic challenge. These findings agree with the previously reported data on chondrocytes (Guilak, *et al.*, 2002). However, primary chondrocytes subjected to hypo-osmotic challenge did not appear to show such obvious bleb formation, unlike that observed here. This suggests that the differentiated hMSCs examined in the present study were not all fully differentiated into chondrocytes. Another study suggested that cell blebbing during hypo-osmotic challenge is controlled by dynamic changes in plasma membrane tension (Barfod, *et al.*, 2011). Increased membrane tension creates mechanical stress on membrane-actin cortex linker proteins causing localised disruption of these proteins.

These findings demonstrate that cells exhibit bleb formation within the first minutes under hypo-osmotic challenge followed by bleb retraction and cell shape recovery. It is well know that bleb retraction is dependent on actin-myosin II interactions, which are regulated by myosin light chain kinase (MLCK) (Charras, *et al.*, 2008). Inhibition with ROCK and with myosin II ATPase has previously been shown to prevent bleb formation under hypo-osmotic conditions. This suggested that MLCK invokes contraction which results in bleb retraction (Barfod, *et al.*, 2011). In this study, we suggest that hMSCs differentiated to the chondrogenic lineage increase membrane-actin cortex adhesion resulting in decreased blebbing ability or 'blebability' under hypo-osmotic challenge.

CHAPTER 5
Differentiation regulates Actin and ERM expression to control cell mechanics and blebbing

5.1 INTRODUCTION

5.2 METHODS

5.2.1 Regulation of ezrin and ERM expression

5.2.2 Micropipette aspiration to measure membrane-cortex detachment pressure and cortical tension

5.2.3 Quantification of actin organization

5.2.4 Fluorescence recovery after photobleaching (FRAP)

5.2.5 Membrane-actin cortex interaction model

5.2.6 Polymerase chain reaction (PCR)

5.2.7 Western blots

5.2.8 ERM immunohistochemistry

5.2.9 Statistical analysis

5.3 RESULTS

5.3.1 Chondrogenic differentiation increases critical detachment pressure but not cortical tension

5.3.2 Chondrogenic differentiation changes actin organization

5.3.3 Modelling of membrane-actin cortex interaction during micropipette aspiration

5.3.4 Membrane-actin cortex linker protein expression

5.4 DISCUSSION

5.4.1 Stem cell differentiation regulates membrane-actin cortex adhesion

5.4.2 Organisation of cortical actin during the differentiation

5 DIFFERENTIATION REGULATES ACTIN AND ERM EXPRESSION TO CONTROL CELL MECHANICS AND BLEBBING

5.1 Introduction

Previous chapters demonstrated that hMSCs differentiated down a chondrogenic lineage increased viscoelastic properties and reduced susceptibility to mechanically and osmotically induced membrane blebbing. This was associated with a slower actin remodelling rate during micropipette aspiration.

Previous studies have examined the role of membrane mechanical properties associated with cortical actin existence (Titushkin and Cho, 2006). In addition, another study has demonstrated that cytoskeleton organization in stem cells can be regulated by substrate stiffness that is associated with focal adhesions (Yim, *et al.*, 2010). Stem cell differentiation was associated with membrane-actin cortex linker protein distribution. Cells under mechanical stimuli have shown ability of bleb formation, which was correlated with stem cell differentiation (Hemsley, *et al.*, 2011).

In eukaryotic cells, the lipid membrane is connected to the actin cortex via the family of ERM linker proteins, including ezrin, radixin and moesin (Charras, *et al.*, 2006). Localised breakdown of the cortical cytoskeleton or detachment of the membrane from the cortex following rupture of these linker proteins, results in the formation of a membrane bleb. The bleb expands due to cytoplasmic fluid pressure until polymerisation of actin beneath the membrane slows bleb growth and may eventually cause bleb retraction (Charras, *et al.*, 2008, Charras, *et al.*, 2005, Cunningham, 1995).

Here we utilise a combined experimental and computational approach based on micropipette aspiration. The study investigates the interaction between the cell membrane and the actin cortex. In particular we examine the role of ERM proteins and how these regulate cell membrane-actin cortex adhesion during chondrogenic differentiation. In addition, the cortical actin organisation in monolayer and rounded cells was monitored. Fluorescence recovery after photobleaching (FRAP) was used to estimate the actin turnover rate during hMSCs differentiation.

5.2 Methods

5.2.1 Regulation of ezrin and ERM expression

Undifferentiated hMSCs were seeded at 5 x 10^3 cells/cm^2 and cultured as described in section 2.2.1. In further experiments hMSCs were induced toward chondrogenic differentiation by culture for seven days in chondrogenic culture medium as described in section 2.2.2.

Undifferentiated hMSCs were transfected with a plasmid expressing active ezrin T567D causing over expression of the membrane-cortex linker protein, while differentiated cells were transfected with an inactive ERM plasmid. Ezrin point mutation T567D (active actin binding and impaired head to tail association) and F-ERM (inactive) were a kind gift from G. Charras (University College London, UK) (Charras*, et al.*, 2006). To confirm successful transfection, the active ezrin was tagged with GFP and the inactive ERM to RFP. To prepare these plasmids, bacterial cells were cultured on agar petri dishes at 37°C overnight. A single colony of bacterial cells was placed into the tube with bacterial culture media and placed on the shaker in a 37°C incubator for 16-20 hours. For more details on bacterial culture see (Appendix B). The cDNA was extracted using a High Pure plasmid isolation kit (Roche Diagnostics, Burgess Hill, UK). Prior to transfection, cells were cultured in antibiotic free X-PAN media for 30 minutes to 1 hour. Plasmid transfection was effected using Lipofectamine LTX Plus (Invitrogen, Paisley, UK). For 2 x 10^4 cells, 0.2 μg of cDNA was used. The procedure for preparation of transfection media is presented in table 5.1. Cells were cultured for 6 hours in transfection media according to the provider's protocols followed by replacement with either X-PAN media for undifferentiated hMSCs or CDM for hMSCs induced toward chondrogenic differentiation.

Table 5.1: Procedure of preparation of transfection media.

Procedure	Volume	Steps
Opti-MEM medium	25 µl	Dilute Lipofectamine reagent
Lipofectamine Reagent	3 µl	in Opti-MEM medium
Opti-MEM medium	25 µl	Dilute DNA in Opti-MEM
DNA	0.2 µg	medium and add PLUS
PLUS reagent	0.5 µl	reagent
Diluted DNA with PLUS reagent		Add diluted DNA to diluted
Diluted Lipofectamine reagent		Lipofectamine reagent
Incubate for 5 min at room temperature		Incubate

5.2.2 Micropipette aspiration to measure membrane-cortex detachment pressure and cortical tension

The micropipette aspiration experiments were performed on transfected cells the day after transfection and on non-transfected control cells. Micropipette aspiration was used to determine the pressure required for detachment of the cell membrane from the actin cortex and associated membrane blebbing. The micropipette aspiration system is similar to that described previously (Pravincumar, *et al.*, 2012). A peristaltic pump is used to provide precise temporal control over the head of water and hence the aspiration pressure as described in section 2.2.3. Micropipettes were made by pulling the capillary glass, more details provided in section 2.2.1. A cell suspension prepared in IM was placed in a chamber at room temperature on the inverted stage of a confocal microscope with a x63/1.4 NA oil immersion objective lens. An individual cell was subjected to negative pressure in a series of seven increments of 1.5 cm of water (0.147 kPa) every 15 seconds to a maximum pressure of 10.5 cm of water (1.03 kPa). The critical pressure for membrane detachment was taken at the pressure at which a membrane bleb was first seen using brightfield images. Cells that did not bleb were recorded as having a detachment pressure greater than the maximum aspiration pressure. The same experimental protocol was also used to calculate the cellular cortical tension as previously described (Tinevez, *et al.*, 2009). More details of protocol and calculations can be found in section 2.3.2.

5.2.3 Quantification of actin organization

Undifferentiated hMSCs and cells differentiated to a chondrogenic lineage were fixed either in monolayer or in suspension following trypsinisation. Cells were then stained with AlexaFluor555 phalloidin for F-actin visualisation. More details on F-actin staining can be found in section 2.7.2. Images were taken of a single confocal section bisecting the centre of the cell. The fluorescence intensity of the cortical actin staining was measured as described previously (Chen*, et al.*, 2012). The mean fluorescence intensity was calculated for each cell within a bagel region of interest of 1μm thickness and outside diameter approximately equal to the cell diameter using LAS AF Lite software (Leica, Germany).

5.2.4 Fluorescence recovery after photobleaching (FRAP)

Individual cells in suspension transfected to express LifeAct-GFP, as described in section 2.7.2, were attached to the micropipette with a small tare pressure 0.5 cm H_2O (0.05 kPa) to prevent cell movement. An initial confocal image (488nm excitation 1% laser power) was obtained bisecting the centre of the cell. This was used to position five circular regions of interest (ROIs, 2 μm diameter) over the cell cortex. The FRAP protocol consisted of four pre-bleach images, followed by five bleach images of the selected ROIs (100% laser power) and then a further sixty consecutive post-bleach images of the whole cell with a dwell time of 1.64 s/image. Pre- and post-bleach images were obtained at a 512 x 512 format yielding a pixel size of 0.15 x 0.15 μm. Cells were maintained at room temperature during all experiments which were conducted within 1 hour of trypsinisation. The FRAP analysis was performed using an Easy FRAP tool implemented using MATLAB (Rapsomaniki*, et al.*, 2012).

For analysis, the fluorescence intensity was measured at $I(t)_{ROI1}$, $I(t)_{ROI2}$ and $I(t)_{ROI3}$ with correspondent regions of interest (ROI1) in this case five circular regions of bleached measurement of cell cortex, one circular region (ROI2) of whole cell and one circular region (ROI3) of background at the corresponding time points. Before data analysis, the background intensity was subtracted from all measurements so that new intensities for bleached regions of cell cortex $I'(t)_{ROI1}$ and whole cells $I'(t)_{ROI2}$ are given as follows:

$$I'(t)_{ROI1} = I(t)_{ROI1} - I(t)_{ROI3} \qquad\qquad (5.1)$$

$$I'(t)_{ROI2}= I(t)_{ROI2} - I(t)_{ROI3} \qquad\qquad (5.2)$$

For further analysis the double normalization method was applied as previously reported (Phair, *et al.*, 2003). In this method the average of pre-bleach intensity of whole cell is divided by the intensities of whole cell at each time points and multiplied by the ratio of post bleach FRAP measurements at each point. This gives the normalised intensity with the bleached regions as presented in equation 5.3.

$$I''(t) = \left[\frac{\frac{1}{n_{pre}} \sum_{t=1}^{n_{pre}} I'(t)_{ROI2}}{I'(t)_{ROI2}} \right] \times \left[\frac{I'(t)_{ROI1}}{\frac{1}{n_{pre}} \sum_{t=1}^{n_{pre}} I'(t)_{ROI1}} \right] \qquad (5.3)$$

Temporal changes in the normalised intensity were fitted with a double term exponential equation as follows:

$$I_{frap} = I_0 - ae^{-\beta t} - \gamma e^{-\delta t} \qquad\qquad (5.4)$$

At bleaching time point t=0, $I_{frap} = I_0 - a - \gamma$ and the plateau of curve is I_0.

The mobile fraction (mf) represents the fraction of molecules which diffuse freely and can be estimated as follows:

$$mf = \frac{I_\infty - I_a}{1 - I_a} \qquad\qquad (5.5)$$

Where, I_∞ is the normalised fluorescence intensity after full recovery and I_a the normalised intensity of the first post bleach time point. I_∞ is the plateau and is equal to I_0 for exponential equations. Using a double exponential equation, when t=0 and $I_a = I_0 - a - \gamma$, the mobile fraction is given as follows:

$$mf = \frac{a + \gamma}{1 - (I_0 - a - \gamma)} \qquad\qquad (5.6)$$

Furthermore, the half-life t_{half} value is defined as half maximum recovery time at the point when the intensity equals half of the maximum intensity. Solving the exponential equation 5.4 for t_{half} provides the following equation:

$$t_{half} = \frac{ln\,2}{\beta} \qquad\qquad (5.7)$$

5.2.5 Membrane-actin cortex interaction model

A mathematical model was used to investigate the effect of bleb formation on apparent cellular mechanical properties determined using micropipette aspiration. The model in equation 5.8 is a dynamic version of the widely used static "liquid-drop" model for micropipette aspiration experiments (Hochmuth, 2000), amended to account for both the pressure drop due to the motion of the fluid within the cell and the wall friction (Brugues, *et al.*, 2010, Tinevez, *et al.*, 2009)

$$\eta \frac{dL}{dt} = \Delta p - G_{mbr}(L - L_0) - G_{ctx}(L - L^*) \tag{5.8}$$

where t is the time variable, L^* is a reference length, $G_{mbr}(L - L_0)$ is a linear elastic term representing the resistive pressure due to stretching of the membrane, and $G_{ctx}(L - L^*)$ is the elastic pressure due to stretching of the cortex attached to the membrane. The pressure drop term $\eta \frac{dL}{dt}$ on the left hand side models the viscous dissipation within the cell and the friction with the pipette wall; η is a coefficient which is assumed constant. The right-hand side of equation 5.8 can be recognised as the Laplace pressure $\cong 2(\gamma_{mbr}/R_{mbr} + \gamma_{ctx}/R_{ctx})$ acting across the composite interface made by the lipid membrane plus the actin cortex. The terms R_{mbr} and R_{ctx} are the radii of curvature of membrane and cortex respectively, and γ_{mbr} and γ_{ctx} are the corresponding surface tensions. In the linear regime, $\gamma_{mbr} = k_{mbr}\alpha$ and $\gamma_{ctx} = k_{ctx}\alpha$,

$$\alpha \cong \frac{R_p(L - L_{ref})}{2R_c^2} \tag{5.9}$$

Where α is the areal strain, and k_{mbr} and k_{ctx} are the area compressibility moduli of the membrane and cortex respectively. L_{ref} is the aspirated length in the reference (unstrained) configuration, R_p is the inner pipette radius ($\approx$ 3.5 μm), and R_c is the initial radius of curvature of the portion of the cell outside of the pipette ($\approx$ 12.5 μm) table 5.2. Since R_{mbr} and R_{ctx} are approximately equal to R_p,

$$G_{mbr} \cong k_{mbr} / R_c^2 \tag{5.10}$$

$$G_{ctx} = k_{ctx} / R_c^2 \tag{5.11}$$

For a lipid membrane, $k_{mbr} \cong 0.8 mN/m$ (Brugues, *et al.*, 2010), thus $G_{mbr} \cong 5 Pa/\mu m$. For this experiment, the corresponding membrane tension when $L - L_0 = R_p$ is $\gamma_{mbr} \cong GR_p^2/2 \cong 30 pN/\mu m$, comparable to the value $40 pN/\mu m$ reported by Tinevez et al. (2009). The sum $G_{ctx} + G_{mbr}$, and from this the elastic constant of the cortex, can be estimated from the average equilibrium length observed for non-blebbing cells, $L_{eq} \cong 9 \mu m$. Using the stationary solution of equation 5.8 we obtain $G_{cortex} + G_{mbr} = \Delta p/(L_{eq} - L_0) \cong 100 Pa/\mu m$. With $G_{mbr} \cong 5 Pa/\mu m$, this gives $G_{ctx} \cong 95 Pa/\mu m$. The elastic constant of the cortex is thus much larger than that of the lipid membrane. The viscous pressure drop is taken to be proportional to the tongue velocity dL/dt via a friction coefficient η. There is disagreement in the literature as to whether η should be taken as a constant (Evans and Yeung, 1989) or a function of L (Brugues, *et al.*, 2010). While the length of the protrusion within the pipette increases, which would suggest a monotonically increasing dependence of η on L, most of the dissipation is expected to occur near the hemispherical cap (the "tongue" of the protrusion). The latter observation would suggest a constant value of η (at least asymptotically). In these simulations, we have initially assumed a constant friction coefficient η = η₀, and later evaluate the effect of replacing this constant with the linear relation $\eta = \eta_0(1 + L/R_p)$ suggested by Brugues et al. (2010). Fitting the dynamics of non-blebbing cells to an exponential with a single relaxation time gives $\eta_0 \cong 1500 Pa \cdot s/\mu m$. Note that the effective friction coefficient is known to depend strongly on the ratio between the pipette and cell radii (Evans and Yeung, 1989), and may also be a strong function of cell rigidity, since a stiffer cell should produce a larger friction with the wall.

Table 5.2: Values of parameters used to the membrane-actin cortex interaction model.

Parameter	Value	Cell type	Reference
Micropipette radius	3.5 µm	-	Present study
Cell radius	12.5 µm	hMSCs	Present study
Equilibrium aspirated length	9 µm	hMSCs	Present study
Membrane compressibility	0.8 mN/m	E. histolytica HM1-IMSS	(Brugues, *et al.*, 2010)
Membrane elastic constant	5 Pa/µm	hMSCs	Present study
Cortex elastic constant	95 Pa/µm	hMSCs	Present study
Friction coefficient	1500 Pa.s/ µm	hMSCs	Present study

5.2.6 Polymerase chain reaction (PCR)

RNA was extracted from undifferentiated hMSCs and hMSCs induced to undergo chondrogenic differentiation. Cells were cultured in 6 well plates under control and chondrogenic differentiation conditions, then lysed in buffer containing β-mercaptoethanol and scraped to remove cells from the plate surface. The RNA was isolated according to manufacturer's instructions using a RNeasy Plus Mini Kit (Qiagen, Manchester, UK). RNA samples were quantified using a NanoDrop ND-100 spectrophotometer (Thermo Scientific, Waltham, USA) and quality assessed on 2% agarose MOPS formaldehyde gel. RNA was reverse transcribed to cDNA using the Qiagen Quantitect cDNA synthesis kit (Qiagen, Manchester, UK). Primer sets were designed and purchased (Sigma-Aldrich). The cDNA was amplified using a MX3000P qPCR system (Agilent Technologies, Santa Clara, USA) in a 10 µl reaction volume containing the required concentrations of PCR reagents. The amplification was performed under the following conditions: the reaction was denatured at 95°C for 15 min, followed by 40 cycles of amplification (denaturation at 95°C for 3 s; annealing 60°C for 30 s and extension at 95°C for 30 s). Human glyceraldehyde-3-phosphate dehydrogenase (GAPDH) was chosen as a housekeeping control gene. A serial dilution of known cDNA was used to establish a standard curve. The ΔCt for specific gene expression was determined relative to the Ct value of GAPDH. A primer for ezrin linker protein was used (Jiang, *et al.*, 2012) as follows: 5'-AGCGCATCACTGAGGCAGAG-3' (forward), 5'-

GCCGCAGCGTCTTGTACTTG-3' (reverse). The sequences of ezrin, radixin and moesin are very similar so this primer is likely to detect changes in other ERM genes (Toms, *et al.*, 2012).

5.2.7 Western blots

Protein was isolated and quantified using standard methods (Chen, *et al.*, 2013). Cells were cultured and differentiated for 7 days as explained above. Cells were then washed with chilled PBS and lysed in RIPA (Radio Immuno Precipitation Assay) buffer (150 mM sodium chloride, 1% NP-40, 0.5% sodium deoxycholate, 0.1% SDS and 50 mM Tris-HCl) containing 200 mM activated Na_3VO_4 and protease inhibitors (Complete mini, Roche) and lysed on ice for 15 min. This was followed by repetitive disruption of the lysate through a 21 gauge needle and centrifugation at 12000 g for 15 minutes at 4°C. The protein concentration in the supernatant was determined using a bicinchoninic acid (BCA) protein assay kit (Fisher Scientific, UK). Cell lysates of 10 μg were mixed with Laemmeli buffer and denatured by heating at 100°C for 5 min. Samples were then loaded into a Mini-Protean TGX Precast Gel (Bio-Rad, UK), and proteins were transferred to Mini Nitrocellulose Transfer membranes (Bio-Rad, UK). The membranes were blocked with 5% non-fat milk in Tris-buffered saline (TBS) with 0.1% Tween before incubation overnight with primary antibodies with 1:1000 dilutions for rabbit polyclonal Ezrin/Radixin/Moesin (ERM) and rabbit monoclonal phosphorylated Ezrin/Radixin/Moesin (pERM) (Cell Signaling Technology, Leiden, Netherlands) and 1:5000 dilutions for mouse monoclonal anti-β-actin (Sigma Aldrich), β-actin was used as a control. After washing with TBS+0.1% Tween and incubation for 1 hour with secondary antibodies (1:10000 dilutions for 680RD Goat anti-Mouse IgG and 800CW Donkey anti-Rabbit IgG). Membranes were washed again in TBS+0.1% Tween and prepared for image processing using an Odyssey infrared Imaging system (LI-COR).

5.2.8 ERM immunohistochemistry

Undifferentiated hMSCs and those differentiated toward the chondrogenic lineage were trypsinised, fixed in 4% PFA and suspended in PBS. Cell suspension was centrifuged and blocked with goat serum for 30 min. Cells then were incubated for 1 hour at room temperature with the primary antibody, rabbit polyclonal anti-Ezrin/Radixin/Moesin (ERM) (Cell Signaling Technology, Leiden, Netherlands) at a concentration of 1:200, washed with PBS and incubated in the secondary antibody,

Alexa Fluor 594 conjugated goat anti-rabbit IgG antibody (Molecular Probes, Paisley, UK) at a concentration of 1:1000 for 1 hour at room temperature. Cells then were washed twice in PBS+0.5% BSA and suspended in de-ionised water. A drop of cell suspension was placed on coverslip, allowed dry, and mounted with ProLong Gold.

5.2.9 Statistical analysis

The ezrin gene expression and ERM protein quantity were all assumed to have a normal distribution and are hence described using parametric statistics in the form of mean and standard deviation values. The Student's t test was used to estimate significant differences between groups.

The pressure required for membrane-actin cortex detachment, cortical actin quantity and half life recovery after photo bleaching were assumed to be non-parametrically distributed and values are presented as a population with a bar indicating the median value. Accordingly, the Mann-Whitney U test was used to determine significant differences between groups. In both the parametric and non-parametric analysis the significance level for differences presented is (* $p<0.05$, ** $p<0.01$ and *** $p<0.001$), unless otherwise stated.

5.3 Results

5.3.1 Chondrogenic differentiation increases critical detachment pressure but not cortical tension

A micropipette aspiration system was used to estimate the detachment pressure required to break the linkage between the membrane and the actin cortex of undifferentiated hMSCs and those differentiated to the chondrogenic lineage. The numbers of cells used for measurement of membrane-actin cortex adhesion are presented in Table 5.3. Cells that were exposed to transfection media but did not show GFP or RFP fluorescence signal are considered transfection controls.

Table 5.3: Number of cells used for micropipette aspiration experiments to assess membrane-actin cortex adhesion.

Experiments	Number of cells
Experiment 1 (Fig. 5.2 B)	
MSC	**47**
Diff	**50**
Experiment 2 – Ezrin up regulation (Fig. 5.3 A)	
MSC	**30**
MSC ezrin T567D	**36**
Transfection control	**14**
Experiment 3 - ERM down regulation (Fig. 5.3 B)	
Diff	**30**
Diff ERM	**22**
Transfection control	**24**

Membrane bleb initiation was clearly visible from brightfield images (Fig. 5.1) enabling calculation of the critical aspiration pressure required for membrane-actin cortex detachment. The formation of a membrane bleb resulted in a sudden large increase in aspiration length (Fig. 5.2 A). By contract, in the absence of blebbing, the aspirated length increased more gradually with each increment of pressure. The pressure at which the bleb initiation occurred and hence the strength of the membrane-actin cortex adhesion was significantly lower in undifferentiated hMSCs compared to hMSCs differentiated to the chondrogenic lineage (Fig. 5.2 B). This shows that hMSCs are more susceptible to membrane blebbing than differentiated cells.
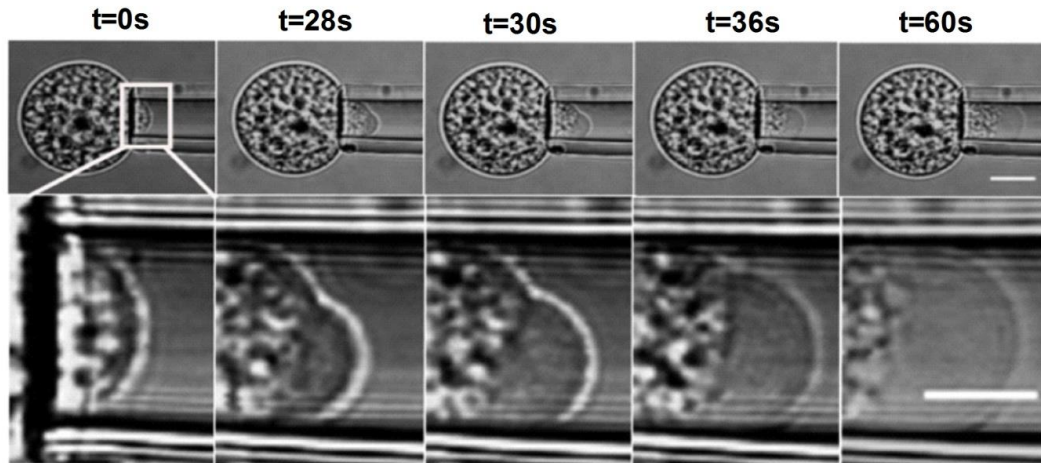
Figure 5.1: Initiation of a membrane bleb was clearly visible from brightfield microscopy images enabling calculation of the corresponding critical pressure for membrane-cortex detachment. Bright field images of a single representative cell with increasing applied aspiration pressure showing the formation of a membrane bleb at t=28 seconds and pressure 0.15 kPa, scale bar represent 10 μm. Lower images show a magnified view of the leading edge inside the micropipette. Scale bar represent 5 μm.
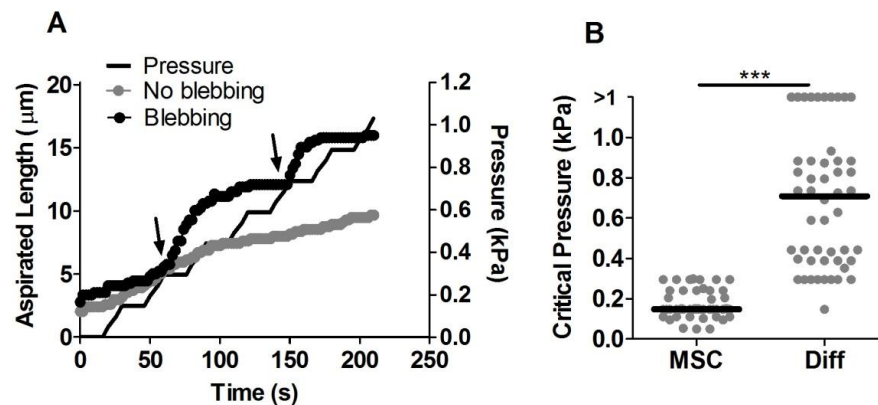
Figure 5.2: Differentiation strengthens membrane-cortex adhesion quantified by a significant increase in the critical pressure for membrane-cortex detachment. (A) Representative data showing the temporal change in aspiration length in response to incremental increases in aspiration pressure. Arrows indicate the onset of a membrane bleb. A non-blebbing cell is shown for comparison. (B) Plot showing the critical pressure required for membrane detachment and onset of blebbing for hMSCs (MSC) and differentiated cells (Diff). Cells that did not exhibit bleb formation during testing are classified as having a detachment pressure greater than the maximum pressure of 1.0 kPa. Mann-Whitney U test (*** p<0.001), n values shown in table 5.2.

To test the extent to which the membrane-actin cortex bond strength and bleb initiation is dependent on the membrane-cortex linker proteins (ERM), micropipette aspiration was performed on undifferentiated hMSCs transfected to over express ezrin (T567D). The data show that the critical pressure for bleb formation and detachment of the membrane-cortex significantly increased for cells transfected with T567D compared to control cells. There was no significant difference between control cells and hMSCs in transfection control group (Fig. 5.3 A). Further studies examined whether transfection of differentiated cells with inactive ERM would recapitulate the hMSC phenotype. In this case despite a reduction in median value, the critical pressure was not significantly different (Fig. 5.3 B). We also examined whether the difference in pressure required for membrane-cortex detachment was associated with cortical tension. There was no significant difference in the cortical tension measured for hMSCs and differentiated cells (Fig. 5.4).
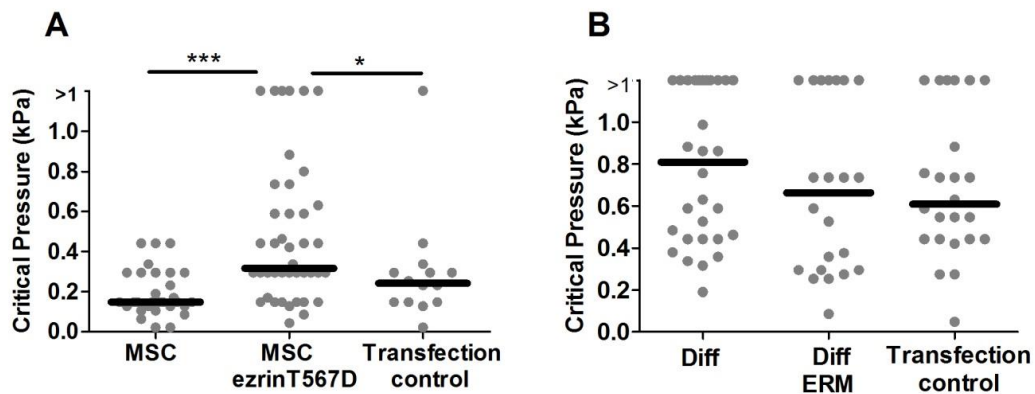
Figure 5.3: ERM expression regulates membrane-cortex adhesion and blebbing. (A) Scatter plot showing increased critical pressure required for membrane-cortex detachment in hMSCs following transfection with ezrin T567D. (B) Scatter plot showing no statistically significant effect on differentiated hMSCs transfected with the non-active ERM construct. In both cases data is also shown for cells exposed to transfection media which did not express either GFP or RFP (transfection control). Mann-Whitney U test, * p<0.05, *** p<0.001.
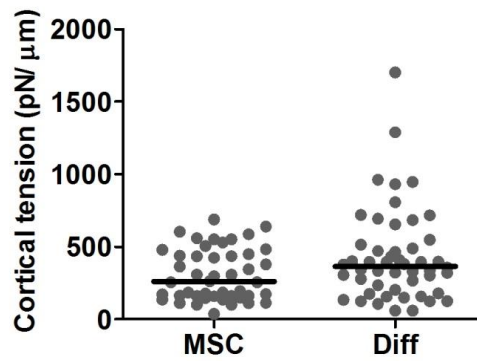
Figure 5.4: Differentiation has no effect on cortical tension. Scatter plot showing cortical tension for undifferentiated hMSCs (MSC) and cells induced toward chondrogenic differentiation (Diff). There was no significant difference. (Mann-Whitney U test, p=0.08).

5.3.2 Chondrogenic differentiation changes actin organization

The membrane-actin cortex adhesion is dependent on the density and strength of ERM linker proteins (Fig. 5.3). This in turn may be influenced by the organisation of the cortical actin. Therefore, to examine whether chondrogenic differentiation was associated with changes in F-actin organisation, the quantification of cortical actin staining was performed. Fixed cells in monolayer and suspension were labelled with Alexa Fluor 555-phalloidin and imaged using confocal fluorescence microscopy. Representative images of undifferentiated hMSCs and cells differentiated to chondrogenic lineage are shown in figure 5.5A. Cells induced to undergo chondrogenic differentiation had more pronounced actin stress fibres in monolayer, compared with undifferentiated hMSCs. Similarly, differentiated cells in suspension exhibited a higher intensity of actin cortex with a corresponding significant increase in the median fluorescence intensity of cortical actin staining (Fig. 5.5 B).
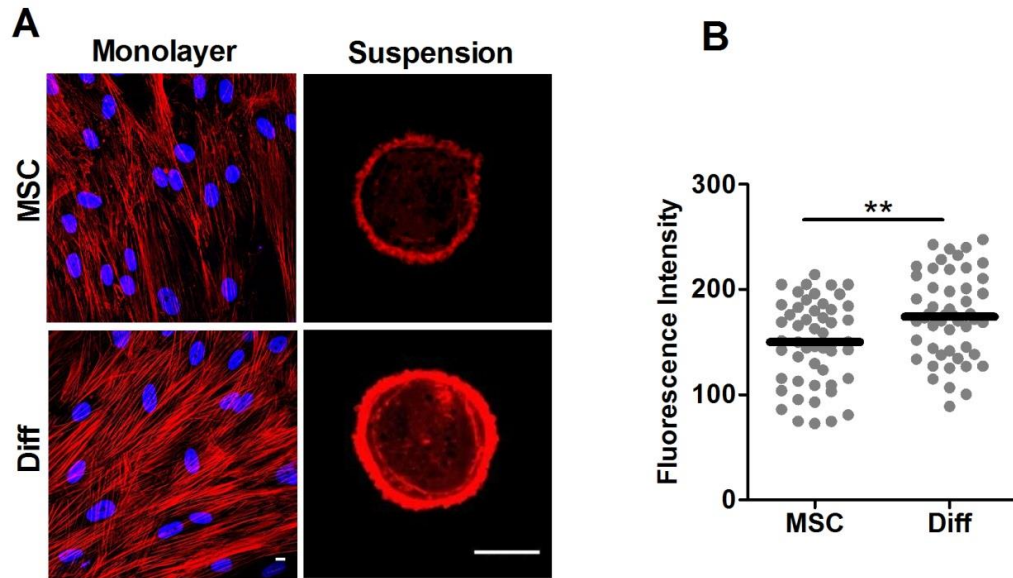
Figure 5.5: Differentiation increases cortical F-actin staining. (A) Confocal images showing increased F-actin organisation in differentiated cells (Diff) compared to hMSCs in monolayer and suspension. F-actin labelled with Alexa Fluor 555-phalloidin (red) and nuclei (monolayer only) with Hoechst 33342 (blue). Scale bar represents 10 μm. (B) Scatter plot showing the increased cortical actin staining intensity for differentiated cells in suspension compared to hMSCs. Mann-Whitney U test, ** p<0.01. Median values indicated by bars, n=51 cells (MSC) and 50 cells (Diff).

To examine steady state of actin dynamics/turnover, further studies used a customised confocal fluorescence recovery after photobleaching (FRAP) protocol similar to that adopted from previous studies (Campbell and Knight, 2007). Representative images of FRAP are provided in (Fig. 5.6 A). The cortical actin in both hMSCs and differentiated cells exhibited characteristic FRAP behaviour with a mobile fraction of approximately 50% indicative of F-actin turnover or treadmilling. Images from a FRAP protocol and the corresponding temporal change in intensity for a single cell are shown in figure 5.6 A and 5.6 B respectively. The rate of remodelling was slower in differentiated cells as shown by statistically significant differences in the FRAP half-life, t_{half} (Fig. 5.6 C). However, there was no significant difference in the relative mobile fraction (Fig. 5.6 D).
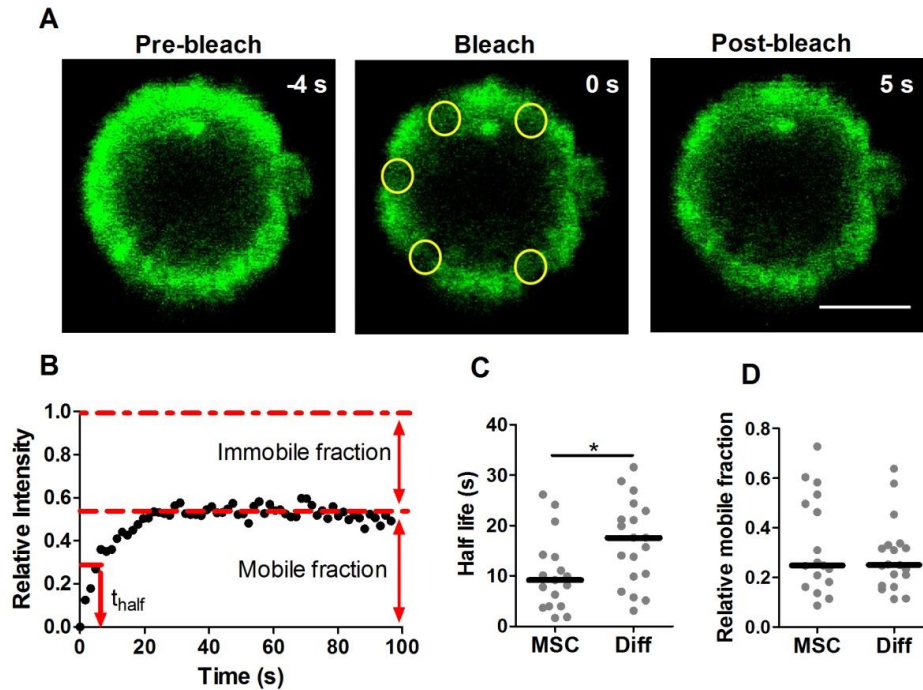
Figure 5.6: FRAP analysis of LifeAct-GFP indicates that chondrogenic differentiation slows down actin turnover. (A) Representative confocal images pre-bleach and at 0 s and 5 s after photobleaching of five circular regions of interest (ROIs) positioned on the actin cortex (yellow circles). Scale bar represents 10 μm. **(B)** Temporal changes in mean intensity within the ROIs showing characteristic FRAP behaviour. **(C)** Scatter plot showing a significant difference in the recovery half-life indicating slower remodelling in differentiated cells (Diff) compared to hMSCs (* p<0.05). (D) Differentiation has no effect on cortical actin mobile fraction based on FRAP analysis, p=0.76, Mann-Whitney U test. Data plotted from two independent experiments with median values indicated by bars, n=17 cells (MSC) and 19 cells (Diff).

5.3.3 Modelling of membrane-actin cortex interaction during micropipette aspiration

To further examine whether alterations in membrane-actin adhesion and blebabillity are responsible for changes in cell mechanics, a one-dimensional viscoelastic model of bleb formation during the micropipette aspiration was developed in collaboration with Dr Lorenzo Botto (QMUL). This builds upon previous studies by Brugues et al. (Brugues*, et al.*, 2010) and retains many of the features seen in the experimental micropipette aspiration data. The model allows investigation of the effect of membrane-actin cortex rupture on the overall temporal dynamics of the aspirated

membrane and hence the apparent cellular mechanical properties. The governing equation for the viscoelastic model is given in equation 5.8.

This model accounts for the competing effects of viscous dissipation due to the fluid motion within the cell and friction with the pipette walls (left-hand side of equation 5.8, applied pressure (Δp), elastic resistance due to the stretched membrane $(G_{mbr}(L - L_0))$ and elastic resistance due to the cortex $(G_{ctx}(L - L^*))$. The model introduces the following failure criterion leading to multi blebbing: when $G_{ctx}(L - L^*)$ is equal to a critical failure pressure Δp_c, the cortex resistance is set to zero $(G_{ctx} = 0)$ and the reference length L^*, which at time t=0 is equal to the initial protrusion length L_0, is set to the current protrusion length. The cortex thus ruptures repeatedly according to a yield deformation length $\sim \Delta p_c / G_{ctx}$. This approach is illustrated schematically in figure 5.7A, has been previously shown to give a reasonable description of experimental data for multi blebbing cells (Brugues, *et al.*, 2010), and seems to semi-quantitatively capture the present data as well.

In figure. 5.7 B, we plot the numerical solution of equation 5.8 for values of $\Delta p_c / \Delta p$ = 0, 0.25, 0.5, 0.75 and 1.0. At $\Delta p_c / \Delta p$ = 1.0 no blebbing occurs since the pressure applied to the cortex (ΔP) is never larger than that required for membrane cortex detachment $\Delta p_c / \Delta p$. Reducing Δp_c increases the number of membrane-cortex rupturing events, so called multi-blebbing, which can be identified as the points where the L versus t curve displays slope discontinuities. Experimentally, such slope discontinuities at bleb initiation are unambiguously identified due to the limited time-resolution and the fact that cortex-membrane adhesion failure is unlikely to be a sharp, "on-off" event.

As the critical pressure Δp_c decreases a larger number of blebbing events occur, the observed equilibrium aspirated length increases, and the L versus t curve more closely approximates a smooth curve. An effective elastic constant (G_{eff}) can be calculated from multi blebbing simulation data from the following equation where $L_{eq,multibleb}$ is the limiting value of the aspirated length in the simulation:

$$G_{eff} = \frac{\Delta P}{L_{eq,multibleb} - L_0} \tag{5.12}$$

For consistency with the experimental approach, the value at t=200 seconds is taken to be the equilibrium value. This effective elastic constant corresponds to the value obtained by fitting these theoretical multi-blebbing $L\,versus\,t$ curves with an exponential and therefore allows comparison with the equilibrium modulus (E_∞) calculated directly from experimental data based on the following equation

$$E_\infty = \frac{3R_p}{\pi} G_{eff} \qquad\qquad (5.13)$$

In figure. 5.7 C, it can be seen that increased adhesion strength, defined by the pressure required for membrane detachment (Δp_c), results in an increased effective equilibrium modulus for the cell. The elastic constant varies from that of the bare membrane for $\Delta p_c/\Delta p = 0$, to that of the compound actin cortex-membrane for $\Delta p_c/\Delta p = 1$. Therefore, our model demonstrates that the apparent elastic properties of the cell determined by micropipette aspiration can be modulated by changes in the membrane-actin cortex adhesion strength.

The model reveals that the dependence of the effective elastic constant on the critical pressure is stronger for larger values of G_{mbr}. Accounting for a length-dependent friction coefficient instead of a constant one, as suggested by Brugues et al. (2010), gives a weaker dependence. Experimental measurement of the critical pressure for membrane detachment (Δp_c), provides median value of approximately 0.15 kPa for hMSCs and 0.71 kPa for differentiated cells (Fig. 5.2 B). These correspond to values for $\Delta p_c/\Delta p$ of 0.21 and 0.92 and thus the theoretical model using no drag (G_{mbr}=5) predicts effective equilibrium moduli for hMSC and differentiated cells of 0.15 kPa and 0.3 kPa respectively (Fig. 5.7 C). These very closely mimic the experimental data reported in chapter 3 (Fig. 3.9 B).

In addition necessary to mention that the model was designed with several assumptions and not all physical parameters used in this model were measured in present cells. This suggests that sensitivity of model to specific cells could be lost. Also, the model does not take into account the density of actin cortex and ERM linker proteins those would provide more precise information of membrane-cortex interaction.
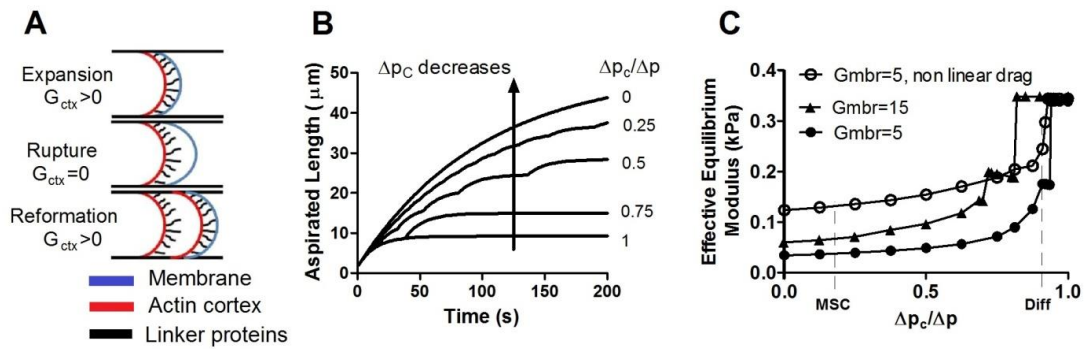
Figure 5.7: Theoretical model of cell membrane-actin cortex rupture and actin reformation during micropipette aspiration. (A) Schematic representation of the hemispherical leading edge of the cell being aspirated within the micropipette. The parameter G_{ctx} models the elastic response of the cortex when attached to the membrane see equation 5.1. (B) Theoretically derived temporal changes in aspiration length within the micropipette under the same applied pressure as that used experimentally. The different curves indicate the influence of the membrane adhesion strength as given by the detachment pressure (Δp_c). (C) The effective equilibrium elastic modulus plotted as a function of $\Delta p_c/\Delta p$, for $G_{mbr} = 5\ Pa/\mu m$ and $G_{mbr} = 15\ Pa/\mu m$. For the case $G_{mbr} = 5\ Pa/\mu m$ we also report the curve corresponding to non-linear drag defined by a length-dependent friction coefficient $\eta = \eta_0(1 + L/R_p)$ which shows excellent agreement with experimental data for hMSCs and differentiated cells. Dashed lines indicate the experimental median values for $\Delta\boldsymbol{p_c}/\Delta\boldsymbol{p}$ for hMSCs and differentiated cells.

5.3.4 Membrane-actin cortex linker protein expression

Previous studies have examined that ERM proteins are involved in cell mechanics and membrane-cortex interactions (Hemsley, *et al.*, 2011, Titushkin and Cho, 2011). Differentiated cells had significantly greater ezrin gene expression compared with hMSCs (Fig. 5.8 A). There was also an increase in filamin β gene expression but the difference was not statistically significant (Fig. 5.8 B).

The distribution of ERM protein in cells visualized using confocal immunofluorescence, showed that in undifferentiated hMSCs, ERM appeared as a less brighter cortex localized to the cell membrane in contrast to more widespread appearance in differentiated cells (Fig. 5.9 A). The quantitative analysis of ERM proteins from western blotting has shown that differentiated cells have greater total ERM and phosphorylated ERM protein expression compared to undifferentiated hMSCs (Fig. 5.9 B and C).
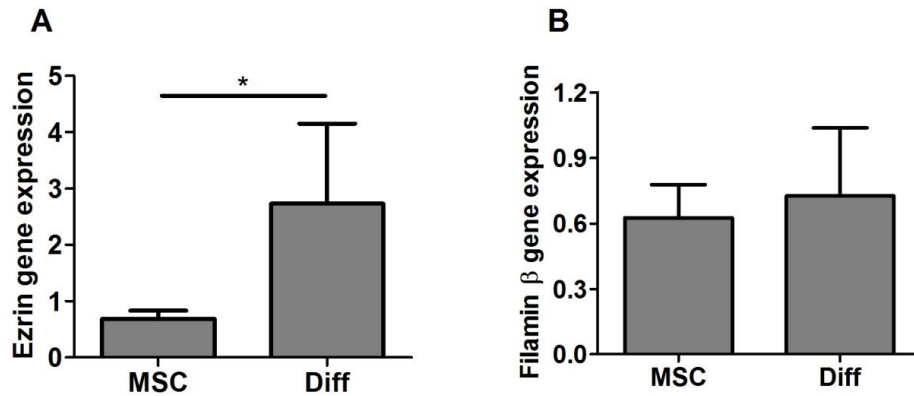
Figure 5.8: Chondrogenic differentiation regulates membrane-actin cortex linker protein gene expression. Real time RT-PCR analysis showing (A) increased ezrin gene expression in differentiated cells compared to hMSCs (* p<0.05) but (B) no significant difference in filamin β gene expression (p=0.319). Student t-test was used to determine significant differences. The level of expression was normalised to GAPDH.
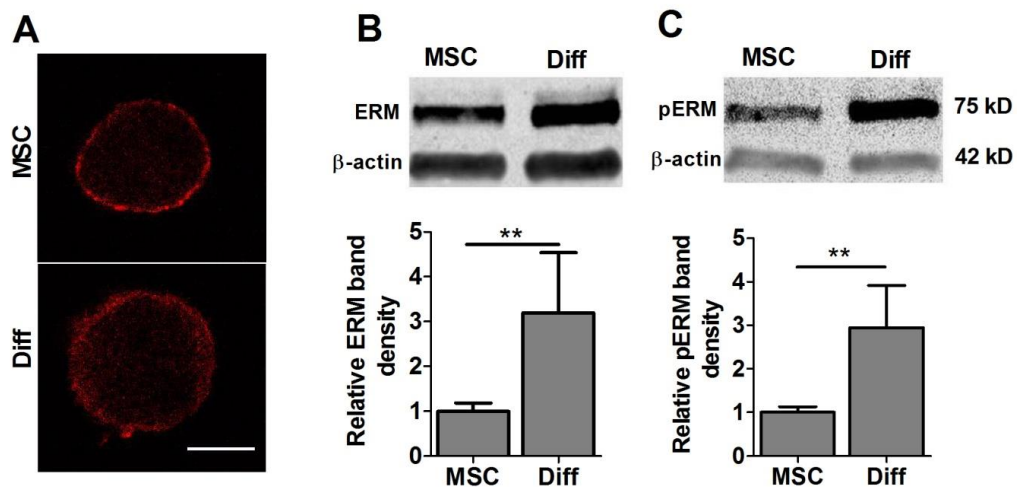
Figure 5.9: Chondrogenic differentiation regulates membrane-actin cortex linker protein expression. (A) Representative confocal images bisecting the centre of single cells in suspension showing thicker cortical localisation of ERM (red) in differentiated cells compared to hMSCs. Scale bar represents 10 μm. Western blot analysis showing increased (B) total ERM protein and (C) phosphorylated ERM protein levels in differentiated cells with quantification of 75 kDa immuno-blots were combining ezrin, radixin and moesin (ERM). Data normalized to β-actin, which showed no changes during differentiation.

.

5.4 Discussion

5.4.1 Stem cell differentiation regulates membrane-actin cortex adhesion

In this study we develop a novel technique for measuring the membrane-actin cortex detachment pressure or bond strength. The micropipette aspiration coupled with brightfield imaging was used to estimate the critical pressure required for membrane-actin cortex bond detachment. The data have shown that critical pressure is increased with hMSC differentiation to the chondrogenic lineage which is associated with decreased blebbing (Fig. 5.2). The ERM family of membrane-cortex linker proteins have been shown to regulate stem cell differentiation (Hemsley, *et al.*, 2011) as well as cancer metastasis (Hunter, 2004). Here we show that ERM is up-regulated with chondrogenic differentiation at gene and protein level (Fig. 5.8-5.9) and that transfection of hMSCs with the active form of ezrinT567D increases the membrane-cortex bond strength. This is supported by previous studies which report that phosphorylation of ezrin from the inactive form to the active form increases affinity binding to F-actin (Zhu, *et al.*, 2007). ERM has also been shown to influence cell mechanics (Titushkin, *et al.*, 2013).

To investigate whether the increased bond strength between the actin cortex and cell membrane and reduced blebabillity during differentiation was responsible for the altered mechanical properties, a theoretical model of membrane bleb formation during micropipette aspiration was developed. Using this theoretical model it was shown that the predicted apparent equilibrium modulus is indeed dependent on the strength of the membrane-actin cortex adhesion. Thus the measured difference in the critical pressure (Δp_c) required for membrane detachment and bleb formation between hMSCs and differentiated cells (Fig. 5.2) causes the corresponding observed differences in the elastic moduli (Fig. 5.7). The model predicts a stronger dependence on Δp_c than is actually seen in the experimental data. However the model does not take into account phenomena that are observed in practice, such as the fact that blebs do not form along a straight line but deviate about the long axis of the pipette and that single nucleating blebs frequently have a radius that is smaller than the pipette radius. However, the simulation results corroborate the hypothesis that the membrane-cortex adhesion strength plays a key role in explaining the different

effective viscoelastic properties between blebbing and non-blebbing cells, and between hMSCs and differentiated cells.

The present study is the first to show that chondrogenic differentiation increases ERM expression leading to increased membrane-cortex adhesion which in turn influences cell mechanics by reducing bleb formation. ERM expression is also linked to bleb-based motility (Jiang, *et al.*, 2012). These studies suggest that the biomechanical changes in membrane-cortex interaction which occur during differentiation of hMSCs impact on cell mechanics, and may potentially influence other fundamental areas of cell behavior including migration and mechanotransduction.

5.4.2 Organisation of cortical actin during the differentiation

To examine the mechanism responsible for increased bond strength we used quantitative confocal microscopy to measure changes in actin organization and dynamics. We found that cortical actin in differentiated cells was more developed than in hMSCs, similar to that reported in previously (Titushkin and Cho, 2011). Differentiated cells in monolayer have exhibited denser and thicker stress fibers compared to undifferentiated hMSCs (Fig. 5.5). Furthermore, FRAP in live cells transfected with LifeAct-GFP, demonstrated that the differentiated cells have a longer half life recovery time indicative of a more stable actin cortex with slower turnover compared to hMSCs (Fig. 5.6). However, it is unclear how much this recovery time is related to actin dynamic. Previously it was demonstrated that LifeAct-GFP has a fast recovery, which might effect the direct measurements of actin dynamics (Riedl, *et al.*, 2008). On the other hand, recovery times for both undifferentiated hMSCs and differentiated cells are much higher than previously reported LifeAct-GFP, this suggests that recovery time estimated in the present study is also actin recovery. The slower turnover of differentiated cells could be due to greater density of F-actin organisation (Fig. 5.5), which leads to a greater number of connections between actin filaments resulting in slower dynamics. This difference in actin organisation and dynamics may have both a direct effect on cell mechanics by stabilising the cortex as well as an indirect effect by influencing the bond strength with the cell membrane. Actin disruption with cytochalasinD resulted reduction in viscoelastic properties (Appendix C) and reduction was seen higher for differentiated

cells. In addition the slower turnover rate of actin may be associated with greater expression of the ERM proteins, which link the membrane to the actin cortex.

CHAPTER 6
Chondrocyte mechanics – effect of culture and comparison with stem cell differentiation

6 CHONDROCYTE MECHANICS – EFFECT OF CULTURE AND COMPARISON WITH STEM CELL DIFFERENTIATION

6.1 Introduction

In previous chapters it was shown that changes in cell mechanical properties and membrane-actin cortex interaction occur during hMSCs differentiation down a chondrogenic lineage. However, little is known about how the mechanical properties of isolated articular chondrocytes change during dedifferentiation, which occurs with increasing passage in monolayer and is characterised by changes in actin organisation and increased expression of collage type I (Benya and Shaffer, 1982, Goessler, *et al.*, 2005). A previous study has indicated that chondrocytes exhibit an increase in equilibrium and instantaneous moduli following dedifferentiation (Darling, *et al.*, 2009). The present study therefore set out to test the hypothesis that dedifferentiation increases cell stiffness due to increased membrane-actin cortex adhesion and changes in actin organisation. Primary articular chondrocytes at passage 0 (P0) and passage 1 (P1) were subjected to micropipette aspiration in order to determine the cellular viscoelastic parameters. The membrane-actin cortex adhesion strength was also measured as described in chapter 5 and the same theoretical model implemented to predict the role of changes in membrane-actin cortex adhesion on cell mechanics. The expression of ezrin, radixin and moesin (ERM) were quantified along with actin organisation.

6.2 Methods

6.2.1 Cell culture

Primary articular chondrocytes were isolated from adult bovine full depth cartilage and suspended in DMEM with 16% FBS as described in sections 2.2.3 and 2.1.4. Cells were seeded in the culture plates and maintained in monolayer culture for 9 days. The cells were then detached from the culture plate surface with trypsin and resuspended in media as described in section 2.2.4. These cells are referred to as passage 1 (P1). Freshly isolated chondrocytes are termed passage 0 (P0) and were used as a control. Previous studies indicated that primary chondrocytes undergo dedifferentiation by passage 1 under these culture conditions (Darling, *et al.*, 2009).

6.2.2 Cell diameter measurements

Chondrocytes at P0 and P1 were suspended in imaging media. The chamber with cell suspension was mounted on the stage of a confocal microscope and brightfield images of fields of cells were captured using a x63 NA 1.4 oil immersion objective lens and pixel size of 0.46 μm. Cell diameter was estimated as described in section 2.6.1.

6.2.3 Micropipette aspiration

The micropipette aspiration system, as described in section 2.3.2, was used to determine the viscoelastic properties of single P0 and P1 chondrocytes. Micropipettes were prepared with an internal diameter of 5-6 μm as described in section 2.3.1. Both groups of cells were prepared in suspension in imaging media and placed in a chamber on the stage of confocal microscope. The tare pressure of 0.5 cmH$_2$O (0.049 kPa) was applied to hold the cell on the micropipette as described in section 2.4.1. The experiment was initiated by applying a step of 7.7 cmH$_2$O (0.76 kPa) negative pressure at a rate of 3.85 cmH$_2$O/s (0.38 kPa/s). The resulting cell aspiration into the micropipette was visualised for 180 seconds using brightfield microscopy with a x63/1.4 NA oil immersion objective. Images were recorded every 2 seconds with a pixel size of 0.27 μm. Cell aspirated length was measured from brightfield images as described in section 2.5.3 and plotted as a function of time. The equilibrium and instantaneous moduli and viscosity were determined using the theoretical SLS model as described in section 2.4.2.

In addition, the brightfield images were used to estimate the percentage of cells showing membrane-actin cortex detachment during micropipette aspiration. To estimate the critical pressure for membrane-actin cortex detachment, micropipette aspiration was repeated with cells subjected to a step negative pressure of 1.1 cmH_2O (0.11 kPa), 3.3 cmH_2O (0.32 kPa) or 5.5 cmH_2O (0.54 kPa) applied at a rate of 3.85 cmH_2O/s (0.38 kPa/s) and held for 180 seconds. The percentage of cells exhibiting blebbing behaviour at each pressure was observed from brightfield images.

The micropipette aspiration protocol was then modified to provide a more precise estimate of the critical pressure required for membrane-actin cortex detachment. For this approach individual cells were subjected to negative pressure in a series of seven increments of 1.5 cmH_2O (0.147 kPa) up to a maximum pressure of 10.5 cmH_2O (1.03 kPa). Two different protocols were adopted to examine the effect of pressure rate. For the slow rate protocol each increment was applied at a rate of 0.1 cmH_2O/s (0.01 kPa/s) with 15 seconds between increments generating an equivalent average pressure rate of 0.005 kPa/s as described in section 2.4.3. For the fast rate protocol negative pressure increments were applied at a rate of 3.85 cmH_2O/s (0.38 kPa/s) with 5 seconds between increments such that the average pressure rate was 0.024 kPa/s. The critical pressure required for membrane-actin cortex detachment was taken as the pressure at which a membrane bleb was initiated. Cells that did not bleb were recorded as having a detachment pressure greater than the maximum aspiration pressure and were included in subsequent non-parametric statistical analysis.

6.2.4 Membrane - actin cortex interaction model

A mathematical model with interpretation of membrane-actin cortex interaction was used to predict the equilibrium modulus of P0 and P1 chondrocytes. The model description is presented in chapter 5. The parameters used in this study are presented in table 6.1.

Table 6.1 : Values of parameters used to the membrane-actin cortex interaction model.

Parameter	Value	Cell type	Reference
Micropipette radius	2.65 µm	-	Present study
Cell radius	6.6 µm	Chondrocytes	Present study
Equilibrium aspirated length	9.2 µm	Chondrocytes	Present study
Membrane compressibility	0.8 mN/m	E. histolytica HM1-IMSS	(Brugues, *et al.*, 2010)
Membrane elastic constant	63 Pa/µm	Chondrocytes	Present study
Cortex elastic constant	86 Pa/µm	Chondrocytes	Present study
Friction coefficient	1500 Pa.s/ µm	Chondrocytes	Present study

6.2.5 Actin visualization and quantification

P0 and P1 chondrocytes were prepared in suspension and fixed with 4% PFA. Cells were stained with Alexa Fluor 555 phalloidin for F-actin visualisation. More details on fixing and staining cells can be found in section 2.7.2. Quantification of F-actin was based on measuring the fluorescence intensity of cortical actin as in previous studies (Chen, *et al.*, 2012). The mean fluorescence intensity was calculated within a beigel region of interest positioned over the cell cortex. More details of F-actin quantification can be found in section 5.2.3.

6.2.6 Western blots

Freshly isolated chondrocytes (P0) and chondrocytes cultured for 9 days (P1) were used for protein isolation. The procedure involved washing cells with chilled PBS and lysing in RIPA buffer. More details on protein isolation and quantification can be found in section 5.2.6. Cell lysates of 10 µg proteins mixed with Laemmeli buffer in ratio 3:1 and denatured by heating at 100°C for 5 minutes. Protein samples were loaded into a gel and transferred to membrane. Primary antibodies with dilutions 1:1000 for rabbit polyclonal anti-Ezrin/Radixin/Moesin (ERM) and rabbit monoclonal anti-phosphorylated Ezrin/Radixin/Moesin (pERM) (Cell Signaling Technology, Leiden, Netherlands) and 1:5000 for mouse monoclonal anti-β-tubulin (Sigma Aldrich) were incubated with shaking overnight at 4°C. Membranes were washed with TBS+0.1% Tween and incubated for 1 hour with secondary antibodies (1:10,000 dilutions for 680RD Goat anti-Mouse IgG and 800CW Donkey anti-Rabbit

IgG). Membranes were washed again in TBS+0.1% Tween and imaged using an Odyssey infrared Imaging system (LI-COR).

6.2.7 Statistics

Cell diameter, viscoelastic properties, critical pressure required for membrane-actin cortex detachment and F-actin fluorescence intensity were assumed to be non-parametrically distributed and values are therefore presented as frequency histograms and/or population scatters with bars indicating median values. The Mann-Whitney U test was used to determine significant differences between cell groups.

ERM protein quantity was assumed to be normally distributed and values of mean and standard deviation are presented in the plots. The Student's t-test was used to estimate the significant differences between cell groups. In both, non-parametric and parametric analyses, the level of significance is presented as * $p<0.05$, ** $p<0.01$ and *** $p<0.001$, unless otherwise stated.

6.3 Results

6.3.1 Cell size changes during chondrocyte dedifferentiation

The median values of cell diameter for P0 and P1 chondrocytes before aspiration experiments were found to be 12.6 μm and 13.9 μm respectively. The cell diameter histograms show that the cell size of P1 chondrocytes has a wider spread compared to P0 chondrocytes (Fig. 6.1). Statistical analysis indicated that cell diameter was significantly different between groups ($p<0.001$).
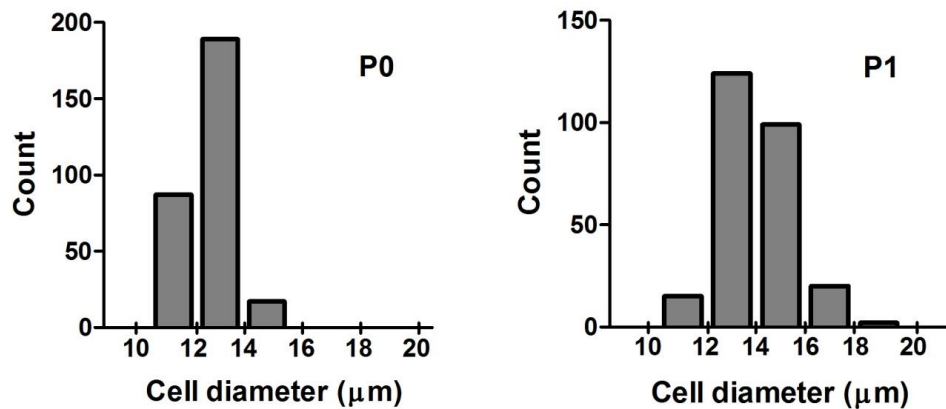
Figure 6.1: The cell size distribution of P0 and P1 chondrocytes in suspension. Number of cells n=260 (P0) and 300 (P1).

6.3.2 Dedifferentiation increases chondrocyte modulus

In order to understand the influences of chondrocyte dedifferentiation on the cell viscoelastic properties, micropipette aspiration was performed on P0 and P1 chondrocytes. The number of cells tested for each experiment is indicated in table 6.2. For both P0 and P1 chondrocyte groups 84% of cells were successfully aspirated. However, the percentage of cells that fitted the analytical SLS model was slightly lower at P1 compared to P0, with values of 66% and 75% respectively.

Table 6.2: Number of chondrocytes used for aspiration experiments.

Cell type	Total No. of cells	No. of successful aspirations	No. used for model $R^2 > 0.95$
Chondrocytes (P0)	88 (100%)	74 (84%)	66 (75%)
Chondrocytes (P1)	83 (100%)	70 (84%)	55 (66%)

Freshly isolated chondrocytes (P0) and cells at passage 1 (P1) were subjected to a step negative pressure of 0.76 kPa applied over 2 seconds (0.38 kPa/s) which was maintained over 180 seconds. Brightfield images of a representative cell at each condition are presented in figure 6.2 A. The aspirated length into the micropipette was plotted as function of time. Cells exhibited three different modes of deformation in response to applied pressure based on the change in aspirated length from 120 to

180 seconds. These modes were classified as increase, equilibrate and decrease (Fig. 6.2 B). Cells that exhibited increase in aspirated length higher than 5% were named increase. Aspirated length changes below than -5% represented the decrease mode. Cells that exhibited changes of aspirated length which were between these two conditions are classified as equilibrate mode. At both P0 and P1 the majority of cells (>80%) reached equilibrium with 180 seconds (Fig. 6.2 C). However, there is a statistically significant difference in the percentage of cells showing each response, such that at P1 there is a reduction in the percentage of cells showing increase response and greater percentage of cells showing an equilibrium response. Furthermore, at P1 about 4% of cells exhibited a decrease response which was not observed at P0.
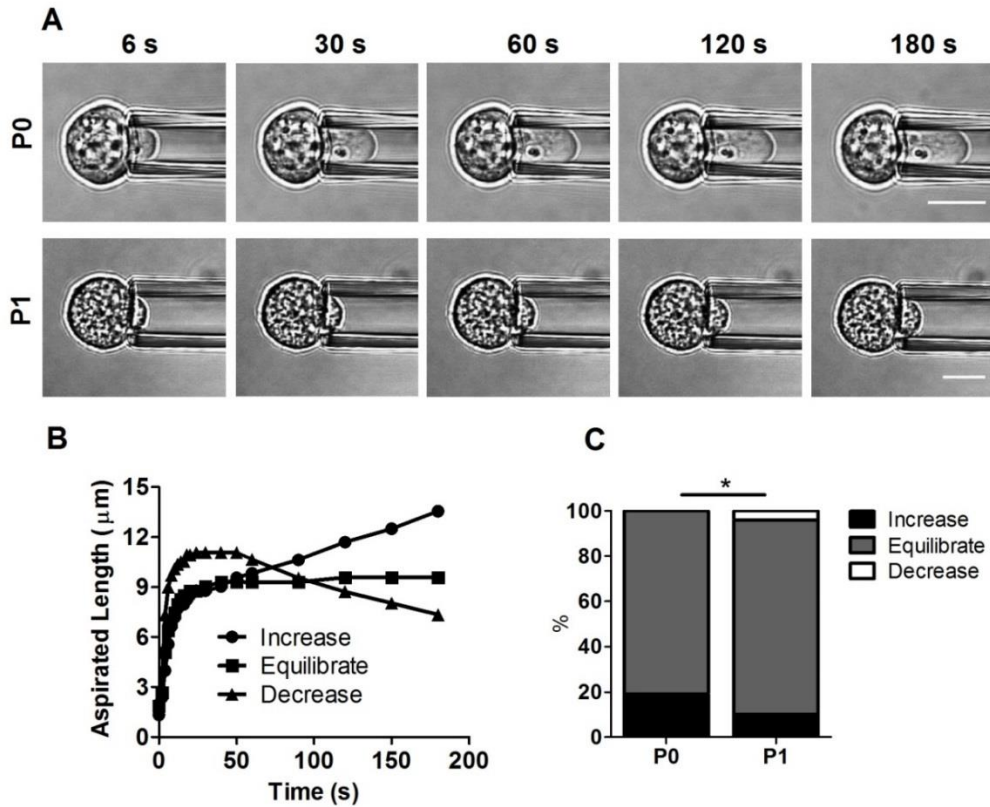
Figure 6.2: Cell behaviour into the micropipette in response to chondrocyte dedifferentiation. (A) Brightfield images of representative P0 and P1 chondrocytes aspirated into the micropipette at 6, 30, 60, 120 and 180 second time points. Scale bars 10 μm. (B) Representative temporal changes in aspirated length for the three different types of cell behaviour inside the micropipette based on the change in aspiration length from 120 to 180 seconds after the application of aspiration pressure. (C) There were significant differences in the percentages of P0 and P1 chondrocytes exhibiting each type of behaviour. (Chi-squared test, *$p<0.05$).

The changes of aspirated length with time for P0 and P1 chondrocytes are shown in figure 6.3 A. Both cell groups exhibited viscoelastic behaviour in response to a step negative pressure. The majority of cells demonstrated a sudden increase in aspirated length into the micropipette followed by equilibration within 180 seconds. However, P0 chondrocytes take a longer time to equilibrate compared to P1 cells as shown by the higher percentage of cells for which aspirated length is still increasing at 120-180 seconds. Similarly the aspirated length at 180 seconds is significantly longer in P0 cells compared to P1, suggesting that passage increases cell stiffness (Fig. 6.3 B). Indeed this was confirmed when the data was fitted to the SLS model such that chondrocytes at P1 had a greater equilibrium modulus with a median value of 0.40

kPa compared to 0.16 kPa at P0, the difference being statistically significant (Fig. 6.3 C). There were no significant differences in the instantaneous modulus or the viscosity between P0 and P1 (Fig. 6.3 D and E).
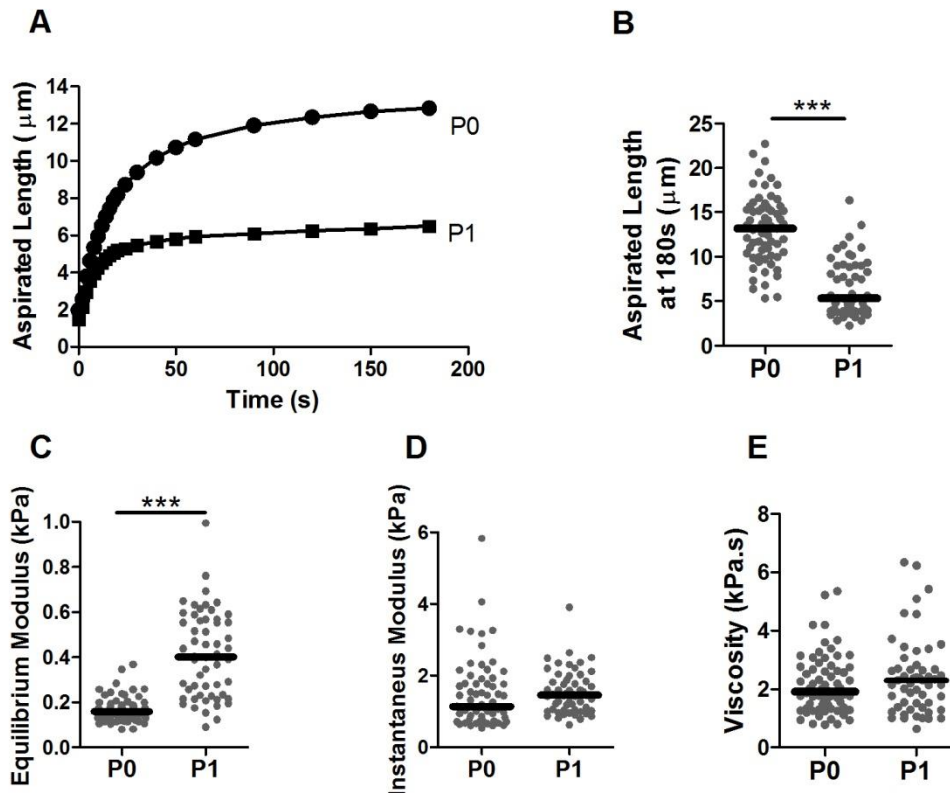
Figure 6.3: Chondrocyte dedifferentiation is associated with changes in viscoelastic properties. (A) Median plots of aspirated length verse time for P0 and P1 chondrocytes. (B) Aspirated length at 180 seconds, (C) equilibrium modulus, (D) instantaneous modulus and (E) viscosity of P0 and P1 cells. The data is presented as a population with median value indicated by bar. Mann-Whitney U test, *** $p < 0.001$.

6.3.3 Dedifferentiation reduces mechanically induced bleb formation

In order to better understand the changes in viscoelastic properties following chondrocyte passage and associated dedifferentiation, the formation of membrane blebs during aspiration was studied. At 0.76 kPa, a subpopulation of cells exhibited the formation of one or more membrane blebs at the leading edge of the aspirated part of the cell within the micropipette (Fig. 6.4 A). This phenomenon was visible

from brighfield images such that blebs appeared relatively transparent and extended rapidly within the micropipette. Where, multi blebbing behaviour was observed, the first bleb was followed by a subsequent bleb initiating from the leading edge of the first bleb. In some cases as many as 3-5 separate blebs occurred in quick succession over 180 seconds. More than 80% of P0 chondrocytes demonstrated blebbing compared to 42% at P1 (Fig. 6.4 B). Furthermore, a change in the nature of blebbing was observed with all blebbing cells at P0 exhibiting only one bleb each compared to cells at P1 where 37% of cells demonstrated multi blebbing behaviour. The difference in blebbing behaviour between P0 and P1 chondrocytes was statistically significant ($p<0.001$).
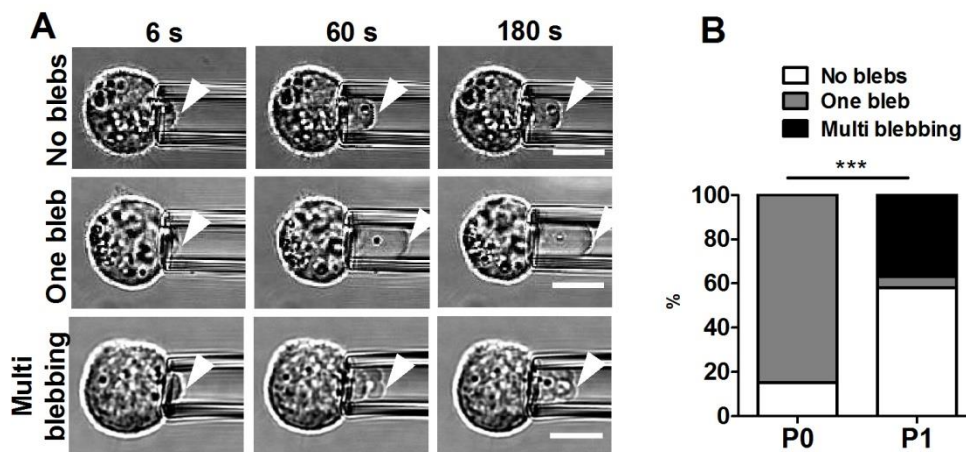
Figure 6.4: Chondrocyte dedifferentiation regulates bleb formation during micropipette aspiration. (A) Examples of brightfield images of cells at time points 6, 60 and 180 seconds, showing different bleb behaviour inside the pipette. Cells with no blebs move smoothly inside the pipette without membrane protrusions. Cells with one bleb show membrane detachment and a transparent bleb which elongates rapidly. Cells with multi blebbing move inside the micropipette by forming successive membrane blebs. White arrow heads indicate the leading edge of the cell. Scale bars represent 10 µm. (B) Percentages of cells exhibiting different modes of bleb formation. P0 and P1 chondrocytes show statistically significant differences (Chi-square test, *** $p<0.001$).

6.3.4 Dedifferentiation strengthens membrane-actin cortex adhesion

Micropipette aspiration was used to determine the effect of dedifferentiation on the membrane-actin cortex adhesion strength. Chondrocytes at P0 and P1 were subjected to an aspiration pressure of either 0.11, 0.32, 0.54 or 0.76 kPa applied rapidly at a rate of 0.38 kPa/s (Fig. 6.5 A). Cells were imaged for the subsequent 180 seconds and bleb initiation and growth was observed from brighfield images (Fig. 6.5 B). At the lowest aspiration pressure of 0.11 kPa, only 3% of cells showed bleb formation with no difference between P0 and P1 cells (Fig. 6.5 C). With increased aspirated pressure there was an increase in the percentage of cells exhibiting blebs. However, cells at P0 had a greater tendency to form blebs compared to cells at P1, the difference being statistically significant at 0.32, 0.54 and 0.76 kPa. Interestingly this increased percentage of blebbing cells was due to an additional subpopulation of approximately 30% of P0 cells for which bleb initiation occurred between 0.11 and 0.32 kPa (Fig 6.5 D). The median values for critical pressures for membrane-actin cortex detachment are in the region of 0.32 to 0.76 kPa for both P0 and P1 cells under these aspiration conditions.
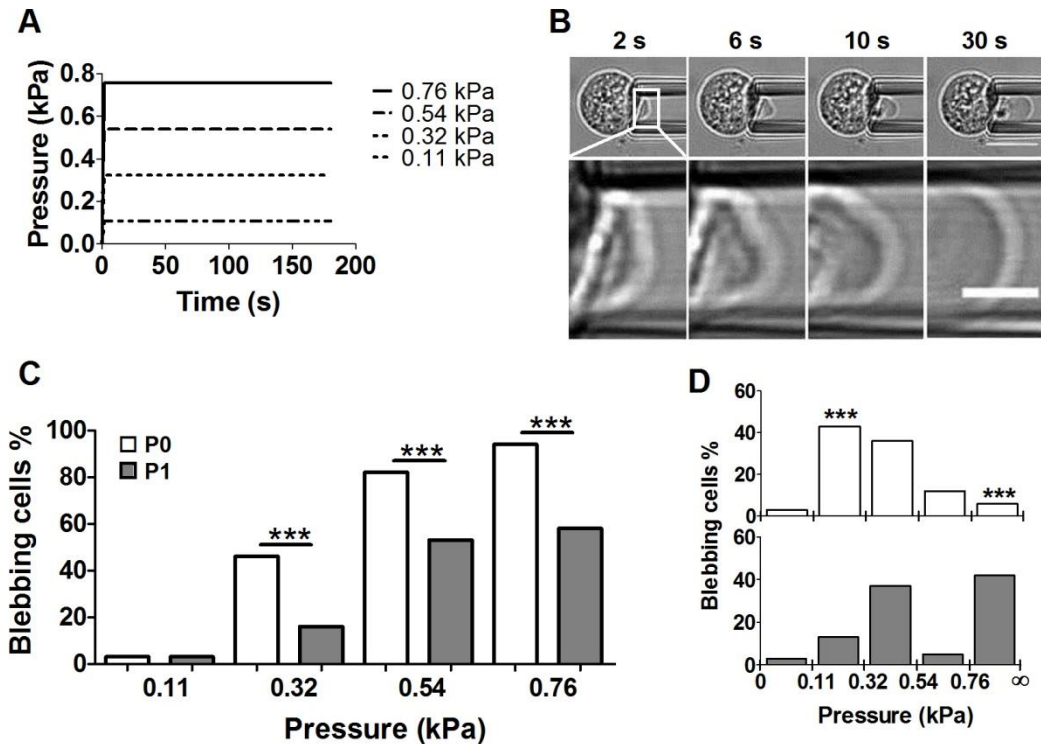
Figure 6.5: Chondrocyte dedifferentiation strengthens membrane-actin cortex adhesion thereby reducing blebability. (A) Plot showing the 4 separate aspiration protocols with different magnitudes of pressure all applied at 0.38 kPa/s. (B) Representative brightfield images of a single cell showing the membrane detachment from the actin cortex at 6 seconds after the application of aspiration pressure, scale bar, 10 μm.. Lower images show a magnified view of the leading edge inside the micropipette. Scale bars represent 5 μm. (C) Percentage of both P0 and P1 chondrocytes demonstrating bleb formation in response to applied pressures (Chi-squared test, *** $p < 0.001$). Data is presented from two independent experiments. (D) Corresponding percentage of cells for which bleb initiation occurred between each pressure increment. P0 cells show significantly greater bleb formation at pressures between 0.11 and 0.32 kPa compared to P1 (Chi-squared test, *** $p < 0.001$).

However, to provide a more precise estimate of the critical pressure for membrane-cortex detachment and bleb initiation, the micropipette aspiration protocol was modified as follows. Individual chondrocytes at P0 and P1 were subjected to aspiration pressure applied as a series of seven increments of approximately 0.147 kPa with different overall pressure rates of 0.024 kPa/s and 0.005 kPa/s (Fig. 6.6 A). When the pressure was applied slowly with overall rate of 0.005 kPa/s (0.01 kPa/s and 15 seconds between increments) there was no significant difference between P0 and P1 in terms of the critical pressure at which membrane-actin cortex detachment

occurred. By contrast, when pressure was applied at a faster overall rate of 0.024 kPa/s (0.38 kPa/s and 5 seconds between increments), P1 chondrocytes required a higher critical pressure with median value of 0.74 kPa compared to 0.59 kPa for P0 cells, the difference being statistically significant (Fig. 6.6 B). Comparing the two pressure rates, P0 cells required significantly higher critical pressure using the slower overall rate of 0.024 kPa/s, but this was not the case for P1 cells. It should be noted that the faster rate of aspiration more closely corresponds to the protocol used to estimate cell viscoelastic properties (Fig. 6.3).
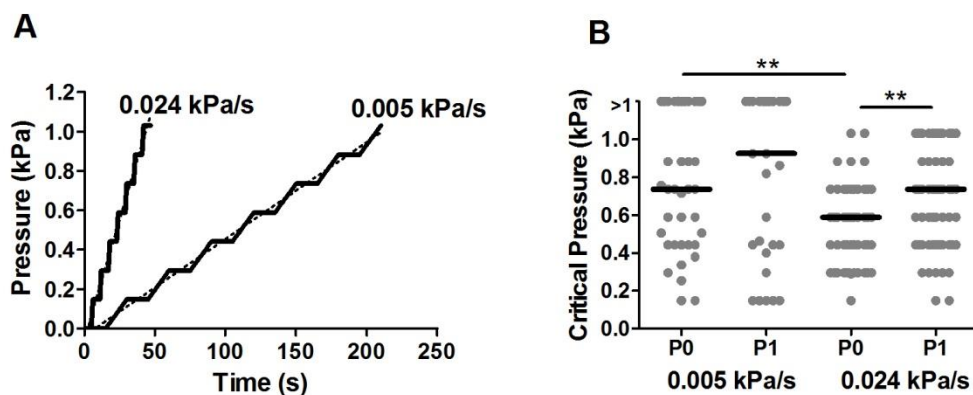
Figure 6.6: Membrane-actin cortex detachment pressure is associated with chondrocyte dedifferentiation. (A) Plot presenting the two protocols for application of pressure increments with overall pressure rates of 0.024 kPa/s and 0.005 kPa/s. Dotted lines represent overall rate of pressure application. (B) Scatter plot showing the critical pressure required for membrane detachment for P0 and P1 cells using overall pressure rates of 0.005 kPa/s and 0.024 kPa/s. Cells that did not exhibit bleb formation during testing are classified as having a detachment pressure greater than the maximum pressure of 1.03 kPa. (Mann-Whitney U test, ** $p < 0.01$).

6.3.5 Computational modelling of membrane blebbing and cell mechanics

To examine whether the changes in membrane-actin cortex adhesion and blebability are responsible for changes in viscoelastic properties of chondrocytes undergoing dedifferentiation, a model of bleb formation was developed. Values of $\Delta p_c / \Delta p$ represent the critical pressure for bleb initiation into the micropipette (Δp_c) relative to the appied pressure used to measure cell moduli (Δp). When $\Delta p_c / \Delta p \geq 1.0$ no bleb formation occurs as the critical pressure required for membrane-actin cortex

detachment is always higher than applied pressure. The effective elastic constant G_{eff} can be calculated from the simulation for no blebbing, single bleb or multi blebbing data, and is proportional to the effective equilibrium modulus (equation 6.6). Increasing the critical pressure required for membrane-actin cortex detachment causes an increase in the effective equilibrium modulus (Fig. 6.7 A). Experimental data shows that the critical pressures for membrane-actin cortex detachment using fast rate protocol for P0 and P1 cells were 0.59 kPa and 0.74 kPa respectively. Those correspond to values for $\Delta p_c/\Delta p$ of 0.78 for P0 and 0.97 for P1 chondrocytes. Thus the equilibrium moduli predicted by this bleb based theoretical model are presented in figure 6.7 B alongside the experimental values calculated using the SLS model. The bleb based model predicts an increase in equilibrium modulus from P0 to P1 based on the increased critical detachment pressure Δp_c measured experimentally. Indeed the bleb based model predicts an equilibrium modulus for P0 cells of 0.15 kPa which closely matches the experimental equilibrium modulus of 0.17 kPa. However, the bleb based model underestimated the equilibrium modulus for P1 chondrocytes. This suggests that other factors in addition to increased membrane-actin cortex adhesion contribute to the increase in cell modulus observed at P1.
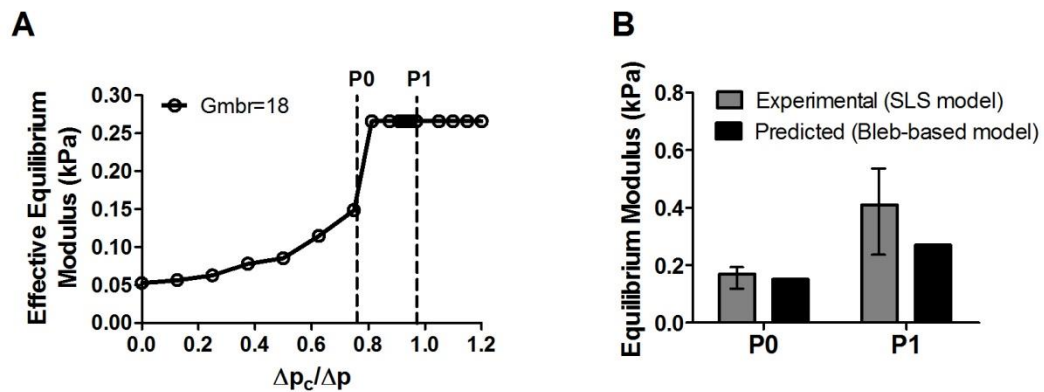
Figure 6.7: Theoretical model of cell membrane-actin cortex rupture. (A) The effective equilibrium elastic modulus plotted as a function of $\Delta p_c/\Delta p$, for $G_{mbr} = 18$ Pa/μm. (C) Plots of experimental and theoretically estimated equilibrium moduli. Error bars represent quartiles.

6.3.6 Dedifferentiation regulates F-actin organisation and ERM protein expression

Cell moduli and membrane-actin cortex interaction is believed to be associated with organisation of cortical actin (Titushkin and Cho, 2011). Therefore studies were conducted to test whether passage in monolayer influences cortical F-actin. P0 and P1 chondrocytes were fixed, labelled with AlexaFluor555-phalloidin and imaged using confocal microscopy. Fluorescent images of cortical actin of representative P0 and P1 chondrocytes are presented in figure 6.8 A. At P1, chondrocytes exhibited a thicker more brightly stained actin cortex compared to P0 cells. The quantitative analysis of fluorescent images demonstrated that the fluorescence intensity of the cortical F-actin significantly increased from P0 to P1 (Fig. 6.8 B).
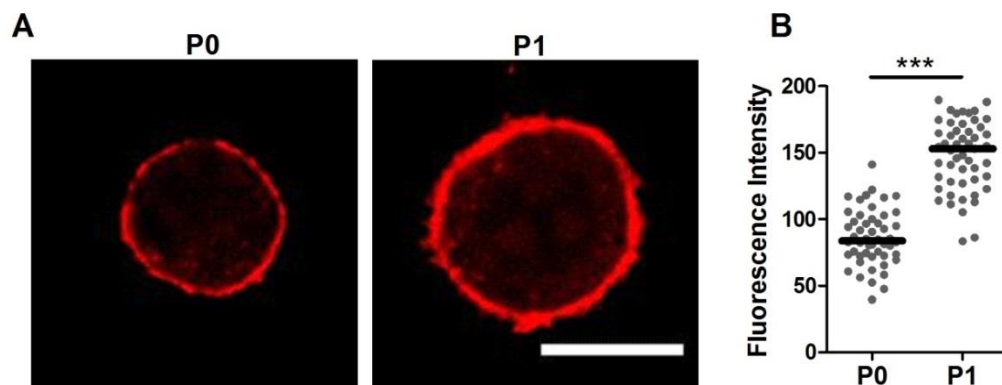
Figure 6.8: Chondrocyte dedifferentiation increases cortical F-actin organisation. (A) Representative confocal images showing increased F-actin staining in chondrocytes in suspension at P1 compared to P0. F-actin was labelled with Alexa Fluor 555-phalloidin (red). Scale bar represents 10 μm. (B) Scatter plot showing increased cortical actin staining intensity for P1 cells compared to P0 cells. (Mann-Whitney U test, *** $p < 0.001$).

For further investigation, the level of membrane-actin cortex linker proteins ezrin, radixin and moesin (ERM), were measured using western blot analysis for P0 and P1 chondrocytes. The quantitative analyses of total ERM and phosphorylated ERM proteins show that both proteins significantly increased at P1 compared to P0 (Fig. 6.9 A and B).
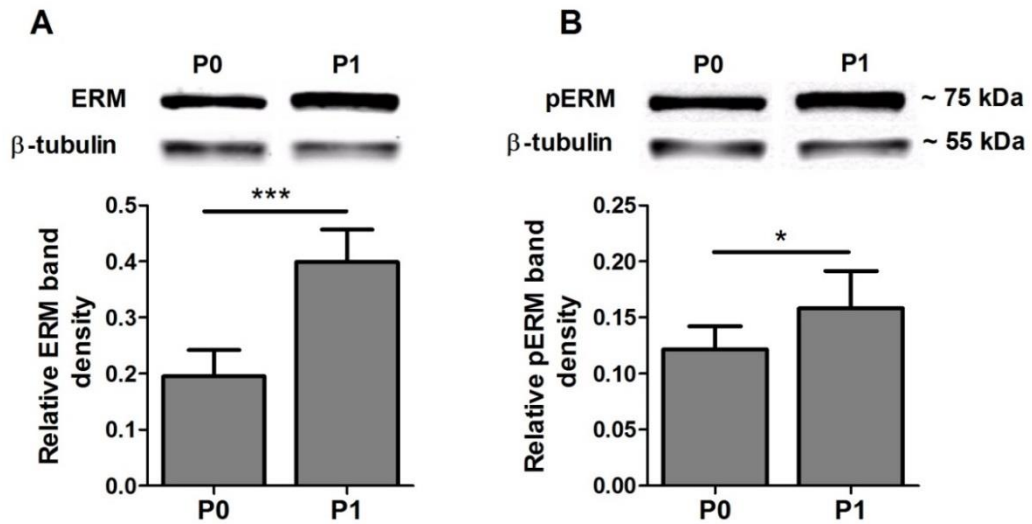
Figure 6.9: Chondrocyte passage increases ERM protein expression. Western blot analysis showing increased (A) total ERM protein and (B) phosphorylated ERM protein levels in P0 and P1 chondrocytes. Data is normalised to β-tubulin. Error bars indicate standard deviation (t-test * $p<0.05$ and *** $p<0.001$).

6.4 Discussion

6.4.1 Cell size changes during passage and dedifferentiation

It is known that chondrocyte shape, size and density vary between cartilage zones (Poole, 1997, Siczkowski and Watt, 1990). The superficial zone, furthest away from the bone, has flattened and ellipsoidal-shaped chondrocytes. The middle zone consists of rounded single cells randomly oriented. In the deep zone, chondrocytes are larger than in the other zones and usually grouped in vertical columns. Chondrocytes cultured in monolayer, lose their chondrogenic phenotype and develop a fibroblast-like phenotype (Benya and Shaffer, 1982). During dedifferentiation changes occur in gene and protein synthesis; for example, freshly isolated chondrocytes produce more collagen type II, as present in situ in articular cartilage. However, for chondrocytes cultured in monolayer there is a reduction in collagen type II synthesis and an increase in collagen type I (Schnabel, *et al.*, 2002).

The findings of this study demonstrated that cell size changes occur with chondrocyte passage in monolayer and associated dedifferentiation. P1 chondrocytes were significantly larger than chondrocytes at P0 (Fig. 6.1). Changes in cell size are likely due to increased metabolic activity and an increase in the volume of associated

cytoplasmic organelles such as mitochondria and endoplasmic reticulum. Furthermore, P1 chondrocytes exhibited a wider variability in cell size compared to P0 cells. This may be due to differences in the degree of dedifferentiation with only a subset of cells dedifferentiating by day 9.

6.4.2 Chondrocyte passage regulates cell viscoelastic properties

The finding of this study indicates that viscoelastic properties of chondrocytes changed following dedifferentiation in monolayer. These changes appear rapidly within the first passage as reported by others (Darling, *et al.*, 2009). Both cell types (P0 and P1) exhibited viscoelastic solid–like behaviour such that the aspirated length suddenly increased and reached equilibrium state in agreement with other studies on chondrocytes (Jones, *et al.*, 1999, Trickey, *et al.*, 2000) and other cell types (Sato, *et al.*, 1990, Tan, *et al.*, 2008b). However a small subpopulation of cells exhibited different modes such that the aspirated length did not reach equilibrium within 180 seconds (Fig. 6.2). Similar cell behaviour during micropipette aspiration was demonstrated with undifferentiated hMSCs and hMSCs differentiated to the chondrogenic lineage (chapter 3). Using the SLS model, the equilibrium modulus increased from 0.16 kPa at P0 to 0.40 kPa at P1, which is in close agreement with previous studies (Darling, *et al.*, 2009). The instantaneous modulus and viscosity did not change with passage which could be due to the applied pressure rate being too fast to enable actin remodelling.

The mechanism regulating changes in cell mechanical properties with passage is not known but may be related to the observed alterations in the actin cytoskeleton which is known to influence cell mechanical properties.

6.4.3 Dedifferentiation reduces cell blebbing by controlling membrane-actin cortex interaction

It is known that ERM liker proteins are responsible for membrane-actin cortex interaction and play a role in cell mechanical properties (Titushkin, I. and Cho, M., 2009, Titushkin, Igor A and Cho, Michael R, 2009). This study demonstrated that P1 chondrocytes exhibited an increase in expression of ERM linker proteins compared to P0, which suggests the membrane-actin cortex interaction is stronger in P1 chondrocytes. Furthermore, the study showed that chondrocyte cultures in monolayer to P1 had reduced susceptibility to bleb formation during micropipette aspiration compared to P0. Examination of membrane-actin cortex interaction indicated that

this was due to a subpopulation of approximately 30% of P0 cells for which membrane-actin cortex detachment occurred at a pressure between 0.11 and 0.32 kPa (Fig. 6.5 D). At P1 there was a significant reduction in the percentage of cells which blebbed at a pressure between 0.11 and 0.32 kPa and a corresponding increase in the percentage of cells that did not bleb at the maximum pressure of 0.76 kPa. Although it is not clear if the 30% subpopulation of cells that bleb between 0.11 and 0.32 kPa at P0 give rise to the 30% subpopulation of P1 cells that do not bleb at all below 0.76 kPa. In order to more precisely define the detachment pressure it was necessary to apply the aspiration pressure more gradually. The critical pressure estimated from the protocol with the applied pressure rate of 0.024 kPa/s was significantly different between P0 and P1 cells with median values of 0.59 kPa and 0.74 kPa respectively. However, this was not the case when the pressure was applied with a slower rate of 0.005 kPa. Furthermore, bleb formation was more susceptible in P0 cells at all pressure rates (Fig. 6.10).
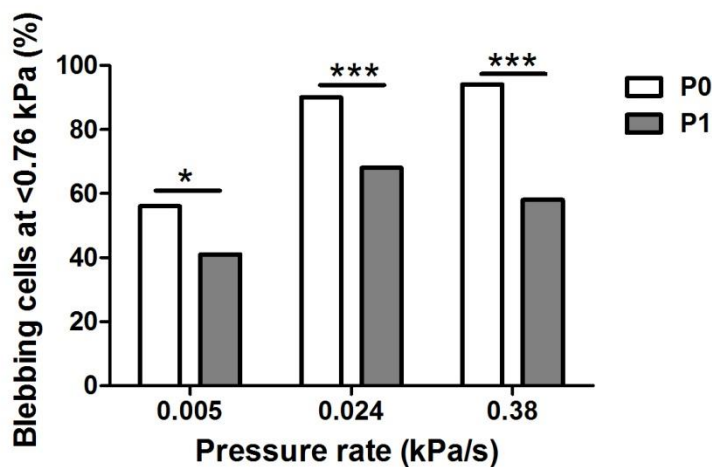
Figure 6.10: Chondrogenic dedifferentiation in passage reduced cell blebbing. Percentage of P0 and P1 cells showing cell blebbing in response to pressure rates. (Chi-squared test, * $p < 0.05$, *** $p < 0.001$).

In conclusion dedifferentiation reduces membrane-actin cortex adhesion associated with increased expression of ERM linker proteins. This causes an increase in equilibrium modulus by reducing the percentage of cells that bleb during micropipette aspiration. In addition the theoretical model of bleb formation indicated

that equilibrium modulus can be predicted for P0 cells, but not for P1 cells. This suggests that increased membrane-actin cortex adhesion is not the only factor causing the increased cell modulus. The increased actin cortex organisation observed in P1 chondrocytes may also directly increase the equilibrium modulus as well as potential modulation of membrane-actin cortex adhesion.

CHAPTER 7
General discussion

7   CHAPTER. GENERAL DISCUSSION

7. GENERAL DISCUSSION

7.1. Introduction

The overall objective of this thesis was to investigate the role of membrane-actin cortex interaction regulating cell viscoelastic properties during hMSC differentiation down a chondrogenic lineage. This was achieved by measuring the critical pressure required for membrane-actin cortex detachment by using a micropipette aspiration system. The studies presented in this thesis have demonstrated that membrane-actin cortex interaction is associated with cell mechanical properties which are regulated by cell blebbing, actin cortex organisation and ERM linker proteins during chondrogenic differentiation of hMSCs.

The first pilot study (Chapter 2) demonstrated that viscoelastic properties of undifferentiated hMSCs did not correlate with passage number. However, cells in later passages showed changes in cell morphology. In Chapter 3 it is demonstrated that biochemical induction with growth factors can be successfully used for hMSC differentiation to the chondrogenic lineage. This resulted in increased collagen type II expression in the matrix of differentiated cells. Changes in viscoelastic properties were associated with chondrogenic differentiation, which increased equilibrium and instantaneous moduli and reduced viscosity. In addition, mechanically and osmotically induced bleb formation was reduced in differentiated cells (Chapter 4). The rate of actin remodelling within an aspirated bleb observed using LifeAct-GFP was altered with differentiation, which resulted the reduction in actin remodelling. Additionally, pilot study II demonstrated that LifeAct-GFP had no effect on actin dynamics and cell mechanical properties (Chapter 2).

It was demonstrated that hMSCs differentiated to the chondrogenic lineage require higher pressure for membrane-actin cortex detachment compared to undifferentiated hMSCs (Chapter 5). This was associated with increased F-actin organisation and expression of ERM linker proteins in differentiated cells. It was further demonstrated that over expression of ezrin in undifferentiated hMSCs results in greater membrane-actin cortex interaction.

Finally, the effect of chondrocyte dedifferentiation on membrane-actin cortex interaction was investigated. It was demonstrated that mechanical properties and

susceptibility of bleb formation was associated with chondrocyte dedifferentiation. This resulted in changes in actin cortex organisation and increased expression of ERM linker proteins, which led to an increase in membrane-actin interaction. Membrane-actin cortex interaction can be used as mechanical marker to predict cell mechanical properties and changes in actin organisation during processes such cell differentiation, dedifferentiation and of cells in pathological conditions.

7.2. Choice of cell culture system

7.2.1. Stem cells

With an aging population, the demands for tissue engineering and regenerative medicine have increased in recent years. Due to limited therapeutic options and a lack of donors, stem cells have been widely used as alternative sources. Stem cells have a capacity for self renewal and the potential to differentiate toward specific cell types (Caplan and Bruder, 2001). Both adult and embryonic stem cells can be used for tissue engineering and regenerative medicine. Embryonic stem cells are more versatile in terms of proliferation and differentiation but are restricted due to ethical regulations. Adult stem cells have advantages over embryonic stem cells in terms of cell source as they can be easily obtained from patients and isolation methods are more robust. In addition the protocols for adult stem cell proliferation and differentiation are well established, but limitations exist in protocols for treatment of embryonic stem cells. According to the requirements and applications for this project, commercially available hMSCs isolated from bone marrow aspirates were chosen.

7.2.2. Chondrogenic differentiation

Chondral injuries or degenerative diseases such osteoarthritis are the most common causes of cartilage damage (Falah, *et al.*, 2010). Available treatments are tissue transplantation from autologous sources or cell based therapies. Chondrocytes can be isolated from the patient, expanded in vitro and injected into the defect site, or stem cells can be proliferated and differentiated in vitro prior to injection into the defect (Mobasheri, *et al.*, 2014, Tuan, *et al.*, 2003). In this study hMSCs were chemically induced to undergo chondrogenic differentiation using TGF-β3 as in numerous previous studies (Thorpe, *et al.*, 2010, Yourek, *et al.*, 2007).

7.2.3. Bovine metacarpal articular chondrocytes

As mentioned above isolated articular chondrocytes can be expanded in vitro and used for transplantation. While animal models cannot be directly used for human applications, they are critical for testing techniques and applications prior to clinical trials. Articular chondrocytes, isolated from the proximal surface of the metacarpal-interphalangeal joint of various donors such as bovine, rabbit, canine or human, were successfully used by other researchers in a variety of experiments from studies of mechanotransduction (Bougault, *et al.*, 2012) to cell mechanical properties (Chen, *et al.*, 2001, Guilak, 1995, Knight, *et al.*, 2002, Trickey, *et al.*, 2000). In this study, bovine articular chondrocytes were chosen according to well established protocols and availability within the host laboratory. The chondrocytes were isolated from the full depth of cartilage which includes cells from superficial and middle/deep zones.

7.2.4. Population heterogeneity
hMSCs

hMSCs represent a heterogeneous population and can be isolated from many different human tissues. This heterogeneity may lead to differences in biological functions and structure within the same population. Due to cellular diversity, surface markers are used to characterise hMSCs within a mixed population of isolated cells. The minimal criteria for hMSCs were established by the International Society for Cellular Therapy (ISCT) and include the capacity to adhere to tissue culture plastic, differentiation at least to chondrogenic, osteogenic and adipogenic lineages and expression of specific surface markers, such CD73, CD90 and CD105 (Dominici, *et al.*, 2006). In addition other surface markers such as endothelial CD31, monocytic CD14, lymphocyte CD45 and hematopoietic CD34 should be absent (Cao, *et al.*, 2005).

The commercially obtained hMSCs used in these studies were characterised by the distributer for surface marker profile and adhered to that outlined above. In addition, the same cell populations were shown to be capable of differentiation to chondrogenic, osteogenic and adipogenic lineages (other studies) in our laboratory. In future studies homogenous populations of stem cells can be obtained by using a flow cytometer. However, this method is expensive and poorly developed for hMSCs due to the lack of specific surface markers as they can also exist on other cell types (Docheva, *et al.*, 2008).

Differentiated hMSCs

The population of hMSCs induced to the chondrogenic lineage is likely a mixture of differentiated and undifferentiated cells. The extracellular matrix molecules which represent chondrogenic differentiation include proteoglycan, aggrecan and collagen type II. Staining with Alcian blue, aggrecan can be used as an indicator of chondrogenic differentiation. Also collagen type II can be determined using immunohistochemistry (Thorpe, *et al.*, 2010). However, the recognition of single differentiated cells is still limited due to the lack of suitable surface markers for live cell populations.

Chondrocytes (P0 and P1)

The chondrocytes isolated from full depth articular cartilage tissue represent a heterogeneous population of cells from different zones. The shape and morphology of chondrocytes changes through the depth of articular cartilage. Chondrocytes in the superficial zone are more oblate ellipsoids and chondrocytes in the middle /deep zone have a spherical shape (Youn, *et al.*, 2006). It has been reported that cell size increases with zone depth and that mechanical properties decrease; cells appear to be softer (Darling, *et al.*, 2009).

It might be expected that chondrocytes at P1 will have the same heterogeneity as at P0. However, it was previously reported that chondrocytes from cartilage middle/deep zone attach and spread and ultimately proliferate more rapidly than those from superficial zone (Siczkowski and Watt, 1990). Thus the heterogeneity at P1 may differ to that at P0. Hence, differences in mechanical properties of the cell populations at P0 and P1 may indicate differences in the relative percentages of surface and deep zone cells.

7.3. Micropipette aspiration

7.3.1. Choice of micropipette aspiration

The micropipette aspiration technique in combination with various theoretical models has been used to determine the viscoelastic properties of multiple types of mammalian cells and the influence of disease conditions (Jones, *et al.*, 1999, Tan, *et al.*, 2008a, Trickey, *et al.*, 2000, Yu, *et al.*, 2010). In the present study, the micropipette aspiration technique was chosen due to its availability in the host lab and its suitability for estimation of the mechanical properties of individual cells

including stem cells with simultaneous confocal visualisation of actin cytoskeleton structure and dynamics. Moreover, new protocols were developed enabling micropipette aspiration to be used to measure the membrane-actin cortex adhesion strength.

7.3.2. Choice of SLS model

The SLS theoretical model has been widely used in many micropipette aspiration studies on hMSCs (Tan, *et al.*, 2008a) and other cell types (Sato, *et al.*, 1990, Trickey, *et al.*, 2000). This model works under the assumption that a negative pressure is applied instantaneously. In order to account for the finite rate of pressure application, the Boltzmann standard linear solid (BSLS) model was derived (Merryman, *et al.*, 2009). This model accounts for the creep behaviour that occurs during the application of the aspiration pressure. Previous computational studies of micropipette aspiration demonstrated that creep and viscous effects are negligible if a pressure of 0.5 kPa is applied in under 2.5 seconds. This is equivalent to a minimum rate of 0.2 kPa /s. In the majority of work described in this thesis a pressure of 0.76 kPa was applied in 2 seconds using a peristaltic pump system, which resulted in a rate of 0.38 kPa/s. The pressure rate is above the minimum required by the SLS model therefore justifying the use of this model in these studies.

7.3.3. Choice of R^2 exclusion threshold

Cell viscoelastic properties determined by micropipette aspiration are based on prediction of the SLS theoretical model. The aspirated length measured at different time points is fitted to the theoretical model. The quality of this fit is given by an R^2 value enabling cells for which the R^2 value is below a threshold to be rejected from analysis. However it is unclear what this threshold should be. The present study demonstrated that viscoelastic properties such as the equilibrium and instantaneous moduli of hMSCs did not change in response to R^2 values (Fig. 7.1 A and B). The same trend with no changes in equilibrium and instantaneous moduli was found for hMSCs differentiated to the chondrogenic lineage (Fig. 7.1 C and D). This indicates that viscoelastic properties of cells with $R^2 > 0.85$ can be used. In Chapter 3 it was demonstrated that the SLS model fitted least to cells which exhibited an increasing or a decreasing mode. This suggests that the ''bad'' fit could be due to the assumption of the SLS model that the cell is a homogenous material; which is false as the cell contains organelles and actin cortex underneath the membrane. The breakage of the

membrane-actin cortex bond results in bleb formation and changes in aspirated length.
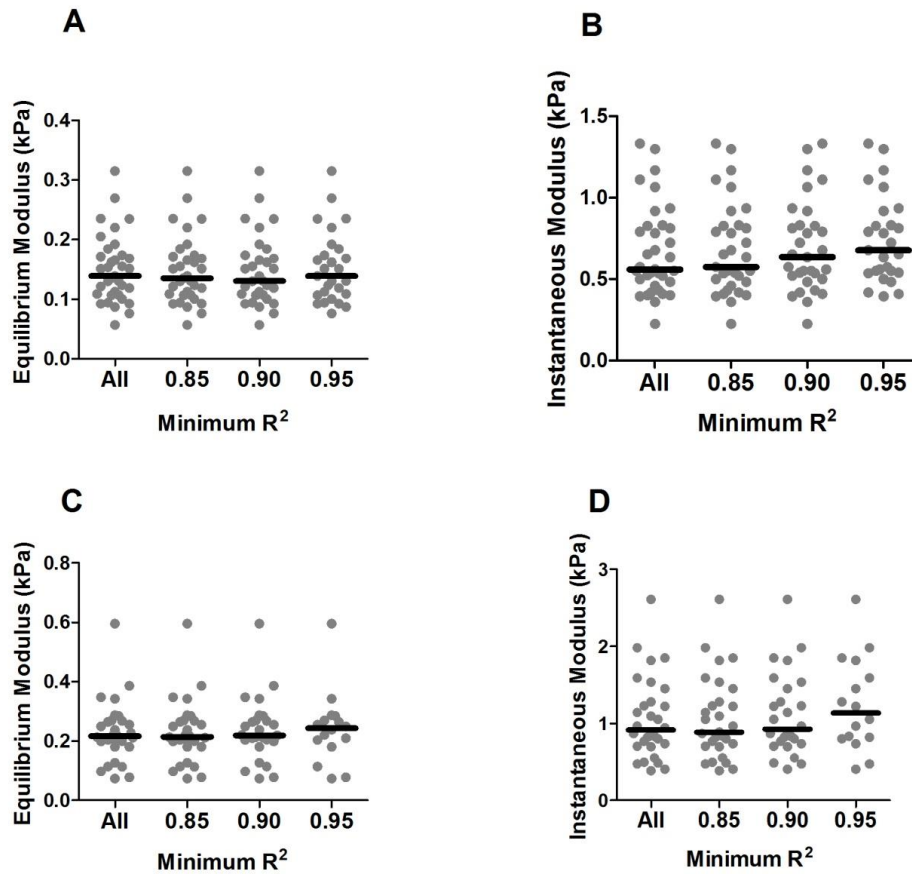
Figure 7.1: The viscoelastic properties of cells calculated for samples of hMSCs and differentiated cells with exclusion criteria based on the determination coefficient (R^2). The equilibrium and instantaneous moduli for hMSCs (A and B) and chondrogenic differentiated hMSCs (C and D). The data is presented as sample populations with median values indicated by bars. Mann-Whitney U test. The proportions of cells at minimum R^2 thresholds of 0.85, 0.90 and 0.95 are 92%, 86% and 75% for hMSCs are; and for Diff cells are 97%, 87% and 53% respectively.

7.3.4. Choice of hold time and effect on apparent viscoelastic properties

The SLS theoretical model assumes that as the cell is aspirated into the micropipette, the aspirated length reaches equilibrium without retraction or complete aspiration. However it is unclear what the aspiration time required for estimation of viscoelastic properties using the SLS model is. Some studies have indicated that cells reached

equilibrium within seconds; others demonstrated that equilibration takes more time. In the present study it was demonstrated that with increasing magnitude of pressure, the aspirated length took longer to reach equilibrium (section 7.3.5). This indicates that the equilibrium state is pressure dependant.

Changes in viscoelastic properties of cells are associated with time constant τ. This parameter represents the time needed for step response. The time constant is 3 times greater for undifferentiated hMSCs compared to those differentiated to the chondrogenic lineage with median values of 31.8 and 10.3 seconds respectively (Fig. 7.2).
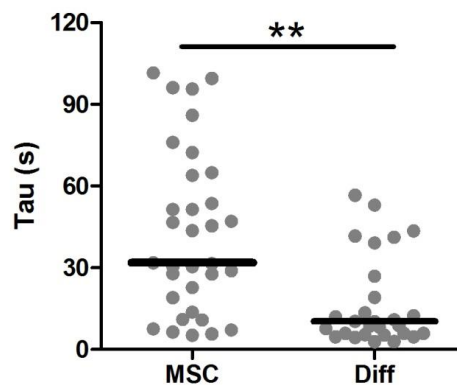
Figure 7.2: Time constant (tau) in response to hMSCs differentiated to the chondrogenic lineage. The data is presented as a population with median value indicated by bar. Mann-Whitney U test **$p<0.01$. Number of cells n= 33 hMSCs and 30 Diff.

As evident from the results in chapter 2 (Fig. 2.9), the aspirated length is showing approximate equilibrium by 90 seconds. The number of cells which were aspirated and successfully used for the SLS model are presented in table 7.1.

Figure 7.3 represents the viscoelastic properties of undifferentiated hMSCs and hMSCs differentiated to the chondrogenic lineage in response to different holding times. It should be noted that cells appear stiffer at shorter holding times compared to 180 seconds. The equilibrium modulus was significantly higher at a 30 seconds holding time compared to 180 seconds for undifferentiated hMSCs and differentiated cells. The difference was greater for hMSCs ($p<0.001$) compared to differentiated

cells (p<0.05). The instantaneous modulus was significantly higher for both cell groups at 30 seconds holding time compared to 180 seconds (p<0.001).

Table 7.1: Number of undifferentiated hMSCs and hMSCs differentiated to the chondrogenic lineage used for micropipette aspiration experiments and calculation of viscoelastic properties using the SLS model.

Holding time (seconds)	Total No. of cells	No. of successful aspirations	No. used for model $R^2 > 0.85$
	hMSCs		
30	36 (100%)	35 (97%)	35 (95%)
60	36 (100%)	35 (97%)	35 (95%)
120	36 (100%)	35 (97%)	33 (95%)
180	36 (100%)	35 (97%)	33 (95%)
	Diff		
30	30 (100%)	30 (100%)	30 (100%)
60	30 (100%)	30 (100%)	30 (100%)
120	30 (100%)	30 (100%)	28 (93%)
180	30 (100%)	30 (100%)	30 (100%)
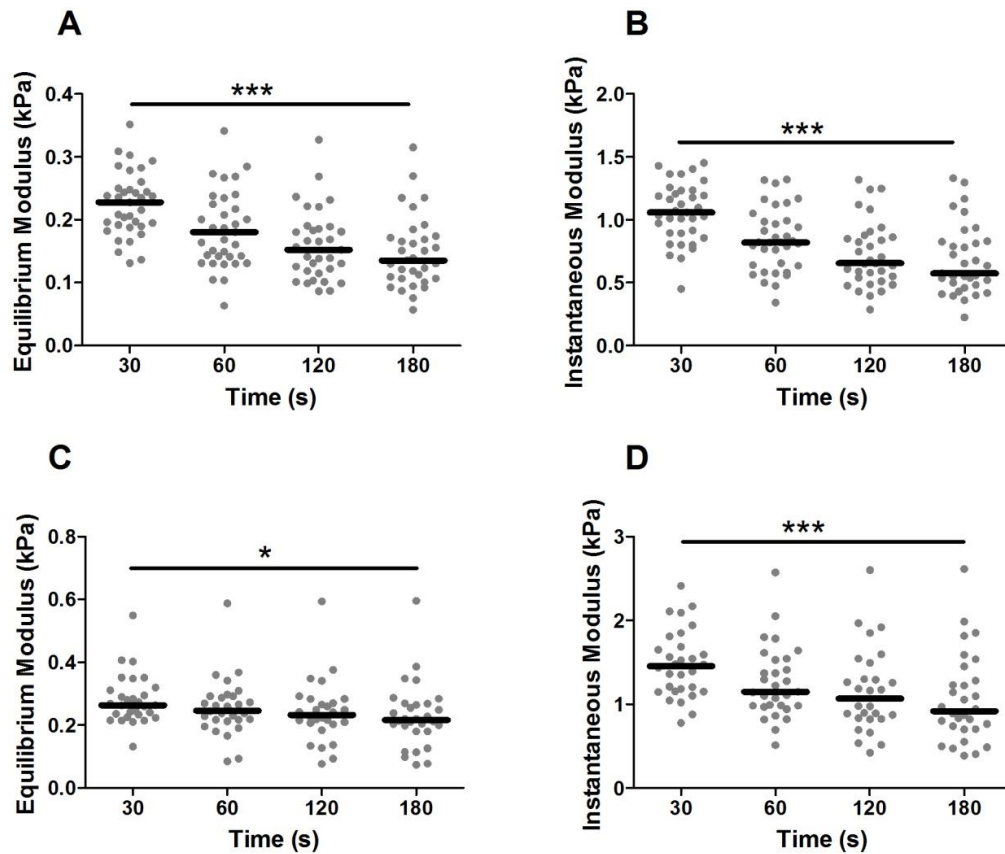
Figure 7.3: The effect of holding time on the viscoelastic properties for hMSCs and differentiated cells. The equilibrium and instantaneous moduli for hMSCs (A and B) and chondrogenic differentiated hMSCs (C and D). The data is presented as sample populations with median values indicated by bars. (Mann-Whitney U test, * $p<0.05$, *** $p<0.001$).

The holding time during micropipette aspiration affects the measurements of viscoelastic properties using the SLS model below a certain threshold time. The threshold time above which moduli values are not affected by time varies between cell types and is related to the viscoelastic half time which is influenced by actin organisation and dynamics with the membrane.

In the present study a holding time of 180 seconds was chosen, corresponding to previous studies (Jones, *et al.*, 1999, Tan, *et al.*, 2008a). This gives an accurate estimation of the viscoelastic properties of cells and comparison between cell groups.

7.3.5. Choice of aspiration pressure magnitude

Introduction

Micropipette aspiration has been used with application of different negative pressures according to the tested cell type (Merryman, *et al.*, 2009, Tan, *et al.*, 2008a, Trickey, *et al.*, 2000). It was previously demonstrated that pressure rate has an effect on cell mechanical properties (Pravincumar, *et al.*, 2012). Chondrocytes tested at lower pressure rates appear to be stiffer than those at higher rates associated with a greater propensity to form membrane blebs at higher rates. However, no study has examined how pressure magnitude effects cell viscoelastic properties measured by micropipette aspiration. In the previous chapters the pressure of 0.76 kPa was used to estimate cell viscoelastic properties of undifferentiated hMSCs, those differentiated to the chondrogenic lineage and chondrocytes at P0 and P1. A further study was therefore conducted to examine the influence of pressure magnitude on cell viscoelastic properties.

Methods

Bovine articular primary chondrocytes (P0) were isolated from adult bovine full depth cartilage as described in section 2.1.3. The micropipette aspiration system as described in section 2.2.3 was used to estimate the viscoelastic properties. The experiments were initiated by applying a step of 3.3 cmH$_2$O (0.32 kPa), 5.5 cmH$_2$O (0.54 kPa), 7.7 cmH$_2$O (0.75 kPa) and 16.5 cmH$_2$O (1.62 kPa) negative pressure at a rate of 3.85 cmH$_2$O/s (0.38 kPa/s). Cells were aspirated and visualised over 180 seconds. Cell aspirated length was measured from images as described in section 2.4.3. Viscoelastic properties were estimated using the theoretical SLS model as described in section 2.3.1.

Results

This study demonstrated that 59% to 93% of chondrocytes were successfully aspirated, however, the percentage of cells used for analysis of viscoelastic parameters decreased further due to the exclusion criteria of R^2>0.85 (table 7.2). At the lowest pressure of 0.32 kPa, only 57% of tested cells were successfully aspirated and fitted by the SLS model (R^2>0.85). The low number of cells was due to a population of stiff cells which were not aspirated at all. In addition the low number of cells successfully aspirated was at highest pressure, which caused complete aspiration for 39% of cells.

Table 7.2: Number of chondrocytes used for micropipette aspiration experiments and calculation of viscoelastic properties using the SLS model.

Aspirated pressure (kPa)	Total No. of cells	No. of successful aspirations	No. used for model $R^2>0.85$
0.32 kPa	37 (100%)	22 (59%)	21 (57%)
0.54 kPa	40 (100%)	37 (93%)	36 (90%)
0.76 kPa	88 (100%)	74 (84%)	73 (83%)
1.62 kPa	13 (100%)	8 (61%)	8 (61%)

Aspirated length changes with time indicated that pressure magnitude did not have an effect on cell behaviour during aspiration. Chondrocytes in all groups have exhibited viscoelastic creep behaviour, which was characterised by a sudden increase in aspirated length followed by equilibration (Fig. 7.4). Chondrocytes subjected to step negative pressures of 0.32 kPa, 0.54 kPa, 0.75 kPa and 1.62 kPa exhibited aspirated lengths at 180 seconds with median values of 5.7 μm, 8.4 μm, 13.0 μm and 22.3 μm respectively (Fig. 7.5 A). There were significant differences in aspirated length between all groups and a significant positive 1 to 1 correlation between applied pressure and aspirated length at 180 seconds. In addition the slope of the line plotted for aspirated length versus pressure represents the elastic modulus, which was 0.19 kPa. The equilibrium modulus shows no change between groups with values from 0.14 to 0.16 kPa (Fig. 7.5 B). However, the instantaneous modulus demonstrated changes similar to those in aspirated length. The values increased with increasing negative pressure and were significantly different between groups (Fig. 7.5 C). Viscosity exhibited a similar trend with significant increases in viscosity above 0.54 kPa aspiration pressure (Fig 7.5 D).
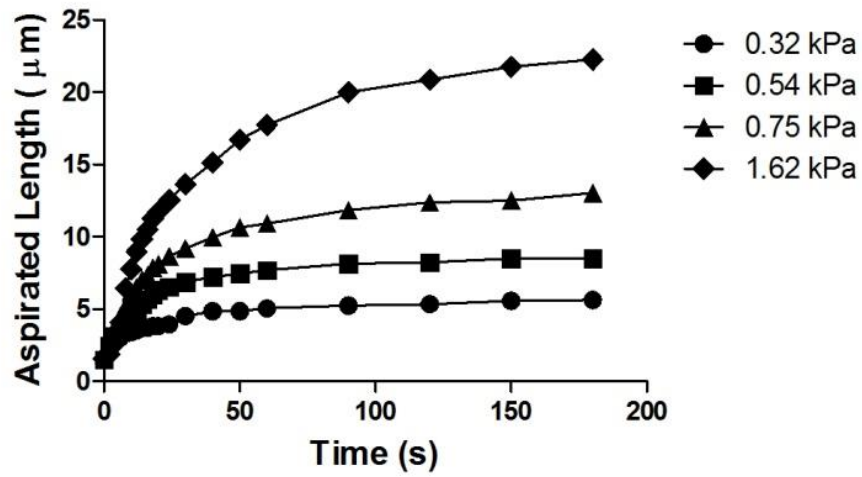
Figure 7.4: Plots of median aspirated length versus time for chondrocytes aspirated at different pressure magnitude. Cells were aspirated by applying a negative pressure of 3.3 cmH_2O (0.32 kPa), 5.5 cmH_2O (0.54 kPa), 7.7 cmH_2O (0.76 kPa) and 16.5 cmH_2O (1.62 kPa) at rate of 3.85 cmH_2O/s (0.38 kPa/s). Number of aspirated cells is given in table 7.2.
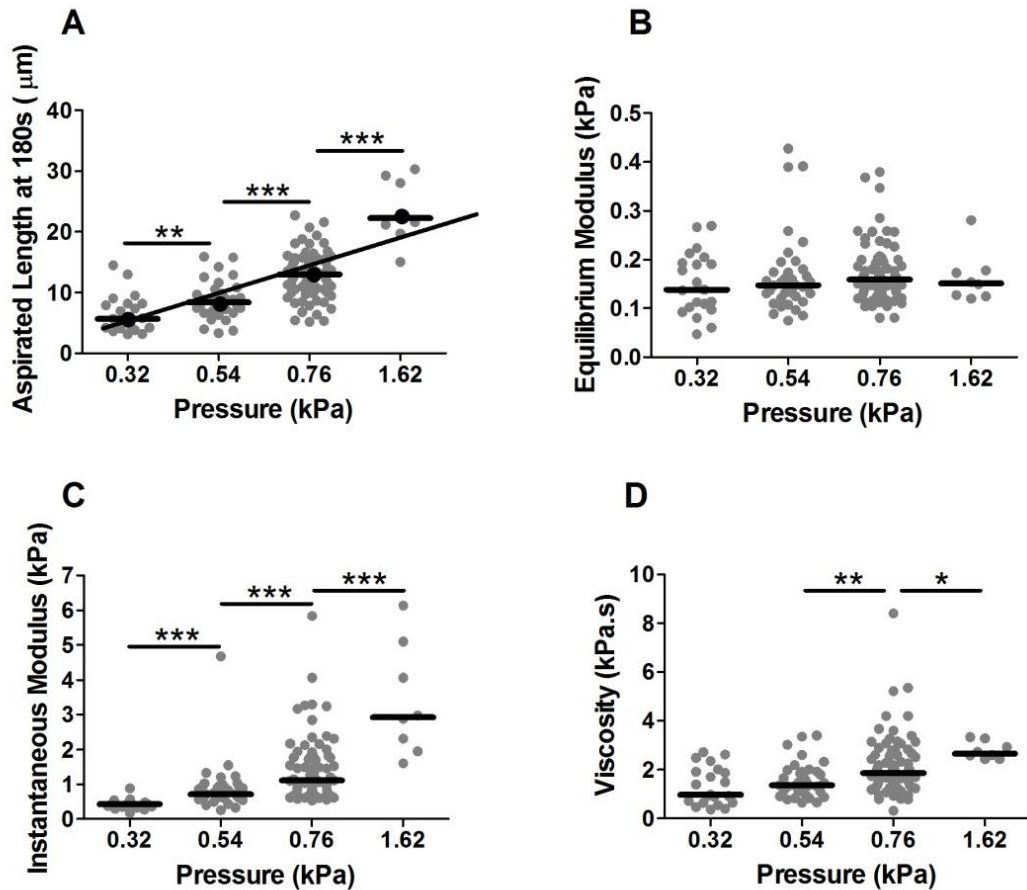
Figure 7.5: The aspirated length and viscoelastic properties of chondrocytes at different pressure magnitudes. (A) The aspirated length at 180 seconds and correlation between pressure and aspirated length fitted by linear model, (B) the equilibrium modulus, (C) the instantaneous modulus and (D) the viscosity of cells used for micropipette aspiration. The data is presented as a population with median value indicated by bar. Mann-Whitney U test, * p<0.05, ** p<0.01 and *** p<0.001. Number of cells is given in table 7.2.

Discussion

This study demonstrated that different magnitudes of negative pressure can be used to estimate viscoelastic properties of chondrocytes. Independent from pressure magnitude, chondrocytes exhibited viscoelastic behaviour. Differences of applied pressure partially affected cell viscoelastic properties. The equilibrium modulus did not change but instantaneous modulus and viscosity were affected. This suggests that those parameters are time dependent and rely on the time which was used to initiate aspiration. Applying higher pressures at a constant pressure rate results in a longer application time, this correlated with increased instantaneous modulus with increasing pressure.

7.4. Effect of cell size on mechanical properties

In this study the SLS theoretical model was used to determine the viscoelastic properties of individual cells modelled as homogeneous and incompressible half spaces. The micropipette radius is involved in the SLS model (equation 2.3), however, the model does not account cell size. Instead, the model assumes that the ratio of the cell diameter to micropipette diameter is greater than 3. If this criteri is met, then the viscoelastic parameters predicted by SLS half space model agrees with those obtained using finite element models of cell deformation during micropipette aspiration (Baaijens*, et al.*, 2005). In the present study the ratio of the cell to micropipette diameter was maintained at between 2.5 to 3.5. This was important as hMSCs undergoing chondrogenic differentiation significantly increased in size (Fig. 3.3) and could therefore affect the apparent mechanical properties estimated using the SLS model. By adjusting the micropipette diameter related to the cell diameter it is possible to examine the true relationship between cell size and mechanical properties. As evident from the results presented in figure 7.6, the mechanical properties were tested on representative cells of hMSCs and those differentiated to chondrogenic lineage populations. Data analysis have demonstrated that there is a correlation between the equilibrium modulus and cell size of differentiated cells ($p<0.001$). However, there were no correlations between instantaneous moduli and cell size in both cell groups, and cell size and equilibrium modulus of hMSCs ($p>0.08$). A similar finding was reported for chondrocytes even with a wider range of ratios of cell to micropipette diameter (Jones*, et al.*, 1999). This suggest that

differences in viscoelastic properties of hMSCs and differentiated cells are more likely due to physiological and morphological changes during differentiation than to physical parameters such as cell size.

In addition, the cell size could be not the one factor influences cell mechanical properties, but also cell nuclear. In the present study, the nuclear position during micropipette aspiration was ignored. However, it is unclear if the nuclear could be causing no cell aspiration by clogging the micropipette. In future work additional studies could be performed to study whether the position of cell nuclear have influence to cell mechanical properties.
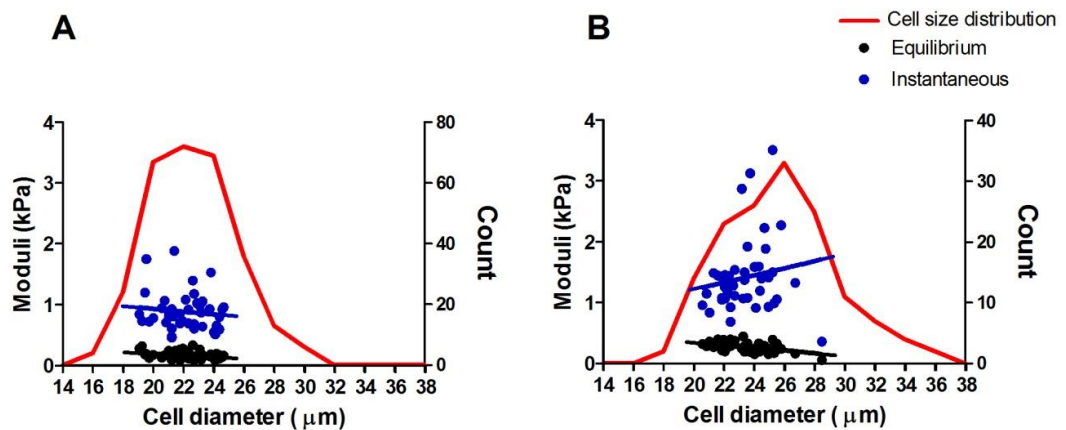
Figure 7.6: Correlation between cell diameter and equilibrium and instantaneous moduli. Representative plots of (A) undifferentiated hMSCs and (B) hMSCs differentiated to the chondrogenic lineage (Diff). Data of equilibrium and instantaneous moduli is presented as population. There is a significant correlation between cell diameter and the equilibrium modulus of differentiated cells (p<0.001). Other parameters showed no significant correlations.

7.5. Effect of membrane-actin cortex adhesion on cell migration

7.5.1. Introduction

Cell migration plays a key role in mammalian cells in many cellular processes including cancer (Friedl and Wolf, 2003), wound healing (Krawczyk, 1971), embryogenesis, and tissue regeneration (Mitchison and Cramer, 1996, Pollard and Borisy, 2003). Migration of stem cells is essential for tissue repair and new tissue

formation following cell differentiation (Zhao*, et al.*, 2011). Cell migration is based on cell movement by formation of a protrusion at the leading edge. Depending on cell type and environment, cells use different protrusion types, such as lamellipodia for which growth is associated with actin polymerisation, or spherical blebs which are driven by intracellular pressure (Bergert*, et al.*, 2012, Charras and Paluch, 2008, Cojoc*, et al.*, 2007, Diz-Munoz*, et al.*, 2010).

The scratch assay is a commonly used method to study cell migration in multiple cell types (Chen*, et al.*, 2013, Huang*, et al.*, 2003). In previous chapters it has been shown that chondrogenic differentiation of hMSCs is associated with changes in membrane-actin cortex adhesion, blebbing and actin cortex organisation. A further study was therefore conducted to test the hypothesis that chondrogenic differentiation is associated with changes in cell migration.

The present study therefore used a scratch assay to measure the speed of migration in monolayer for hMSCs and hMSCs differentiated to the chondrogenic lineage.

7.5.2. Methods
Undifferentiated hMSCs and those differentiated to the chondrogenic lineage were cultured on 12-well plates until 90% confluent as described in sections 2.2.1 and 2.2.2. The "scratch" was created using a 2 µl pipette tip. Medium was aspirated and cells were washed twice with warm PBS. Fresh medium was then added to each plate. At 0, 3, 6, 9, 12, 24 and 30 hours, brightfield images of the wound area were taken with a x10 objective lens (Leica DMIL). ImageJ and a Matlab script based on a previous study (Zheng*, et al.*, 2012) were used to calculate the wound area at different time points.

7.5.3. Results
The representative brightfield images of the scratch area at different time points are presented in figure 7.7. Undifferentiated hMSCs migrate faster than differentiated cells such that gap area was significantly different between cell groups at 12, 24 and 30 hours after scratch creation (Fig. 7.8).
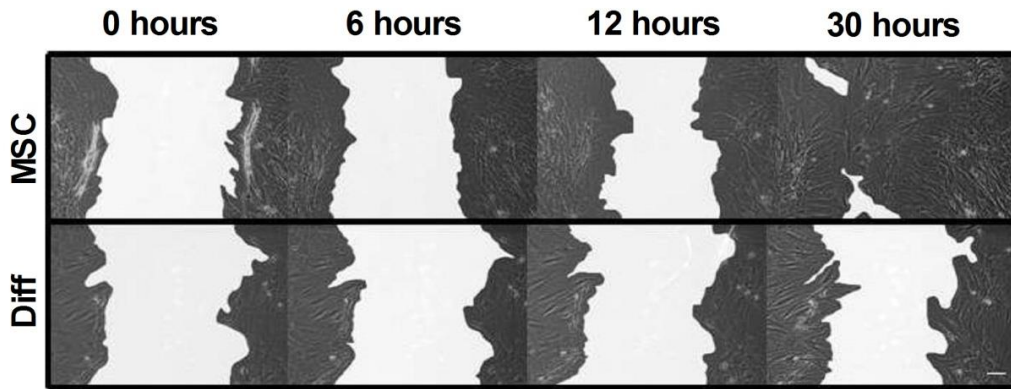
Figure 7.7: Migration of undifferentiated hMSCs and those differentiated to the chondrogenic lineage is assessed based on a scratch assay. Brightfield microscopy images showing gap closure with cell migration at 0, 6, 12 and 30 hours. Scale bar represents 100 μm.
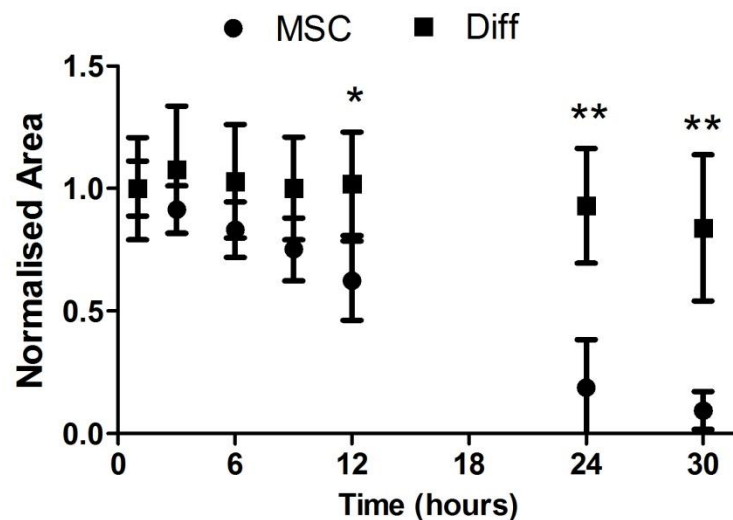
Figure 7.8: Differentiation reduces cell migration. To evaluate the rate of cell migration, the area of the gap was calculated at each time increment and normalised to the initial area. Undifferentiated hMSCs exhibit faster migration compared to differentiated cells as shown by significantly lower scratch areas at 12, 24 and 30 hours after scratch formation. Data is presented as means of 5-7 scratch areas for each condition. Error bars indicate standard deviations. (* $p < 0.05$, ** $p < 0.01$, t-test).

7.5.4. Discussion

The present study demonstrates that hMSC differentiation to the chondrogenic lineage is associated with slower cell migration (Fig. 7.8). This also agreed with our previous findings that differentiated cells are stiffer and have a thicker, more defined cortical actin shell compared to undifferentiated hMSCs. Moreover, differentiation has an effect on membrane-actin cortex adhesion, such that bleb formation is reduced. Thus, these results suggest that enhanced migration in hMSCs is more likely resulted by less defined cortical actin which could cause a relatively decreased number of membrane-actin cortex connections. This agrees with a lower ERM linker protein expression in undifferentiated hMSCs compared to differentiated cells. Moreover, this study demonstrates that hMSCs migration is more likely based on actin polymerisation that bleb formation. A weaker memebrane-actin cortex adhesion could be indirectly involved in cell migration. Lower number of ERM connections between membrane-actin cortex could lead to faster actin polymerisation and cell migration. For further investigation to understand whether the increased bleb susceptibility in hMSCs is involved in cell migration, additional experiments in 3D matrixes are necessary. This could answer the question if bleb based migration is influenced by memebrane-actin cortex interations during stem cell differentiation.

7.6. Summary of key findings

In these studies, the protocols for micropipette aspiration were developed to determine viscoelastic properties of single cells. In addition new protocols for micropipette aspiration allowed measurement of the critical pressure required for membrane-actin cortex detachment. A series of experiments were performed to measure viscoelastic properties of cells in response to hMSC passage, differentiation toward the chondrogenic lineage and chondrocyte dedifferentiation. In all cases viscoelastic properties were related to changes in actin organisation and ERM linker protein expression and associated membrane-actin cortex adhesion. The key findings of this thesis are presented below:

1 Validation of micropipette aspiration protocols for measuring cellular viscoelastic properties using the SLS model revealed the importance of hold time, pressure magnitude and R^2 cut off. (Section 7.3 and paper in preparation)

2 LifeAct-GFP did not affect cell mechanical properties whilst actin-GFP increased cell moduli. Thus LifeAct-GFP is a better tool for visualisation of actin dynamics during micropipette aspiration (Section 2.7 and paper submitted to Cytoskeleton)

3 Passage in monolayer did not affect mechanical properties of hMSCs but did increase cell size (Section 2.6)

4 Chondrogenic differentiation of hMSCs
➢ regulates membrane-actin cortex adhesion via ERM linker proteins
➢ this increases apparent equilibrium and instantaneous moduli
➢ reduces blebbing in response to micropipette aspiration and hypo-osmotic challenge
➢ increases critical detachment pressure
➢ increases F-actin organisation in cell monolayer and suspension, but reduces actin remodelling rate within blebs during micropipette aspiration
(Paper published in Scientific Reports)

5 Dedifferentiation of articular chondrocytes with passage in monolayer
➢ increases F-actin organisation and expression of ERM linker proteins
➢ increases viscoelastic properties and reduces mechanically induced blebbing
➢ increases pressure rate dependent membrane-actin cortex interaction
(Paper in preparation for Biophysical J)

6 Slower cell migration is associated with chondrogenic differentiation
(Section 7.5, included in paper accepted in Scientific Reports and the subject of future investigation)

In conclusion, apparent cellular mechanical properties are altered during chondrogenic differentiation of hMSCs and dedifferentiation of articular

chondrocytes as a result of changes in F-actin organisation and the expression of ERM linker proteins which modulate bleb formation.

7.7. Future work

7.7.1. Cancer cell mechanics, bleb formation and migration

Cell migration in the human body is essential and is involved in processes such as wound healing, or cancer metastasis (Friedl and Gilmour, 2009, Nobes and Hall, 1999). Migration is based on a few parameters including actin polymerisation, actomyosin contractility, deformation of the cell membrane (bleb formation) and cell-matrix adhesion (Tozluoglu, *et al.*, 2013). The modes of cell migration are classified based on cell morphology and are cell type dependant. Mesenchymal cell migration relies on actin polymerisation which pushes the membrane forward, forming lamellipodia and finger like filopodia protrusions (Le Clainche and Carlier, 2008). Another type of migration is known as amoeboid or rounded which refers to the movement of rounded cells and is dependent on actomyosin contraction. The intracellular pressure generated by actomyosin contraction cause the membrane detachment from the cortex forming a membrane blebs (Charras and Paluch, 2008). For the last decade, lamellipodia based cell migration has been studied to understand cell migration during cancer metastasis. However it has been demonstrated that cancer cells have an ability to switch to bleb based motility (Petrie and Yamada, 2012). The mechanism controlling such as behaviour is unclear but it is believed that adhesions between cell-matrix and interactions between the cell membrane and actin cortex play an important role. One hypothesis is that a change in the density of a membrane-actin cortex linker protein such as ERM results in bleb formation at regions with decreased linker protein density. The present study demonstrated that hMSCs differentiated to chondrogenic lineage underwent slower cell migration and less blebbing which was associated with increased expression of ERM linker proteins and greater F-actin organisation.

For better understanding cancer metastasis, the future studies need to examine the linkage between expression of ERM linker proteins, bleb formation and migration in cancer cells. This can involve measurements of ERM linker protein distribution and F-actin structure during cell migration using traction force microscopy.

7.7.2. Rapid throughput biomechanics analysis

The micropipette aspiration technique is a versatile tool and widely used to measure single cell mechanical properties, however it has a few major limitations. Firstly, micropipette fabrication requires expensive techniques and skills for operating them. Secondly, the manipulation of single cells and data collection for a large number of samples is a time consuming process. Indeed the majority of studies employ relatively small sample sizes (n ≈ 10-20) which are poorly associated with population heterogeneity. An alternative solution to these limitations of the micropipette aspiration technique is the micro-channel system which has been developed with single or multi channels (Kim and Han, 2011, Yap and Kamm, 2005). In such systems a single cell or a multiple cells can be aspirated simultaneously. For these micro-channel systems micropipettes are not required, although the skills of soft lithography are needed to create the micro-channel system (Weibel, *et al.*, 2007). Once the aspiration channels are filled with fluid and cells are trapped, the negative pressure is applied to aspirate cells simultaneously. Cell mechanical properties can be estimated using a similar theoretical SLS model as is used for micropipette aspiration experiments.

Using the micro-channel system would save time and increase the sample size for data analysis. However, the micro-channel system has a few limitations for the present study. One of the limitations of this technique is that cells used for measurements should be a similar size, but the present study demonstrated that hMSCs have a wide size variability, which could invalidate assumptions associated with the SLS model and in extreme cases cause no aspiration for large cells and full aspiration for small cells. Additionally, the micro-channels are square in cross section and this may cause poor sealing between the cell and the channel wall. Although some studies demonstrated that semi-circle channels can be obtained by applying a thermal reflow process (Kim, *et al.*, 2010) or by applying a liquid PDMS polymer on the walls of square channels. To the latter, the precise diameter of micro-channels can be achieved by changing coating conditions such as flow rate, viscosity of polymer or baking temperature (Abdelgawad, *et al.*, 2010). Also due to the size of device, the image of cell aspiration will lose resolution due to image capture of large fields containing multiple cells instead of imaging a single cell.

7.7.3. Modelling

Mechanical properties of cells are important in predicting cell deformation under mechanical stimuli and may reflect information on cell structure and phenotype (Darling, *et al.*, 2008, Gonzalez-Cruz, *et al.*, 2012) or pathological disorders (Trickey, *et al.*, 2000). The micropipette aspiration system in combination with the theoretical SLS model was been widely used to estimate cell viscoelastic properties in a variety of cell types. The SLS model assumes that the cell is an infinitely large half space subjected to an instantaneously applied negative pressure (Sato, *et al.*, 1990). However, the model is analysing the behaviour of cell but clearly the cell does not represent a homogenous solid visoelastic material. Hence the model cannot account for bleb formation, the presence of a stiffer nucleus or a stiff contractile actin cortex and associated intracellular pressure. Furthermore the model can not reflect the dynamic nature of the cell and the potential for remodelling and adaptation to biomechanical stimuli and temperature changes. To address limitations of SLS model mentioned above, finite element models have been developed to determine viscoelastic properties of cells during micropipette aspiration (Baaijens, *et al.*, 2005, Boudou, *et al.*, 2006, Zhao, *et al.*, 2009). The models account for boundary conditions, material and geometric nonlinearities and a realistic geometry, which leads to more precise predictions of viscoelastic properties. However, they still model the cell as a solid homogenous material. The present study demonstrated that membrane-actin cortex interaction plays a key role in determining cell mechanical properties. In Chapter 5 the simplified model for bleb formation was developed based on previous studies (Brugues, *et al.*, 2010) which incorporate the critical pressure required for membrane-actin cortex detachment. This model accurately predicted the elastic properties of undifferentiated hMSCs and differentiated cells. However, the model was not able to accurately predict elastic properties for chondrocytes undergoing dedifferentiation (chapter 6). This suggests that in future, additional parameters such as F-actin density and ERM linker protein distribution should be incorporated with resulting changes in cortex modulus (G_{ctx}). Finite element models based on micropipette aspiration could also be developed to involve membrane-actin cortex parameters and actin cortex density as these are the major factors resulting changes in cell mechanical properties. In Chapter 6 was demonstrated that membrane-actin cortex adhesion is pressure rate dependant. This

suggests that in future work and modelling the pressure rate parameter could be impremented to study dynamics of membrane-actin cortex interaction.

Table 7.3: Summary of viscoelastic properties of cells estimated using the SLS model during micropipette aspiration experiments.

Experiment	E_0 (kPa)	E_∞ (kPa)	Explanation	Section in thesis
hMSCs **Differentiated hMSCs**	0.84 1.33	0.15 0.29	Instantaneous and equilibrium moduli increased within hMSCs differentiation.	3.3.6
Chondrocytes **P0** **P1**	 1.14 1.45	 0.16 0.40	Chondrocyte dedifferentiation in monolayer increased in equilibrium modulus but did not affect instantaneous modulus.	6.3.2
Chondrocytes P0 **ΔP (kPa)** **0.32** **0.54** **0.76** **1.62**	 0.42 0.71 1.11 2.93	 0.14 0.15 0.16 0.15	Pressure magnitude did not affect equilibrium modulus of chondrocytes, but increased in instantaneous modulus with increased pressure.	7.3.5

APPENDIXES

Appendix A – MatLab codes
A1 Cell diameter measurements

```matlab
clear all
clc

%%
%INPUT

%Pixel size in um
PSize = 0.465030;

%File name for the excel output
OutputName = 'msc.xls';

%marker size (need to be even)
Dot = zeros(20,20);

%%
Filename = dir('*.tif');

for i = 1:size(Filename,1)
    reply = 'n';
    I = imread(Filename(i,1).name);
    Ibackup = I;
    I = I';
    j = 1;

    while reply ~= 'y'
        close all
        imshow(I,'InitialMagnification',170,'Border','tight')

        reply = input('Are you finished? y/n/r:','s');
        if isempty(reply)
            reply = 'n';
        end

        if reply == 'n'
            h = impoint;
            Pos = wait(h);
            Pos = round(Pos);
            PosH1 = Pos;

            h = impoint;
            Pos = wait(h);
            Pos = round(Pos);
            PosH2 = Pos;

            h = impoint;
            Pos = wait(h);
            Pos = round(Pos);
```

```matlab
            PosV1 = Pos;

            h = impoint;
            Pos = wait(h);
            Pos = round(Pos);
            PosV2 = Pos;

            CDiameterH = abs(PosH1(1,1)-PosH2(1,1))*PSize;
            CDiameterV = abs(PosV1(1,2)-PosV2(1,2))*PSize;
            CellDiameter = (CDiameterH+CDiameterV)/2;
            CellDiameterList(j,1) = CellDiameter;
            j = j+1;

            hold on

line([PosH1(1,1),PosH2(1,1)],[PosH1(1,2),PosH2(1,2)]);

line([PosV1(1,1),PosV2(1,1)],[PosV1(1,2),PosV2(1,2)]);

            img = getframe;
            Ibackup = I;
            %I = img.cdata;
            MLoc                        =                [PosH1(1,2)
PosH1(1,1)+round((abs(PosH1(1,1)-PosH2(1,1)))/2)];
            I(MLoc(1,1)-(size(Dot,1)/2):MLoc(1,1)-
(size(Dot,1)/2)+size(Dot,1)-1,MLoc(1,2)-
(size(Dot,2)/2):MLoc(1,2)-(size(Dot,2)/2)+size(Dot,2)-1)      =
Dot;
        elseif reply == 'r'
            I = Ibackup;
            j = j-1;
        end
    end

    if i < 2
        CellDiameterListComb = CellDiameterList;
    else

CellDiameterListComb(length(CellDiameterListComb)+1:length(Cel
lDiameterListComb)+length(CellDiameterList),1)               =
CellDiameterList;
    end
    clear CellDiameterList
end

%%
xlswrite(OutputName,CellDiameterListComb,1,'A1')
```

A2 Cell aspirated length during time

```matlab
clear all
clc

%%
%INPUT

%Pixel size in um
PSize = 0.185966;

% Pressure
P = 7.7;
Pressure = P*98.1;

% Phi wall function
phi = 2.1;

%The starting time point image
Start = 2;

%Time step for each image frame
dt = 2;

%Time distance between each measurements
Measurement1 = 11;
StepSizeMeasurement1 = 1;
Measurement2 = 1;
StepSizeMeasurement2 = 2;
Measurement3 = 1;
StepSizeMeasurement3 = 3;
Measurement4 = 3;
StepSizeMeasurement4 = 5;
Measurement5 = 4;
StepSizeMeasurement5 = 15;


%Marker thickness
MarkerT = 1;

%File name for the excel output
OutputName = 'Series140.xls';


%%
Filename = dir('msc_Series140*');
Filename = Filename(Start:size(Filename,1),:);

TimeAll = zeros(size(Filename,1),1);



for i = 2:size(TimeAll,1)
    TimeAll(i,1) = TimeAll(i-1,1)+dt;
end
```

218

```matlab
%%
%Creating Index of images to be measured
TStart = 1;
TEnd = Measurement1;
deltaT = StepSizeMeasurement1;
Index1 = TStart:deltaT:TEnd;
Index = Index1';

TStart = TEnd+StepSizeMeasurement2;
TEnd = ((Measurement2-1)*StepSizeMeasurement2)+TStart;
deltaT = StepSizeMeasurement2;
Index2 = TStart:deltaT:TEnd;
Index(size(Index,1)+1:size(Index,1)+size(Index2,2),1)      = ...
Index2';

TStart = TEnd+StepSizeMeasurement3;
TEnd = ((Measurement3-1)*StepSizeMeasurement3)+TStart;
deltaT = StepSizeMeasurement3;
Index3 = TStart:deltaT:TEnd;
Index(size(Index,1)+1:size(Index,1)+size(Index3,2),1)      = ...
Index3';

TStart = TEnd+StepSizeMeasurement4;
TEnd = ((Measurement4-1)*StepSizeMeasurement4)+TStart;
deltaT = StepSizeMeasurement4;
Index4 = TStart:deltaT:TEnd;
Index(size(Index,1)+1:size(Index,1)+size(Index4,2),1)      = ...
Index4';

TStart = TEnd+StepSizeMeasurement5;
TEnd = ((Measurement5-1)*StepSizeMeasurement5)+TStart;
deltaT = StepSizeMeasurement5;
Index5 = TStart:deltaT:TEnd;
Index(size(Index,1)+1:size(Index,1)+size(Index5,2),1)      = ...
Index5';

%%
%Time points of the images to be measured
Time = TimeAll(Index,1);

%%
%Choosing the field of view for measurement, based on last
image
I = imread(Filename(Index(length(Index)),1).name);
I = I';
Zoom = (288/size(I,1))*250;
Zoom = round(Zoom);
imshow(I,'InitialMagnification',Zoom,'Border','tight')

h = impoint;
Pos = wait(h);
Pos = round(Pos);
PosT = [Pos(1,2) Pos(1,1)];

h = impoint;
```

219

```matlab
Pos = wait(h);
Pos = round(Pos);
PosB = [Pos(1,2) Pos(1,1)];

h = impoint;
Pos = wait(h);
Pos = round(Pos);
PosS1 = [Pos(1,2) Pos(1,1)];

h = impoint;
Pos = wait(h);
Pos = round(Pos);
PosS2 = [Pos(1,2) Pos(1,1)];

%%
%Cell diameter from 1st image
I = imread(Filename(1,1).name);
I = I';

I = I(PosT(1,1):PosB(1,1),PosS1(1,2):PosS2(1,2));
Zoom = (288/size(I,1))*250;
Zoom = round(Zoom);
imshow(I,'InitialMagnification',Zoom,'Border','tight')

%Vertical diameter
h = impoint;
Pos = wait(h);
Pos = round(Pos);
PosV1 = [Pos(1,2) Pos(1,1)];

h = impoint;
Pos = wait(h);
Pos = round(Pos);
PosV2 = [Pos(1,2) Pos(1,1)];

%Horizontal diameter
h = impoint;
Pos = wait(h);
Pos = round(Pos);
PosH1 = [Pos(1,2) Pos(1,1)];

h = impoint;
Pos = wait(h);
Pos = round(Pos);
PosH2 = [Pos(1,2) Pos(1,1)];


CDiameterH = abs(PosH1(1,2)-PosH2(1,2))*PSize;
CDiameterV = abs(PosV1(1,1)-PosV2(1,1))*PSize;

CellDiameter = (CDiameterH+CDiameterV)/2;

%%
%Pipette diameter from the first image
I = imread(Filename(1,1).name);
I = I';
```

```matlab
I = I(PosT(1,1):PosB(1,1),PosS1(1,2):PosS2(1,2));
Zoom = (288/size(I,1))*250;
Zoom = round(Zoom);
imshow(I,'InitialMagnification',Zoom,'Border','tight')

h = impoint;
Pos = wait(h);
Pos = round(Pos);
PosP1 = [Pos(1,2) Pos(1,1)];

Marker = zeros(MarkerT,size(I,2));
I(PosP1(1,1)-
floor(size(Marker,1)/2):PosP1(1,1)+ceil(size(Marker,1)/2)-1,:)
= Marker;
imshow(I,'InitialMagnification',Zoom,'Border','tight')

h = impoint;
Pos = wait(h);
Pos = round(Pos);
PosP2 = [Pos(1,2) Pos(1,1)];

PDiameterH = abs(PosP1(1,2)-PosP2(1,2))*PSize;
PDiameterV = abs(PosP1(1,1)-PosP2(1,1))*PSize;

PipetteDiameter = sqrt((PDiameterH^2)+(PDiameterV^2));
PipetteRadius = PipetteDiameter/2;

Ratio = CellDiameter/PipetteDiameter;

%%
%Aspiration measurement

for i = 1:length(Index)
    I = imread(Filename(Index(i,1),1).name);
    I = I';

    I = I(PosT(1,1):PosB(1,1),PosS1(1,2):PosS2(1,2));
    Zoom = (288/size(I,1))*250;
    Zoom = round(Zoom);
    %imshow(I,'InitialMagnification',Zoom,'Border','tight')

    reply = input('Do you want to re-set the initial point? y/n [y]:','s');

    if isempty(reply)
        reply = 'n';
    end

    if i < 2
        reply = 'y';
    end

    if reply == 'y'
        close all
        imshow(I,'InitialMagnification',Zoom,'Border','tight')
```

```matlab
        h = impoint;
        Pos = wait(h);
        Pos = round(Pos);
        PosL1 = Pos;

        h = impoint;
        Pos = wait(h);
        Pos = round(Pos);
        PosL2 = Pos;

        hold on
        line([PosL1(1,1),PosL2(1,1)],[PosL1(1,2),PosL2(1,2)]);

        h = impoint;
        Pos = wait(h);
        Pos = round(Pos);
        PosL3 = Pos;

        V = size(I,1)-PosL3(1,2);
        H   =   ((abs(PosL2(1,2)-PosL1(1,2)))/(abs(PosL2(1,1)-
PosL1(1,1))))*V;

        PosL4 = ([PosL3(1,1)+round(H) PosL3(1,2)+V]);

        line([PosL3(1,1),PosL4(1,1)],[PosL3(1,2),PosL4(1,2)]);

    elseif reply == 'n'
        close all
        imshow(I,'InitialMagnification',Zoom,'Border','tight')

        hold on
        line([PosL1(1,1),PosL2(1,1)],[PosL1(1,2),PosL2(1,2)]);
        line([PosL3(1,1),PosL4(1,1)],[PosL3(1,2),PosL4(1,2)]);
    end

    Pos1 = [PosL3(1,2)  PosL3(1,1)];

    h = impoint;
    Pos = wait(h);
    Pos = round(Pos);
    Pos2 = [Pos(1,2)  Pos(1,1)];

    AspLengthH = abs(Pos1(1,2)-Pos2(1,2))*PSize;
    AspLengthV = abs(Pos1(1,1)-Pos2(1,1))*PSize;

    AspLength = sqrt((AspLengthH^2)+(AspLengthV^2));
    AspLengthList(i,1) = AspLength;
end

MaxAspLength = AspLength;

%%
%OUTPUT to excel

Label = cell(1,10);
```

```
Label(Abdallah, et al., 2005) = 'Cell diameter';
Label(Abdallah, et al., 2005) = 'Pipette diameter';
Label(Abdallah, et al., 2005) = 'Pipette radius';
Label(Abdallah, et al., 2005) = 'CD/PD';
Label(Abdallah, et al., 2005) = 'phi';
Label(Abdallah, et al., 2005) = 'Pressure';
Label(Abdallah, et al., 2005) = 'Maximum aspiration length';
Label(Abdallah, et al., 2005) = 'Aspiration length';
Label(Abdallah, et al., 2005) = 'Time (s)';

xlswrite(OutputName,Label,1,'A1');
xlswrite(OutputName,CellDiameter,1,'A2');
xlswrite(OutputName,PipetteDiameter,1,'B2');
xlswrite(OutputName,PipetteRadius,1,'C2')
xlswrite(OutputName,Ratio,1,'D2');
xlswrite(OutputName,phi,1,'E2');
xlswrite(OutputName,Pressure,1,'F2');
xlswrite(OutputName,MaxAspLength,1,'G2');
xlswrite(OutputName,AspLengthList,1,'I2');
xlswrite(OutputName,Time,1,'J2');
```

A3 Standard Linear Solid (SLS) Model

```
function F=Lfun(x)

Data = xlsread('Series142.xls');

%% Parameters

phi = Data(1,5);                        % wall function phi
Dp = Data(1,6);                         % pressure (Pa)
a = Data(1,3);                  % pipette radius (microns)
L = xlsread('Series142.xls','I2:I21');                  %
Aspirated length (microns)
t = xlsread('Series142.xls','J2:J21');                  %
Time (s)


k1=x(1);
k2=x(2);
mu=x(3);

tau=mu*(k1+k2)/(k1*k2);

Lp=phi*a*Dp/(pi*k1)*(1-k2/(k1+k2)*exp(-t/tau));
F=L-Lp;
```

```
close all
clear all
Data = xlsread('Series142.xls');

%% Parameters

phi = Data(1,5);                        % wall function phi
Dp = Data(1,6);                         % pressure (Pa)
a = Data(1,3);                  % pipette radius (microns)
L = xlsread('Series142.xls','I2:I21');          % Aspirated
length (microns)
t = xlsread('Series142.xls','J2:J21');          % Time (s)

%%
%File name for the excel output
OutputName = 'Series142_180.xls';

%%
% Calculation

x0 = [10;10;10];
x = lsqnonlin(@Lfun,x0)

k1 = x(1)
k2 = x(2)
mu = x(3)

tau = mu*(k1+k2)/(k1*k2)
```

```matlab
Lp=phi*a*Dp/(pi*k1)*(1-k2/(k1+k2)*exp(-t/tau));

Eeq = (3/2)*k1;
Einst = 3/2*(k1+k2);

Lmean=mean(L);
Serr=sum((L-Lp).^2)
Stot=sum((L-Lmean).^2)
R2=1-Serr./Stot
figure(1)
plot(t,L,'b*')
hold on
plot(t,Lp,'r')
xlabel('t (s)','FontSize',14)
ylabel('Aspirated length um','FontSize',14)
title('Series142','FontSize',16)

%%
%Output
Label = cell(1,5);
Label(Abdallah, et al., 2005) = 'k1 (Pa)';
Label(Abdallah, et al., 2005) = 'k2 (Pa)';
Label(Abdallah, et al., 2005) = 'tau';
Label(Abdallah, et al., 2005) = 'mu';
Label(Abdallah, et al., 2005) = 'Eeq';
Label(Abdallah, et al., 2005) = 'Einst';
Label(Abdallah, et al., 2005) = 'R2';

xlswrite(OutputName, Label,1,'A1');
xlswrite(OutputName, k1,1,'A2');
xlswrite(OutputName, k2,1,'B2');
xlswrite(OutputName, tau,1,'C2');
xlswrite(OutputName, mu,1,'D2');
xlswrite(OutputName, Eeq,1,'E2');
xlswrite(OutputName, Einst,1,'F2');
xlswrite(OutputName, R2,1,'G2');
saveas(figure(1),'Series142_180.jpg');
```

Appendix B – Protocol for bacterial culture
B1 Preparation of solid media LB-agar plates

Lubria broth (LB) media consisted of 500 ml distilled water with the addition of 17 g of LB agar (Invitrogen) and 2.5 g NaCl (Sigma). Everything was mixed and autoclaved. Media was cooled to below 50°C and antibiotics added. Then the media was poured into plates on a clean bench next to a Bunsen burner to sterilize the surrounding environment. Bubbles were removed from the surface and the plates left to dry. Plates are stored inverted at 4°C in the dark to preserve light sensitive antibiotics. Before seeding cells, inverted plates were incubated at 37°C for 30 minutes.

B2 Preparation of liquid media

Liquid media consisting of 500 ml distilled water mixed with 12.5 g Luria Broth base (Invitrogen) and autoclaved. After autoclaving media is aliquoted and stored at -20°C. Before use, the media was defrosted and antibiotics added.

B3 Growth of E. coli cultures

Bacteria from glycerol stocks were streaked on the plate using a wire loop or pipette tip. The plate was incubated upside down at 37°C for 24 hours until colonies developed. A healthy single colony is picked from the plate and inoculated in liquid media. This ensures that cells growing in the culture are from a single colony and have the same genetics. The colony was incubated overnight at 37°C on a shaker at 225 rpm. DNA was then isolated from the bacterial culture using a plasmid isolation kit according to manufacturers instructions (Invitrogen).

Appendix C – Mechanical properties in response to actin disruption during chondrogenic differentiation of hMSCs

C1 Introduction

Viscoelastic properties of undifferentiated hMSCs and those induced to differentiation has been reviewed in chapter 3. Previous studies have demonstrated that hMSCs exhibited changes in viscoelastic properties as they undergo differentiation (Gonzalez-Cruz, *et al.*, 2012). The present study indicated that hMSCs differentiated to the chondrogenic lineage increased in stiffness compared to undifferentiated hMSCs. This was associated with a higher quantity of cortical actin and ERM linker proteins. It is known that chemical inhibition of actin polymerization effects cell mechanical properties (Tan, *et al.*, 2008a). In order to test whether the cytochalasin D has the same effect on undifferentiated hMSCs and those differentiated to the chondrogenic lineage, both groups of cells were treated with cytochalasin D and the viscoelastic properties estimated.

C2 Methods

Undifferentiated hMSCs and those differentiated to the chondrogenic lineage were cultured as described in sections 2.2.1-2.2.2. Prior to micropipette aspiration, cells in monolayer were treated with 2 μM cytochalasin D for 2 hours and then prepared in suspension for micropipette aspiration experiments as described in section 2.4.1. Viscoelastic properties were determined as described in section 2.4.2.

C3 Results

The effect of cytochalasin D on cell mechanics of undifferentiated hMSCs and cells differentiated to chondrogenic lineage were estimated using the micropipette aspiration system. The exclusion criteria were adopted as described in section 2.5.5. The total number of cells used for the micropipette experiment is given in table C1. The number of cells that were used for the SLS model varies from 42% to 75%. However, there was no correlation between the percentages of cells used for SLS model analysis and the experimental groups. Changes of aspirated length with time

are indicated in figure C1. Both undifferentiated hMSCs and cells differentiated to the chondrogenic lineage demonstrate viscoelastic behaviour. All cell groups have exhibited a sudden elongation of aspirated length followed by equilibration which is more obvious for hMSCs differentiated to the chondrogenic lineage than for control cells (Fig. C1 B). Moreover, the plots have demonstrated that aspirated length increased in both undifferentiated hMSCs and differentiated cells treated with cytochalasin D.

Table C.0.1: Number of cells used for micropipette aspiration and calculation of viscoelastic properties using the SLS model.

Cell type	Total No. of cells	No. of successful aspirations	No. used for model $R^2 > 0.95$
hMSC control	36 (100%)	35 (97%)	27 (75%)
hMSC cytoD	45 (100%)	43 (96%)	19 (42%)
Diff control	30 (100%)	30 (100%)	16 (53%)
Diff cytoD	32 (100%)	32 (100%)	22 (73%)
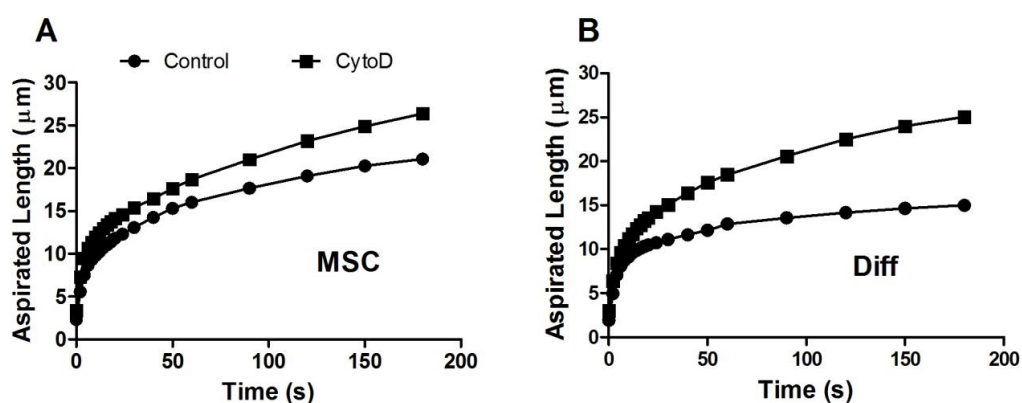
Figure C.0.1: Plots of median aspirated length versus time for cells in response to cytochalasin D treatment. (A) Undifferentiated hMSCs and (B) hMSCs differentiated to the chondrogenic lineage. For number of cells, see table C1.

The results demonstrate that the aspirated length at 180 seconds was longer and significantly different for cells treated with cytochalasin D compared to control

groups (Fig. C2 A). Moreover, the aspirated length was significantly shorter for differentiated cells compared to undifferentiated hMSCs in control groups. However, results show that there was no difference in aspirated length of cells in groups treated with cytochalasin D. In addition the equilibrium and instantaneous moduli significantly decreased for treated cell groups compared to control cell groups (Fig. C2 B and C). Differentiated cells in the control group were found to be significantly stiffer than their undifferentiated hMSC controls. Viscosity significantly increased in differentiated cells treated with cytochalasin D, however the treatment has no effect on undifferentiated hMSCs (Fig. C2 D).
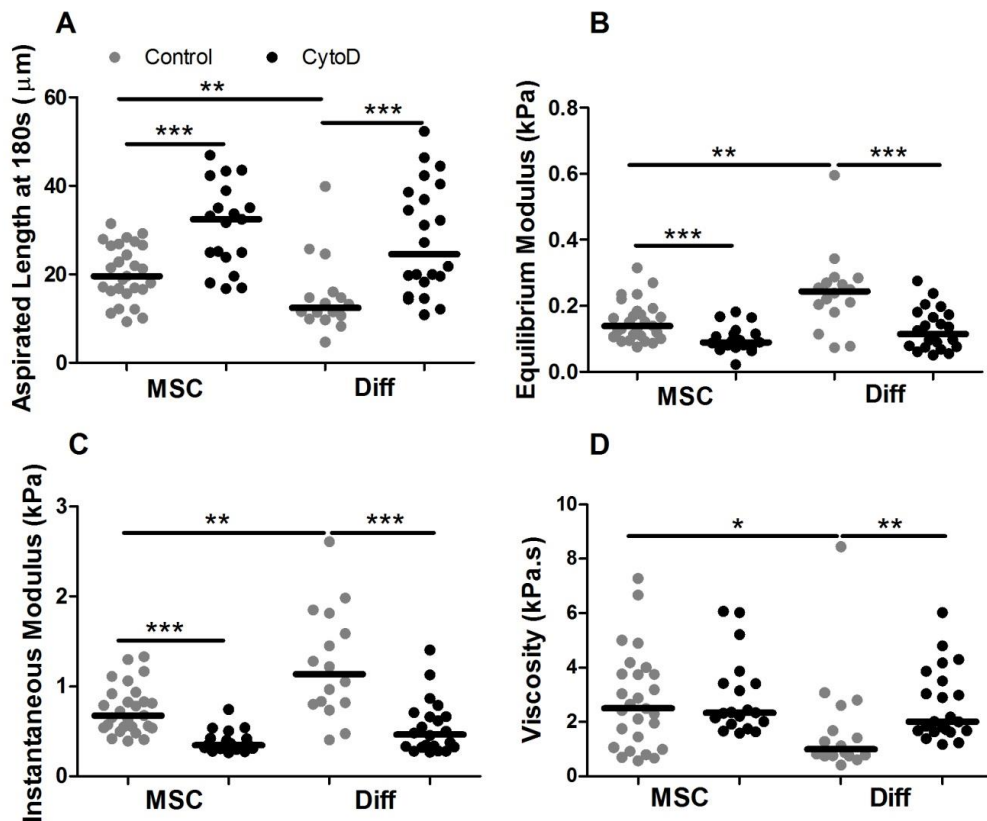
Figure C.0.2: The aspirated length and viscoelastic properties of undifferentiated hMSCs and cells differentiated to the chondrogenic lineage in response to cytochalasin D treatment. (A) The aspirated length at 180 seconds, (B) the equilibrium modulus, (C) the instantaneous modulus and (D) the viscosity of cells used for the micropipette aspiration. The data is presented as a population with median value indicated by bar. Mann Whitney-U test (* $p < 0.05$, ** $p < 0.01$, *** $p < 0.001$).

In conclusion, it needs to be noted that viscoelastic properties of undifferentiated hMSCs and those differentiated to the chondrogenic lineage are dependent on actin disruption and polymerisation. This indicates that the actin cortex plays a crucial role in cell mechanical properties. The present study has demonstrated that cytochalasin D treatment has a higher effect on hMSCs differentiated to the chondrogenic lineage than undifferentiated hMSCs as their equilibrium modulus with median values dropped from 0.24 kPa to 0.11 kPa compared with 0.14 kPa to 0.09 kPa for undifferentiated hMSCs. Furthermore, it was demonstrated that actin disruption with cytochalasin D has an effect on membrane tether elongation in fibroblast cells but no effect on hMSCs (Titushkin and Cho, 2006). hMSCs differentiated to the chondrogenic lineage demonstrated greater cortex organisation (Fig. 5.5), but a higher level of disruption (Fig C2) maybe is due to different size and structure of actin filaments between cell types.

BIBLIOGRAPHY

Abdallah, M., B'Chir Hamzaoui, S., Bouslama, K., Mestiri, H., Harmel, A., Ennafaa, M., M'Rad, S., and Ben Dridi, M. (2005) [Acute pancreatitis associated with hemophagocytic syndrome in systemic lupus erythematous: a case report]. *Gastroenterol Clin Biol* 29(10):1054-1056.

Abdelgawad, M., Chien, W.-Y., Liang, K., and Sun, Y. (2010) Microfluidic platform with circular microchannels for facile cell trapping and single cell analysis. *Proc 14th International Conference on Miniaturized Systems for Chemistry and Life Science*, pp 235-237.

Aizawa, H., Sameshima, M., and Yahara, I. (1997) A green fluorescent protein-actin fusion protein dominantly inhibits cytokinesis, cell spreading, and locomotion in Dictyostelium. *Cell Struct Funct* 22(3):335-345.

Amit, M., Carpenter, M.K., Inokuma, M.S., Chiu, C.P., Harris, C.P., Waknitz, M.A., Itskovitz-Eldor, J., and Thomson, J.A. (2000) Clonally derived human embryonic stem cell lines maintain pluripotency and proliferative potential for prolonged periods of culture. *Dev Biol* 227(2):271-278.

Aplin, A.E., Howe, A., Alahari, S.K., and Juliano, R.L. (1998) Signal transduction and signal modulation by cell adhesion receptors: the role of integrins, cadherins, immunoglobulin-cell adhesion molecules, and selectins. *Pharmacol Rev* 50(2):197-263.

Ashkin, A. (1970) Acceleration and trapping of particles by radiation pressure. *Physical review letters* 24(4):156-159.

Ashkin, A., Dziedzic, J.M., Bjorkholm, J.E., and Chu, S. (1986) Observation of a single-beam gradient force optical trap for dielectric particles. *Opt Lett* 11(5):288.

Ayala, R., Zhang, C., Yang, D., Hwang, Y., Aung, A., Shroff, S.S., Arce, F.T., Lal, R., Arya, G., and Varghese, S. (2011) Engineering the cell–material interface for controlling stem cell adhesion, migration, and differentiation. *Biomaterials* 32(15):3700-3711.

Baaijens, F.P., Trickey, W.R., Laursen, T.A., and Guilak, F. (2005) Large deformation finite element analysis of micropipette aspiration to determine the mechanical properties of the chondrocyte. *Ann Biomed Eng* 33(4):494-501.

Bader, D.L. and Knight, M.M. (2008) Biomechanical analysis of structural deformation in living cells. *Med Biol Eng Comput* 46(10):951-963.

Barfod, E.T., Moore, A.L., Van de Graaf, B.G., and Lidofsky, S.D. (2011) Myosin light chain kinase and Src control membrane dynamics in volume recovery from cell swelling. *Mol Biol Cell* 22(5):634-650.

Benya, P.D. and Shaffer, J.D. (1982) Dedifferentiated chondrocytes reexpress the differentiated collagen phenotype when cultured in agarose gels. *Cell* 30(1):215-224.

Bergert, M., Chandradoss, S.D., Desai, R.A., and Paluch, E. (2012) Cell mechanics control rapid transitions between blebs and lamellipodia during migration. *Proceedings of the National Academy of Sciences* 109(36):14434-14439.

Berryman, M., Franck, Z., and Bretscher, A. (1993) Ezrin is concentrated in the apical microvilli of a wide variety of epithelial cells whereas moesin is found primarily in endothelial cells. *Journal of Cell Science* 105(4):1025-1043.

Bhattacharyya, S. (2012) Advances and Applications in Stem Cell Biology. *Journal of Postgraduate Medicine, Education & Research* 46(2).

Binnig, G., Quate, C.F., and Gerber, C. (1986) Atomic force microscope. *Phys Rev Lett* 56(9):930-933.

Birmingham, E., Niebur, G., and McHugh, P. (2012) Osteogenic differentiation of mesenchymal stem cells is regulated by osteocyte and osteoblast cells in a simplified bone niche. *Eur Cell Mater* 12:13-27.

Blaser, H., Reichman-Fried, M., Castanon, I., Dumstrei, K., Marlow, F.L., Kawakami, K., Solnica-Krezel, L., Heisenberg, C.P., and Raz, E. (2006) Migration of zebrafish primordial germ cells: a role for myosin contraction and cytoplasmic flow. *Dev Cell* 11(5):613-627.

Blewett, J., Burrows, K., and Thomas, C. (2000) A micromanipulation method to measure the mechanical properties of single tomato suspension cells. *Biotechnology Letters* 22(23):1877-1883.

Boudou, T., Ohayon, J., Arntz, Y., Finet, G., Picart, C., and Tracqui, P. (2006) An extended modeling of the micropipette aspiration experiment for the characterization of the Young's modulus and Poisson's ratio of adherent thin biological samples: numerical and experimental studies. *J Biomech* 39(9):1677-1685.

Bougault, C., Aubert-Foucher, E., Paumier, A., Perrier-Groult, E., Huot, L., Hot, D., Duterque-Coquillaud, M., and Mallein-Gerin, F. (2012) Dynamic compression of chondrocyte-agarose constructs reveals new candidate mechanosensitive genes. *PLoS One* 7(5):e36964.

Bovellan, M., Fritzsche, M., Stevens, C., and Charras, G. (2010) Death-associated protein kinase (DAPK) and signal transduction: blebbing in programmed cell death. *FEBS J* 277(1):58-65.

Bovellan, M., Romeo, Y., Biro, M., Boden, A., Chugh, P., Yonis, A., Vaghela, M., Fritzsche, M., Moulding, D., and Thorogate, R. (2014) Cellular Control of Cortical Actin Nucleation. *Current Biology* 24(14):1628-1635.

Bray, D. (2001) *Cell movements: from molecules to motility* (Garland Science).

Bronkhorst, P., Streekstra, G., Grimbergen, J., Nijhof, E., Sixma, J., and Brakenhoff, G. (1995) A new method to study shape recovery of red blood cells using multiple optical trapping. *Biophys J* 69(5):1666-1673.

Brown, J.W. and McKnight, C.J. (2010) Molecular model of the microvillar cytoskeleton and organization of the brush border. *PLoS One* 5(2):e9406.

Bruder, S.P., Jaiswal, N., and Haynesworth, S.E. (1997) Growth kinetics, self-renewal, and the osteogenic potential of purified human mesenchymal stem cells during extensive subcultivation and following cryopreservation. *J Cell Biochem* 64(2):278-294.

Brugues, J., Maugis, B., Casademunt, J., Nassoy, P., Amblard, F., and Sens, P. (2010) Dynamical organization of the cytoskeletal cortex probed by micropipette aspiration. *Proc Natl Acad Sci U S A* 107(35):15415-15420.

Bufi, N., Durand-Smet, P., and Asnacios, A. (2015) Single-cell mechanics: The parallel plates technique. *Methods in Cell Biology*.

Bursac, P., Lenormand, G., Fabry, B., Oliver, M., Weitz, D.A., Viasnoff, V., Butler, J.P., and Fredberg, J.J. (2005) Cytoskeletal remodelling and slow dynamics in the living cell. *Nat Mater* 4(7):557-561.

Campbell, J.J. and Knight, M.M. (2007) An improved confocal FRAP technique for the measurement of long-term actin dynamics in individual stress fibers. *Microsc Res Tech* 70(12):1034-1040.

Cantley, L.C. (2002) The phosphoinositide 3-kinase pathway. *Science* 296(5573):1655-1657.

Cao, C., Dong, Y., and Dong, Y. (2005) [Study on culture and in vitro osteogenesis of blood-derived human mesenchymal stem cells]. *Zhongguo Xiu Fu Chong Jian Wai Ke Za Zhi* 19(8):642-647.

Caplan, A.I. and Bruder, S.P. (2001) Mesenchymal stem cells: building blocks for molecular medicine in the 21st century. *Trends Mol Med* 7(6):259-264.

Chan, C.E. and Odde, D.J. (2008) Traction dynamics of filopodia on compliant substrates. *Science* 322(5908):1687-1691.

Charras, G. and Paluch, E. (2008) Blebs lead the way: how to migrate without lamellipodia. *Nat Rev Mol Cell Biol* 9(9):730-736.

Charras, G.T., Coughlin, M., Mitchison, T.J., and Mahadevan, L. (2008) Life and times of a cellular bleb. *Biophys J* 94(5):1836-1853.

Charras, G.T., Hu, C.K., Coughlin, M., and Mitchison, T.J. (2006) Reassembly of contractile actin cortex in cell blebs. *J Cell Biol* 175(3):477-490.

Charras, G.T., Yarrow, J.C., Horton, M.A., Mahadevan, L., and Mitchison, T.J. (2005) Non-equilibration of hydrostatic pressure in blebbing cells. *Nature* 435(7040):365-369.

Chen, J., Irianto, J., Inamdar, S., Pravincumar, P., Lee, D.A., Bader, D.L., and Knight, M.M. (2012) Cell mechanics, structure, and function are regulated by the stiffness of the three-dimensional microenvironment. *Biophys J* 103(6):1188-1197.

Chen, Q.Y., Xu, W., Jiao, D.M., Wu, L.J., Song, J., Yan, J., and Shi, J.G. (2013) Silence of ezrin modifies migration and actin cytoskeleton rearrangements and enhances chemosensitivity of lung cancer cells in vitro. *Mol Cell Biochem* 377(1-2):207-218.

Chen, S.S., Falcovitz, Y.H., Schneiderman, R., Maroudas, A., and Sah, R.L. (2001) Depth-dependent compressive properties of normal aged human femoral head articular cartilage: relationship to fixed charge density. *Osteoarthritis Cartilage* 9(6):561-569.

Cheung, A., Dantzig, J.A., Hollingworth, S., Baylor, S.M., Goldman, Y.E., Mitchison, T.J., and Straight, A.F. (2002) A small-molecule inhibitor of skeletal muscle myosin II. *Nat Cell Biol* 4(1):83-88.

Chowdhury, T. and Knight, M. (2006) Purinergic pathway suppresses the release of. NO and stimulates proteoglycan synthesis in chondrocyte/agarose constructs subjected to dynamic compression. *Journal of cellular physiology* 209(3):845-853.

Claxton, N.S., Fellers, T.J., and Davidson, M.W. (2006) Laser scanning confocal microscopy. *Department of Optical Microscopy and Digital Imaging, National High Magnetic Field Laboratory, The Florida State University*.

Cojoc, D., Difato, F., Ferrari, E., Shahapure, R.B., Laishram, J., Righi, M., Di Fabrizio, E.M., and Torre, V. (2007) Properties of the force exerted by filopodia and lamellipodia and the involvement of cytoskeletal components. *PLoS One* 2(10):e1072.

Croft, D.R., Coleman, M.L., Li, S., Robertson, D., Sullivan, T., Stewart, C.L., and Olson, M.F. (2005) Actin-myosin–based contraction is responsible for apoptotic nuclear disintegration. *The Journal of cell biology* 168(2):245-255.

Cunningham, C.C. (1995) Actin polymerization and intracellular solvent flow in cell surface blebbing. *J Cell Biol* 129(6):1589-1599.

Cuvelier, D., Derenyi, I., Bassereau, P., and Nassoy, P. (2005) Coalescence of membrane tethers: experiments, theory, and applications. *Biophys J* 88(4):2714-2726.

Dai, J. and Sheetz, M.P. (1999) Membrane tether formation from blebbing cells. *Biophysical journal* 77(6):3363-3370.

Daily, B., Elson, E.L., and Zahalak, G.I. (1984) Cell poking. Determination of the elastic area compressibility modulus of the erythrocyte membrane. *Biophys J* 45(4):671-682.

Darling, E.M., Pritchett, P.E., Evans, B.A., Superfine, R., Zauscher, S., and Guilak, F. (2009) Mechanical properties and gene expression of chondrocytes on micropatterned substrates following dedifferentiation in monolayer. *Cell Mol Bioeng* 2(3):395-404.

Darling, E.M., Topel, M., Zauscher, S., Vail, T.P., and Guilak, F. (2008) Viscoelastic properties of human mesenchymally-derived stem cells and primary osteoblasts, chondrocytes, and adipocytes. *J Biomech* 41(2):454-464.

Datar, A., Bornschlögl, T., Bassereau, P., Prost, J., and Pullarkat, P.A. (2015) Dynamics of Membrane Tethers Reveal Novel Aspects of Cytoskeleton-Membrane Interactions in Axons. *Biophysical journal* 108(3):489-497.

Deguchi, S., Ohashi, T., and Sato, M. (2006) Tensile properties of single stress fibers isolated from cultured vascular smooth muscle cells. *J Biomech* 39(14):2603-2610.

Digirolamo, C.M., Stokes, D., Colter, D., Phinney, D.G., Class, R., and Prockop, D.J. (1999) Propagation and senescence of human marrow stromal cells in culture: a simple colony-forming assay identifies samples with the greatest potential to propagate and differentiate. *Br J Haematol* 107(2):275-281.

Discher, D.E. (2000) New insights into erythrocyte membrane organization and microelasticity. *Current opinion in hematology* 7(2):117-122.

Diz-Munoz, A., Krieg, M., Bergert, M., Ibarlucea-Benitez, I., Muller, D.J., Paluch, E., and Heisenberg, C.P. (2010) Control of directed cell migration in vivo by membrane-to-cortex attachment. *PLoS Biol* 8(11):e1000544.

Docheva, D., Haasters, F., and Schieker, M. (2008) Mesenchymal stem cells and their cell surface receptors. *Current Rheumatology Reviews* 4(3):155-160.

Dominici, M., Le Blanc, K., Mueller, I., Slaper-Cortenbach, I., Marini, F., Krause, D., Deans, R., Keating, A., Prockop, D., and Horwitz, E. (2006) Minimal criteria for defining multipotent mesenchymal stromal cells. The International Society for Cellular Therapy position statement. *Cytotherapy* 8(4):315-317.

Dufrene, Y.F. (2002) Atomic force microscopy, a powerful tool in microbiology. *J Bacteriol* 184(19):5205-5213.

Duszyk, M., Schwab, B., 3rd, Zahalak, G.I., Qian, H., and Elson, E.L. (1989) Cell poking: quantitative analysis of indentation of thick viscoelastic layers. *Biophys J* 55(4):683-690.

Endlich, N., Otey, C.A., Kriz, W., and Endlich, K. (2007) Movement of stress fibers away from focal adhesions identifies focal adhesions as sites of stress fiber assembly in stationary cells. *Cell motility and the cytoskeleton* 64(12):966-976.

Engelke, H., Heinrich, D., and Rädler, J.O. (2010) Probing GFP-actin diffusion in living cells using fluorescence correlation spectroscopy. *Physical biology* 7(4):046014.

Engler, A.J., Sen, S., Sweeney, H.L., and Discher, D.E. (2006) Matrix elasticity directs stem cell lineage specification. *Cell* 126(4):677-689.

Engström, K.G. and Meiselman, H.J. (1994) Optical and mathematical corrections of micropipette measurements of red blood cell geometry during anisotonic perifusion. *Cytometry* 17(4):279-286.

Erickson, C. and Trinkaus, J. (1976) Microvilli and blebs as sources of reserve surface membrane during cell spreading. *Experimental cell research* 99(2):375-384.

Esue, O., Tseng, Y., and Wirtz, D. (2009) Alpha-actinin and filamin cooperatively enhance the stiffness of actin filament networks. *PLoS One* 4(2):e4411.

Evans, E. and Yeung, A. (1989) Apparent viscosity and cortical tension of blood granulocytes determined by micropipet aspiration. *Biophys J* 56(1):151-160.

Evans, E.A. (1983) Bending elastic modulus of red blood cell membrane derived from buckling instability in micropipet aspiration tests. *Biophys J* 43(1):27-30.

Evans, M.J. and Kaufman, M.H. (1981) Establishment in culture of pluripotential cells from mouse embryos. *Nature* 292(5819):154-156.

Faix, J. and Rottner, K. (2006) The making of filopodia. *Curr Opin Cell Biol* 18(1):18-25.

Falah, M., Nierenberg, G., Soudry, M., Hayden, M., and Volpin, G. (2010) Treatment of articular cartilage lesions of the knee. *International orthopaedics* 34(5):621-630.

Fath, K.R. and Burgess, D.R. (1995) Microvillus assembly: not actin alone. *Current Biology* 5(6):591-593.

Fehon, R.G., McClatchey, A.I., and Bretscher, A. (2010) Organizing the cell cortex: the role of ERM proteins. *Nat Rev Mol Cell Biol* 11(4):276-287.

Feng, Z., Ning Chen, W., Vee Sin Lee, P., Liao, K., and Chan, V. (2005) The influence of GFP-actin expression on the adhesion dynamics of HepG2 cells on a model extracellular matrix. *Biomaterials* 26(26):5348-5358.

Fischer, R.S., Gardel, M., Ma, X., Adelstein, R.S., and Waterman, C.M. (2009) Local cortical tension by myosin II guides 3D endothelial cell branching. *Curr Biol* 19(3):260-265.

Fletcher, D.A. and Mullins, R.D. (2010) Cell mechanics and the cytoskeleton. *Nature* 463(7280):485-492.

Freeman, P.M., Natarajan, R.N., Kimura, J.H., and Andriacchi, T.P. (1994) Chondrocyte cells respond mechanically to compressive loads. *J Orthop Res* 12(3):311-320.

Friedenstein, A.J., Gorskaja, J.F., and Kulagina, N.N. (1976) Fibroblast precursors in normal and irradiated mouse hematopoietic organs. *Exp Hematol* 4(5):267-274.

Friedl, P., Borgmann, S., and Bröcker, E.-B. (2001) Amoeboid leukocyte crawling through extracellular matrix: lessons from the Dictyostelium paradigm of cell movement. *Journal of leukocyte biology* 70(4):491-509.

Friedl, P. and Gilmour, D. (2009) Collective cell migration in morphogenesis, regeneration and cancer. *Nature reviews Molecular cell biology* 10(7):445-457.

Friedl, P. and Wolf, K. (2003) Tumour-cell invasion and migration: diversity and escape mechanisms. *Nat Rev Cancer* 3(5):362-374.

Friedl, P. and Wolf, K. (2010) Plasticity of cell migration: a multiscale tuning model. *J Cell Biol* 188(1):11-19.

Gaboriaud, F., Parcha, B.S., Gee, M.L., Holden, J.A., and Strugnell, R.A. (2008) Spatially resolved force spectroscopy of bacterial surfaces using force-volume imaging. *Colloids and Surfaces B: Biointerfaces* 62(2):206-213.

Gardel, M., Nakamura, F., Hartwig, J., Crocker, J.C., Stossel, T., and Weitz, D. (2006) Stress-dependent elasticity of composite actin networks as a model for cell behavior. *Physical review letters* 96(8):088102.

Gardel, M.L., Sabass, B., Ji, L., Danuser, G., Schwarz, U.S., and Waterman, C.M. (2008) Traction stress in focal adhesions correlates biphasically with actin retrograde flow speed. *J Cell Biol* 183(6):999-1005.

Gardel, M.L., Shin, J.H., MacKintosh, F.C., Mahadevan, L., Matsudaira, P., and Weitz, D.A. (2004) Elastic behavior of cross-linked and bundled actin networks. *Science* 304(5675):1301-1305.

Gary, R. and Bretscher, A. (1995) Ezrin self-association involves binding of an N-terminal domain to a normally masked C-terminal domain that includes the F-actin binding site. *Molecular Biology of the Cell* 6(8):1061-1075.

Gennis, R.B. (1989) *Biomembranes: molecular structure and function* (Springer-Verlag New York).

Gittes, F., Mickey, B., Nettleton, J., and Howard, J. (1993) Flexural rigidity of microtubules and actin filaments measured from thermal fluctuations in shape. *J Cell Biol* 120(4):923-934.

Goessler, U.R., Bugert, P., Bieback, K., Sadick, H., Verse, T., Baisch, A., Hormann, K., and Riedel, F. (2005) In vitro analysis of matrix proteins and growth factors in dedifferentiating human chondrocytes for tissue-engineered cartilage. *Acta Otolaryngol* 125(6):647-653.

Goldmann, W.H. (2000) Mechanical manipulation of animal cells: cell indentation. *Biotechnology Letters* 22(6):431-435.

Gonzalez-Cruz, R.D., Fonseca, V.C., and Darling, E.M. (2012) Cellular mechanical properties reflect the differentiation potential of adipose-derived mesenchymal stem cells. *Proc Natl Acad Sci U S A* 109(24):E1523-1529.

Goudarzi, M., Banisch, T.U., Mobin, M.B., Maghelli, N., Tarbashevich, K., Strate, I., van den Berg, J., Blaser, H., Bandemer, S., and Paluch, E. (2012) Identification and regulation of a molecular module for bleb-based cell motility. *Developmental cell* 23(1):210-218.

Green, R.A., Paluch, E., and Oegema, K. (2012) Cytokinesis in animal cells. *Annual review of cell and developmental biology* 28:29-58.

Guck, J., Ananthakrishnan, R., Mahmood, H., Moon, T.J., Cunningham, C.C., and Kas, J. (2001) The optical stretcher: a novel laser tool to micromanipulate cells. *Biophys J* 81(2):767-784.

Guck, J., Ananthakrishnan, R., Moon, T.J., Cunningham, C.C., and Kas, J. (2000) Optical deformability of soft biological dielectrics. *Phys Rev Lett* 84(23):5451-5454.

Guck, J., Lautenschlager, F., Paschke, S., and Beil, M. (2010) Critical review: cellular mechanobiology and amoeboid migration. *Integr Biol (Camb)* 2(11-12):575-583.

Guilak, F. (1995) Compression-induced changes in the shape and volume of the chondrocyte nucleus. *J Biomech* 28(12):1529-1541.

Guilak, F., Erickson, G.R., and Ting-Beall, H.P. (2002) The effects of osmotic stress on the viscoelastic and physical properties of articular chondrocytes. *Biophys J* 82(2):720-727.

Guvendiren, M. and Burdick, J.A. (2010) The control of stem cell morphology and differentiation by hydrogel surface wrinkles. *Biomaterials* 31(25):6511-6518.

Heiska, L., Alfthan, K., Gronholm, M., Vilja, P., Vaheri, A., and Carpen, O. (1998) Association of ezrin with intercellular adhesion molecule-1 and -2 (ICAM-1 and ICAM-2). Regulation by phosphatidylinositol 4, 5-bisphosphate. *J Biol Chem* 273(34):21893-21900.

Hemsley, A.L., Hernandez, D., Mason, C., Pelling, A., and Veraitch, F. (2011) Precisely delivered nanomechanical forces induce blebbing in undifferentiated mouse embryonic stem cells. *Cell Health and Cytoskeleton* 3(1):23-34.

Heng, Y.W. and Koh, C.G. (2010) Actin cytoskeleton dynamics and the cell division cycle. *Int J Biochem Cell Biol* 42(10):1622-1633.

Henon, S., Lenormand, G., Richert, A., and Gallet, F. (1999) A new determination of the shear modulus of the human erythrocyte membrane using optical tweezers. *Biophysical journal* 76(2):1145-1151.

Hirao, M., Sato, N., Kondo, T., Yonemura, S., Monden, M., Sasaki, T., Takai, Y., Tsukita, S., and Tsukita, S. (1996) Regulation mechanism of ERM (ezrin/radixin/moesin) protein/plasma membrane association: possible involvement of phosphatidylinositol turnover and Rho-dependent signaling pathway. *J Cell Biol* 135(1):37-51.

Hochmuth, R.M. (2000) Micropipette aspiration of living cells. *J Biomech* 33(1):15-22.

Hochmuth, R.M. and Marcus, W.D. (2002) Membrane tethers formed from blood cells with available area and determination of their adhesion energy. *Biophys J* 82(6):2964-2969.

Hsiao, S.C., Crow, A.K., Lam, W.A., Bertozzi, C.R., Fletcher, D.A., and Francis, M.B. (2008) DNA-coated AFM cantilevers for the investigation of cell adhesion and the patterning of live cells. *Angew Chem Int Ed Engl* 47(44):8473-8477.

Huang, C., Rajfur, Z., Borchers, C., Schaller, M.D., and Jacobson, K. (2003) JNK phosphorylates paxillin and regulates cell migration. *Nature* 424(6945):219-223.

Hunter, K.W. (2004) Ezrin, a key component in tumor metastasis. *Trends Mol Med* 10(5):201-204.

Ishii, M., Koike, C., Igarashi, A., Yamanaka, K., Pan, H., Higashi, Y., Kawaguchi, H., Sugiyama, M., Kamata, N., Iwata, T., Matsubara, T., Nakamura, K., Kurihara, H., Tsuji, K., and Kato, Y. (2005) Molecular markers distinguish bone marrow mesenchymal stem cells from fibroblasts. *Biochem Biophys Res Commun* 332(1):297-303.

Itoh, T., Erdmann, K.S., Roux, A., Habermann, B., Werner, H., and De Camilli, P. (2005) Dynamin and the actin cytoskeleton cooperatively regulate plasma membrane invagination by BAR and F-BAR proteins. *Dev Cell* 9(6):791-804.

Jaasma, M.J., Jackson, W.M., and Keaveny, T.M. (2006) The effects of morphology, confluency, and phenotype on whole-cell mechanical behavior. *Ann Biomed Eng* 34(5):759-768.

Janmey, P.A. and Kinnunen, P.K. (2006) Biophysical properties of lipids and dynamic membranes. *Trends Cell Biol* 16(10):538-546.

Jiang, Q.Y., Xia, J.M., Ding, H.G., Fei, X.W., Lin, J., and Wu, R.J. (2012) RNAi-mediated blocking of ezrin reduces migration of ectopic endometrial cells in endometriosis. *Mol Hum Reprod* 18(9):435-441.

Johnstone, B., Hering, T.M., Caplan, A.I., Goldberg, V.M., and Yoo, J.U. (1998) <i> In Vitro</i> Chondrogenesis of Bone Marrow-Derived Mesenchymal Progenitor Cells. *Experimental cell research* 238(1):265-272.

Jones, W.R., Ting-Beall, H.P., Lee, G.M., Kelley, S.S., Hochmuth, R.M., and Guilak, F. (1999) Alterations in the Young's modulus and volumetric

properties of chondrocytes isolated from normal and osteoarthritic human cartilage. *J Biomech* 32(2):119-127.

Jurado, C., Haserick, J.R., and Lee, J. (2005) Slipping or gripping? Fluorescent speckle microscopy in fish keratocytes reveals two different mechanisms for generating a retrograde flow of actin. *Mol Biol Cell* 16(2):507-518.

Kamm, R., Lammerding, J., and Mofrad, M. (2010) Cellular nanomechanics. *Springer Handbook of Nanotechnology*, (Springer), pp 1171-1200.

Kim, J., Lee, K., Jee, H., Oh, K., and Yoon, Y.-K. (2010) Fabrication of multiple height microstructures using UV lithography on timed-development-and-thermal-reflowed photoresist. *Micro Electro Mechanical Systems (MEMS), 2010 IEEE 23rd International Conference on*, (IEEE), pp 376-379.

Kim, W. and Han, A. (2011) *A micro-aspirator chip using vacuum expanded microchannels for high-throughput mechanical characterization of biological cells* (Texas A&M University).

Knight, M.M., Bomzon, Z., Kimmel, E., Sharma, A.M., Lee, D.A., and Bader, D.L. (2006) Chondrocyte deformation induces mitochondrial distortion and heterogeneous intracellular strain fields. *Biomech Model Mechanobiol* 5(2-3):180-191.

Knight, M.M., van de Breevaart Bravenboer, J., Lee, D.A., van Osch, G.J., Weinans, H., and Bader, D.L. (2002) Cell and nucleus deformation in compressed chondrocyte-alginate constructs: temporal changes and calculation of cell modulus. *Biochim Biophys Acta* 1570(1):1-8.

Koay, E.J., Hu, J.C., Lin, P., Athanasiou, K.A., Ofek, G., and Willard, V.P. (2009) Mechanical characterization of differentiated human embryonic stem cells. *Journal of biomechanical engineering* 131(6):061011.

Krawczyk, W.S. (1971) A pattern of epidermal cell migration during wound healing. *J Cell Biol* 49(2):247-263.

Kujawska, T., Wójcik, J., and Filipczyński, L. (2004) Possible temperature effects computed for acoustic microscopy used for living cells. *Ultrasound in medicine & biology* 30(1):93-101.

Kung, C. (2005) A possible unifying principle for mechanosensation. *Nature* 436(7051):647-654.

Lai, W.M., Hou, J.S., and Mow, V.C. (1991) A triphasic theory for the swelling and deformation behaviors of articular cartilage. *J Biomech Eng* 113(3):245-258.

Lämmermann, T. and Sixt, M. (2009) Mechanical modes of 'amoeboid'cell migration. *Current opinion in cell biology* 21(5):636-644.

Le Clainche, C. and Carlier, M.F. (2008) Regulation of actin assembly associated with protrusion and adhesion in cell migration. *Physiol Rev* 88(2):489-513.

Lee, C.W., Vitriol, E.A., Shim, S., Wise, A.L., Velayutham, R.P., and Zheng, J.Q. (2013) Dynamic localization of G-actin during membrane protrusion in neuronal motility. *Curr Biol* 23(12):1046-1056.

Lee, D.A., Noguchi, T., Knight, M.M., O'donnell, L., Bentley, G., and Bader, D.L. (1998) Response of chondrocyte subpopulations cultured within unloaded and loaded agarose. *Journal of orthopaedic research* 16(6):726-733.

Letourneau, P.C. (2009) Actin in axons: stable scaffolds and dynamic filaments. *Cell Biology of the Axon*, (Springer), pp 265-290.

Li, L. and Xie, T. (2005) Stem cell niche: structure and function. *Annu Rev Cell Dev Biol* 21:605-631.

Lieleg, O., Claessens, M.M., and Bausch, A.R. (2010) Structure and dynamics of cross-linked actin networks. *Soft Matter* 6(2):218-225.

Lim, C., Zhou, E., Li, A., Vedula, S., and Fu, H. (2006) Experimental techniques for single cell and single molecule biomechanics. *Materials Science and Engineering: C* 26(8):1278-1288.

Liu, Y.-J., Le Berre, M., Lautenschlaeger, F., Maiuri, P., Callan-Jones, A., Heuzé, M., Takaki, T., Voituriez, R., and Piel, M. (2015) Confinement and low adhesion induce fast amoeboid migration of slow mesenchymal cells. *Cell* 160(4):659-672.

Lodish, H., Berk, A., Zipursky, S.L., Matsudaira, P., Baltimore, D., and Darnell, J. (2000) The actin cytoskeleton.

Louvet-Vallee, S. (2000) ERM proteins: from cellular architecture to cell signaling. *Biol Cell* 92(5):305-316.

Lu, L., Oswald, S.J., Ngu, H., and Yin, F.C. (2008) Mechanical properties of actin stress fibers in living cells. *Biophys J* 95(12):6060-6071.

MacKintosh, F.C., Kas, J., and Janmey, P.A. (1995) Elasticity of semiflexible biopolymer networks. *Phys Rev Lett* 75(24):4425-4428.

Mallavarapu, A. and Mitchison, T. (1999) Regulated actin cytoskeleton assembly at filopodium tips controls their extension and retraction. *The Journal of Cell Biology* 146(5):1097-1106.

Maver, U., Maver, T., Peršin, Z., Mozetič, M., Vesel, A., Gaberšček, M., and Stana-Kleinschek, K. (2013) Polymer Characterization with the Atomic Force Microscope.

McNamara, L.E., McMurray, R.J., Biggs, M.J., Kantawong, F., Oreffo, R.O., and Dalby, M.J. (2010) Nanotopographical control of stem cell differentiation. *Journal of tissue engineering* 1(1):120623.

Merkel, R., Simson, R., Simson, D.A., Hohenadl, M., Boulbitch, A., Wallraff, E., and Sackmann, E. (2000) A Micromechanic Study of Cell Polarity and

Plasma Membrane Cell Body Coupling in Dictyostelium. *Biophysical journal* 79(2):707-719.

Merryman, W.D., Bieniek, P.D., Guilak, F., and Sacks, M.S. (2009) Viscoelastic properties of the aortic valve interstitial cell. *J Biomech Eng* 131(4):041005.

Mironov, V., Visconti, R., and Markwald, R. (2004) What is regenerative medicine? Emergence of applied stem cell and developmental biology. *Expert opinion on biological therapy* 4(6):773-781.

Mitchison, T.J. and Cramer, L.P. (1996) Actin-based cell motility and cell locomotion. *Cell* 84(3):371-379.

Mobasheri, A., Kalamegam, G., Musumeci, G., and Batt, M.E. (2014) Chondrocyte and mesenchymal stem cell-based therapies for cartilage repair in osteoarthritis and related orthopaedic conditions. *Maturitas*.

Mofrad, M.R. and Kamm, R.D. (2006) *Cytoskeletal Mechanics: Models and Measurements in Cell Mechanics* (Cambridge University Press).

Nicotera, P., Leist, M., and Ferrando-May, E. (1999) Apoptosis and necrosis: different execution of the same death. *Biochem Soc Symp*, pp 69-73.

Nobes, C.D. and Hall, A. (1999) Rho GTPases control polarity, protrusion, and adhesion during cell movement. *J Cell Biol* 144(6):1235-1244.

Noguchi, T. and Mabuchi, I. (2001) Reorganization of actin cytoskeleton at the growing end of the cleavage furrow of Xenopus egg during cytokinesis. *Journal of cell science* 114(2):401-412.

Pablo Rodríguez, J., González, M., Ríos, S., and Cambiazo, V. (2004) Cytoskeletal organization of human mesenchymal stem cells (MSC) changes during their osteogenic differentiation. *Journal of cellular biochemistry* 93(4):721-731.

Pajerowski, J.D., Dahl, K.N., Zhong, F.L., Sammak, P.J., and Discher, D.E. (2007) Physical plasticity of the nucleus in stem cell differentiation. *Proc Natl Acad Sci U S A* 104(40):15619-15624.

Paluch, E., Piel, M., Prost, J., Bornens, M., and Sykes, C. (2005) Cortical actomyosin breakage triggers shape oscillations in cells and cell fragments. *Biophys J* 89(1):724-733.

Paluch, E.K. and Raz, E. (2013) The role and regulation of blebs in cell migration. *Current opinion in cell biology* 25(5):582-590.

Pattappa, G., Thorpe, S.D., Jegard, N.C., Heywood, H.K., de Bruijn, J.D., and Lee, D.A. (2013) Continuous and uninterrupted oxygen tension influences the colony formation and oxidative metabolism of human mesenchymal stem cells. *Tissue Eng Part C Methods* 19(1):68-79.

Peeters, E.A., Oomens, C.W., Bouten, C.V., Bader, D.L., and Baaijens, F.P. (2005) Mechanical and failure properties of single attached cells under compression. *J Biomech* 38(8):1685-1693.

Pellegrin, S. and Mellor, H. (2007) Actin stress fibres. *Journal of cell science* 120(20):3491-3499.

Petrie, R.J. and Yamada, K.M. (2012) At the leading edge of three-dimensional cell migration. *Journal of cell science* 125(24):5917-5926.

Phair, R.D., Gorski, S.A., and Misteli, T. (2003) Measurement of dynamic protein binding to chromatin in vivo, using photobleaching microscopy. *Methods in enzymology* 375:393-414.

Pittenger, M.F., Mackay, A.M., Beck, S.C., Jaiswal, R.K., Douglas, R., Mosca, J.D., Moorman, M.A., Simonetti, D.W., Craig, S., and Marshak, D.R. (1999) Multilineage potential of adult human mesenchymal stem cells. *Science* 284(5411):143-147.

Pollard, T.D., Blanchoin, L., and Mullins, R.D. (2000) Molecular mechanisms controlling actin filament dynamics in nonmuscle cells. *Annu Rev Biophys Biomol Struct* 29(1):545-576.

Pollard, T.D. and Borisy, G.G. (2003) Cellular motility driven by assembly and disassembly of actin filaments. *Cell* 112(4):453-465.

Pollard, T.D. and Cooper, J.A. (2009) Actin, a central player in cell shape and movement. *Science* 326(5957):1208-1212.

Ponti, A., Machacek, M., Gupton, S.L., Waterman-Storer, C.M., and Danuser, G. (2004) Two distinct actin networks drive the protrusion of migrating cells. *Science* 305(5691):1782-1786.

Poole, C.A. (1997) Review. Articular cartilage chondrons: form, function and failure. *Journal of anatomy* 191(1):1-13.

Pravincumar, P., Bader, D.L., and Knight, M.M. (2012) Viscoelastic cell mechanics and actin remodelling are dependent on the rate of applied pressure. *PLoS One* 7(9):e43938.

Ra, H.J., Picart, C., Feng, H., Sweeney, H.L., and Discher, D.E. (1999) Muscle cell peeling from micropatterned collagen: direct probing of focal and molecular properties of matrix adhesion. *J Cell Sci* 112 (Pt 10)(10):1425-1436.

Rand, R.P. and Burton, A.C. (1964) Mechanical Properties of the Red Cell Membrane. I. Membrane Stiffness and Intracellular Pressure. *Biophys J* 4(2):115-135.

Rapsomaniki, M.A., Kotsantis, P., Symeonidou, I.E., Giakoumakis, N.N., Taraviras, S., and Lygerou, Z. (2012) easyFRAP: an interactive, easy-to-use tool for qualitative and quantitative analysis of FRAP data. *Bioinformatics* 28(13):1800-1801.

Reilly, G.C. and Engler, A.J. (2010) Intrinsic extracellular matrix properties regulate stem cell differentiation. *Journal of biomechanics* 43(1):55-62.

Rentsch, P.S. and Keller, H. (2000) Suction pressure can induce uncoupling of the plasma membrane from cortical actin. *Eur J Cell Biol* 79(12):975-981.

Revenu, C., Ubelmann, F., Hurbain, I., El-Marjou, F., Dingli, F., Loew, D., Delacour, D., Gilet, J., Brot-Laroche, E., Rivero, F., Louvard, D., and Robine, S. (2012) A new role for the architecture of microvillar actin bundles in apical retention of membrane proteins. *Mol Biol Cell* 23(2):324-336.

Reyes, M., Lund, T., Lenvik, T., Aguiar, D., Koodie, L., and Verfaillie, C.M. (2001) Purification and ex vivo expansion of postnatal human marrow mesodermal progenitor cells. *Blood* 98(9):2615-2625.

Ribeiro, A.J., Tottey, S., Taylor, R.W., Bise, R., Kanade, T., Badylak, S.F., and Dahl, K.N. (2012) Mechanical characterization of adult stem cells from bone marrow and perivascular niches. *J Biomech* 45(7):1280-1287.

Ridley, A.J. (2011) Life at the leading edge. *Cell* 145(7):1012-1022.

Riedl, J., Crevenna, A.H., Kessenbrock, K., Yu, J.H., Neukirchen, D., Bista, M., Bradke, F., Jenne, D., Holak, T.A., Werb, Z., Sixt, M., and Wedlich-Soldner, R. (2008) Lifeact: a versatile marker to visualize F-actin. *Nat Methods* 5(7):605-607.

Risler, T. (2009) CytoskeletonCytoskeleton and Cell Motility. *Encyclopedia of Complexity and Systems Science*, (Springer), pp 1738-1774.

Ruprecht, V., Wieser, S., Callan-Jones, A., Smutny, M., Morita, H., Sako, K., Barone, V., Ritsch-Marte, M., Sixt, M., and Voituriez, R. (2015) Cortical contractility triggers a stochastic switch to fast amoeboid cell motility. *Cell* 160(4):673-685.

Sato, M., Theret, D.P., Wheeler, L.T., Ohshima, N., and Nerem, R.M. (1990) Application of the micropipette technique to the measurement of cultured porcine aortic endothelial cell viscoelastic properties. *J Biomech Eng* 112(3):263-268.

Sato, N., Funayama, N., Nagafuchi, A., Yonemura, S., and Tsukita, S. (1992) A gene family consisting of ezrin, radixin and moesin. Its specific localization at actin filament/plasma membrane association sites. *Journal of Cell Science* 103(1):131-143.

Schirenbeck, A., Bretschneider, T., Arasada, R., Schleicher, M., and Faix, J. (2005) The Diaphanous-related formin dDia2 is required for the formation and maintenance of filopodia. *Nature cell biology* 7(6):619-625.

Schnabel, M., Marlovits, S., Eckhoff, G., Fichtel, I., Gotzen, L., Vecsei, V., and Schlegel, J. (2002) Dedifferentiation-associated changes in morphology and gene expression in primary human articular chondrocytes in cell culture. *Osteoarthritis Cartilage* 10(1):62-70.

Schutz, K. and Keller, H. (1998) Protrusion, contraction and segregation of membrane components associated with passive deformation and shape recovery of Walker carcinosarcoma cells. *Eur J Cell Biol* 77(2):100-110.

Segundo, C., Medina, F., Rodriguez, C., Martinez-Palencia, R., Leyva-Cobian, F., and Brieva, J.A. (1999) Surface molecule loss and bleb formation by human germinal center B cells undergoing apoptosis: role of apoptotic blebs in monocyte chemotaxis. *Blood* 94(3):1012-1020.

Sen, B., Xie, Z., Case, N., Styner, M., Rubin, C.T., and Rubin, J. (2011) Mechanical signal influence on mesenchymal stem cell fate is enhanced by incorporation of refractory periods into the loading regimen. *Journal of biomechanics* 44(4):593-599.

Sheetz, M.P., Sable, J.E., and Dobereiner, H.G. (2006) Continuous membrane-cytoskeleton adhesion requires continuous accommodation to lipid and cytoskeleton dynamics. *Annu Rev Biophys Biomol Struct* 35:417-434.

Shiu, C., Zhang, Z., and Thomas, C. (1999) A novel technique for the study of bacterial cell mechanical properties. *Biotechnology techniques* 13(10):707-713.

Siczkowski, M. and Watt, F.M. (1990) Subpopulations of chondrocytes from different zones of pig articular cartilage. Isolation, growth and proteoglycan synthesis in culture. *J Cell Sci* 97 (Pt 2)(2):349-360.

Sliogeryte, K., Thorpe, S.D., Lee, D.A., Botto, L., and Knight, M.M. (2014) Stem cell differentiation increases membrane-actin adhesion regulating cell blebability, migration and mechanics. *Sci Rep* 4:7307.

Smith, A.E., Zhang, Z., Thomas, C.R., Moxham, K.E., and Middelberg, A.P. (2000) The mechanical properties of Saccharomyces cerevisiae. *Proc Natl Acad Sci U S A* 97(18):9871-9874.

Solon, J., Levental, I., Sengupta, K., Georges, P.C., and Janmey, P.A. (2007) Fibroblast adaptation and stiffness matching to soft elastic substrates. *Biophys J* 93(12):4453-4461.

Stamenovic, D. and Ingber, D.E. (2002) Models of cytoskeletal mechanics of adherent cells. *Biomech Model Mechanobiol* 1(1):95-108.

Stricker, J., Falzone, T., and Gardel, M.L. (2010) Mechanics of the F-actin cytoskeleton. *J Biomech* 43(1):9-14.

Strohm, E.M. and Kolios, M.C. (2009) Measuring the mechanical properties of cells using acoustic microscopy. *Engineering in Medicine and Biology Society, 2009. EMBC 2009. Annual International Conference of the IEEE*, (IEEE), pp 6042-6045.

Sumanasinghe, R.D., Bernacki, S.H., and Loboa, E.G. (2006) Osteogenic differentiation of human mesenchymal stem cells in collagen matrices: effect

of uniaxial cyclic tensile strain on bone morphogenetic protein (BMP-2) mRNA expression. *Tissue Eng* 12(12):3459-3465.

Svitkina, T.M., Verkhovsky, A.B., McQuade, K.M., and Borisy, G.G. (1997) Analysis of the actin-myosin II system in fish epidermal keratocytes: mechanism of cell body translocation. *J Cell Biol* 139(2):397-415.

Takeda, T. and Chang, F. (2005) Role of fission yeast myosin I in organization of sterol-rich membrane domains. *Curr Biol* 15(14):1331-1336.

Tan, S.C., Pan, W.X., Ma, G., Cai, N., Leong, K.W., and Liao, K. (2008a) Viscoelastic behaviour of human mesenchymal stem cells. *BMC Cell Biol* 9:40.

Tan, S.C., Pan, W.X., Ma, G., Cai, N., Leong, K.W., and Liao, K. (2008b) Viscoelastic behaviour of human mesenchymal stem cells. *BMC Cell Biol* 9(1):40.

Theret, D.P., Levesque, M.J., Sato, M., Nerem, R.M., and Wheeler, L.T. (1988) The application of a homogeneous half-space model in the analysis of endothelial cell micropipette measurements. *J Biomech Eng* 110(3):190-199.

Thomson, J.A., Itskovitz-Eldor, J., Shapiro, S.S., Waknitz, M.A., Swiergiel, J.J., Marshall, V.S., and Jones, J.M. (1998) Embryonic stem cell lines derived from human blastocysts. *Science* 282(5391):1145-1147.

Thorpe, S.D., Buckley, C.T., Vinardell, T., O'Brien, F.J., Campbell, V.A., and Kelly, D.J. (2010) The response of bone marrow-derived mesenchymal stem cells to dynamic compression following TGF-beta3 induced chondrogenic differentiation. *Ann Biomed Eng* 38(9):2896-2909.

Thoumine, O. and Ott, A. (1997) Time scale dependent viscoelastic and contractile regimes in fibroblasts probed by microplate manipulation. *J Cell Sci* 110 (Pt 17)(17):2109-2116.

Thoumine, O., Ott, A., Cardoso, O., and Meister, J.J. (1999) Microplates: a new tool for manipulation and mechanical perturbation of individual cells. *J Biochem Biophys Methods* 39(1-2):47-62.

Tinevez, J.Y., Schulze, U., Salbreux, G., Roensch, J., Joanny, J.F., and Paluch, E. (2009) Role of cortical tension in bleb growth. *Proc Natl Acad Sci U S A* 106(44):18581-18586.

Titushkin, I. and Cho, M. (2006) Distinct membrane mechanical properties of human mesenchymal stem cells determined using laser optical tweezers. *Biophys J* 90(7):2582-2591.

Titushkin, I. and Cho, M. (2009) Regulation of cell cytoskeleton and membrane mechanics by electric field: role of linker proteins. *Biophys J* 96(2):717-728.

Titushkin, I. and Cho, M. (2011) Altered osteogenic commitment of human mesenchymal stem cells by ERM protein-dependent modulation of cellular biomechanics. *J Biomech* 44(15):2692-2698.

Titushkin, I., Sun, S., Paul, A., and Cho, M. (2013) Control of adipogenesis by ezrin, radixin and moesin-dependent biomechanics remodeling. *J Biomech* 46(3):521-526.

Titushkin, I.A. and Cho, M.R. (2009) Controlling cellular biomechanics of human mesenchymal stem cells. *Engineering in Medicine and Biology Society, 2009. EMBC 2009. Annual International Conference of the IEEE*, (IEEE), pp 2090-2093.

Tojkander, S., Gateva, G., and Lappalainen, P. (2012) Actin stress fibers--assembly, dynamics and biological roles. *J Cell Sci* 125(Pt 8):1855-1864.

Toms, A.-M., Davies, M.L., Hargest, R., Hiscox, S.E., and Jiang, W.G. (2012) Distribution and expression of the ERM family members, ezrin, radixin, moesin and EHM2 in human colon cancer and the clinical relevance. *Translational Gastrointestinal Cancer* 1(3):205-214.

Tozluoglu, M., Tournier, A.L., Jenkins, R.P., Hooper, S., Bates, P.A., and Sahai, E. (2013) Matrix geometry determines optimal cancer cell migration strategy and modulates response to interventions. *Nat Cell Biol* 15(7):751-762.

Trickey, W.R., Baaijens, F.P., Laursen, T.A., Alexopoulos, L.G., and Guilak, F. (2006) Determination of the Poisson's ratio of the cell: recovery properties of chondrocytes after release from complete micropipette aspiration. *J Biomech* 39(1):78-87.

Trickey, W.R., Lee, G.M., and Guilak, F. (2000) Viscoelastic properties of chondrocytes from normal and osteoarthritic human cartilage. *J Orthop Res* 18(6):891-898.

Tsukita, S., Oishi, K., Sato, N., Sagara, J., and Kawai, A. (1994) ERM family members as molecular linkers between the cell surface glycoprotein CD44 and actin-based cytoskeletons. *The Journal of cell biology* 126(2):391-401.

Tuan, R.S., Boland, G., and Tuli, R. (2003) Adult mesenchymal stem cells and cell-based tissue engineering. *Arthritis Research and Therapy* 5(1):32-45.

Ušaj, M., Trontelj, K., Hudej, R., Kandušer, M., and Miklavčič, D. (2009) Cell size dynamics and viability of cells exposed to hypotonic treatment and electroporation for electrofusion optimization. *Radiology and Oncology* 43(2):108-119.

Vallenius, T. (2013) Actin stress fibre subtypes in mesenchymal-migrating cells. *Open Biol* 3(6):130001.

Verkhovsky, A.B., Svitkina, T.M., and Borisy, G.G. (1995) Myosin II filament assemblies in the active lamella of fibroblasts: their morphogenesis and role

in the formation of actin filament bundles. *The Journal of Cell Biology* 131(4):989-1002.

Vogel, V. and Sheetz, M. (2006) Local force and geometry sensing regulate cell functions. *Nat Rev Mol Cell Biol* 7(4):265-275.

Wagner, D.R., Lindsey, D.P., Li, K.W., Tummala, P., Chandran, S.E., Smith, R.L., Longaker, M.T., Carter, D.R., and Beaupre, G.S. (2008) Hydrostatic pressure enhances chondrogenic differentiation of human bone marrow stromal cells in osteochondrogenic medium. *Ann Biomed Eng* 36(5):813-820.

Wang, C., Cowen, C., Zhang, Z., and Thomas, C. (2005) High-speed compression of single alginate microspheres. *Chemical engineering science* 60(23):6649-6657.

Weibel, D.B., Diluzio, W.R., and Whitesides, G.M. (2007) Microfabrication meets microbiology. *Nat Rev Microbiol* 5(3):209-218.

Welch, M.D. (2015) Cell Migration, Freshly Squeezed. *Cell* 160(4):581-582.

Wickman, G., Julian, L., Mardilovich, K., Schumacher, S., Munro, J., Rath, N., Zander, S.A., Mleczak, A., Sumpton, D., and Morrice, N. (2013) Blebs produced by actin–myosin contraction during apoptosis release damage-associated molecular pattern proteins before secondary necrosis occurs. *Cell Death & Differentiation* 20(10):1293-1305.

Witkowska-Zimny, M., Walenko, K., Ewa Walkiewicz, A., Pojda, Z., Przybylski, J., and Lewandowska-Szumiel, M. (2012) Effect of substrate stiffness on differentiation of umbilical cord stem cells. *Acta Biochimica Polonica* 59(2):261.

Wu, L. and Derynck, R. (2009) Essential role of TGF-beta signaling in glucose-induced cell hypertrophy. *Dev Cell* 17(1):35-48.

Xue, F., Janzen, D.M., and Knecht, D.A. (2010) Contribution of filopodia to cell migration: a mechanical link between protrusion and contraction. *International journal of cell biology* 2010.

Yap, B. and Kamm, R.D. (2005) Mechanical deformation of neutrophils into narrow channels induces pseudopod projection and changes in biomechanical properties. *Journal of Applied Physiology* 98(5):1930-1939.

Yeung, T., Georges, P.C., Flanagan, L.A., Marg, B., Ortiz, M., Funaki, M., Zahir, N., Ming, W., Weaver, V., and Janmey, P.A. (2005) Effects of substrate stiffness on cell morphology, cytoskeletal structure, and adhesion. *Cell motility and the cytoskeleton* 60(1):24-34.

Yim, E.K., Darling, E.M., Kulangara, K., Guilak, F., and Leong, K.W. (2010) Nanotopography-induced changes in focal adhesions, cytoskeletal organization, and mechanical properties of human mesenchymal stem cells. *Biomaterials* 31(6):1299-1306.

Youn, I., Choi, J.-B., Cao, L., Setton, L., and Guilak, F. (2006) Zonal variations in the three-dimensional morphology of the chondron measured< i> in situ</i> using confocal microscopy. *Osteoarthritis and cartilage* 14(9):889-897.

Yourek, G., Hussain, M.A., and Mao, J.J. (2007) Cytoskeletal changes of mesenchymal stem cells during differentiation. *ASAIO J* 53(2):219-228.

Yu, H., Tay, C.Y., Leong, W.S., Tan, S.C., Liao, K., and Tan, L.P. (2010) Mechanical behavior of human mesenchymal stem cells during adipogenic and osteogenic differentiation. *Biochem Biophys Res Commun* 393(1):150-155.

Zahalak, G.I., McConnaughey, W.B., and Elson, E.L. (1990) Determination of cellular mechanical properties by cell poking, with an application to leukocytes. *J Biomech Eng* 112(3):283-294.

Zhang, Z., Ferenczi, M., and Thomas, C. (1992) A micromanipulation technique with a theoretical cell model for determining mechanical properties of single mammalian cells. *Chemical engineering science* 47(6):1347-1354.

Zhao, R., Wyss, K., and Simmons, C.A. (2009) Comparison of analytical and inverse finite element approaches to estimate cell viscoelastic properties by micropipette aspiration. *J Biomech* 42(16):2768-2773.

Zhao, T., Ling, Z.Q., Yu, W.Q., Long, M., and Cai, S.X. (2002) Adhesive properties of hepatoma cells to collagen IV coated surfaces. *Hepatobiliary Pancreat Dis Int* 1(4):565-569.

Zhao, Z., Watt, C., Karystinou, A., Roelofs, A.J., McCaig, C.D., Gibson, I.R., and De Bari, C. (2011) Directed migration of human bone marrow mesenchymal stem cells in a physiological direct current electric field. *Eur Cell Mater* 22:344-358.

Zheng, C., Yu, Z., Zhou, Y., Tao, L., Pang, Y., Chen, T., Zhang, X., Qiu, H., Zhou, H., Chen, Z., and Huang, Y. (2012) Live cell imaging analysis of the epigenetic regulation of the human endothelial cell migration at single-cell resolution. *Lab Chip* 12(17):3063-3072.

Zhu, L., Zhou, R., Mettler, S., Wu, T., Abbas, A., Delaney, J., and Forte, J.G. (2007) High turnover of ezrin T567 phosphorylation: conformation, activity, and cellular function. *Am J Physiol Cell Physiol* 293(3):C874-884.

PUBLICATIONS AND CONFERENCES

Publications

Sliogeryte K, SD Thorpe, DA Lee, L Botto and MM Knight. 2014. Stem cell differentiation increases membrane-actin cortex adhesion regulating cell blebability, migration and mechanics. Scientific Reports 4:7307.

Sliogeryte K, SD Thorpe, N Gavara and MM Knight. LifeAct-GFP enables actin visualization without disruption of cell and actin biomechanics. In revision.

Sliogeryte K, L Botto and MM Knight. Chondrocyte dedifferentiation in monolayer increases cell stiffness by strengthening membrane-actin adhesion. In preparation

Conferences

"Stem cell differentiation increases membrane-actin adhesion regulating cell blebability, migration and mechanics"
K. Sliogeryte, S.D. Thorpe, D. A. Lee, L. Botto and M.M. Knight
Medical Engineering Centres Annual Meeting and Bioengineering14, London, UK September 2014 **Oral Presentation**

"Change in membrane-actin cortex bond strength mediate alterations in cell mechanics during stem cell differentiation"
K. Sliogeryte, S.D. Thorpe, L. Botto, M.M. Knight
7th World Congress of Biomechanics, Boston, Massachusetts, USA, July 2014 **Poster Presentation**

"Chondrogenic differentiation regulates cell mechanics and migration by strengthening the interaction between the cell membrane and cortical actin"
K. Sliogeryte, S.D. Thorpe, M.M. Knight
7th UK Mesenchymal Stem Cell Meeting, Birmingham, UK, September 2013
Poster Presentation